



UNIVERSITAT DE
BARCELONA

Deciphering the utility of *Galleria mellonella* as an infection and toxicity *in vivo* model

Laura Moya

ADVERTIMENT. La consulta d'aquesta tesi queda condicionada a l'acceptació de les següents condicions d'ús: La difusió d'aquesta tesi per mitjà del servei TDX (www.tdx.cat) i a través del Dipòsit Digital de la UB (diposit.ub.edu) ha estat autoritzada pels titulars dels drets de propietat intel·lectual únicament per a usos privats emmarcats en activitats d'investigació i docència. No s'autoritza la seva reproducció amb finalitats de lucre ni la seva difusió i posada a disposició des d'un lloc aliè al servei TDX ni al Dipòsit Digital de la UB. No s'autoritza la presentació del seu contingut en una finestra o marc aliè a TDX o al Dipòsit Digital de la UB (framing). Aquesta reserva de drets afecta tant al resum de presentació de la tesi com als seus continguts. En la utilització o cita de parts de la tesi és obligat indicar el nom de la persona autora.

ADVERTENCIA. La consulta de esta tesis queda condicionada a la aceptación de las siguientes condiciones de uso: La difusión de esta tesis por medio del servicio TDR (www.tdx.cat) y a través del Repositorio Digital de la UB (diposit.ub.edu) ha sido autorizada por los titulares de los derechos de propiedad intelectual únicamente para usos privados enmarcados en actividades de investigación y docencia. No se autoriza su reproducción con finalidades de lucro ni su difusión y puesta a disposición desde un sitio ajeno al servicio TDR o al Repositorio Digital de la UB. No se autoriza la presentación de su contenido en una ventana o marco ajeno a TDR o al Repositorio Digital de la UB (framing). Esta reserva de derechos afecta tanto al resumen de presentación de la tesis como a sus contenidos. En la utilización o cita de partes de la tesis es obligado indicar el nombre de la persona autora.

WARNING. On having consulted this thesis you're accepting the following use conditions: Spreading this thesis by the TDX (www.tdx.cat) service and by the UB Digital Repository (diposit.ub.edu) has been authorized by the titular of the intellectual property rights only for private uses placed in investigation and teaching activities. Reproduction with lucrative aims is not authorized nor its spreading and availability from a site foreign to the TDX service or to the UB Digital Repository. Introducing its content in a window or frame foreign to the TDX service or to the UB Digital Repository is not authorized (framing). Those rights affect to the presentation summary of the thesis as well as to its contents. In the using or citation of parts of the thesis it's obliged to indicate the name of the author.



UNIVERSITAT DE
BARCELONA

Deciphering the utility of *Galleria mellonella* as
an infection and toxicity *in vivo* model

Laura Moya Andérico

Doctoral Thesis



UNIVERSITAT DE
BARCELONA

UNIVERSIDAD DE BARCELONA

Programa de Doctorado en Biomedicina

Deciphering the utility of *Galleria mellonella* as
an infection and toxicity *in vivo* model

Memoria presentada por Laura Moya Andérico para optar
al grado de Doctora por la Universidad de Barcelona

Director y tutor de tesis: Dr. Eduard Torrents Serra

Barcelona, diciembre 2020

Laura Moya Andérico

To my mother

Table of contents

List of figures.....	VI
Abbreviations	VII
Abstract.....	VIII
INTRODUCTION.....	1
1. The biology of <i>Galleria mellonella</i>	1
1.1. Taxonomy.....	1
1.2. Life cycle	1
1.2.1. Egg stage.....	1
1.2.2. Larva stage.....	2
1.2.3. Pupa stage	2
1.2.4. Adult stage.....	3
2. The immune system of <i>Galleria mellonella</i>	3
2.1. Physical and anatomical barriers	3
2.2. Innate immune system	3
2.2.1. Cellular immune responses	3
2.2.1.1. Hemocyte-driven phagocytosis.....	4
2.2.1.2. Hemocyte-driven encapsulation	5
2.2.1.3. Hemocyte-driven nodulation.....	5
2.2.1.4. Similarities with the mammalian innate immune system.....	5
2.2.2. Humoral immune responses	6
2.2.2.1. Melanization	6
2.2.2.2. Hemolymph clotting	7
2.2.2.3. Antimicrobial peptides.....	7
2.2.2.4. Reactive oxygen species	9
2.2.2.5. Immunological priming.....	9
3. <i>Galleria mellonella</i> as a model of infection	10
3.1. <i>Pseudomonas aeruginosa</i>	11
3.1.1. Ribonucleotide reductases.....	13
3.1.2. <i>P. aeruginosa</i> studies in <i>G. mellonella</i>	15
3.2. <i>Staphylococcus aureus</i>	16
3.2.1. <i>S. aureus</i> studies in <i>G. mellonella</i>	19

3.3. <i>Mycolicibacterium brumae</i>	20
3.4. Antimicrobial studies in <i>G. mellonella</i>	20
3.4.1. Antimicrobial efficacy studies against <i>S. aureus</i> in <i>G. mellonella</i>	22
3.5. Limitations in the use of <i>G. mellonella</i> as an infection model	24
4. <i>Galleria mellonella</i> as a model of toxicity	25
4.1. Toxicity studies in <i>G. mellonella</i>	26
4.1.1. Toxicity studies involving nanoparticles in <i>G. mellonella</i>	28
5. Methodology approaches in <i>G. mellonella</i>	30
5.1. Tissue clearing techniques	31
OBJECTIVES	34
ARTICLES	35
Article 1	35
Monitoring Gene Expression during a <i>Galleria mellonella</i> Bacterial Infection	54
Article 2	54
Novel Oleanolic and Maslinic Acid Derivatives as a Promising Treatment against Bacterial Biofilm in Nosocomial Infections: An in Vitro and in Vivo Study	74
Article 3	74
Utility of <i>Galleria mellonella</i> Larvae for Evaluating Nanoparticle Toxicology	87
Article 4	87
A Clearing Protocol for <i>Galleria mellonella</i> Larvae: Visualization of Internalized Fluorescent Nanoparticles	95
SUMMARY OF THE RESULTS PRESENTED	95
Report on the impact factor of the articles presented	101
Report on the participation in the articles presented	102
DISCUSSION	103
<i>Galleria mellonella</i> as an animal model of infection	103
Bacterial infection studies in <i>Galleria mellonella</i>	104
Antimicrobial efficacy studies in <i>G. mellonella</i>	107
Toxicity studies in <i>G. mellonella</i>	108
Methodology advances in <i>G. mellonella</i>	111
CONCLUSIONS	116
REFERENCES	118
APPENDIX	134

LIST OF FIGURES

Figure 1. The different developmental stages in the life cycle of <i>Galleria mellonella</i>	1
Figure 2. Hemocytes found in <i>Galleria mellonella</i>	4
Figure 3. Simplified representation of the cellular immune processes in <i>G. mellonella</i>	5
Figure 4. Melanization in <i>G. mellonella</i> larvae.....	6
Figure 5. Predicted protein structure of the main AMPs found in <i>Galleria mellonella</i> larvae.....	8
Figure 6. Simplified representation of the differences between acute and chronic <i>P. aeruginosa</i> infections.	13
Figure 7. Graphical representations of bacterial ribonucleotide reductases	14
Figure 8. Simplified representation of a few of the <i>S. aureus</i> virulence factors that are mentioned in section 3.2.....	18
Figure 9. Antimicrobial strategies tested in the <i>G. mellonella</i> model.....	22
Figure 10. Proposed addition of <i>G. mellonella</i> into the traditional drug development pathway.....	28
Figure 11. Overview of tissue clearing classification and methods	32

ABBREVIATIONS

AgNPs	Silver Nanoparticles
AuNPs	Gold Nanoparticles
Au(HAL)NPs	AuNPs functionalized with histidine, arginine, and lysine
AMPs	Antimicrobial Peptides
BABB	Benzyl Alcohol and Benzyl Benzoate
CC ₅₀	Cytotoxicity 50%
CF	Cystic Fibrosis
CFU	Colony-Forming Unit
CLSM	Confocal Laser Scanning Microscopy
COPD	Chronic Obstructive Pulmonary Disease
GFP	Green Fluorescent Protein
LB	Luria-Bertani medium
LD ₅₀	Median lethal dose
LPS	Lipopolysaccharides
MA	Maslinic Acid
MRSA	Methicillin-Resistant <i>Staphylococcus aureus</i>
NPs	Nanoparticles
<i>nrd</i>	<i>Nucleotide reduction</i> (gene encoding for an RNR)
OD	Optical Density
OA	Oleanolic Acid
PFA	Paraformaldehyde
<i>PnrdA</i>	Promoter for the <i>nrdA</i> gene
<i>PnrdJ</i>	Promoter for the <i>nrdJ</i> gene
<i>PnrdD</i>	Promoter for the <i>nrdD</i> gene
<i>PnrdR</i>	Promoter for the <i>nrdR</i> gene
PO	Phenoloxidase
ProPO	Prophenoloxidase
qRT-PCR	Quantitative Real-Time PCR
RFU	Relative Fluorescence Units
RI	Refraction Index
RLU	Relative Luminescence Units
RNR	Ribonucleotide Reductase
ROS	Reactive Oxygen Species
SI	Selectivity Index
T3SS	Type 3 Secretion System

ABSTRACT

Galleria mellonella (greater wax moth) is a popular animal model that has been extensively used as an alternative *in vivo* model for investigating the virulence and pathogenicity of different bacteria. *G. mellonella* has also been shown to be a suitable model for studying the efficacy and toxicity of various compounds. Recently, this model has been gaining popularity as the larvae are conveniently sized for manipulation, they do not need constant feeding, they are inexpensive to purchase and to breed, they do not require much space or special infrastructure, they present a low biohazard risk, and they are more ethically accepted. More importantly, *G. mellonella* has an innate immune system very similar to the one found in mammals. In this thesis, *G. mellonella* was used to develop a standardized and reproducible animal model of infection and toxicity.

Pseudomonas aeruginosa is an opportunistic pathogen that has gained great medical importance as it causes serious illnesses in humans and it can be resistant to many antibiotics. During infection, ribonucleotide reductases (RNR) play an essential role as they catalyze the reduction of ribonucleotides to deoxyribonucleotides, thus providing the precursor molecules needed for DNA synthesis. Since *G. mellonella* has been proven to be a suitable model for *P. aeruginosa* infections, we developed a promoter probe vector with bioluminescence expression to enhance the study and monitoring of a *P. aeruginosa in vivo* infection. This vector was used to construct different RNR gene promoter fusions as proof of concept. Additionally, we optimized a total bacterial RNA extraction protocol to facilitate the study of transcriptional gene levels during *in vivo* infections. By implementing both methods, variable gene expression levels were efficiently measured at different time points throughout the course of a bacterial infection.

Staphylococcus aureus is also considered an opportunistic pathogen. This bacterium is also capable of forming biofilms and it is considered an important cause of biofilm formation in catheters and prostheses. Due to the misuse and overuse of antimicrobials, multi-resistant bacteria are rapidly appearing so there is a critical need for new antimicrobials. The toxicity and antimicrobial efficacy against *S. aureus* of novel oleanolic and maslinic acid derivatives were determined using *G. mellonella*. Out of the 14 derivatives tested, 2 were found to have improved toxicity and efficacy *in vivo* when compared to the *in vitro* results. Therefore, *G. mellonella* can be used as an efficient screening alternative for determining *in vivo* toxicity and efficacy of new antimicrobials before their use in rodents or other more expensive models.

G. mellonella was also used to test the toxicity of other therapeutical strategies and nanoparticles (NPs). *Mycobacterium brumae* was not toxic to *G. mellonella* larvae, and the results

correlated with the results obtained with mice. Therefore, *M. brumae* was deemed as a safe alternative treatment for non-muscle-invasive bladder cancer. The different NPs caused a variety of acute toxicity effects that were detected by an array of indicators within the larvae, such as lethal dose calculation, hemocyte proliferation, NP distribution, behavioral changes, and histological alterations. Therefore, *G. mellonella* is proposed as an alternative non-rodent model of toxicity that can be used as a bridge between *in vitro* and *in vivo* rodent assays.

Due to the broad applicability of the *G. mellonella* model, new methodologies are warranted to exploit its full potential. Besides the optimized RNA extraction protocol already mentioned, an optical clearing protocol was also optimized in this work. As a proof of concept for our larvae clearance protocol, fluorescent rhodamine NPs were injected into larvae that were then fixed with paraformaldehyde, permeabilized with increasing concentrations of methanol, and cleared with BABB (Benzyl Alcohol and Benzyl Benzoate). Visual observations of the internalized NPs were achieved in cleared larvae using confocal microscopy. Quantification of the relative fluorescence emitted by the internalized NPs was also possible only in the cleared larvae.

INTRODUCTION

1. The biology of *Galleria mellonella*

1.1. Taxonomy

Galleria mellonella is also known as the greater wax moth or honeycomb moth. These aliases are derived from the ubiquitous presence of this moth in honeybee colonies. For this reason, they are considered a major pest of honeycombs worldwide as they damage beehives and hive products which has important economic and climatic consequences. *G. mellonella* is a member of the *Galleriinae* subfamily within the *Pyralidae* family of the Lepidopteran order [1,2].

1.2. Life cycle

The life cycle of *G. mellonella* is composed of four main stages: egg, larva, pupa, and adult (Figure 1). The duration of the cycle can vary from weeks to months and it depends on a variety of biotic and abiotic factors. Some examples of biotic factors include competition for food, cannibalism, parasitoids, and diet quality [2-5]. Abiotic factors such as temperature and humidity also have a critical impact on the life cycle. Temperatures ranging from 29-35°C with high humidity (about 70%) are reported as ideal for an optimal life cycle. Under these ideal conditions, the duration of a cycle is about 6 weeks [1,2,6,7].



Figure 1. The different developmental stages in the life cycle of *Galleria mellonella*. First is the egg stage followed by the different larvae instar phases. The pupa (right) is found inside a white cocoon (left). As seen in the adult figure insert, the adult moth can be differentiated in male (left) and female (right). Adapted from [1,8].

1.2.1. Egg stage

Female moths lay eggs in clusters of 50-150. The color of the eggs ranges from pearly white to light pink and they have a rough texture due to scattered wavy lines on their surface. The eggs are

spherically shaped with an average length of 0.478 mm and an average width of 0.394 mm [1,2]. This stage can last anywhere between 3 and 30 days depending on the temperature of the environment. At warm temperatures (29-35°C), the eggs will develop in a few days but at cold temperatures (18°C), the development can be delayed by 30 days. Eggs cannot survive in temperatures $\leq 0^{\circ}\text{C}$ or $\geq 46^{\circ}\text{C}$ [1,2,9].

1.2.2. Larva stage

Recently-hatched larvae have an off-white color and measure about 1-3 mm in length and 0.12-0.15 mm in diameter. Fully grown larvae can measure up to 25-30 mm and 5-7 mm in length and diameter, respectively, and the color darkens to a cream-color with gray to dark gray markings. The larvae are poly pod with 6 legs on the thorax and 8 prolegs between the third and sixth abdominal segments. During the larval stage, male and female sexing is not possible as sex-specific external morphological traits are not yet present. The larva can molt 8-10 times throughout its development and release silk threads in all stages but only the last instar can spin a silk cocoon [1,7,10].

Upon hatching in nature, the larvae immediately begin feeding on honeycomb and eventually destroy the comb structure. In the laboratory, larvae can be maintained on an artificial diet consisting of honey, wax, and cereal products. Early instar larvae feed more intensively compared to late instar ones. If the diet and temperature conditions are favorable, early instars grow at a surprisingly accelerated rate with the majority of the increases in growth and size occurring during the last two final instar stages. Under optimal conditions (29-32°C with abundant food), the larval stage lasts 6 to 7 weeks but can be increased up to 5 months if there is a shortage of food and cold temperatures [1,2,9,10].

1.2.3. Pupa stage

The pupa is found immobile within a white silk cocoon. When pupation begins, the color is white to yellow but it gradually changes to brown and dark brown as the pupa develops. The average pupa measures 12-20 mm and 5-7 mm in length and diameter, respectively. At this stage, sexual dimorphism is first evident as females develop a cloven sternum representing the copulatrix's aperture on the eighth abdominal segment. On the other hand, males acquire a pair of external rounded knobs representing the phallomeres on the ninth abdominal segment. The duration of this stage ranges from 1 to 9 weeks, and it is temperature-dependent as higher temperatures shorten the duration [2,9,10].

1.2.4. Adult stage

The adult moth has grayish-brown forewings and cream-colored hindwings. The average adult moth is about 15-19 mm long with a 14-38 mm wingspan. The male moth is slightly smaller than the female moth and is easily distinguishable by many additional characteristics: lighter wing color, indented and scalloped front wing, shorter antennae, and snub-nosed appearance. Adult moths do not feed, and female moths lay an average of 300-600 eggs about 4-10 days after emergence from pupation. Females will continue laying eggs as long as their vitality lasts and can deposit more than 100 eggs in 1 minute. Female moths live for about 12 days while male moths live for approximately 21 days and the lifespan can be increased if they are kept at colder temperatures [1,2,9,10].

2. The immune system of *Galleria mellonella*

G. mellonella fights off intruders with physical and anatomical barriers as well as with innate immune defenses. The larval stage of *G. mellonella* is commonly used as an *in vivo* model for studying pathogenesis, virulence, and toxicity and efficacy of new drugs, among other uses. The main reason for this is that the larvae have an innate immune system that closely resembles the one found in mammals. Additionally, the larvae can withstand incubation at 37°C which allows experiments to be performed at the same temperature as the human body. Unlike mammals, *G. mellonella* larvae do not have adaptive immunity [11,12].

2.1. Physical and anatomical barriers

The larval cuticle is composed of a single layer of epithelium that is soaked with chitin and is found on the basal membrane. This hardened cover protects the worm against physical injury and pathogen entry, similarly to mammalian skin [13]. The trachea also possesses antimicrobial features such as chitin lining, low humidity, and lack of nutrients. The oral infection route is further protected by a chitin lining in both the foregut and hindgut and by the unfavorable biochemical conditions of the gut. Additionally, there is antibiosis and competition in the gut. All of these barriers prevent microorganisms from infecting the larvae [11].

2.2. Innate immune system

2.2.1. Cellular immune responses

The cellular responses in *G. mellonella* are mediated by hemocytes, which are found in free circulation within the hemolymph (analogous to mammalian blood, found within the hemocoel) or

attached to internal organs such as the digestive tract or fat body [14]. Hemocytes are involved in phagocytosis, encapsulation, and nodulation [15]. Hemocyte levels in the hemolymph can fluctuate during different processes. An increased level is associated with the movement of hemocytes from internal organs to the hemolymph in response to foreign intruders such as microorganisms and toxic compounds [16,17]. On the other hand, decreased hemocyte levels have been linked to nodulation or encapsulation processes during infection [18].

In *G. mellonella*, there are at least five types of hemocytes: prohemocytes, plasmatocytes, granulocytes, oenotocytes, and spherulocytes. The most predominant hemocytes found in *G. mellonella* larvae are plasmatocytes and granulocytes, and these are the ones involved in the majority of cellular defenses [19]. An image and a brief description of each type of hemocyte can be found in Figure 2.

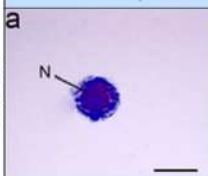
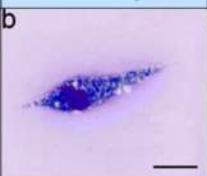
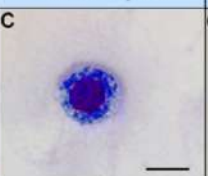
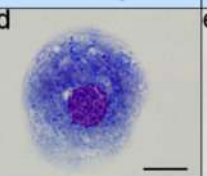
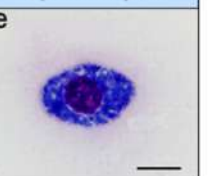
	Prohemocytes	Plasmatocytes	Granulocytes	Oenotocytes	Spherulocytes
IMAGES					
DESCRIPTION	<ul style="list-style-type: none"> • Small and circular cells • Contain a large nucleus and a basophilic cytoplasm • Can differentiate into various cell types 	<ul style="list-style-type: none"> • Most common hemocyte • Shaped like a leaf • The cytoplasm contains lysosomal enzymes • Participate in phagocytosis and capsule formation 	<ul style="list-style-type: none"> • Most common hemocyte • Small nucleus • Abundant granules are found in the cytoplasm • Indirectly involved in phagocytosis • Directly involved in encapsulation 	<ul style="list-style-type: none"> • Large and bi-nucleated spherule cells • Non-adhesive and non-phagocytic cells • Contain components of the phenoloxidase cascade 	<ul style="list-style-type: none"> • Display various shapes • Contain many small spherical inclusions • Transport and secrete components of the cuticle • Role in immunity not yet fully understood

Figure 2. Hemocytes found in *Galleria mellonella*. Top row (a-e): light microscopy images of stained hemocytes. Scale bar: 5 μ m. Adapted from [20]. Bottom row: Morphology and functions of the different types of hemocytes. Information gathered from [15,19,21].

2.2.1.1. Hemocyte-driven phagocytosis

Phagocytosis in *G. mellonella* is mediated directly by plasmatocytes and indirectly by granulocytes [22]. During this process, hemocytes engulf pathogens and release enzymes through degranulation to destroy them (Figure 3A). For phagocytosis to occur, hemocytes first need to recognize the target as foreign. Pathogens are recognized by humoral pattern recognition molecules or by hemocyte receptors such as calreticulin and apolipoprotein. Once opsonic ligands bind and recognize external molecules of the pathogens, an intracellular cascade is triggered which ends with the internalization of the pathogen. Then, a membrane-bound enzyme system is activated,

superoxide is produced, and degranulation begins releasing enzymes that not only kill the pathogen but also trigger inflammatory responses and local tissue damage in the infection area [15,23].

2.2.1.2. Hemocyte-driven encapsulation

In *G. mellonella*, encapsulation is mediated by granulocytes. These cells recognize the presence of large intruders such as protozoa, nematodes, and parasitic insect eggs or larvae in the hemolymph [24]. Granulocytes degrade upon contact with the intruders, which promotes the binding of plasmatocytes [25]. A smooth capsule is formed by superimposed layers of plasmatocytes around the foreign object (Figure 3B). During the formation of the capsule, the number of circulating hemocytes decreases as they are focused on this process. Once the capsule is complete, there is an increase of hemocytes with enzymatic activity [26].

2.2.1.3. Hemocyte-driven nodulation

Nodulation is the main cellular defense in response to an infection as large quantities of bacteria can be cleared from the hemolymph by the binding of multiple hemocytes to bacterial clusters (Figure 3C). The group of hemocytes bind together and form an overlapping sheath around the bacteria followed by the activation of prophenoloxidase and melanization of nodules [15,19].

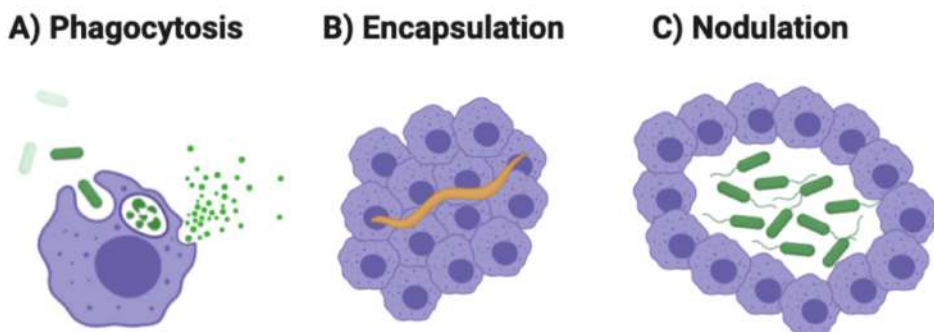


Figure 3. Simplified representation of the cellular immune processes in *G. mellonella*. **A)** Phagocytosis: hemocytes internalize and destroy pathogen. **B)** Encapsulation: Hemocytes form a capsule around a large pathogen (e.g., nematode). **C)** Nodulation: Hemocytes layer around a large group of bacteria. Created with BioRender.com.

2.2.1.4. Similarities with the mammalian innate immune system

As previously mentioned, the innate immune system of *G. mellonella* closely resembles the innate immune system of mammals. The latter has phagocytes such as macrophages, neutrophils, and dendritic cells that function similarly to plasmatocytes and granulocytes found in *G. mellonella* by their quick activation and defense against infection. Other similar functions in mammals are the recruitment of immune cells to the infection site, detection and elimination of foreign objects by

specialized phagocytic cells, and antigen presentation on the cell surface to trigger the activation of the immune system, among others [15]. Both types of immune systems have effectors and receptors alike and also regulate gene expression in a related manner. An example of this is that plasmatocytes and granulocytes have surface receptors, like calreticulin, that are similar to the ones found in mammalian neutrophils [27]. Another example is that the method for superoxide production in hemocytes is almost identical to the one in human phagocytes [15].

2.2.2. Humoral immune responses

The humoral immune response of *G. mellonella* involves melanization, clotting, antimicrobial peptide synthesis, and reactive oxygen species. All play an important role in the final defense against pathogens.

2.2.2.1. Melanization

The phenoloxidase (PO) enzyme oxidizes phenolic substances to quinones that are later converted to melanin, resulting in the blackening of the trauma site. PO is generally found in both prokaryotes and eukaryotes in its inactive form as a proenzyme called prophenoloxidase (ProPO). In *G. mellonella*, ProPO was one of the first immune-related molecules found. Purified and characterized in 1995 and 2012, respectively, this proenzyme is present in the hemocytes (mainly oenocytoides) of unchallenged *G. mellonella* [28-30]. After pathogen recognition, oenocytoides release the enzyme which becomes activated by cascades of serine proteases. The ProPO complex ends with: the darkening of the infected larvae, the generation of products that are toxic to invading pathogens, and the trigger of other antimicrobial molecules to help fight off infection [31]. The extent of melanization often relates to larval health as higher larval mortality is associated with higher levels of melanization [12] (Figure 4).

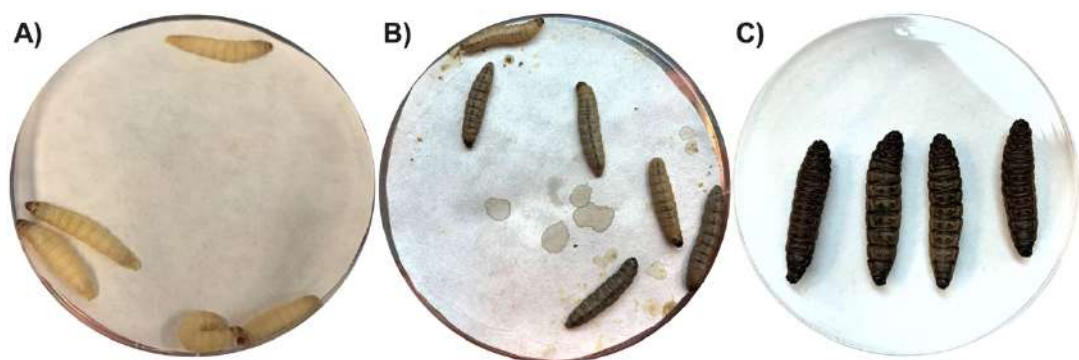


Figure 4. Melanization in *G. mellonella* larvae. **A)** Healthy larvae. **B)** Melanization taking over the larvae in response to bacterial infection. **C)** Fully melanized larvae that died from the infection.

Melanization also takes part during wound healing, sclerotization, and cuticle hardening. Furthermore, it aids with the encapsulation and nodulation of parasites and microbes during the cellular immune response [32]. Although the ProPO system is described as part of the humoral immune system, it also involves cellular components such as ProPO itself [33]. The activation of the ProPO cascade has been reported to be similar to the complement system found in mammals [34].

2.2.2.2. Hemolymph clotting

Hemolymph clotting, also known as coagulation, is a complex yet necessary process for hemostasis, healing, and immunity. Clotting helps to seal wounds and prevent blood loss, a process similar to the one occurring in vertebrates. In *G. mellonella*, clotting is mediated by hemocytes, mainly granulocytes [12,35]. When an external wound occurs, initial soft clots consist of a fibrous matrix embedded with numerous granulocytes and then, the clot hardens due to protein cross-linking and melanization [21]. If hemocytes are removed from the hemolymph, the cell-free hemolymph does not clot which further demonstrates the important role of these cells during clotting. Besides hemocytes, clotting also involves soluble factors such as transglutaminase, lipophorin, and apolipoproteins [36]. Coagulation is inhibited by chelating Ca^{+2} , so the presence of Ca^{+2} is also critical for coagulation [33].

Similar to platelets in mammals, hemocytes are activated after stimulation and become highly adhesive. But unlike platelets, hemocytes can contribute to microbial clearance by participating in nodulation and melanization [37]. The activation of the prophenoloxidase (ProPO) cascade links the coagulation cascade and melanization process [33,38]. The ProPO cascade and clotting are both activated by components present on the cell wall of microorganisms like lipopolysaccharides. Then, melanized nodules form and trap bacteria, but it is not known whether clotting also plays a role in the killing of the bacteria [36]. The activation of the coagulation process is also dependent on the presence of extracellular nucleic acids that are released from activated oenocytoides and damaged tissues [37].

2.2.2.3. Antimicrobial peptides

Antimicrobial peptides (AMPs) are small and cationic molecules that have broad-spectrum activity against bacteria, fungi, parasites, and viruses. They can have many mechanisms of action, ranging from disintegrating membranes to containing intracellular processes such as protein synthesis [39,40]. AMPs are mainly produced in the hemocytes, fat body, digestive tract, salivary glands, and reproductive tract of insects [41].

When *G. mellonella* larvae are presented with an immune challenge, a plethora of structurally and functionally diverse AMPs are secreted. This varies according to the infecting pathogen. For instance, the AMPs released during a fungal infection are not the same as during a bacterial infection [42]. *G. mellonella* larvae have about 20 known or putative defense peptides and many of those have been found in the hemolymph of immune-challenged larvae [43-45]. The AMPs that have been reported most in the literature (Figure 5) are listed below:

- Cecropin: active against filamentous fungi and Gram-positive and Gram-negative bacteria [43].
- Galiomicin: insect defensin that lacks antimicrobial activity but is active against some filamentous fungi and yeast [44].
- Gallerimycin: defensin-like peptide that is active against filamentous fungi yet not against yeast or bacteria although its expression increases significantly during a bacterial infection [12,42].
- Gloverins and moricins: active against filamentous fungi as well as yeast, Gram-positive, and Gram-negative bacteria but to a lesser extent [46].

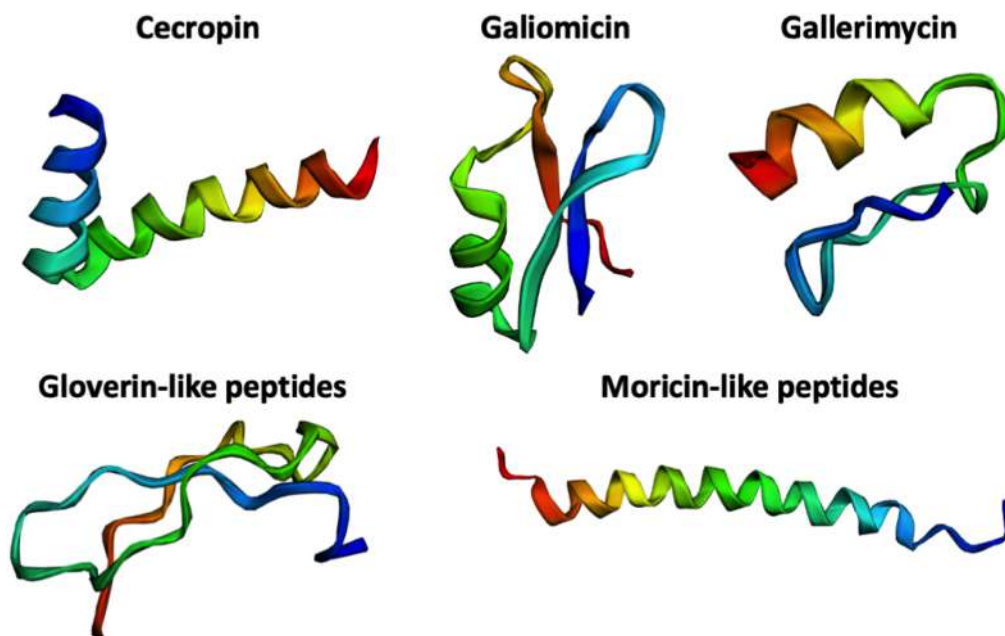


Figure 5. Predicted protein structure of the main AMPs found in *Galleria mellonella* larvae. Predictions obtained with Phyre2 [47] and visualized with EzMol [48]. The chain ribbon is colored using a rainbow gradient from the amino-terminus to the carboxyl-terminus of the protein. The protein sequences used for the predictions were: NCBI Reference Sequence XP_026754247.1 and XP_026757665.1 for cecropin and gloverin-like peptides, respectively, and GenBank accession number AAS19170.1, AAM46728.1, and ABQ42573.1 for galiomicin, gallerimycin, and moricin-like peptide A, respectively.

Additionally, there are immune-related proteins and peptides (e.g., lysozyme, apolipoprotein III, moricin-like peptides, among others) that are normally present in the hemolymph, become induced once there is a foreign body, and team up with other antimicrobial proteins and peptides to combat the infection [49,50]. The isolation and characterization of some of these antimicrobial peptides offer a promising prospect for the development of new antimicrobial therapies.

2.2.2.4. Reactive oxygen species

In human phagocytes, reactive oxygen species (ROS) are produced during phagocytosis and in response to pathogen destruction as these molecules are toxic to microorganisms [51,52]. Insects are also able to produce ROS as cytotoxic agents during defense responses against pathogens [53,54]. In *G. mellonella*, hemocytes are the main producers of ROS as they generate superoxide radicals, nitric oxide, and hydrogen peroxide during phagocytic and pathogen-destruction processes [55]. ROS can also be freely found in the hemolymph as hydrogen peroxide and superoxide; these are derived from enzymatic oxidation-reduction reactions resulting from the activation of the phenoloxidase (PO) cascade due to melanization [56,57]. The exact mechanism of ROS production in *G. mellonella* is unknown. Nevertheless, it is believed to be related to melanization through the activation of the PO cascade. The way PO is activated depends on the kind of infecting pathogen (bacteria or fungi) since it affects the different responses in the production of ROS. However, the correlation between different types of pathogen and specific ROS-production pathways is still unclear [12].

Tissue toxicity can be caused by non-selective ROS activity. Several antioxidant mechanisms exist in mammals to degrade ROS to prevent the cytotoxic activity on the organism [58]. In insects, antioxidant mechanisms have also been found that include enzymes such as superoxide dismutase, glutathione-S-transferase, and peroxidase [59,60]. In *G. mellonella*, antioxidant systems involving similar enzymes also exist. Furthermore, the antioxidant action of non-enzymatic components has also been reported [61].

2.2.2.5. Immunological priming

Besides innate immunity, mammals also have acquired or adaptive immunity which can develop memory responses and is mediated by B cells and T cells [62]. Although insects do not have acquired immunity, they have a similar phenomenon termed “immunological priming” which consists in exposing the insect to sublethal concentrations of a pathogen which causes an increase in hemocyte density and AMPs expression for 24-48h. When the insect is again exposed to the same

pathogen but at lethal concentrations, the insect resists and lives [12,63]. In *G. mellonella* larvae, immunological priming has been reported many times; a few examples are listed below:

- A study performed with *Candida albicans* demonstrated that larvae were able to resist lethal doses of the yeast due to an increase in AMPs expression after pre-exposure to a non-lethal dose [64].
- In another study, larvae were able to survive infection with *C. albicans* after previously receiving high doses of a polysaccharide found in the fungal cell wall called beta-glucan. High concentrations of glucan caused an increase in hemocyte density along with a decrease in yeast proliferation [65].
- In a different study, larvae were first primed with injections of heat-killed *Photobacterium luminescens* TT01 and *Bacillus thuringiensis* HD-1 strains. Then, the larvae were able to survive posterior injection with lethal doses of the same strains due to an elevated hemocyte density and an increased antimicrobial activity in the cell-free hemolymph of the primed larvae [66].

3. *Galleria mellonella* as a model of infection

For experiments using *G. mellonella* as an infection model, last instar larvae are generally used. These larvae are easy to manipulate as they measure 2-2.5 cm long and weigh about 250 mg. Before inoculation, the larvae can be stored at 15°C to delay pupation and it is recommended that the larvae are starved 24 hours prior to their inoculation [67]. Due to their relatively large size, the larvae can be easily and accurately infected by intrahemocoelic injection through the prolegs. Oral infection can also be done by ingestion or by force-feeding the larvae through the mouth, but this type of infection is less common. The results obtained with larvae infected with bacteria through injection have been consistently correlated with results from similar mammalian studies [67-69]. Before injecting the microbial inoculum into the larvae, it is important to first wash the cells to remove any virulence factors that were secreted during the bacterial *in vitro* growth [41]. Also, it is suggested to include a group of larvae injected with a placebo (e.g., PBS) so to control any potential physical trauma from the injection [70].

Infection studies can be carried out at temperatures ranging up to 37°C [70]. This is particularly significant as experiments can be done at the same temperature as the human body which is important for the expression of certain microbial virulence factors [71]. Microbial virulence can be assessed in various ways:

- Survival rate at different time points: larvae are injected with various doses of bacteria and the median lethal dose (LD₅₀) can be determined as the bacterial concentration required to kill 50% of the larvae [41].
- Expression of AMPs in response to infection: larvae are injected with bacteria and several hours post-infection, the hemolymph is extracted to measure levels of different AMPs [44].
- Degree of melanization: lethality of bacteria is determined by the melanization degree of the larvae after infection. Larvae that are completely melanized (all black) correlates with larval death [41].
- Measurement of bacterial proliferation inside the larvae: at different time points after infection, larval hemolymph, or homogenized larvae are plated on agar plates for bacterial enumeration [72]. Another method is using bioluminescent bacteria to determine bacterial load inside intact and infected larvae using bioluminescence imaging [73].

G. mellonella has been used as a model of infection for many microorganisms including *Acinetobacter baumannii* [74], *Burkholderia cenocepacia* [75], *Burkholderia cepacia* complex [76], *Campylobacter jejuni* [77], *Candida albicans* [78], *Escherichia coli* [79], *Mycobacterium abscessus* [80], *Mycobacterium tuberculosis* complex [81], *Pseudomonas aeruginosa* [82], *Staphylococcus aureus* [83], *Vibrio anguillarum* [84], and *Yersinia pseudotuberculosis* [85], among many others.

3.1. *Pseudomonas aeruginosa*

Pseudomonas aeruginosa is a Gram-negative, bacillus (rod-shaped) bacterium that is ubiquitous in soil and water, but it can also be found in plant, insect, and animal tissues [73,86]. This bacterium is considered an opportunistic pathogen and it is a major cause of hospital-acquired infections since it causes serious infection in patients who have a previous illness or are immunocompromised, especially in patients with chronic obstructive pulmonary disease (COPD), cancer, AIDS, and severe burns [87]. In fact, *P. aeruginosa* is the leading cause of death in patients with cystic fibrosis (CF) [88]. This pathogen also causes hospital-acquired pneumonia, gastrointestinal infections, urinary tract infections, dermatitis, skin infections (e.g. external otitis), bacteremia, soft tissue infections, bone and joint infections, among many others [87]. *P. aeruginosa* is naturally resistant to many antibiotics and has progressively developed multi-drug resistance which further limits the therapeutic options available. Some strains are resistant to almost all antibiotics including aminoglycosides, cephalosporins, fluoroquinolones, and carbapenems [88,89].

P. aeruginosa has a large genome (about 6.3 million base pairs long) with a wide repertoire of regulatory genes and networks that are the basis for the pathogen's ability to respond and adapt to diverse environments [90,91]. This pathogen is responsible for both acute and chronic infections. *P. aeruginosa* isolates from chronic infections are phenotypically different than those isolated from acute infections [92]. During acute infections, *P. aeruginosa* isolates express a wide variety of virulence factors such as adhesins (i.e., flagella and pili), lipopolysaccharides (LPS), and type 3 secretion system (T3SS). Flagella and pili play a major role in bacterial motility, adhesion to host cells, and initiation of the inflammatory response [87]. LPS is a complex glycolipid and main component of the outer membrane of Gram-negative bacteria that acts as a physical barrier and protects the bacteria from the host immune defenses. It also plays a part in the inflammatory response and antibiotic interactions [93]. T3SS allows the direct transfer of toxins from the bacteria to the host cells [87]. In contrast, isolates from chronic CF infections lack inflammatory factors (e.g. adhesins) while virulence mechanisms, such as the type 3 secretion system, are attenuated [94]. Instead, chronic isolates can readily form biofilms, and the strains become mucoid due to the overexpression of the exopolysaccharide alginate [95]. *P. aeruginosa* also has quorum sensing mechanisms that facilitate cell-to-cell communication to coordinate gene expression for environmental adaptation. The activation of these mechanisms promotes the formation of bacterial biofilms, which are bacterial communities embedded in an extracellular matrix that contain proteins, polysaccharides, and extracellular DNA. This matrix protects the bacteria by blocking the effects of immune cells, antibodies, and most antibiotics [96]. Since biofilms are highly resistant to antibiotics and disinfectants, they pose a serious medical problem. Biofilm development during chronic infections is associated with poor prognosis, worsened disease progression, and increased mortality [97]. A graphical summary depicting the differences between acute and chronic *P. aeruginosa* infections can be found in Figure 6.

P. aeruginosa also has other virulence factors that contribute to its pathogenicity such as proteases (disrupt epithelial tight junctions and degrade immunoglobulins and fibrin in the host), exotoxin A (inhibits protein synthesis in host cells), lipases and phospholipases (disrupt lipids and phospholipids in the host cell membrane), pyocyanin (causes oxidative stress to the host), and pyoverdine (sequesters iron from host storage), among others [87].

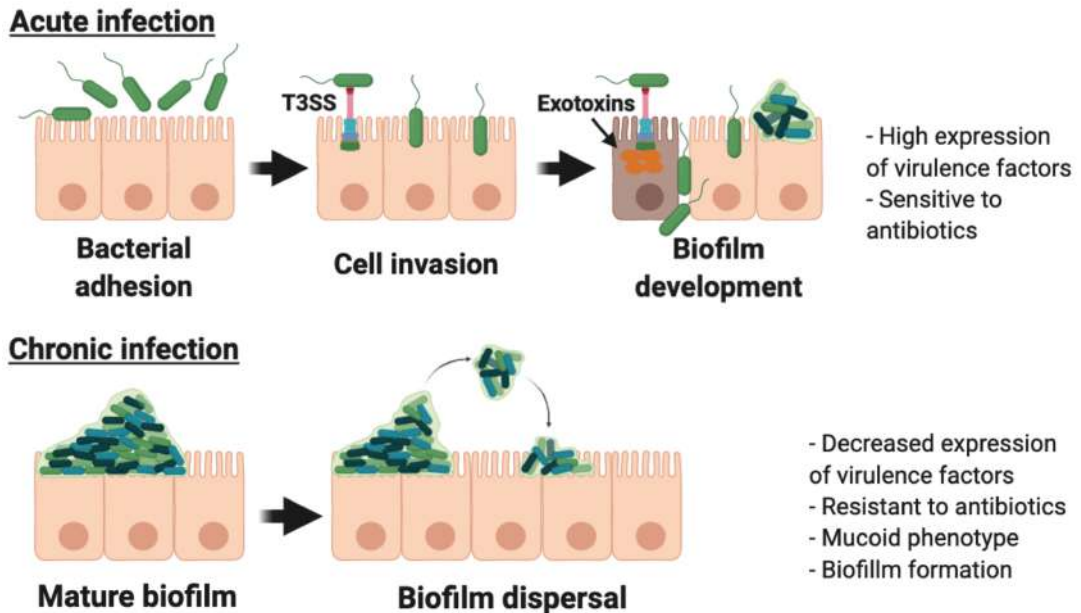


Figure 6. Simplified representation of the differences between acute and chronic *P. aeruginosa* infections. In acute infections, *P. aeruginosa* employs a variety of virulence features such as pili, flagella, T3SS, and secreted virulence factors. Damage to the epithelial cells facilitates initial biofilm development. In chronic infections, biofilm matures and disperses to neighboring cells to renew the biofilm formation cycle. Adapted from [98]. Created with BioRender.com.

3.1.1. Ribonucleotide reductases

P. aeruginosa must be able to replicate within its host to establish an infection, hence it needs an active DNA synthesis. Ribonucleotide reductases (RNR) are vital enzymes that catalyze the reduction of NTPs to dNTPs thus providing the precursor molecules required for DNA synthesis (Figure 7A). These enzymes require a protein radical to initiate catalysis. There are three classes of RNR: I, II, and III. Class I RNR is oxygen dependent as the radical is only generated under aerobic conditions. This class is further divided into three subclasses: Ia, Ib, and Ic. Class Ia is encoded by the *nrdAB* genes and requires a di-ferric center to generate the tyrosyl radical while class Ib is encoded by the *nrdHIEF* genes and requires a di-manganese or di-ferric center to generate the tyrosyl radical. Class Ic is also encoded by the *nrdAB* genes, but the tyrosyl radical is generated by a manganese-iron center instead. Class II RNR is encoded by a single *nrdJ* gene and it uses S-adenosylcobalamine (vitamin B₁₂) to generate the cysteinyl radical. This class functions under both aerobic and anaerobic conditions as the generation of the radical is only dependent on the availability of S-adenosylcobalamine (AdoCob). In class III RNR (encoded by the *nrdDG* genes), the radical is produced after the binding of S-adenosylmethionine (SAM) to an iron-sulfur metal center located in

the NrdG subunit, but this radical is oxygen-sensitive so it only forms under anaerobic conditions [99]. All three RNR classes must be tightly regulated to sustain an adequate level of dNTPs, which is needed for DNA synthesis and repair. For this reason, RNR gene expression is controlled by a regulatory protein termed NrdR that is encoded by the *nrdR* gene. This protein is a transcriptional regulator that binds to the regulatory regions of the different RNR operons. Several studies have demonstrated that it suppresses the transcription of the RNR genes depending on the oxygenation and growing conditions of the bacteria [100,101].

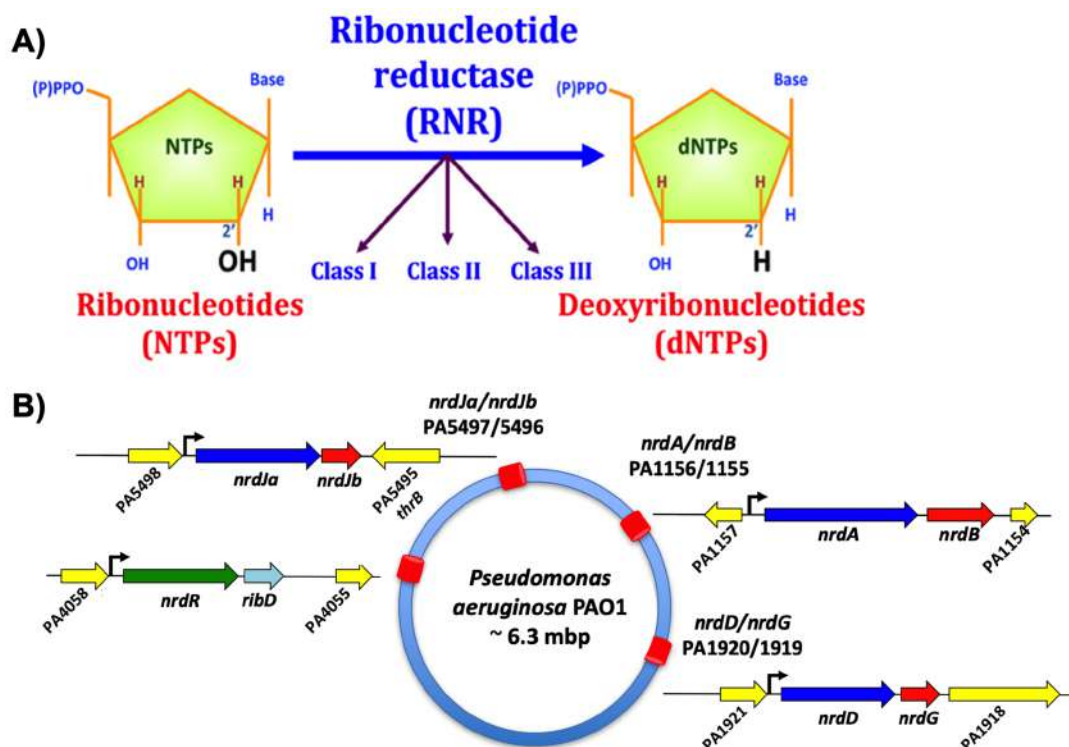


Figure 7. Graphical representations of bacterial ribonucleotide reductases. **A)** Simplified representation of the enzymatic reduction of ribonucleotides to deoxyribonucleotides by RNR. Adapted from [99]. **B)** RNR classes present in the genome of *P. aeruginosa* PAO1 with their corresponding encoding genes. Mbp: million base pairs.

P. aeruginosa is one of the few organisms that encodes all three RNR classes in its genome (Ia, II, and III) (Figure 7B), and it has been shown that RNR play a key role during infection and in biofilm formation. The expression of *nrdJ* and *nrdD* increased during infection studies done with *P. aeruginosa* PAO1 in *Drosophila melanogaster* and *Danio rerio* while the deletion of these RNR genes led to a decreased pathogenicity in both models [102,103]. Class II and III RNR are also induced during biofilm formation, and they have been shown to play an important role in proper cell division

during the development and maturation of biofilms. In previous biofilm studies with *P. aeruginosa* PAO1 (laboratory strain), PAO1 Δ *nrdJ* and PAO1 Δ *nrdD* displayed a reduced anaerobic growth capacity that caused a considerable reduction in biofilm formation. Additionally, the PAO1 Δ *nrdJ* Δ *nrdD* strain had no anaerobic growth, so it was unable to form biofilms [104].

3.1.2. *P. aeruginosa* studies in *G. mellonella*

G. mellonella larvae have been used in many studies to investigate the virulence of *P. aeruginosa*. More importantly, a positive correlation in the virulence of *P. aeruginosa* mutants in both *G. mellonella* and mice has been established [82]. *P. aeruginosa* is highly virulent to *G. mellonella* larvae as it has been shown that as little as 25 CFU per larva of PA14 is enough to kill the larvae [82]. Decreased virulence studies using mutant strains have been carried out in *G. mellonella*. An example of this is a study where an attenuation in virulence was obtained by inactivating an adenosine DNA methyltransferase present in *P. aeruginosa* PAO1 [105]. Another study found that multiple deletions of glucose uptake genes in PAO1 also resulted in decreased virulence [106]. The virulence results obtained in *G. mellonella* with PA14 wild-type and mutant strains were positively correlated with the results obtained in mice with the same strains [82]. This demonstrates the suitability of the *G. mellonella* model for detecting and characterizing bacterial genes that are involved in mammalian infections.

The immune response of the larvae to *P. aeruginosa* has been frequently analyzed in *G. mellonella*. Some studies have shown that sublethal doses of elastase B, one of the proteolytic enzymes secreted by *P. aeruginosa*, trigger the humoral immune response by inducing AMPs (specifically apolipoprotein III) and lysozyme in the hemolymph of larvae. This led to an increased larval survival against a lethal dose of *P. aeruginosa* [107]. Additionally, protease IV and elastase B have been suggested to be responsible for the degradation of apolipoprotein III present in the hemolymph [108,109]. The humoral immune response in *G. mellonella* larvae depends on the *P. aeruginosa* strain used. A study done with three different *P. aeruginosa* strains (one entomopathogenic and two clinical strains) revealed that the larvae were able to distinguish between the three strains as seen by the activation of different immune responses, especially seen by the AMPs, lysozyme, and phenoloxidase levels. High levels of elastase A were detected only in the entomopathogenic strain while elastase B and alkaline protease production was equal in all three strains. The apolipoprotein III levels in the hemolymph of infected larvae also varied depending on the strain [110]. *G. mellonella* infection with an entomopathogenic strain of *P. aeruginosa* caused significant changes in morphology, viability, and spreading ability of hemocytes [111].

3.2. *Staphylococcus aureus*

Staphylococcus aureus is a Gram-positive, coccus (round-shaped) bacterium that is considered both a commensal and a human pathogen. This opportunistic pathogen is most frequently found in the anterior nares of the nose, but it is also typically found in the skin, perineum, and pharynx. Less frequent carriage sites include the gastrointestinal tract, vagina, and axillae [112]. *S. aureus* is capable of causing a wide range of infections. It is the leading cause of bacteremia and infective endocarditis; it can also cause skin and soft tissue, osteoarticular, pleuropulmonary, and device-related infections as well as other syndromes such as toxic shock syndrome and meningitis [113].

Infections with *S. aureus* account for significant morbidity and mortality in the US. In 2017, there were about 119,000 cases of *S. aureus* bloodstream infections alone with ~19,800 associated deaths [114]. Many *S. aureus* strains are resistant to methicillin and penicillin antibiotics. MRSA strains are a worldwide burden since they are responsible for a high percentage of all the hospital-associated and community-acquired *S. aureus* infections. MRSA infections are linked to prolonged hospital stays, expensive treatments, and poor clinical outcomes. The antibiotic of choice for treating MRSA infections has been vancomycin for many years [115-117]. Prolonged therapy with vancomycin for these patients led to the appearance of MRSA strains with decreased susceptibility to the antibiotic followed by the emergence of *S. aureus* isolates with high-level resistance to vancomycin. These strains acquired the vancomycin-resistance through the transfer of plasmid-borne copies of the Tn1546 transposon that originated in vancomycin-resistant *Enterococcus faecalis* [118]. Since *S. aureus* can easily acquire and develop resistance to antibiotics, alternative treatment options are urgently needed.

Besides its ability to resist antibiotics, *S. aureus* has plenty of other strategies for evading the innate immune defenses of the human host. This bacterium secretes a variety of highly selective proteins which enable it to escape attacks from the complement system and neutrophils [119]. A few examples of these proteins are as follows:

- Staphylokinase: binds to the α -defensins secreted by neutrophils and inhibits their bactericidal effect [120].
- Aureolysin: cleaves and destroys the antibacterial activity of cathelicidin LL-37, a human bactericidal peptide that has potent anti-staphylococcal activity [121].
- Catalase: inactivates toxic hydrogen peroxide and free radicals generated by polymorphonuclear neutrophils after bacterial ingestion [122].

- Staphylococcal complement inhibitor: blocks human complement by interacting specifically with the C3 convertases that are necessary for complement activation [123].

Additionally, *S. aureus* has numerous other virulence factors that facilitates its ability to lyse host cells, promote the invasion and destruction of tissues, and manipulate the adaptive immune responses. The inhibition of some of these virulence factors is studied as potential alternative treatment strategies [124]. Since the list of these factors is extensive, only a few ones are mentioned in Table I and depicted in Figure 8. A more complete listing can be found in a couple of reviews that describe the *S. aureus* virulence factors more extensively [124,125].

Table I. Some of the virulence factors expressed by *S. aureus*.

Virulence factor	Function	Known interference	Ref.
Protein A (SpA)	Binds to Fc portion of immunoglobulins, von Willibrand factor, TNFR-1, and complement protein C3	Anti-opsonic and anti-phagocytic; increases bacteria adhesion to platelets; reduces TNF- α proinflammatory signaling	[126-128]
Coagulase	Activates prothrombin and the conversion of fibrinogen to fibrin	Promotes the clotting of plasma or blood; facilitate formation of abscesses	[129]
α toxin	Forms pores in erythrocytes and monocytes	Proinflammatory cytokine; induces TNF- α	[130]
Toxic shock syndrome toxin-1 (TSST1)	T cell superantigen	Induce T lymphocyte proliferation; suppresses immunoglobulin production	[131]
Staphyloxanthin	Carotenoid	Interacts with ROS; confers resistance to ROS-mediated killing by neutrophils	[132]
Teichoic acids	Binds to Toll-like Receptor 2	Can confer secretion of cytokines and chemoattractants	[133]
Adhesins	Adheres to extracellular matrix and plasma proteins of host cells	Allows the colonization and dissemination of the bacteria throughout the host; triggers bacterial internalization	[134]

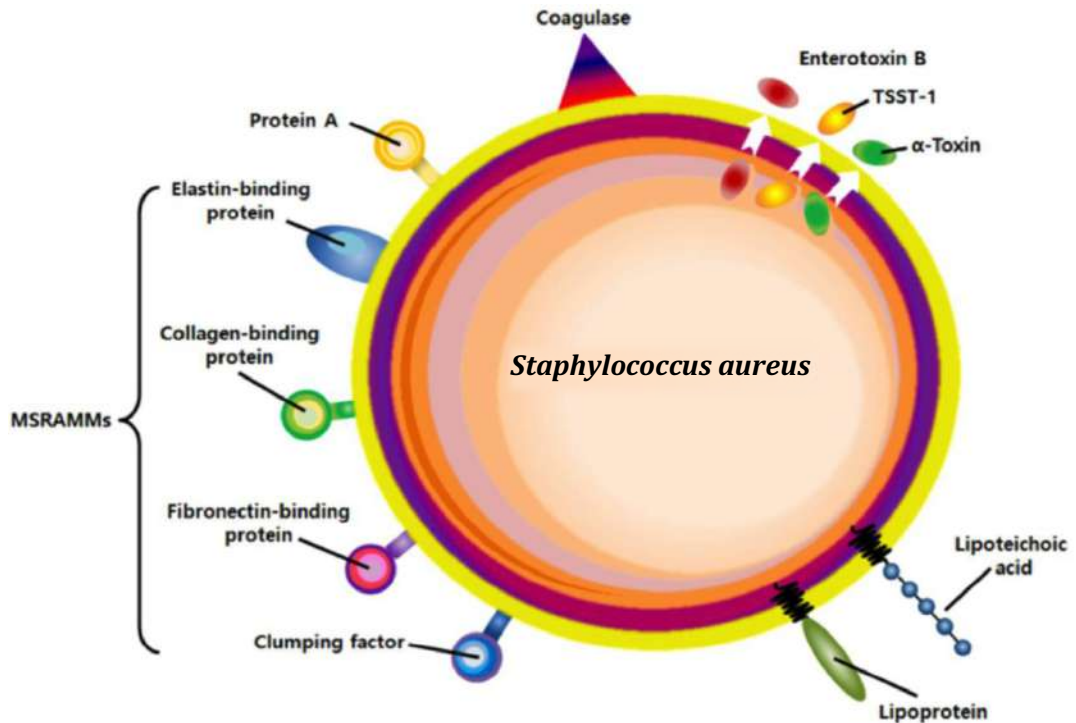


Figure 8. Simplified representation of a few of the *S. aureus* virulence factors that are mentioned in section 3.2. MSRAMM or Microbial Surface Recognizing Adhesive Matrix Molecules are a type of adhesins. Adapted from [135].

S. aureus can also escape immune defenses and antimicrobials by its ability to form biofilms. This bacterium is very proficient at forming biofilms on the surfaces of foreign bodies that are present inside the human host, such as prosthetic cardiac valves, prosthetic joints, intravascular catheters, among other devices. *S. aureus* regulates biofilm formation through quorum sensing, which is a communication process that allows the transfer of information between bacteria (e.g., nutrient availability and bacterial density). Biofilm infections are impossible to eradicate without surgical removal of the device [113,136]. Besides humans, *S. aureus* also infects animals such as dogs, cats, sheep, cattle, and poultry [137,138]. A high prevalence of infections is seen particularly in the udder of dairy cows. These infections affect the yield and quality of the milk produced by the cows which results in significant losses for the dairy industry [139]. The importance of *S. aureus* as a pathogen along with the increasing prevalence of MRSA strains calls for further studies with animal models, other than mice, to gain more knowledge on the pathogenesis of *S. aureus* [140].

3.2.1. *S. aureus* studies in *G. mellonella*

The utility of *G. mellonella* for analyzing the virulence of *S. aureus* was first reported in a study that identified the pathogenic consequences of *S. aureus* strains with reduced vancomycin susceptibility during infection [69]. *S. aureus* was first injected at doses ranging from 10^4 to 10^7 CFU/ml, and the larvae were incubated at 30°C and 37°C. Larval mortality was dependent on the bacterial concentration and incubation temperature, with greater killing observed with 10^7 CFU/ml and at 37°C. Then, the effects of *agr* functional status and vancomycin susceptibility on *S. aureus* virulence were studied. The results showed that functional loss of *agr* and resistance to vancomycin are associated with impaired *S. aureus* virulence thus showing that the *G. mellonella* model can be effectively used to study *S. aureus* virulence *in vivo*. Decreased virulence was also achieved by infecting *G. mellonella* larvae with a *secDF* *S. aureus* mutant strain [141]. This was consistent with reduced cytotoxicity, adhesion, and invasion in human umbilical vein endothelial cells. Another study examined the interaction of *S. aureus* with the immune system response of *G. mellonella* larvae [83]. Larval mortality increased dose-dependently after infection with *S. aureus*. This was accompanied by extensive melanization and significant proliferation and dissemination of *S. aureus* which led to the formation of nodules within the larvae. Significant hemocyte proliferation was seen in the larvae after inoculation with *S. aureus*. Proteomics analysis showed that at 6 hours post-infection, the larval hemolymph was enriched with AMPs, ProPO cascade proteins, and various peptidoglycan recognition proteins. At 24 hours post-infection, there was a significant increase in the expression of AMPs with anti-staphylococcal activity as well as proteins associated with nodule formation. The results of this study revealed the cellular and humoral responses of larvae against *S. aureus* infection and its similarities to the responses seen in human infections with *S. aureus*.

G. mellonella was also used to study the virulence of different *S. aureus* clinical isolates from acute and chronic implant-associated bone infections [142]. Larval survival analysis showed various levels of lethality with high, intermediate, and low virulence phenotypes. Furthermore, the results obtained with *G. mellonella* had good correlation with the results obtained in osteoblast invasion and biofilm formation assays done with the same strains. *S. aureus* biofilms cultivated in a flow system were shown to secrete high amounts of functional virulence factors that were found in the extracellular matrix and in the biofilm flow-through [143]. These virulence factors were tested in the *G. mellonella* animal model to reveal that the factors were active as seen by the increased larval mortality.

3.3. *Mycolicibacterium brumae*

Previously denominated *Mycobacterium brumae*, *Mycolicibacterium brumae* is a Gram-positive bacillus with acid-alcohol fastness that was first described in 1993. This strain is a rapidly growing, non-photochromogenic, and saprophytic mycobacterium that is capable of forming clumps and cords [144]. *M. brumae* is considered an environmental mycobacterium as it is commonly found in soil and water sources. No infections caused by *M. brumae* have been reported in humans, animals, or plants [145]. In 2004, a catheter-related infection caused by *M. brumae* was reported, but it was later established that the strain isolated from this infection was not *M. brumae* [146,147].

Mycobacteria cell walls have a high lipid content which makes them hydrophobic, so the cells tend to clump when resuspended in aqueous solutions [148]. Additionally, the cell wall of *M. brumae* contains cord factors which consist of α -mycolates that are able to induce variable amounts of different pro-inflammatory cytokines such as TNF- α , IL-1 β , IL-6, IL-12p40, and IL-23 that are relevant to tuberculosis, so they are considered as potential adjuvants [149]. *M. brumae* has been shown to have immunomodulatory and antitumor activity. This mycobacterium is capable of activating macrophages, inhibiting the proliferation of bladder cancer cells, and prolonging the survival of tumor-bearing mice. For this reason, *M. brumae* is indicated as a promising therapeutic agent for non-muscle-invasive bladder cancer [150,151].

No studies using *M. brumae* in the *G. mellonella* animal model have been reported.

3.4. Antimicrobial studies in *G. mellonella*

Since antibiotic resistance among numerous pathogens has been increasing at an alarming rate, there is a critical need to discover and develop novel antimicrobial agents. Typically, novel agents are first screened *in vitro* to assess their efficacy and the most promising candidates are then tested in an animal model, generally murine or other rodent models. However, *in vivo* mammalian studies involving rodents are expensive, time-consuming, and ethically controversial [41]. On the other hand, *G. mellonella* is a simple, inexpensive, and highly versatile model that can be used to rapidly assess the *in vivo* effectiveness of antimicrobial agents against any pathogen to which the *G. mellonella* larva is susceptible. By using this model for preliminary screenings, the likelihood of an antimicrobial agent with promising results *in vitro* from progressing to an unsuccessful performance in mammalian models can be reduced thus saving time, money, and mammals from unnecessary experiments. Therefore, *G. mellonella* can be used as an additional pre-screening alternative model to justify the number of antimicrobial drugs proceeding to mammalian *in vivo* testing [152].

G. mellonella larvae can be accurately infected with defined bacterial concentrations, and it is important to select a dose that kills the larvae at a sufficient proportion during the chosen incubation time. The larvae can also be injected with precise doses of the antimicrobial agent which can be administered in different treatment regimens such as the number of doses given in total, timings of the different doses given after infection, and total dose administered. By injecting the antimicrobial, it is delivered directly into the hemocoel, and this systemic application mimics the typical delivery route used in mammalian studies [41,152]. Several studies have demonstrated that effective antibiotic doses in *G. mellonella* are similar to the doses recommended for humans [70,153-155]. Therefore, unlike *in vitro* MIC values, antimicrobial doses determined in *G. mellonella* provide a more accurate prediction of the doses needed for subsequent mammalian studies. *G. mellonella* can not only be used to test agents with direct antimicrobial activity, but it can also be used to test combinations of different antibiotics and to evaluate the therapeutic efficacy of antivirulence compounds, bacteriophage treatments, and alternative strategies (e.g., substances obtained from plants) [41,152] (Figure 9). After infection and antimicrobial agent administration, larval survival is monitored as it is the most suitable criteria for assessing antimicrobial efficacy. Additionally, microbial burden within the larvae can be measured by plating and enumerating bacteria from the hemolymph and by using GFP-tagged or bioluminescent bacteria [77,81,152]. To detect activation of the larval immune response against pathogens and antimicrobial toxicity, hemocyte density within the larvae can be measured [83,156]. Furthermore, hemocytes can be isolated from the larvae to perform *ex vivo* assays to determine the response of the larvae to the pathogens and to detect the cellular effects of antimicrobial agents [157]. However, it is important to establish whether hemocyte proliferation is due to immune priming as this will add to the apparent antimicrobial efficacy of the agent [158].

G. mellonella has been used to test the antimicrobial efficacy of different agents against a multifold of microorganisms including *Acinetobacter baumannii* [159], *Burkholderia cenocepacia* [160], *Clostridium difficile* [161], *Enterobacter cloacae* [162], *Enterococcus* species [163], *Escherichia coli* [164], *Helicobacter pylori* [165], *Klebsiella pneumoniae* [166], *Listeria monocytogenes* [167], *Mycobacterium abscessus* [168], *Mycobacterium tuberculosis* [169], *Porphyromonas gingivalis* [170], *Pseudomonas aeruginosa* [171], *Shigella sonnei* [172], and *Staphylococcus aureus* [173], among several others.

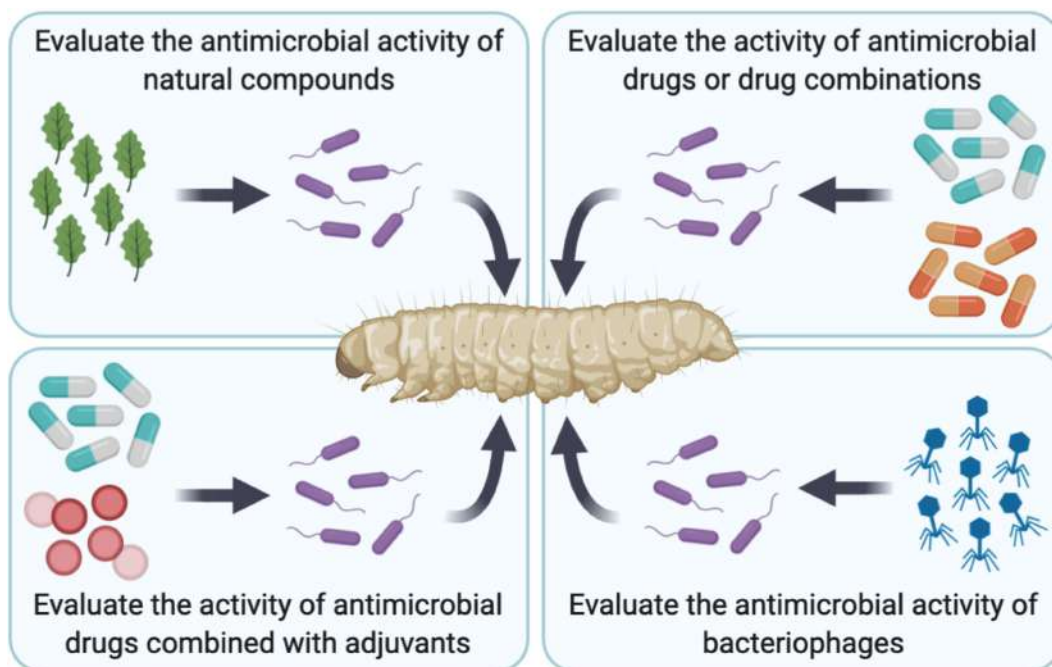


Figure 9. Antimicrobial strategies tested in the *G. mellonella* model. *G. mellonella* larvae can be used to evaluate different antimicrobial therapies, including classical drugs or drug combinations (top right), natural compounds such as a plant derived-extract like cinnamaldehyde (top left), classical drugs combined with adjuvants such as AMPs (bottom left), and bacteriophages or phage therapy (bottom right). Adapted from [174]. Created with BioRender.com.

3.4.1. Antimicrobial efficacy studies against *S. aureus* in *G. mellonella*

Several studies have been conducted in *G. mellonella* to test different antibiotic therapies against *S. aureus*. In one study, larvae were infected with two *S. aureus* strains (one methicillin-susceptible and one methicillin-resistant) and then treated with daptomycin, penicillin, or vancomycin [70]. All three treatments were effective against the methicillin-susceptible strain as seen by the increased larval survival. Daptomycin and vancomycin were also effective when administered to the larvae prior to *S. aureus* infection. On the other hand, only daptomycin and vancomycin were active against the methicillin-resistant strain since penicillin had no antimicrobial effects in the infected larvae. Larval survival was also enhanced by vancomycin treatment after infection with two MRSA strains [175]. Another study tested the *in vivo* efficacy of three different pleuromutilins alone or in combination with tetracycline or ciprofloxacin against various *S. aureus* strains [173]. When pleuromutilins were combined with tetracycline to treat larvae infected with *S. aureus*, enhanced survival rates were obtained when compared to pleuromutilins or tetracycline

alone. In contrast, no synergy effects were seen with the combination of pleuromutilins and ciprofloxacin as compared to monotherapy.

Alternative antimicrobial compounds against *S. aureus* have also been tested in *G. mellonella*. One study analyzed the effects of the flavonoid myricetin against three different *S. aureus* strains [176]. After infection with *S. aureus*, the larvae treated with myricetin demonstrated an increase in survival as myricetin exhibited antivirulence effects without modulating bacterial growth. Another plant-derived active compound, cinnamaldehyde, was tested in *S. aureus*-infected larvae. Treatment with this compound also resulted in enhanced larval survival and diminished bacterial load within the larvae [177]. Hamamelitannin, an antibiofilm compound, increased the survival of *G. mellonella* larvae that were previously infected with two different MRSA strains [175]. Furthermore, the larval survival was even greater after treatment with a combination of hamamelitannin and vancomycin. The therapeutic potential of temporin-10La was assessed by determining its *in vivo* efficacy against a *S. aureus* infection in *G. mellonella* [178]. Prior treatment with this antimicrobial peptide protected the larvae from the staphylococcal infection. In a different study, a single dose of the commercially available Raf kinase inhibitor GW5074 was sufficient to rescue *G. mellonella* larvae from an MRSA *in vivo* infection [179]. Furthermore, GW5074 demonstrated long-term protection capacity as seen by the 42% larval survival rate at 5 days post-infection.

Additionally, *G. mellonella* can be used to test the efficacy of novel antimicrobial agents against *S. aureus* infections. A novel protonophore 1-(4-chlorophenyl)-4,4,4-trifluoro-3-hydroxy-2-buten-1-one (compound 1) that showed bacteriostatic effects against MRSA *in vitro*, also prolonged the survival of MRSA-infected larvae when administered before or after infection [180]. Furthermore, the antibacterial effects of the compound were comparable to the ones seen with the vancomycin control group. Another study synthesized *N*-phenyl-1*H*-pyrazole-4-carboxamide derivatives and other pyrazoles to evaluate their ability to inhibit biofilm formation in three *S. aureus* strains [180]. The *in vivo* efficacy of the most active compound (14d) was then tested using *G. mellonella*. When the compound was administered 1 hour before infecting the larvae with *S. aureus*, a protective effect was demonstrated as seen by the increased larval survival. Compounds 1 and 14d were proposed as potential antibacterial and antivirulence agents, respectively, for *S. aureus* infections.

3.5. Limitations in the use of *G. mellonella* as an infection model

G. mellonella has a few limitations in its use as an infection model. The short life span of the larvae can interfere with the study of chronic infection processes [8]. Another limitation is that the larvae have a high tolerance to polyphenol compounds such as theaflavin and epicatechin as seen by the lack of toxicity with high concentrations of these compounds [181]. Similar results were obtained when testing pulp extract from *Eugenia brasiliensis* Lam. (grumixama), which is rich in polyphenols, in *G. mellonella* larvae [182]. This resistance is probably due to the natural diet of the larvae. Bee honeycombs are rich in phenolic and polyphenolic compounds, so the larvae may have naturally adapted to tolerate these compounds [181,183]. For this reason, the *in vivo* interactions between microbial infections and antimicrobial agents with high phenolic and polyphenolic levels cannot be determined using the *G. mellonella* model. Unlike *C. elegans* and *D. melanogaster*, *G. mellonella* is not as well established as an infection model. A first draft genome sequence has only been recently published and few microarrays and RNA interference and mutant strains libraries are available [184,185]. Furthermore, there are no stock centers that sell specific genotypes like the ones seen with *D. melanogaster* [41].

The major limitation in using *G. mellonella* as an infection model is the lack of standardized procedures [186]. There are many experimental variations during infection studies in *G. mellonella*, including preparation and quantity of the inoculum, subjective interpretation of morbidity and mortality parameters, and experimental conditions (e.g., temperature). These can lead to variable results thus impeding the comparison between different published studies. Larvae can be easily purchased from breeders that sell them as food for reptile and bird pets or as fishing bait. However, these larvae do not have a defined age or weight, may contain antibiotic and hormone residues, and all life cycles have been kept under differing conditions [186]. Larvae can also be reared and standardized directly in research labs [8]. Variations in breeding conditions, feeding status, physical handling of the larvae, and maintenance can influence the susceptibility of the larvae to infections [41,187,188]. Additionally, the presence of antibiotics and hormones can alter their metabolism [189]. Therefore, factors such as age, weight, diet, and breeding conditions should be included in every publication involving *G. mellonella* as a way to standardize experiments between research groups. A few companies like BioSystems Technology in the UK provide standardized *G. mellonella* larvae for scientific purposes. Although they are more expensive than common larvae, the results obtained with these larvae are more consistent and reproducible [190].

4. *Galleria mellonella* as a model of toxicity

Due to the rising prevalence of antibiotic resistance and the emergence of multi-drug resistant bacterial phenotypes, there is a critical need to develop alternative antimicrobial agents [191]. Once new antimicrobial compounds are shown to be nontoxic *in vitro*, their toxicity has to then be tested *in vivo* using animal infection models. *In vivo* assays enable the detection of different factors that could prevent the potential application of the compounds in humans, such as decreased efficacy *in vivo* due to degradation by host enzymes, interaction with host components, and the effects of physiological conditions of the host (e.g., pH, metabolism). Furthermore, *in vivo* testing can reveal maximum tolerable doses and possible short and long-term toxicity effects which are necessary for clinical trials [152,192]. The animals typically used for toxicity studies are murine or rodent models due to their anatomical, physiological, and genetic similarities with humans [193]. However, the use of these models is expensive, time-consuming, and ethically controversial. For this reason, alternative non-mammalian animal models like *Danio rerio*, *Drosophila melanogaster*, and *Caenorhabditis elegans* have been implemented in laboratories as they provide significant data at a low cost and do not require the same ethical considerations as murine studies [152,194-196]. These non-mammalian models are not only useful for testing the antimicrobial efficacy of new compounds but also for detecting any toxicity effects that could not be determined *in vitro*. Recently, *G. mellonella* has been gaining popularity as a model for studying the virulence of different pathogens, and it has also shown to be highly suitable for evaluating the efficacy and toxicity of new antimicrobial agents as well as other compounds [152].

There are many benefits to using *G. mellonella* as a toxicity model. The larvae used for testing are relatively large (about 2 cm in length) which facilitates handling as well as the administration of precise doses of compounds by intra-hemocoel injection, and this delivery route closely mimics systemic injections typically used for drug delivery in humans. Although less common, drug administration can also occur through force-feeding and topical application [152,197]. Another advantage is that the larvae can be bred quickly and at a low cost. Therefore, many larvae can be used in one experiment thus producing statistically valid results in a short period of time. Additionally, the larvae can survive at 37°C, so toxicity studies can be performed at the same temperature as the human body. The use of larvae for toxicological screenings does not involve any of the legal or ethical restraints that apply to rodent models. Larvae produce a large amount of hemolymph (about 70 µl per larva), so pharmacokinetic data can be easily obtained [152,158,185]. Pharmacokinetic data generated with *G. mellonella* larvae such as antibiotic clearance time,

elimination half-life of the drug, and maximum drug concentration can correctly directly with the values reported in humans [198]. All of these advantages validate *G. mellonella* as a suitable model for toxicity studies.

4.1. Toxicity studies in *G. mellonella*

G. mellonella has been used to assess the *in vivo* toxicity of various compounds. The acute toxicity of 19 chemicals was studied using *G. mellonella* larvae, and the results were compared against the LD₅₀ values previously obtained with cytotoxicity *in vitro* and oral toxicity *in vivo* studies using NHK or 3T3 cells and rats, respectively [199]. *G. mellonella* was found to be a reliable predictor for low toxicity chemicals when compared to cell culture systems, and the authors proposed that a more robust assessment of chemical toxicity could be achieved by using both cell cultures and *G. mellonella*. Another study supported the use of *G. mellonella* larvae for acute toxicity studies [200]. The LD₅₀ values of 11 different compounds that were established in *G. mellonella* correlated to the values obtained in mice and rats. Similar results were seen when evaluating the toxicity of food preservative agents [197]. The larvae were administered various food additives by feeding or intra-hemocoel injection, and the LD₅₀ values obtained showed a strong correlation to the LD₅₀ values determined in rats. The acute toxicity of ionic liquids was also assayed in *G. mellonella* [201]. The data obtained revealed that 1-alkyl-3-methylimidazolium chloride ionic liquids were toxic to the larvae, which was directly related to the length of the alkyl side chain. Although it was suggested that the high lipid content of the larvae made them slightly more sensitive to ionic liquids, *G. mellonella* was still shown to be a reliable and robust model for evaluating the toxicity of these compounds.

Besides assessing *in vivo* toxicity, *G. mellonella* can also be used to study the mode of action of different compounds. Larvae were administered potassium nitrate by intra-hemocoel injection which yielded a significant increase in circulating hemocytes, but it reduced the killing ability of these cells by potential inhibition of superoxide production [17]. The compound also led to an increase in superoxide dismutase activity and in proteins associated with mitochondrial function, oxidative stress response, and nitrate metabolism. This study demonstrated a correlation between the acute effects of potassium nitrate seen in both larvae and mammals. The effects of caffeine were also studied in *G. mellonella* [202]. Larvae that were administered caffeine by feeding had reduced movement and pupae formation. They also exhibited an increase in proteins associated with brain trauma and a decrease in proteins involved in development and protein degradation. These results indicate that caffeine is metabolized similarly in both *G. mellonella* and mammals. Novel copper

phenanthroline-phenazine cationic complexes with promising chemotherapeutic potential were tested in *G. mellonella* [203]. The results showed low immunogenicity and upregulation of metabolic and detoxification proteins that may provide an opportunity for developing drug targeting. *G. mellonella* was successfully used as a first step in assessing the *in vivo* tolerance and mode of action of these complexes, and it is proposed as a model for testing future therapeutic and targeting improvements.

G. mellonella has also been used to evaluate the toxicity of various alternative antimicrobial agents. Two triazole analogues of natural bioactive precursors were synthesized as promising anti-biofilm agents and since they showed efficacy in *in vitro* assays, their toxicity was tested in *G. mellonella* [204]. The results showed that concentrations up to 2.5 mg/ml of the compounds did not affect the larvae. Additionally, the hemocyte density of the larvae was not altered significantly with the same concentration, indicating a lack of immune response towards the compounds. A series of thiourea-containing compounds were also synthesized as potential antimicrobial agents and their toxicity was evaluated using *G. mellonella* [205]. Different concentrations of the compounds were found to be non-toxic to the larvae and they did not seem to interfere with larval development. Using *G. mellonella*, the lethal dose for different thiazolyldihydrazone compounds was found to be >10 mg/kg [206]. Therefore, 10 mg/kg of the most promising compound was subsequently tested in murine models and the results corroborated the safety and antifungal efficacy seen with *G. mellonella* at this concentration. Similar results were seen in a study that assessed the toxicity of potential antimicrobial copper(II) and silver(I) complexes, as the toxicity levels obtained in *G. mellonella* were also similar to the levels observed in Swiss mice [207]. While the order of toxicity differed slightly, the most toxic compound in larvae was the same one as in mice.

G. mellonella is a simple and inexpensive animal model that facilitates the rapid and reliable detection of any potential toxicity effects derived from different compounds. This non-rodent *in vivo* model can be used to screen out compounds that have poor success probabilities while providing greater justification for performing further studies in more expensive and ethically controversial rodent models. Although *G. mellonella* will never replace rodent models completely, it can provide an indication of any toxicity effects encountered *in vivo* during early stages of drug development (Figure 10). Therefore, *G. mellonella* can bridge the gap between *in vitro* and *in vivo* rodent studies thus reducing the number of rodents used during preclinical assessments as well as the overall drug development cost [152].

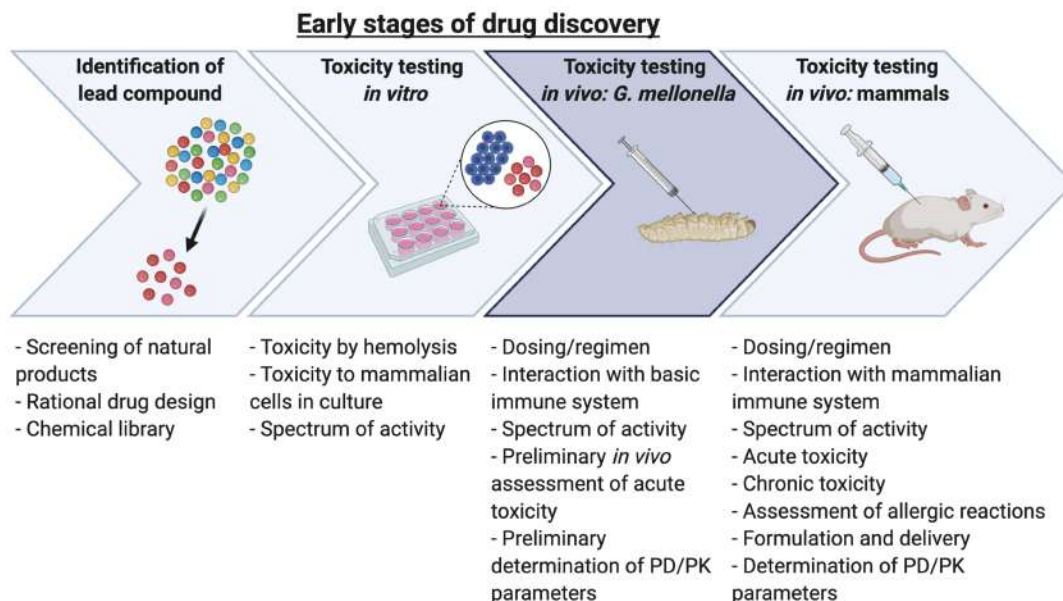


Figure 10. Proposed addition of *G. mellonella* into the traditional drug development pathway. The inclusion of the *in vivo* toxicity testing step with *G. mellonella* (dark blue arrow) could reduce the costs and the number of rodents used in toxicity *in vivo* studies as compounds that display toxic effects in *G. mellonella* would not be pursued in mammalian models. PD: pharmacodynamic, PK: pharmacokinetic. Adapted from [152]. Created with BioRender.com.

4.1.1. Toxicity studies involving nanoparticles in *G. mellonella*

G. mellonella was used as an *in vivo* model to test the toxicity of lipid-core nanocapsule formulations with different surface coatings [208]. Different concentrations of neutral, negative, and positive charged nanocapsules were injected into *G. mellonella* larvae and survival was assessed daily up to 5 days post-injection. The results indicated that none of the nanocapsules were toxic to the larvae which correlated with previous toxicological data obtained with the same nanocapsules in Wistar rats. Consequently, *G. mellonella* was validated as a preliminary toxicological model for nanocapsules and nanoparticles. The toxicity of novel polymeric nanoparticle delivery vehicles for tobramycin was also assessed in *G. mellonella* [209]. Larvae were injected with 250 µg/ml of tobramycin NPs and free tobramycin and survival rates were recorded over 96 hours post-injection. At this concentration, the NPs were not toxic to the larvae as seen by the 90% survival at the end of the experiments. Therefore, the tested concentration was deemed safe for subsequent antimicrobial efficacy testing against *P. aeruginosa* infections in *G. mellonella*. Another strategy against *P. aeruginosa* infections involved a new formulation of AgNPs [156]. Different concentrations of these NPs were administered to *G. mellonella* larvae and viability was observed

for 8 days. No toxicity was seen with AgNPs concentrations below 35 mg/kg, and the LD₅₀ was established as 68.70 mg/kg. Similar results were seen with biogenic AgNPs which failed to elicit toxic effects in *G. mellonella* larvae exposed to concentrations up to 1 mM for 120 hours post-injection [210].

Various other types of NPs with antimicrobial potential have been tested in *G. mellonella*. Miltefosine-loaded alginate NPs were synthesized for the treatment of cryptococcosis and candidiasis [211]. At a concentration of 200 mg/kg, the NPs did not cause larval mortality while the same concentration of free miltefosine caused 22% mortality, thus demonstrating that the encapsulation of miltefosine protected the larvae from its toxic effects. Another study tested the toxicity of itraconazole-loaded nanostructured lipid carriers as topical treatment for sporotrichosis and other fungal infections [212]. Unloaded and itraconazole-loaded carriers showed no toxicity on the larvae as seen by the 100% larval survival. Dry powders consisting of PEGylated C109 (FtsZ inhibitor) nanocrystals were formulated to be used alone or in combination with piperacillin for treating *B. cenocepacia* infections [213]. No toxicity was reported in larvae injected with the C109 nanocrystal formulation or with the antibiotic. A lack of toxicity was similarly seen with free silver(I) complex at concentrations <250 mg/kg [214]. As a new strategy for *H. pylori* infections, the same complex was loaded into polymeric nanoparticles, and it was also nontoxic to the larvae at the highest concentration tested (8 mg/kg).

Besides assessing larval mortality after NP injection, *G. mellonella* larvae can additionally be used to determine other toxicity effects derived from the NPs. One study tested the toxicity of ZnO rod shaped NPs in *G. mellonella* [215]. The LD₅₀ was established as 6.03 µg/10 µl after force feeding the larvae with different concentrations of the NPs. To determine acute toxicity effects in the larvae, total hemocyte counts were analyzed after feeding the larvae with doses lower than the LD₅₀. After 24 hours, the hemocyte density was not significantly affected when compared to the control group. However, the highest concentration tested (5 µg/10 µl) yielded an increased percentage of dead hemocytes which was attributed to the cellular toxic effects of the ZnO NPs. Another study tested the effects of CuO NPs in *G. mellonella* [216]. Fourth instar larvae were fed an environmentally realistic concentration of the NPs (10 µg/L) for about 15 days (until last instar). Then, toxicological effects were evaluated in the midgut and fat body tissues of the larvae. Copper accumulations were seen in both the midgut and fat body. Increased catalase levels were seen in the midgut and fat body while superoxide dismutase levels decreased only in the fat body. In both tissues, no significant changes were observed with glutathione peroxidase while glutathione-S-transferase levels increased. For acetylcholinesterase, the activity decreased in the midgut of the larvae but increased

in the fat body. The results obtained in this study demonstrate that antioxidant enzymes in *G. mellonella* are strongly affected by intoxication with heavy metals.

5. Methodology approaches in *G. mellonella*

Multiple techniques have been employed in the use of *G. mellonella* as an infection model. Bacteria present in the hemolymph extracted from infected larvae have been visualized using fluorescent and confocal microscopes [59,217]. Bacterial load within infected whole larvae has been monitored using a spectrophotometer (for GFP-tagged bacteria) and an IVIS imaging system (for bioluminescent bacteria) [80,218]. Bacterial load can also be determined by assessing CFU at different time points. This can be achieved by plating homogenized larvae or the hemolymph collected from infected larvae onto media plates [59,80]. CFU counts can be substituted by measuring the photon count, photon flux, and radiance in larvae infected with bioluminescent bacteria [80]. Additionally, histopathological analysis of infected larvae can be performed to assess the impact of the infection on the internal tissues of *G. mellonella* larvae [77,81]. To study bacterial biofilm formation *in vivo*, a method involving toothbrush bristles has been developed using *G. mellonella* larvae [219]. The bristles are inserted into the larvae (to mimic a medical device), bacteria are injected into the larvae, and then the bristles are removed to evaluate biofilm formation by CFU quantification and scanning electron microscopy.

Other techniques used during infection studies in *G. mellonella* involve the analysis of hemocytes. GFP-tagged bacteria can be used to determine hemocyte internalization by extracting hemocytes from infected larvae and imaging them under a confocal microscope [59]. The presence of non-fluorescent bacteria within hemocytes can also be detected using immunofluorescence or transmission electron microscopy [81,217]. Bacterial phagocytosis studies can also be achieved by labeling bacteria with FITC before injecting them into the larvae and then isolating the hemocytes for microscopy imaging [220]. The levels of circulating hemocyte within inoculated larvae can be quantified by extracting the hemocytes from the larvae and counting the cells using a hemocytometer or an automated cell counter [215,217]. Although a hemocyte cell culture line has not been established, a protocol has been developed for the isolation and temporary *ex vivo* maintenance of hemocytes derived from *G. mellonella* [221]. By implementing this protocol, several *ex vivo* studies can be accomplished, such as analyzing interactions between microorganisms and hemocytes, determining whether antimicrobial drugs can target intracellular pathogens located

within hemocytes, and comparing the interactions of hemocytes and mammalian phagocytes with pathogens, among others.

5.1. Tissue clearing techniques

Three-dimensional biological samples are difficult to image due to the obscuring effects caused by light scattering. These samples are comprised of water, lipids, and proteins and each component has its own refraction index (RI). When a sample has a mixture of components that are small with varied RI, it lacks transparency due to the interactions of incoming light with the heterogeneous RI of the components. Tissue clearing protocols have been developed to try to homogenize the RI of a biological sample by removing, replacing, and modifying some of its components so that the sample becomes transparent. Therefore, large samples (e.g., whole organs) can be analyzed by using visible wavelengths of light with microscopy [222]. Tissue clearing methods usually involve four steps: i) tissue fixation, ii) permeabilization, iii) decolorizing, and iv) RI-matching by a high-RI medium. Tissue fixation is an important step to preserve the molecules of interest throughout the clearing process and it can be achieved using paraformaldehyde (PFA), hydrogel embedding, and glutaraldehyde-based methods. The permeabilization step substitutes the water within tissues with a high-RI medium. Permeabilizing reagents can be categorized into three groups: water-miscible polar solvents (such as alcohols), hyperhydration reagents without delipidation (such as urea), and delipidation reagents (such as detergents). Decolorizing involves removing endogenous pigments like melanin, heme, and riboflavin that tend to interfere with sample imaging [223,224]. These pigments can be bleached using chemicals like H_2O_2 [225]. The final RI-matching step is done to homogenize the RI of the whole tissue and this can be achieved with high RI-media like benzyl alcohol and benzyl benzoate (BABB) [223,226].

Clearing protocols are chemically divided into organic solvent-based methods and hydrophilic reagent-based methods. After fixation, the first type consists of dehydration, delipidation and/or decolorization, and RI matching (Figure 11A) while the second method involves delipidation and/or decolorization, and RI matching (Figure 11B) [223]. Hydrophilic reagent-based methods are generally limited to small samples and may require longer clearing times. On the other hand, organic solvent-based methods have faster and better clearing results, but they require the use of toxic and corrosive chemicals. Moreover, the use of ethanol, methanol, and organic solvents can affect the fluorescence of some proteins (e.g., GFP). The dehydration step can also cause sample shrinkage which can further disrupt the fluorescence of proteins [222,227]. Determining the best clearing method for a given application can be a challenge due to the numerous protocols available, so many

parameters must be carefully evaluated, including sample size, lipid staining requirements, immunostaining needs, cost, speed, sample conservation, and fluorescence preservation, among others. Despite the challenges, tissue clearing is an attractive methodology that allows three-dimensional views of large tissue samples to facilitate the study of the internal structures of organisms [222-224].

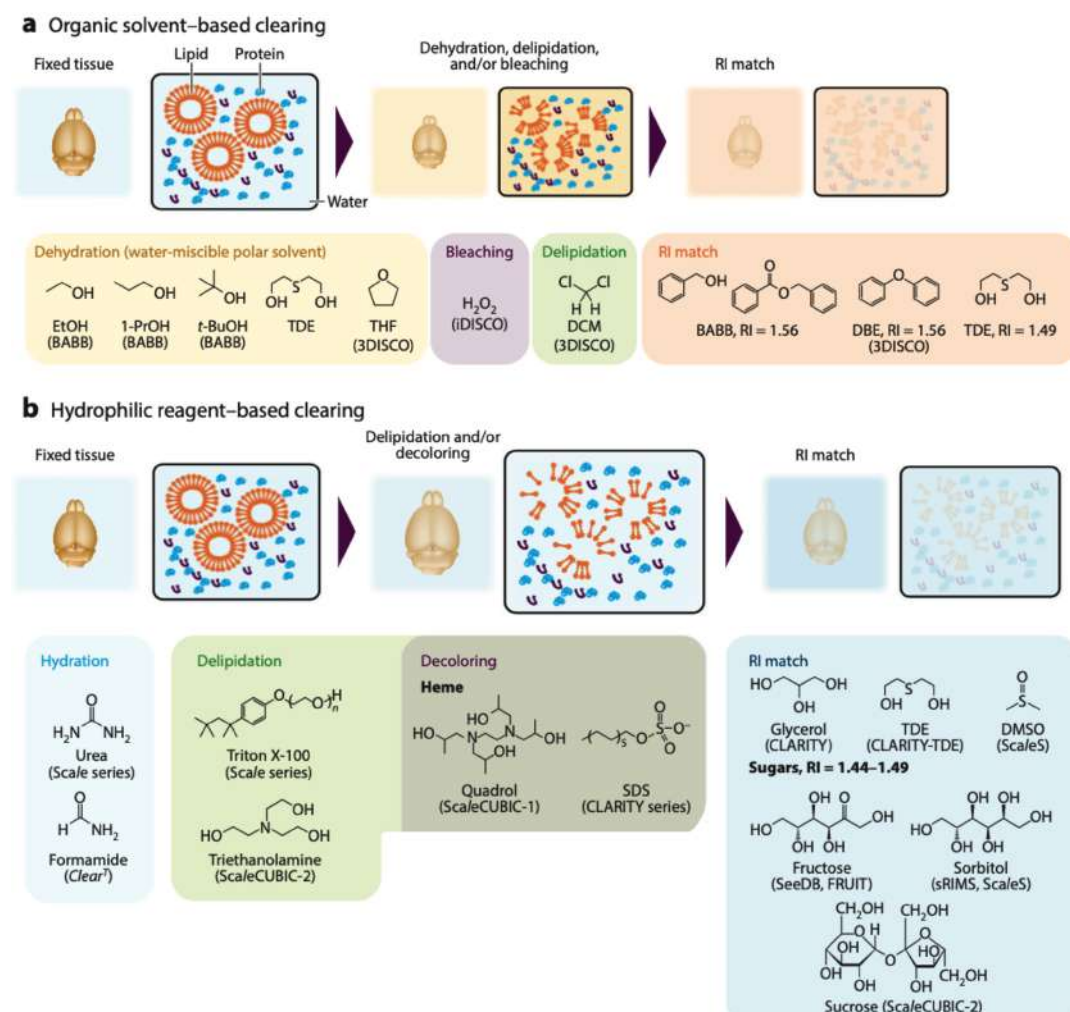


Figure 11. Overview of tissue clearing classification and methods. **A)** Organic solvent-based clearing methods involve dehydration, delipidation, bleaching, and RI matching. **B)** Hydrophilic reagent-based clearing methods include delipidation, decolorizing, and RI matching. For both types of methods, each step depicts different examples of the chemicals used. The name of the specific clearing protocol is found in parenthesis beneath the corresponding chemical (for example, THF and DCM are used for dehydration and delipidation, respectively, in the 3DISCO clearing protocol). Adapted from [223].

Tissue clearing protocols have been successfully used to make a variety of transparent tissues, including human brain section [228], human tumor biopsy [229], adult mice [230], mouse brain [231], marmoset brain [232], mouse embryo [226], mouse intestine [233], mouse lung [234], mouse kidney [235], mouse spinal cord [236], adult *Drosophila melanogaster* [237], heads of diverse ant species [238], *Halobatrachus didactylus* larvae [239], and adult *Danio rerio* [240], among others. The rapid development of numerous tissue clearing techniques coupled with recent advances in microscopy has paved the way for broadening the scientific knowledge on the different biological events occurring within various organs [223].

OBJECTIVES

This work was focused on developing a standardized and reproducible animal model of infection and toxicity by using *Galleria mellonella* and to establish new methodologies and protocols with this model. The main objectives can be defined as follows:

1. Optimize the experimental conditions of *G. mellonella* larvae as an infection model.
2. Study the bacterial infection process *in vivo* by evaluating gene expression in *G. mellonella* larvae.
3. Test the efficacy of different antimicrobial strategies in infected *G. mellonella* larvae.
4. Determine the utility of *G. mellonella* larvae in toxicity screenings.
5. Test new methodology approaches in *G. mellonella* larvae.

ARTICLE 1

Monitoring Gene Expression during a *Galleria mellonella* Bacterial Infection

Published in *Microorganisms* (Q2, IF₂₀₁₉: 4.152)

Selected as the Cover Issue of *Microorganisms* Volume 8, Issue 11

DOI: 10.3390/microorganisms8111798

November 2020

Laura Moya-Andérico^{1,*}, Joana Admella¹, Rodrigo Fernandes¹, Eduard Torrents^{1,2,*}

¹Bacterial Infections and Antimicrobial Therapies group, Institute for Bioengineering of Catalonia (IBEC), The Barcelona Institute of Science and Technology (BIST), 08028 Barcelona, Spain

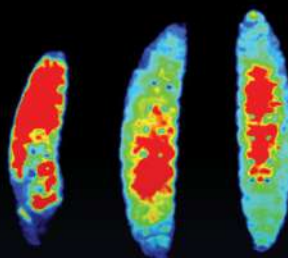
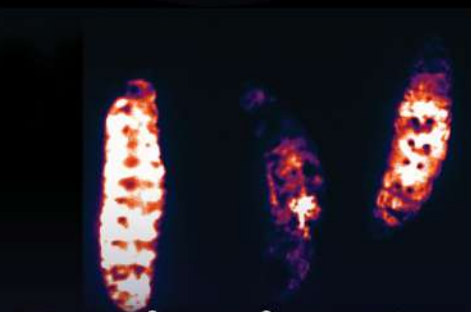
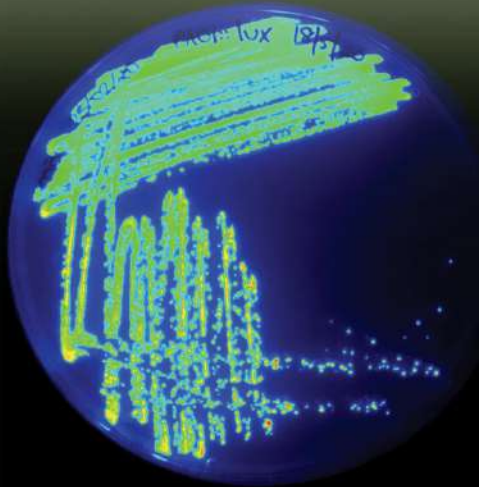
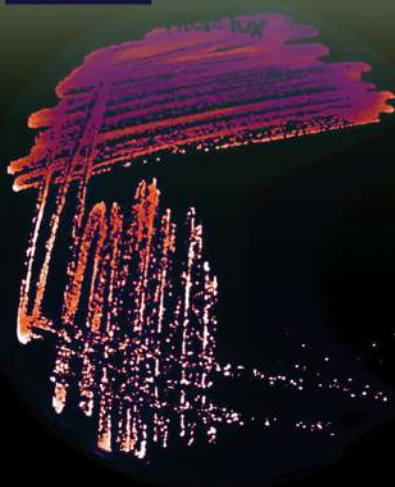
²Microbiology Section, Department of Genetics, Microbiology, and Statistics, Faculty of Biology, University of Barcelona, 08028 Barcelona, Spain

*Corresponding authors: Eduard Torrents (etorrents@ibecbarcelona.eu) and Laura Moya-Andérico (lmoya@ibecbarcelona.eu)



microorganisms

IMPACT
FACTOR
4.152



Monitoring Gene Expression during a *Galleria mellonella* Bacterial Infection

Volume 8 · Issue 11 | November 2020



mdpi.com/journal/microorganisms
ISSN 2076-2607

Article

Monitoring Gene Expression during a *Galleria mellonella* Bacterial Infection

Laura Moya-Andérico ^{1,*}, Joana Admella ¹, Rodrigo Fernandes ¹ and Eduard Torrents ^{1,2,*}

¹ Bacterial Infections and Antimicrobial Therapies Group, Institute for Bioengineering of Catalonia (IBEC), The Barcelona Institute of Science and Technology (BIST), 08028 Barcelona, Spain; jadmella@ibecbarcelona.eu (J.A.); rgaspar@ibecbarcelona.eu (R.F.)

² Microbiology Section, Department of Genetics, Microbiology, and Statistics, Faculty of Biology, University of Barcelona, 08028 Barcelona, Spain

* Correspondence: lmoya@ibecbarcelona.eu (L.M.-A.); etorrents@ibecbarcelona.eu (E.T.)

Received: 27 October 2020; Accepted: 13 November 2020; Published: 16 November 2020

Abstract: *Galleria mellonella* larvae are an alternative in vivo model that has been extensively used to study the virulence and pathogenicity of different bacteria due to its practicality and lack of ethical constraints. However, the larvae possess intrinsic autofluorescence that obstructs the use of fluorescent proteins to study bacterial infections, hence better methodologies are needed. Here, we report the construction of a promoter probe vector with bioluminescence expression as well as the optimization of a total bacterial RNA extraction protocol to enhance the monitoring of in vivo infections. By employing the vector to construct different gene promoter fusions, variable gene expression levels were efficiently measured in *G. mellonella* larvae at various time points during the course of infection and without much manipulation of the larvae. Additionally, our optimized RNA extraction protocol facilitates the study of transcriptional gene levels during an in vivo infection. The proposed methodologies will greatly benefit bacterial infection studies as they can contribute to a better understanding of the in vivo infection processes and pathogen–mammalian host interactions.

Keywords: *Galleria mellonella*; *P. aeruginosa*; hemolymph; hemocytes; bioluminescence; promoter probe vector; optimized RNA extraction; ribonucleotide reductases

1. Introduction

Galleria mellonella (greater wax moth) is a popular animal model for the study of virulence and pathogenicity of different bacteria. The larvae are conveniently sized for manipulation, they do not require feeding, and they are inexpensive to purchase and breed. Moreover, they do not need any special infrastructure, they present a low biohazard risk, and they are more ethically accepted than the traditional murine models [1,2]. With an innate immune response very similar to the one found in mammals, *G. mellonella* larvae possess both cellular and humoral defenses [3]. Furthermore, they are also widely used for testing the efficacy and toxicity of new antimicrobial agents, thus offering an additional pre-screening model to lower the number of drug tests performed in mammalian animals [4,5]. Based on all these advantages, *G. mellonella* has recently become an attractive alternative infection model for gathering initial data.

Studying a bacterial infection in *G. mellonella* larvae can also be challenging due to some methodological limitations. The use of bacterial strains containing GFP (green fluorescent protein) vectors has been widely considered as GFP-tagged bacteria are easily visualized in confocal and fluorescent microscopes, thus allowing bacteria to be tracked within the hemolymph and hemocytes of the larvae [6,7]. The fluorescence of bacteria within infected larvae has also been measured with a

spectrophotometer [8]. Unfortunately, most of the studies overlook that *G. mellonella* larvae possess natural green and red autofluorescence [8,9]. Therefore, the use of green and red fluorophores is associated with background autofluorescence problems that hinder the real measurement of bacterial fluorescence. For this reason, bioluminescence currently seems like the best methodology alternative to monitor an in vivo infection in *G. mellonella*. Bioluminescence is a rapid, cost-effective, and non-invasive imaging technique based on the synthesis of light derived from the *luxCDABE* operon's presence in bacteria [10]. The use of vectors that can confer a genetically encoded luminescent phenotype to bacterial strains has already been reported in the literature [11,12].

Galleria mellonella has been recognized as a suitable model for studying *Pseudomonas aeruginosa* infections [13]. Currently one of the most multidrug-resistant pathogens alive, it is also a formidable opportunistic pathogen that can cause invasive and fulminant infections, such as acute pneumonia or bloodstream infections, especially in immunocompromised hosts. Remarkably, the same pathogen also causes chronic infections that can persist for months to decades, such as chronic lung infections in individuals who have a genetic disease such as cystic fibrosis [14]. *P. aeruginosa* divides rapidly during its infection, requiring a high and persistent supply of dNTPs to replicate its DNA quickly. Ribonucleotide reductases (RNRs) are key enzymes that catalyze the reduction of ribonucleotides to deoxyribonucleotides, thus providing the precursor molecules needed for DNA synthesis and repair. There are three RNR classes (I, II, and III), which are encoded by the *nrdAB*, *nrdJab*, and *nrdDG* genes, respectively. Curiously, *P. aeruginosa* is one of the few organisms that encode all three classes (Ia, II, and III) in its genome. Although how each RNR class works is not yet completely understood, it is established that a particularly tight regulation is required to guarantee bacterial viability. RNR gene expression is controlled by NrdR, a transcriptional factor that binds to NrdR boxes in the promoter regions of the different *nrd* genes and is key for the transcriptional regulation of RNRs [15,16].

Here, we report the construction and utilization of several *lux* vectors containing different *nrd* promoter fusions as a better approach to study and monitor a *P. aeruginosa* in vivo infection in *Galleria mellonella*. Additionally, we optimized a protocol for the isolation of total bacterial RNA during a *G. mellonella* infection. The optimized methodologies will be valuable for the study of different infections and further applications in *G. mellonella*.

2. Materials and Methods

2.1. Bacterial Strains, Plasmids, and Growth Conditions

The bacterial strains and plasmids used in this study are listed in Table S1. *E. coli* and *P. aeruginosa* cells were routinely grown in Luria-Bertani (LB; Scharlab, Barcelona, Spain) medium at 37 °C. Antibiotics were added when required at the following concentrations: ampicillin, 50 µg/mL; and gentamicin, 10 µg/mL (*E. coli*) and 100 µg/mL (*P. aeruginosa*).

2.2. Recombinant DNA and PCR Methods

Recombinant DNA manipulations were performed using standard procedures [17] and following the manufacturers' instructions. DNA fragments were amplified by PCR using Phusion™ High-Fidelity DNA Polymerase (Thermo Scientific, Madrid, Spain) for cloning and DreamTaq Green PCR Master Mix (Thermo Scientific, Madrid, Spain) for colony PCR. All primers used in this study are listed in Table S2. Isolation of DNA fragments from agarose gels was carried out using the Monarch® DNA Gel Extraction Kit (New England BioLabs, Ipswich, MA, USA). DNA fragments were digested with corresponding restriction enzymes (Thermo Scientific, Madrid, Spain) and ligated with T4 DNA ligase (Invitrogen, Carlsbad, CA, USA). Plasmid DNA was isolated using the GeneJET™ Plasmid Miniprep Kit (Thermo Scientific, Madrid, Spain) and quantified using a NanoDrop™ 1000 spectrophotometer (Thermo Scientific, Madrid, Spain). DNA was transformed into *P. aeruginosa* PAO1 cells by electroporation using a Gene Pulser Xcell™ electroporator (Bio-Rad, Hercules, CA, USA) as previously described [18].

2.3. Construction of Promoter Probe Vector with Bioluminescence Expression

Specific restriction site sequences were incorporated as needed at the 5' ends of primers to facilitate cloning of fragments into the corresponding vector. The correct insertion of the fragments at each step was verified by colony PCR and DNA sequencing. The promoter probe vector pETS220-BIATlux (pETSlux) containing bioluminescence expression was made by first cloning the *SacI-KpnI* fragment containing the *luxCDABE* operon part of pMDM513 into the pBAM-Gm vector. From here, the *luxCDABE* genes (6109 bp, without promoter) were amplified by PCR using the Lux_SmaI_fw/pBAM-Gm up primers, and the amplicon was ligated into the pJET1.2 vector. Meanwhile, the pETS130 vector was digested with *HindIII* to remove the chloramphenicol acetyltransferase (*cat*) and GFP (mut3-GFP variant) genes. Both the resulting vector and the pJET1.2 vector containing the *luxCDABE* genes were digested with *HindIII* and ligated together to generate the pETSlux. The nucleotide sequence of the pETS220-BIATlux vector was deposited in GenBank (accession number MW117147).

2.4. Construction of *nrd* Promoter Fusions

Each *nrd* promoter region was amplified from *P. aeruginosa* PAO1 genomic DNA by PCR using a combination of forward and reverse primers that are listed in Table S2. Each fragment (785 bp, 395 bp, 189 bp, 273 bp, and 333 bp for *nrdA*, *nrdJ*, *nrdD*, *nrdR*, and *anr*, respectively) was gel purified and cloned into the pJET1.2 vector. After digestion with *EcoRI-SmaI* for *nrdA*, *SmaI-SacI* for *nrdJ*, and *EcoRI-SacI* for *nrdD*, *nrdR*, and *anr*, fragments were ligated into pETSlux, generating the pETS221, pETS222, pETS223, pETS224, and pETS225 plasmids.

2.5. *Galleria mellonella* Maintenance and Injection

G. mellonella larvae were fed an artificial diet (15% corn flour, 15% wheat flour, 15% infant cereal, 11% powdered milk, 6% brewer's yeast, 25% honey, and 13% glycerol) and reared at 34 °C in darkness as previously published [9]. To prepare the injection inoculum, the bacterial broth of the different strains was centrifuged at 4000 × g rpm for 10 min. The supernatant was discarded, and the pellet was re-suspended in 5 mL of 1 × PBS (Fisher Scientific, Madrid, Spain) during three washes. OD₅₉₀ was measured using a 1/10 dilution with 1 × PBS and equalized to a final OD₅₉₀ of 1. Afterward, 10-fold serialized dilutions of the equalized culture were made with 1 × PBS. *G. mellonella* larvae (200–220 mg each) were injected with 20–40 CFUs per larva through the top right proleg using a 26-gauge microsyringe (Hamilton, Reno, NV, USA). Groups of 3–6 larvae were injected for each condition and kept at 37 °C during the infection course.

2.6. Fluorescence Quantification and Microscopy

G. mellonella larvae were injected with an infective dose of *P. aeruginosa* PAO1 wild-type and *P. aeruginosa* PAO1 containing plasmids derived from pETS130 (Table S1), which encode transcriptional fusions of the *nrdA* and *nrdJ* promoters with GFP and E2Crimson that were previously constructed in our laboratory (pETS134, pETS180, pETS226, and pETS227) [14,19]. As a control, a group of larvae was only injected with 1 × PBS (Fisher Scientific, Madrid, Spain). The larvae were incubated at 37 °C for 16 h and until death (20 h for the infected larvae). After each time point, the larvae were anesthetized on ice for 10 min. Afterward, the tails of the larvae were cut off, and the hemolymph was collected into Eppendorf tubes while kept on ice to prevent melanization. The hemolymph from each group of larvae was pooled, and 1 × PBS was added until 100 µL total volume was reached. Relative fluorescence was measured from the top of a 96-well black, flat-bottom microtiter plate (Fisher Scientific, Madrid, Spain) in an Infinite® M200 Pro microplate reader (Tecan, Männedorf, Switzerland). The optimized Z-position was established as 18,000 µm, and the integration time was set as 20 µs. For GFP, the gain was adjusted to the optimal 142, the excitation wavelength was fixed at 480 nm, and the emission wavelength was set at 515 nm. For E2Crimson, the optimal gain was determined as 255 nm, and the excitation and emission wavelengths were established as 600 and 650

nm, respectively. The results obtained were analyzed using the GraphPad Prism 8.0 software (San Diego, CA, USA).

After fluorescence quantification, the hemolymph was visualized with an inverted fluorescence microscope ECLIPSE Ti-S/L100 (Nikon, Tokyo, Japan) coupled with a DS-Qi2 camera (Nikon, Tokyo, Japan) using a 100×/1.30 oil objective with the GFP and Texas Red filters for green and red fluorescence, respectively. The images obtained were analyzed using the NIS-Elements microscope imaging software (Nikon, Tokyo, Japan).

2.7. Bioluminescence Measurements

Relative luminescence of infected larvae was measured in a 6-well microtiter plate (Caplugs Evergreen, Buffalo, NY, USA) in a Spark[®] multimode microplate reader (Tecan, Männedorf, Switzerland) with an integration time of 1000 ms. The results obtained were analyzed using GraphPad Prism 8.0 software (San Diego, CA, USA). The ImageQuant[™] LAS 4000 mini imager (GE Healthcare, Chicago, IL, USA) allowed us to take chemiluminescence pictures of the worms over different time points of infection. Exposure time was optimized to 30 s, and images were afterward edited with ImageJ FIJI (Version 1.52p, National Institutes of Health, Bethesda, MD, USA). Before each measurement, larvae were anesthetized for ten minutes on ice.

2.8. RNA Extraction, Reverse Transcription, and Real-Time PCR

G. mellonella larvae were injected with an infective dose of *P. aeruginosa* PAO1 wild-type and incubated for about 16 h at 37 °C. Then, the larvae were anesthetized on ice for 10 min. Subsequently, the tails of the larvae were cut off using a size 23 sterile surgical blade (Paramount Surgimed, New Delhi, India), and the hemolymph was collected into Eppendorf tubes while kept on ice to avoid melanization. The hemolymph from each group of larvae was pooled, and hemocytes were pelleted by centrifuging at 1000× g for 5 min at 4 °C. The cell-free hemolymph was treated with RNAprotect[®] Bacteria Reagent (Qiagen, Hilden, Germany), as stated in the manufacturer's handbook for subsequent RNA purification. As a reference, *P. aeruginosa* PAO1 wild-type cells were grown in LB medium to mid-exponential growth phase (OD₅₅₀ = 0.5) and then treated with RNAprotect[®].

In both samples, the RNA was purified using the GeneJET[™] RNA Purification Kit (Thermo Scientific, Madrid, Spain) according to the manufacturer's instructions. DNase (Turbo DNA-free[™], Applied Biosystems, Foster City, CA, USA) was used to remove DNA contamination that was verified by PCR. For cDNA synthesis, RNA was quantified using a NanoDrop[™] 1000 spectrophotometer (Thermo Scientific, Madrid, Spain), and 0.25 µg of RNA was reverse transcribed using Maxima Reverse Transcriptase (Thermo Scientific, Madrid, Spain) along with random hexamer primers (Thermo Scientific, Madrid, Spain) by following the manufacturer's guidelines.

Quantitative real-time PCR (qRT-PCR) was performed using PowerUp[™] SYBR[™] Green Master Mix (Applied Biosystems, Foster City, CA, USA) in a StepOnePlus[™] Real-Time PCR System (Applied Biosystems, Foster City, CA, USA) according to the manufacturer's protocol. All of the qRT-PCR reactions used specific gene primers that are listed in Table S2. The *gapA* gene was used as an internal standard as its expression is vital during *P. aeruginosa* growth. Three replicates were performed for each sample, and the entire experiment was independently performed twice. The results were analyzed using the comparative Ct (cycle threshold) method ($\Delta\Delta Ct$) and plotted using GraphPad Prism 8.0 software (San Diego, CA, USA).

2.9. Other Methods

G. mellonella larvae were injected with an infective dose of *P. aeruginosa* PAO1 wild-type, *P. aeruginosa* PAO1 expressing GFP (PAO1::eGFP), and *P. aeruginosa* PAO1 expressing the *luxCDABE* genes (PAO1::lux) followed by incubation at 37 °C for about 19 h or until death. The larvae infected with PAO1 wild-type and PAO1::eGFP were imaged in a Gel Doc[™] XR+ imaging system (Bio-Rad, Hercules, CA, USA) using the Alexa Fluor[™] 488 protocol with UV trans-illumination. The same larvae were also imaged directly under an LSM 800 confocal laser scanning microscope (Zeiss, Jena,

Germany) with the 20×/0.8 air and 63×/1.4 oil objectives. The larvae infected with PAO1 wild-type and PAO1::lux were visualized in the ImageQuant™ LAS 4000 mini (GE Healthcare, Chicago, IL, USA) and Odyssey® Fc (LI-COR, Lincoln, NE, USA) imaging systems using the chemiluminescence method with a 30-s exposition time. In the LAS 4000 mini, the larvae were also pictured using the digitization (epi-illumination) method with an exposure time of 1/30 s. As a reference, free bacteria grown in LB media were also imaged with the same methodologies. Images were analyzed using ImageJ FIJI (Version 1.52p, National Institutes of Health, Bethesda, MD, USA) and GraphicConverter (Version 11, Lemke Software, Peine, Germany).

3. Results and Discussion

3.1. Optimization of Reporter Genes for Gene Expression Studies

To first determine the best reporter gene for bacterial gene expression studies in *G. mellonella*, larvae were infected with two *P. aeruginosa* PAO1 strains, each harboring either green fluorescent protein (GFP) or luciferase genes (*lux*) inserted in its chromosome (PAO1::eGFP and PAO1::lux, respectively). These were chosen as they represent the most commonly used non-enzymatic reporter genes. The larvae were incubated at 37 °C until their death, which is when sufficient bacterial load should be available to detect its fluorescence or bioluminescence. Then, the larvae were visualized in imaging systems readily available in the laboratory.

The first instrument tested was the Gel Doc™ imaging system (see Materials and Methods). This instrument or an analog is readily available in most laboratories as it is commonly used to image protein and nucleic acid gels, blots, and macroarrays. This system also supports multiple detection methods, including fluorescence and colorimetric detection [20]. Using the preset Alexa Fluor™ 488 protocol, *P. aeruginosa* PAO1 WT and PAO1::eGFP on LB plates were first imaged. As seen in Figure 1A, green luminescence was seen with PAO1::eGFP but not with the wild-type strain as it is not expressing a fluorescent protein. The next step was to image larvae infected with the two previous strains to see whether the same result could be obtained. Unfortunately, both groups of larvae showed some green fluorescence around the body's edges that is most likely autofluorescence. Specific bacterial fluorescence was not seen inside the larvae as the fluorescence probably cannot be detected through the larval cuticle. Additionally, we tried to image the same samples under a confocal microscope. Entire larvae were visualized using the green (488 nm) laser for PAO1::eGFP and the differential interference contrast (DIC) mode for non-fluorescent bacteria (PAO1 WT). As seen in Figure 1B, no bacterial fluorescence could be seen as the laser could not penetrate the cuticle of the larvae. Instead, only green autofluorescence was again detected in both types of samples. In all cases, the use of protein fluorescence was not the best option for monitoring gene expression during a *G. mellonella* infection as it cannot overcome the larval cuticle. Furthermore, as seen in our experiments, the particularly high autofluorescent background of the worms can hinder the precise quantification of the protein.

As the fluorescence detection systems were not successful, the next step was to try using bioluminescence. This methodology is commonly used to study ongoing biological processes in living organisms [21]. *P. aeruginosa* PAO1 WT and PAO1::lux on LB plates were first imaged in two different devices, the ImageQuant™ LAS 4000 mini and the Odyssey® Fc imaging systems (see Materials and Methods). These two instruments or equivalent ones are commonly found in laboratories as they are used to analyze chemiluminescent Western blots, among other applications. In both systems, the LB plate with *P. aeruginosa* PAO1::lux showed a high amount of bioluminescence while the PAO1 WT plate did not. The same result was obtained with the larvae infected with *P. aeruginosa* PAO1::lux and PAO1 WT (Figure 1C). One finding worth emphasizing is that the larvae that were not infected with bacteria expressing the *lux* genes had almost negligible background bioluminescence. Thus far, it appears that bioluminescence is the best method for studying bacterial infections using whole larvae.

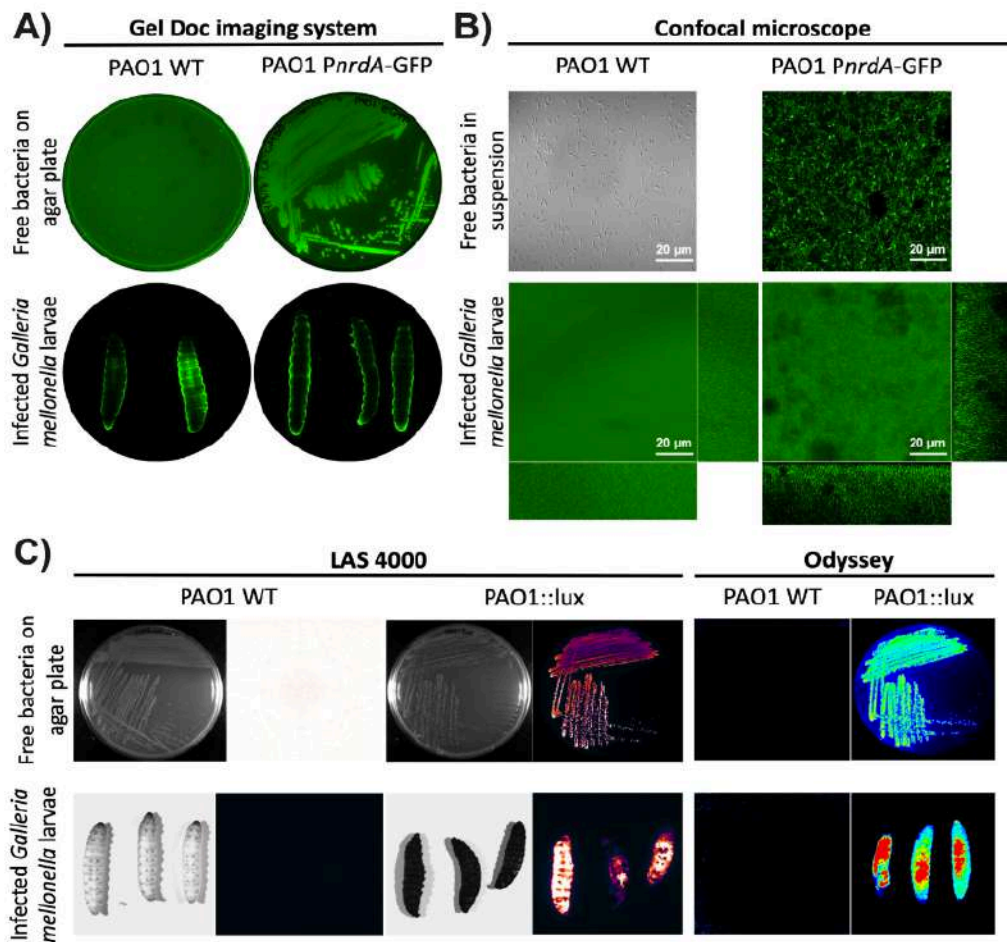


Figure 1. Visualization of *G. mellonella* larvae using different imaging methodologies. *P. aeruginosa* PAO1 wild-type (WT) and PAO1::eGFP strains were imaged using (A) the Gel Doc™ imaging system and (B) the LSM 800 confocal microscope. Free bacteria were imaged on LB media as well as inside *G. mellonella* larvae. (C) *P. aeruginosa* PAO1 wild-type (WT) and PAO1::lux were imaged as free bacteria on an LB plate and within *G. mellonella* larvae using the ImageQuant™ LAS 4000 mini and Odyssey® Fc imaging systems.

3.2. Determining Autofluorescence in *Galleria mellonella*

As was clearly shown previously, the larval cuticle is impermeable to the light emitted by the different fluorescent proteins used in this work. As a way to overcome the cuticle's opacity, further experiments were done to try to measure the signal emitted directly from fluorescent proteins present in the hemolymph extracted from infected larvae. For this, *G. mellonella* larvae were injected with *P. aeruginosa* PAO1 wild-type (WT), two *P. aeruginosa* PAO1 strains expressing GFP (*PnrdA*-GFP [pETS134] and *PnrdJ*-GFP [pETS180]), two *P. aeruginosa* PAO1 strains expressing E2Crimson (*PnrdA*-E2Crimson [pETS226] and *PnrdJ*-E2Crimson [pETS227]), and PBS. The hemolymph from each group was extracted, and then, green and red fluorescence was measured in a Tecan plate reader using GFP (Figure 2A) and E2Crimson (Figure 2B) settings, respectively. At 16 and 20 h post-infection, *P. aeruginosa* PAO1 WT presented an inherent amount of both green and red autofluorescence when compared to the bacterial strains expressing GFP and E2Crimson (Figure 2A,B). Similar results were

also seen with bacteria expressing mOrange and eYFP (data not shown). At 16 and 20 h post-injection, the hemolymph of larvae injected with PBS also had high autofluorescence with both GFP and E2Crimson that resulted in values comparable to the ones obtained with the expression vectors. The only difference between non-infected and infected larvae is that PAO1 WT causes hemocyte proliferation within the larvae in response to the infection [22], so it seems that hemocytes also possess intrinsic autofluorescence. Additionally, it can be noticed that the *PnrDA* strains show more fluorescence than the *PnrDJ* strains, but this is related to their genetic expression during infection, as we previously reported [14]. When quantifying GFP and E2Crimson fluorescence, all strains follow the same pattern, and it is undeniable that *G. mellonella*'s autofluorescence cannot pass unnoticed any longer.

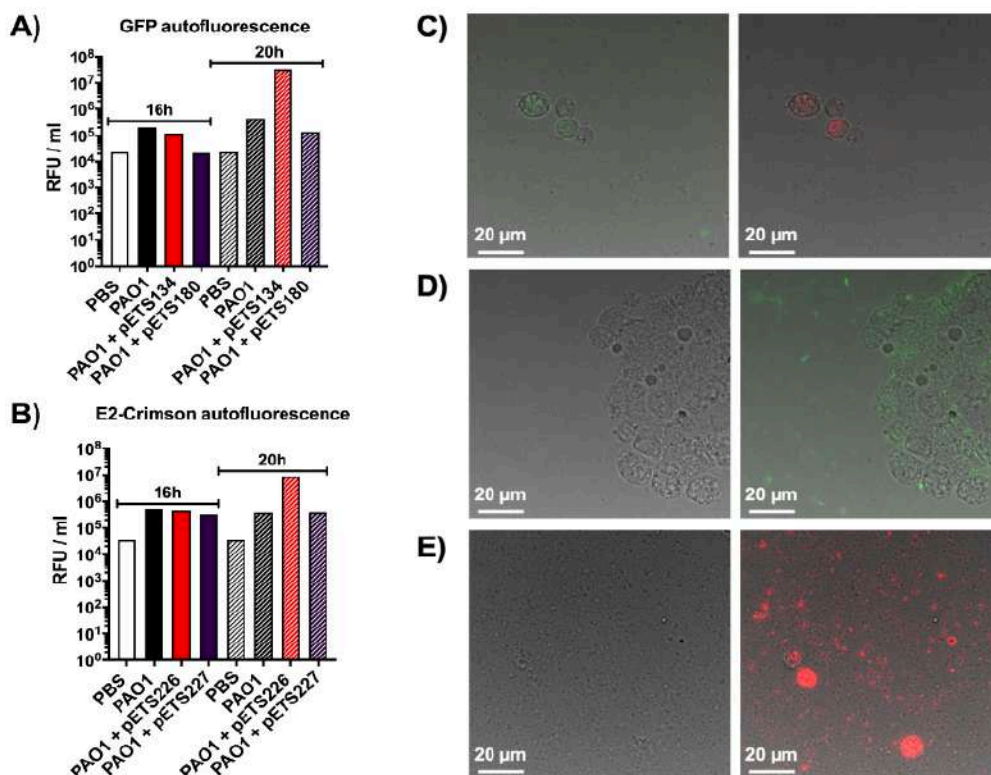


Figure 2. Autofluorescence studies in the hemolymph of *G. mellonella*. **(A)** Quantification of green autofluorescence, in relative fluorescence units per milliliter of hemolymph, using larvae infected with different *P. aeruginosa* strains and PBS (negative control) at 16 and 20 h post-infection. **(B)** Quantification of red autofluorescence, in relative fluorescence units per milliliter of hemolymph, using larvae infected with different *P. aeruginosa* strains and PBS (negative control) at 16 and 20 h post-infection. **(C)** Phase contrast merged with green and red fluorescence images of hemolymph extracted from larvae infected with *P. aeruginosa* PAO1 wild-type showing the green and red autofluorescence of hemocytes, respectively. **(D)** Phase contrast only and phase contrast merged with green fluorescence images of hemolymph extracted from larvae infected with *P. aeruginosa* PAO1 *PnrDA*-GFP. **(E)** Phase contrast only and phase contrast merged with red fluorescence images of hemolymph extracted from larvae infected with *P. aeruginosa* PAO1 *PnrDA*-E2Crimson.

Additionally, the same hemolymph was visualized under a fluorescence microscope to reinforce the plate reader results. In Figure 2C, the hemolymph of larvae infected with *P. aeruginosa* PAO1 WT was used to observe the natural green and red autofluorescence of hemocytes. Hemolymph

containing *P. aeruginosa* PAO1 *PnrdA*-GFP appears in Figure 2D, where bacteria can be seen expressing green fluorescence along with the green autofluorescence of hemocytes. The same happens in the hemolymph containing *P. aeruginosa* PAO1 *PnrdA*-E2Crimson, as seen in Figure 2E, where bacteria and hemocytes appear red when merging the phase contrast and red channels.

Fluorescent promoter probe vectors are widely used for gene expression analysis under different conditions [23,24], so these vectors would be ideal to use in a *G. mellonella* infection. However, the results obtained with the hemolymph studies confirmed that fluorescent protein vectors could not be used in *G. mellonella*. The autofluorescence of hemocytes during *P. aeruginosa* infections poses a critical limitation in using fluorescent vectors as changes in fluorescence expression cannot be easily distinguished. For this reason, vectors expressing bioluminescence seem like the most optimal alternative.

3.3. Construction of pETS220-BIATlux Vector and *nrd* Fusions

To study gene expression using bioluminescence in *G. mellonella* larvae, a vector containing the *lux* genes was first needed. The approach was to create a promoter probe vector that could be used with any gene promoter and not just a vector containing the promoters required for our purpose. For this, the pETS130 vector [14] was modified by replacing the *cat* and *mut3*-GFP variant genes with the *luxCDABE* genes, thus generating the pETS220-BIATlux (pETSlux) vector with a final size of 10,677 base pairs (see Materials and Methods). This plasmid (Figure 3) offers several advantages: (1) it has a multi-cloning site (MCS) containing unique restriction sites for easy insertion of the promoter fragment of interest, (2) it carries gentamicin resistance for simple selection, and (3) it is a broad-host-range vector as it contains both pBBR1 *oriV* and pBBR1 *Rep* that allow its replication in a variety of microorganisms [25].

Once the vector was successfully constructed, the promoters of interest were cloned using the unique cutter restriction enzymes within the multi-cloning site. As a proof of concept, the promoters of the different *P. aeruginosa* ribonucleotide reductase genes (*nrd*) (*PnrdA*, *PnrdJ*, *PnrdD*, and *PnrdR*) were all included to efficiently detect differences in gene expression during infection. These genes were previously characterized by our group during infection in *Drosophila melanogaster* [14] and *Danio rerio* [24]. As a negative control, a fragment of the *anr* gene similar in size to the promoters used was inserted in the vector using the MCS. This was done to detect the vector's intrinsic levels of bioluminescence. After all the *nrd* promoter fusions were successfully constructed, the vectors were electrotransformed into *P. aeruginosa* PAO1 wild-type cells. Although the vector is relatively large (>10 kb), all the DNA manipulations were carried out effortlessly, and the vector was easily electroporated into the PAO1 cells in the first attempt. Finally, positive clones were selected using gentamicin. Using the pETSlux for cloning the different promoters facilitated the process in many ways: the promoters were easily cloned using the MCS, the promoter fusions could be cultured in both *E. coli* and *P. aeruginosa*, and positive clones were readily detected using gentamicin selection. These advantages demonstrate the high practicality of the pETSlux vector in bacterial gene expression studies.

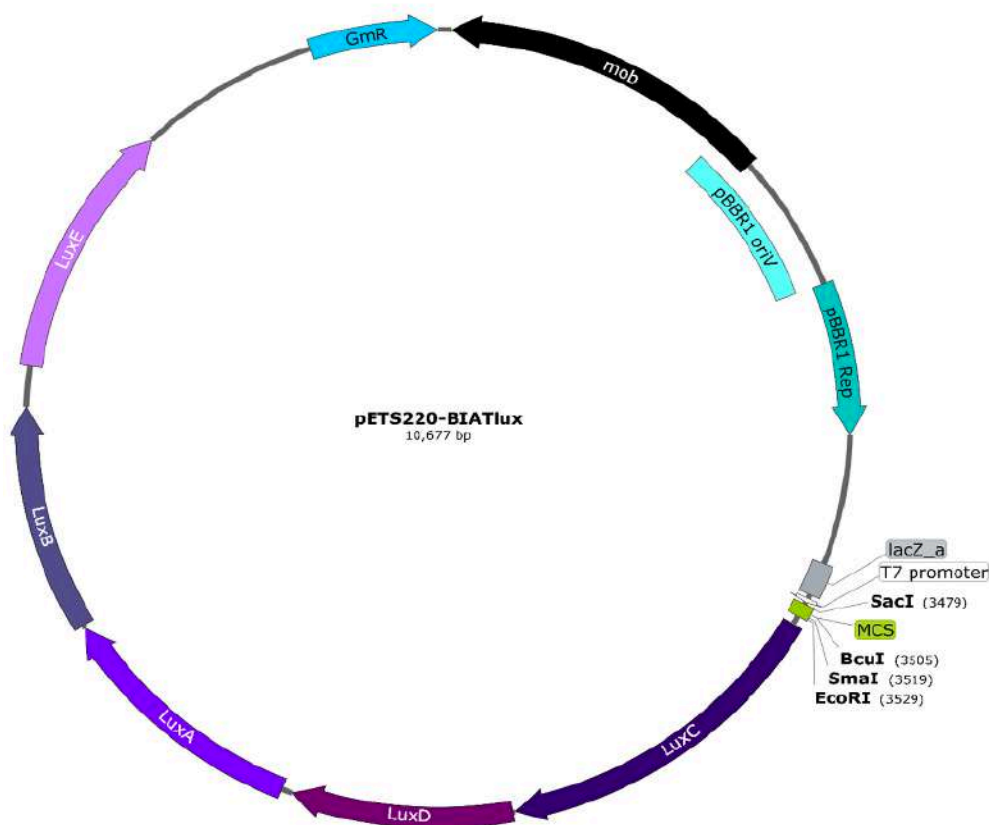


Figure 3. Map of the pETS220-BIATlux (pETSlux) promoter-probe vector. The *luxCDABE* genes were inserted into the backbone of the pETS130 vector. Relevant genetic elements include: gentamicin resistance (Gm^R) imparted by *aacCI*, plasmid mobilization functions encoded by *mob*, and pBBR1 *oriV* and pBBR1 *Rep* as the replication origin and replication protein, respectively, that are essential for broad-host-range capability. Unique cutter restriction enzymes within the multi-cloning site (MCS) are shown in bold. All genes are represented in scale according to the total length of the plasmid. The vector map was designed with SnapGene® version 5.0.8 (GSL Biotech, San Diego, CA, USA).

3.4. Monitoring a *P. Aeruginosa* Infection in *G. Mellonella* Larvae

As proof of concept for our bioluminescence vector, we evaluated the expression of the well-known ribonucleotide reductase (*nrd*) genes [15,16] to track an in vivo infection. *G. mellonella* larvae were injected with the *P. aeruginosa* PAO1 wild-type strains containing the different *nrd* promoter-*lux* fusion constructions. Relative luminescence was measured for each larval group at several time points during the infection course: 8, 14, 17, and 20 h post-infection with the latter corresponding to larval death. The bioluminescence within the larvae should vary depending on the level of expression of the different *nrd* genes as regulated by the promoters controlling the *lux* operon. In effect, the infection could be monitored at different time points as the relative luminescence units (RLU) within the larvae increased over time for the different strains (Figure 4A). The expression of both *PnrdR-lux* and *PnrdJ-lux* started rising at 14 h post-infection (4059 and 2740 RLU, respectively) and continued escalating throughout the remainder of the infection. In contrast, *PnrdD-lux* and *PnrdA-lux* both had a lower expression that did not reach similar levels as *PnrdJ-lux* (about 2.5×10^5 RLU) until the larvae were dead. At 20 h post-infection (death), *PnrdR-lux* had the highest RLU values (3.5×10^6), thus indicating that *nrdR* is highly expressed not only at death but throughout the whole infection. The

negative control, *Anr-lux*, had low levels of bioluminescence that ranged from 36 to 2600 RLU, which were consistent with background signals caused by leaking reporter expression. Despite the leaking, the values of all the other strains were much higher than *Anr-lux* at all time points. The highest RLU value obtained with *Anr-lux* was only 2600 at 20 h post-infection, which is about 1340 times less than the corresponding value for *PnrdR-lux* (3.5×10^6 RLU).

Bioluminescence images were also taken at 17 and 20 h post-infection for each of the larvae conditions using the ImageQuant™ LAS 4000 mini imaging system (Figure 4B). The images show that the larvae emitted more or less bioluminescence according to their respective *nrd* expression (depending on the RNR class expressed), which coincided with the results obtained in Figure 4A. Additionally, the induction in the expression of the different *nrd* genes during the infection was quantified (Figure 4C). *Anr-lux* (negative control) displayed a luminescent background signal, as previously mentioned, which was subtracted from each of the strains and time points. Therefore, the values that appear for each strain in Figure 4C correspond to its induction factor of expression compared to itself at the initial stage of infection (8 h post-infection). A high induction in *nrdR* expression was distinctly noticed during all time points (119, 18,217, and 106,174-fold induction at 14, 17, and 20 h, respectively), followed by *nrdJ* (73, 3988, and 6706-fold induction) and *nrdD* (12, 543, and 3557-fold induction) at the same time points. On the other hand, a small induction (4–46-fold) in *nrdA* expression was seen in the first hours until it suddenly increased at the last time point (up to 6838 times). However, this induction value was still considerably smaller than the one seen with the *nrdR* gene (106,174) at the same time point. A broadened view of Figure 4 confirmed the shift of *nrd* expression during a *P. aeruginosa* infection in *G. mellonella* larvae that was possible to observe and monitor due to the *lux* constructions. Furthermore, the shift seen corresponds with previous results obtained in our lab. In the *Drosophila melanogaster* and *Danio rerio* infection models, the expression of *nrdJ* and *nrdD* (RNR class II and III, respectively) was also highly induced during the course of a *P. aeruginosa* infection [14,24]. This demonstrates the importance of anaerobic environments for the in vivo expression of these RNR classes [14,16,26].

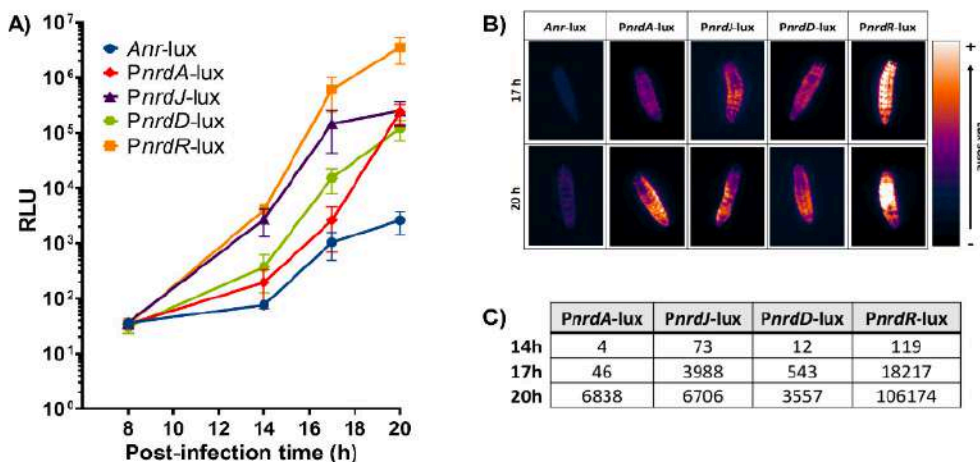


Figure 4. Study of a *P. aeruginosa* PAO1 infection in *G. mellonella* larvae using the different *lux* constructions. (A) Measurements of relative luminescence (RLU) in *G. mellonella* during several time points after infection within the different strains. (B) Images of *G. mellonella* larval bioluminescence taken with the ImageQuant™ LAS 4000 mini imager at 17 and 20 h post-infection and visualized using the Gem lookup table from ImageJ FIJI. (C) Bioluminescence induction factors during the different time points (14, 17, and 20 h post-infection). *Anr-lux* background was subtracted from each of the strains.

Another approach for measuring gene expression during infection in *G. mellonella* was attempted using qRT-PCR. For this, a protocol to extract RNA from the bacterial cells inside the *G. mellonella* larvae was initially optimized (Figure 5A). First, larvae were injected with an infection dose of *P. aeruginosa* PAO1 wild-type (WT) and then kept at 37 °C for about 16 h. This time point was chosen based on previous growth curves done with PAO1 WT in *G. mellonella* that revealed that at 16 h post-infection, close to 10⁸ bacterial cells per milliliter were present within the larvae (Figure 5B). According to the GeneJET™ RNA purification kit protocol, a bacterial concentration near 10⁹ is recommended for optimal RNA yield. After incubation, the larvae were anesthetized on ice for 10 min before cutting their tail off to extract the hemolymph. The hemolymph from each larvae group was pooled and then centrifuged at low speed for 5 min at 4 °C to remove the hemocytes. Up to this point, it is important to maintain the hemolymph on ice to prevent melanization. The cell-free hemolymph containing PAO1 WT was treated with RNAprotect® and afterward used for RNA extraction, cDNA preparation, and qRT-PCR analysis. By using this optimized protocol, *P. aeruginosa* PAO1 cells that were infecting *G. mellonella* larvae in vivo were able to be isolated for efficient RNA purification, which yielded high and pure RNA concentrations (Table S3) that were successfully used in downstream applications.

The RNA expression of the infection cells was analyzed relative to the gene expression in *P. aeruginosa* PAO1 wild-type cells grown in LB medium to a mid-exponential growth phase. This control was selected based on the growth curve seen in Figure 5B that shows that the bacterial cells within the larvae are in the mid-exponential growth phase during sample collection. The growth curve also indicates that an active DNA synthesis is underway due to the involvement of RNR during the infection process. To ensure the reaction specificity of the qRT-PCR results, a melting curve analysis was performed, which showed a single, pure amplicon for each of the genes assessed (Figure S1). The results were then analyzed using the comparative Ct (cycle threshold) method ($\Delta\Delta C_t$) by comparing the Cts of the different genes in a PAO1 WT infection against the Cts of the same genes in a PAO1 WT exponential culture, and the transcript levels of each gene were normalized using the *gapA* internal control. Differences in the expression of the different *nrd* genes could be clearly seen (Figure 5C). The highest inductions were seen with *nrdR* and *nrdJ*, which were 7.7 and 7.5 times, respectively, more induced in infection than in planktonic culture. Less induction was seen with *nrdA* (3.1-fold change), while *nrdD* only had a 1.7-fold change induction. A 5.3-fold increase in the expression of the *norC* gene, a marker of anaerobiosis, indicated a decrease in oxygen levels, leading to a shift in the anaerobic metabolism of PAO1 WT during infection. When compared to the results obtained with the different pETSlux constructions, the RNR expression pattern is very similar except for *nrdD* and *nrdA* since *PnrdD-lux* had higher expression than *PnrdA-lux*. It is important to keep in mind that the RNA was extracted about 1 h before the time point used in the pETSlux measurements, and gene expression depends on the metabolic state of the bacteria at the time of RNA extraction. Therefore, measurements using pETSlux are more efficient since gene expression can be measured in vivo at multiple time points (independent of bacterial concentration inside the larvae) without much manipulation of the larvae or bacteria. Nevertheless, both the bioluminescence and qRT-PCR experiments revealed that *nrdR* is significantly induced during a *P. aeruginosa* infection. Although *nrdR* expression was reported to increase in vitro when interacting with T84 cells [26], this is the first time that *nrdR* induction is reported in an in vivo infection experiment. Nevertheless, further work is needed to elucidate its biological role under these specific conditions.

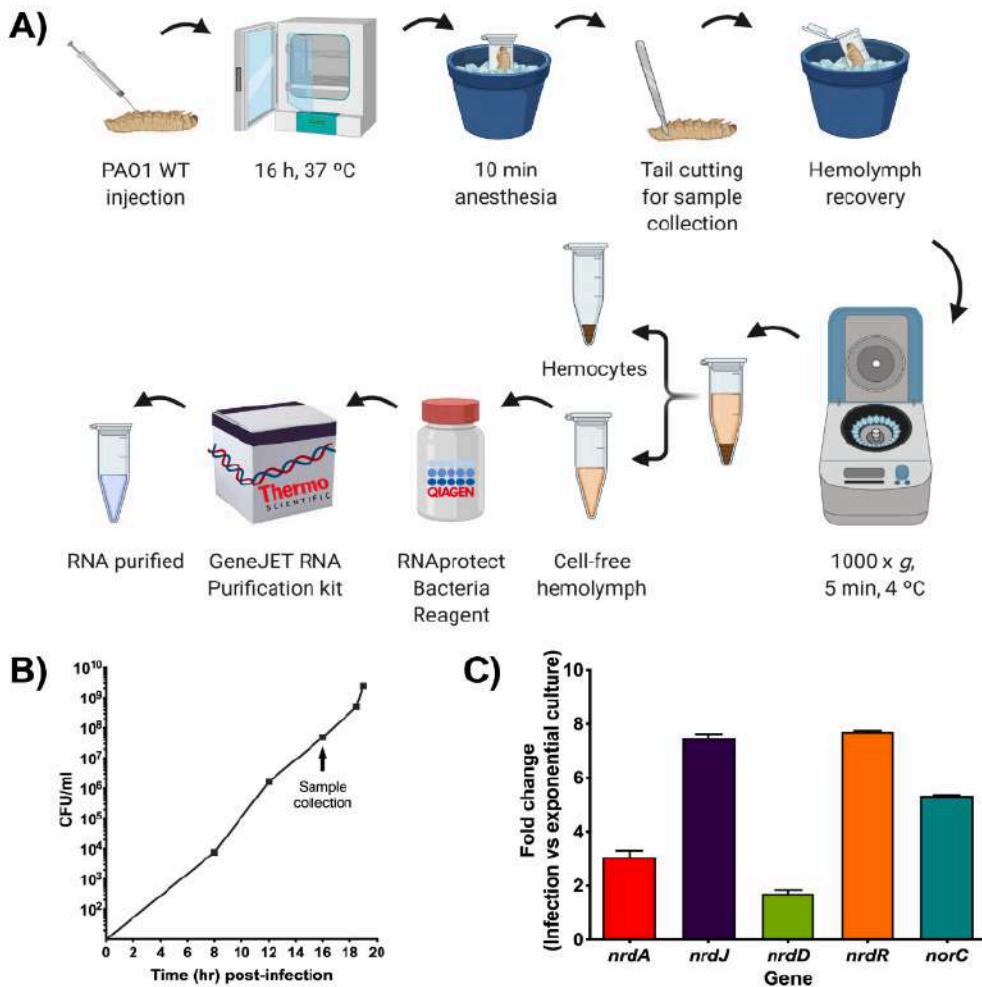


Figure 5. Gene expression studies during a *P. aeruginosa* infection in *G. mellonella*. (A) Schematic representation of the steps involved in the optimized RNA extraction protocol for bacterial cells derived from a *G. mellonella* infection. Created with BioRender.com. (B) *P. aeruginosa* PAO1 wild-type (WT) growth curve in *G. mellonella* larvae that was determined by calculating CFU/mL at different time points after infection as well as at death (last point). Samples for qRT-PCR were taken when the bacteria were in the exponential growth phase (close to 10⁸ CFU/mL) as indicated by the arrow. (C) Fold change of *nrd* and anaerobic (*norC*) genes determined by qRT-PCR during PAO1 WT infection compared to PAO1 WT cells grown to exponential phase in LB medium. The *gap* gene was used as an internal standard. The values shown are the average from two independent experiments, and the error bars indicate a positive standard deviation.

In this study, we demonstrated the limitation with the use of fluorescent vectors in *Calleria mellonella* due to its intrinsic autofluorescence. For this reason, a promoter probe vector containing bioluminescence expression was constructed that offers a simple and effective method for monitoring gene expression in vivo using the *G. mellonella* animal model of infection. Furthermore, an RNA extraction protocol for bacterial cells from within *G. mellonella* larvae was optimized to enable the study of transcriptional levels of genes during an in vivo infection. These findings will allow for a better understanding of the in vivo infection process of different bacteria in a setting that mimics

mammalian body temperature and pathogen–mammalian host interactions that can only be achieved in an economical and ethical manner when using the *G. mellonella* model.

Supplementary Materials: Supplementary materials can be found at www.mdpi.com/2076-2607/8/11/1798/s1, Table S1: Bacterial strains and plasmids used in this study, Table S2: Primers used in this study, Table S3: RNA quality, Figure S1: qRT-PCR melting curves.

Author Contributions: The manuscript was written through the contributions of all authors. L.M.-A., J.A., and R.F. performed biological assays and wrote the manuscript. E.T. directed the research, revised the experimental data, and wrote the manuscript. All authors have read and agreed to the published version of the manuscript.

Funding: This study was partially supported by grants from the Ministerio de Economía, Industria y Competitividad, MINECO, and Agencia Estatal de Investigación (AEI), Spain, co-funded by Fondo Europeo de Desarrollo Regional, FEDER, European Union (RTI2018-098573-B-I00), the CERCA program and AGAUR-Generalitat de Catalunya (2017SGR-1079), the European Regional Development Fund (FEDER), Catalan Cystic Fibrosis association and Obra Social “La Caixa”. L.M.-A. is thankful to the Generalitat de Catalunya for its financial support through the FI program (2017 FI_B2 00830).

Acknowledgments: The authors wish to thank Ana Morton (Department de Biologia Animal, Biologia Vegetal i Ecologia (BABVE) at the UAB for providing *G. mellonella* eggs. We thank Donald T. Moir for providing plasmid pMDM513 and Tim Tolker Nielsen for providing the MKI71 strain.

Conflicts of Interest: The authors declare no conflicts of interest. The funders had no role in the design of the study; in the collection, analyses, or interpretation of data; in the writing of the manuscript, or in the decision to publish the results.

References

1. Champion, O.L.; Wagley, S.; Titball, R.W. *Galleria mellonella* as a Model Host for Microbiological and Toxin Research. *Virulence* **2016**, *7*, 840–845, doi:10.1080/21505594.2016.1203486.
2. Benthall, G.; Touzel, R.E.; Hind, C.K.; Titball, R.W.; Sutton, J.M.; Thomas, R.J.; Wand, M.E. Evaluation of Antibiotic Efficacy Against Infections Caused by Planktonic or Biofilm Cultures of *Pseudomonas aeruginosa* and *Klebsiella pneumoniae* in *Galleria mellonella*. *Int. J. Antimicrob. Agents* **2015**, *46*, 538–545, doi:10.1016/j.ijantimicag.2015.07.014.
3. Wojda, I. Immunity of the Greater Wax Moth *Galleria mellonella*. *Insect Sci.* **2016**, *24*, 342–357, doi:10.1111/1744-7917.12325.
4. Desbois, A.P.; Coote, P.J. Utility of Greater Wax Moth Larva (*Galleria mellonella*) for Evaluating the Toxicity and Efficacy of New Antimicrobial Agents. *Adv. Appl. Microbiol.* **2012**, *78*, 25–53, doi:10.1016/b978-0-12-394805-2.00002-6.
5. Tsai, C.J.-Y.; Loh, J.M.S.; Proft, T. *Galleria mellonella* Infection Models for the Study of Bacterial Diseases and for Antimicrobial Drug Testing. *Virulence* **2016**, *7*, 214–229, doi:10.1080/21505594.2015.1135289.
6. Champion, O.L.; Cooper, I.A.M.; James, S.L.; Ford, D.; Karlyshev, A.V.; Wren, B.W.; Duffield, M.; Oyston, P.C.F.; Titball, R.W. *Galleria mellonella* as An Alternative Infection Model for *Yersinia pseudotuberculosis*. *Microbiology* **2009**, *155*, 1516–1522, doi:10.1099/mic.0.026823-0.
7. Leuko, S.; Raivio, T. Mutations That Impact the Enteropathogenic *Escherichia coli* Cpx Envelope Stress Response Attenuate Virulence in *Galleria mellonella*. *Infect. Immun.* **2012**, *80*, 3077–3085, doi:10.1128/iai.00081-12.
8. Parthuisot, N.; Rouquette, J.; Ferdy, J.-B. A High-Throughput Technique to Quantify Bacterial Pathogens’ Virulence on the Insect Model *Galleria mellonella*. *J. Microbiol. Methods* **2018**, *152*, 69–72, doi:10.1016/j.mimet.2018.07.013.
9. Moya-Andérico, L.; Admella, J.; Torrents, E. A Clearing Protocol for *Galleria mellonella* Larvae: Visualization of Internalized Fluorescent Nanoparticles. *New Biotechnol.* **2020**, doi:10.1016/j.nbt.2020.08.002.
10. Francis, K.P.; Joh, D.; Bellinger-Kawahara, C.; Hawkinson, M.J.; Purchio, T.F.; Contag, P.R. Monitoring Bioluminescent *Staphylococcus aureus* Infections in Living Mice Using a Novel *luxABCDE* Construct. *Infect. Immun.* **2000**, *68*, 3594–3600, doi:10.1128/iai.68.6.3594-3600.2000.
11. La Rosa, S.L.; Diep, D.B.; Nes, I.F.; Brede, D.A. Construction and Application of a *luxABCDE* Reporter System for Real-Time Monitoring of *Enterococcus faecalis* Gene Expression and Growth. *Appl. Environ. Microbiol.* **2012**, *78*, 7003–7011, doi:10.1128/aem.02018-12.

12. Riedel, C.U.; Casey, P.G.; Mulcahy, H.; O’Gara, F.; Gahan, C.G.; Hill, C. Construction of p16Slux, a Novel Vector for Improved Bioluminescent Labeling of Gram-Negative Bacteria. *Appl. Environ. Microbiol.* **2007**, *73*, 7092–7095, doi:10.1128/aem.01394-07.
13. Andrejko, M.; Mizerska-Dudka, M.; Jakubowicz, T. Changes in *Galleria mellonella* Apolipoprotein III Level during *Pseudomonas Aeruginosa* Infection. *J. Invertebr. Pathol.* **2008**, *97*, 14–19, doi:10.1016/j.jip.2007.06.003.
14. Sjoeborg, B.-M.; Torrents, E. Shift in Ribonucleotide Reductase Gene Expression in *Pseudomonas aeruginosa* during Infection. *Infect. Immun.* **2011**, *79*, 2663–2669, doi:10.1128/iai.01212-10.
15. Torrents, E. Ribonucleotide Reductases: Essential Enzymes for Bacterial Life. *Front. Cell. Infect. Microbiol.* **2014**, *4*, 52, doi:10.3389/fcimb.2014.00052.
16. Crespo, A.; Pedraz, L.; Astola, J.; Torrents, E. *Pseudomonas aeruginosa* Exhibits Deficient Biofilm Formation in the Absence of Class II and III Ribonucleotide Reductases Due to Hindered Anaerobic Growth. *Front. Microbiol.* **2016**, *7*, 688, doi:10.3389/fmicb.2016.00688.
17. Sambrook, J.; Fritsch, E.F.; Maniatis, T. *Molecular Cloning: A Laboratory Manual*, 2nd ed.; Cold Spring Harbor Laboratory Press: Cold Spring Harbor, NY, USA, 1989.
18. Crespo, A.; Pedraz, L.; Torrents, E. Function of the *Pseudomonas aeruginosa* NrdR Transcription Factor: Global Transcriptomic Analysis and Its Role on Ribonucleotide Reductase Gene Expression. *PLoS ONE* **2015**, *10*, e0123571, doi:10.1371/journal.pone.0123571.
19. Crespo, A.; Pedraz, L.; Van Der Hofstadt, M.; Gomila, G.; Torrents, E. Regulation of Ribonucleotide Synthesis by the *Pseudomonas aeruginosa* Two-Component System AlgR in Response to Oxidative Stress. *Sci. Rep.* **2017**, *7*, 17892, doi:10.1038/s41598-017-17917-7.
20. Gel Doc XR+ Gel Documentation System. Available online: <https://www.bio-rad.com/en-us/product/gel-doc-xr-gel-documentation-system?ID=O494WJESZ> (accessed on 10 September 2020).
21. Sadikot, R.T.; Blackwell, T.S. Bioluminescence Imaging. *Proc. Am. Thorac. Soc.* **2005**, *2*, 537–540.
22. Bergin, D.; Brennan, M.; Kavanagh, K. Fluctuations in Haemocyte Density and Microbial Load May Be Used as Indicators of Fungal Pathogenicity in Larvae of *Galleria mellonella*. *Microbes Infect.* **2003**, *5*, 1389–1395, doi:10.1016/j.micinf.2003.09.019.
23. García-Cayuela, T.; De Cadiñanos, L.P.G.; Mohedano, M.L.; De Palencia, P.F.; Boden, D.; Wells, J.; Peláez, C.; López, P.; Requena, T. Fluorescent Protein Vectors for Promoter Analysis in Lactic Acid Bacteria and *Escherichia coli*. *Appl. Microbiol. Biotechnol.* **2012**, *96*, 171–181, doi:10.1007/s00253-012-4087-z.
24. Crespo, A.; Gavaldà, J.; Julián, E.; Torrents, E. A Single Point Mutation in Class III Ribonucleotide Reductase Promoter Renders *Pseudomonas aeruginosa* PAO1 Inefficient for Anaerobic Growth and Infection. *Sci. Rep.* **2017**, *7*, 13350, doi:10.1038/s41598-017-14051-2.
25. Jain, A.Y.; Srivastava, P. Broad Host Range Plasmids. *FEMS Microbiol. Lett.* **2013**, *348*, 87–96, doi:10.1111/1574-6968.12241.
26. Dreux, N.; Cendra, M.D.M.; Massier, S.; Darfeuille-Michaud, A.; Barnich, N.; Torrents, E. Ribonucleotide Reductase NrdR as a Novel Regulator for Motility and Chemotaxis during Adherent-Invasive *Escherichia coli* Infection. *Infect. Immun.* **2015**, *83*, 1305–1317, doi:10.1128/iai.02772-14.

Publisher’s Note: MDPI stays neutral with regard to jurisdictional claims in published maps and institutional affiliations.



© 2020 by the authors. Licensee MDPI, Basel, Switzerland. This article is an open access article distributed under the terms and conditions of the Creative Commons Attribution (CC BY) license (<http://creativecommons.org/licenses/by/4.0/>).

Supplementary Material

Table S1. Bacterial strains and plasmids used in this study. For each element, a general description is provided, together with an alternative self-explanatory name which will be commonly used in figures to make interpretation of the data easier for the reader. Throughout all the paper, a "P" before the name of a gene indicates the promoter controlling this gene (e.g., *P_{nrdA}* for *nrdAB* operon promoter).

Name	Reference name	Description	Source
Plasmids			
pMDM513	pMDM513	Mini-Tn7-GW-Gm derivative vector carrying <i>luxCDABE</i> ; Amp ^R , Gm ^R	[1]
pBAM-Gm	pBAM-Gm	pBAM derivative carrying Gm ^R	[2]
pJET1.2/blunt	pJET1.2	Blunt-end vector; Amp ^R	Thermo Scientific
pETS130-GFP	pETS130	Broad host range, promoterless GFP (mut3-gfp variant); Gm ^R	[3]
pETS220-BIATlux	pETSlux	Broad host range, promoterless <i>luxCDABE</i> ; Gm ^R	This work
pETS221	<i>P_{nrdA}</i> -lux	pETS220 derivative carrying <i>nrdA</i> promoter; Gm ^R	This work
pETS222	<i>P_{nrdJ}</i> -lux	pETS220 derivative carrying <i>nrdJ</i> promoter; Gm ^R	This work
pETS223	<i>P_{nrdD}</i> -lux	pETS220 derivative carrying <i>nrdD</i> promoter; Gm ^R	This work
pETS224	<i>P_{nrdR}</i> -lux	pETS220 derivative carrying <i>nrdR</i> promoter; Gm ^R	This work
pETS225	<i>Anr</i> -lux	pETS220 derivative carrying <i>anr</i> gene fragment; Gm ^R	This work
pETS134	<i>P_{nrdA}</i> -GFP	pETS130 derivative carrying <i>nrdA</i> promoter; Gm ^R	[3]
pETS180	<i>P_{nrdJ}</i> -GFP	pETS130 derivative carrying <i>nrdJ</i> promoter; Gm ^R	[4]
pETS226	<i>P_{nrdA}</i> -E2Crimson	pETS130 derivative carrying <i>nrdA</i> promoter; Gm ^R	Lab strain
pETS227	<i>P_{nrdJ}</i> -E2Crimson	pETS130 derivative carrying <i>nrdJ</i> promoter; Gm ^R	Lab strain
Strains			
<i>E. coli</i>			
DH5α	DH5α	<i>recA1 endA1 hsdR17 supE44 thi-1 relA1 ΔlacZYA-argF</i> /U1169 <i>deoR φ60dlacZM15</i>	Lab strain
S17.1	S17.1	<i>recA thi pro hsdR- M+RP4::2-Tc::Mu::Km Tn7 Tpr Smr Xpir</i>	[5]
<i>P. aeruginosa</i>			
PAO1	PAO1 WT	Wild-type (ATCC 15692/CECT 4122) - Spanish Type Culture Collection	Lab strain
MKI171	PAO1::eGFP	<i>P. aeruginosa</i> PAO1::mini-Tn7eGFP, Gm ^R	[6]
PAO1::lux	PAO1::lux	<i>P. aeruginosa</i> PAO1::mini-Tn7luxCDABE, Gm ^R	Lab strain

- Moir, D.T.; Ming, D.; Opperman, T.; Schweizer, H.P.; Bowlin, T.L. A high-throughput, homogeneous, bioluminescent assay for *Pseudomonas aeruginosa* gyrase inhibitors and other DNA-damaging agents. *J Biomol Screen* 2007, 12, 855-864, doi:10.1177/1087057107304729.
- Crespo, A.; Gavalda, J.; Julian, E.; Torrents, E. A single point mutation in class III ribonucleotide reductase promoter renders *Pseudomonas aeruginosa* PAO1 inefficient for anaerobic growth and infection. *Sci Rep* 2017, 7, 13350, doi:10.1038/s41598-017-14051-2.
- Sjöberg, B.M.; Torrents, E. Shift in ribonucleotide reductase gene expression in *Pseudomonas aeruginosa* during infection. *Infect Immun* 2011, 79, 2663-2669, doi:10.1128/IAI.01212-10.
- Crespo, A.; Pedraz, L.; Torrents, E. Function of the *Pseudomonas aeruginosa* NrdR Transcription Factor: Global Transcriptomic Analysis and Its Role on Ribonucleotide Reductase Gene Expression. *PLoS One* 2015, 10, e0123571, doi:10.1371/journal.pone.0123571.
- de Lorenzo, V.; Cases, I.; Herrero, M.; Timmis, K.N. Early and late responses of TOL promoters to pathway inducers: identification of postexponential promoters in *Pseudomonas putida* with lacZ-tet bicistronic reporters. *J Bacteriol* 1993, 175, 6902-6907, doi:10.1128/jb.175.21.6902-6907.1993.
- Klausen, M.; Heydorn, A.; Ragas, P.; Lambertsen, L.; Aaes-Jørgensen, A.; Molin, S.; Tolker-Nielsen, T. Biofilm formation by *Pseudomonas aeruginosa* wild type, flagella and type IV pili mutants. *Mol Microbiol* 2003, 48, 1511-1524, doi:10.1046/j.1365-2958.2003.03525.x.

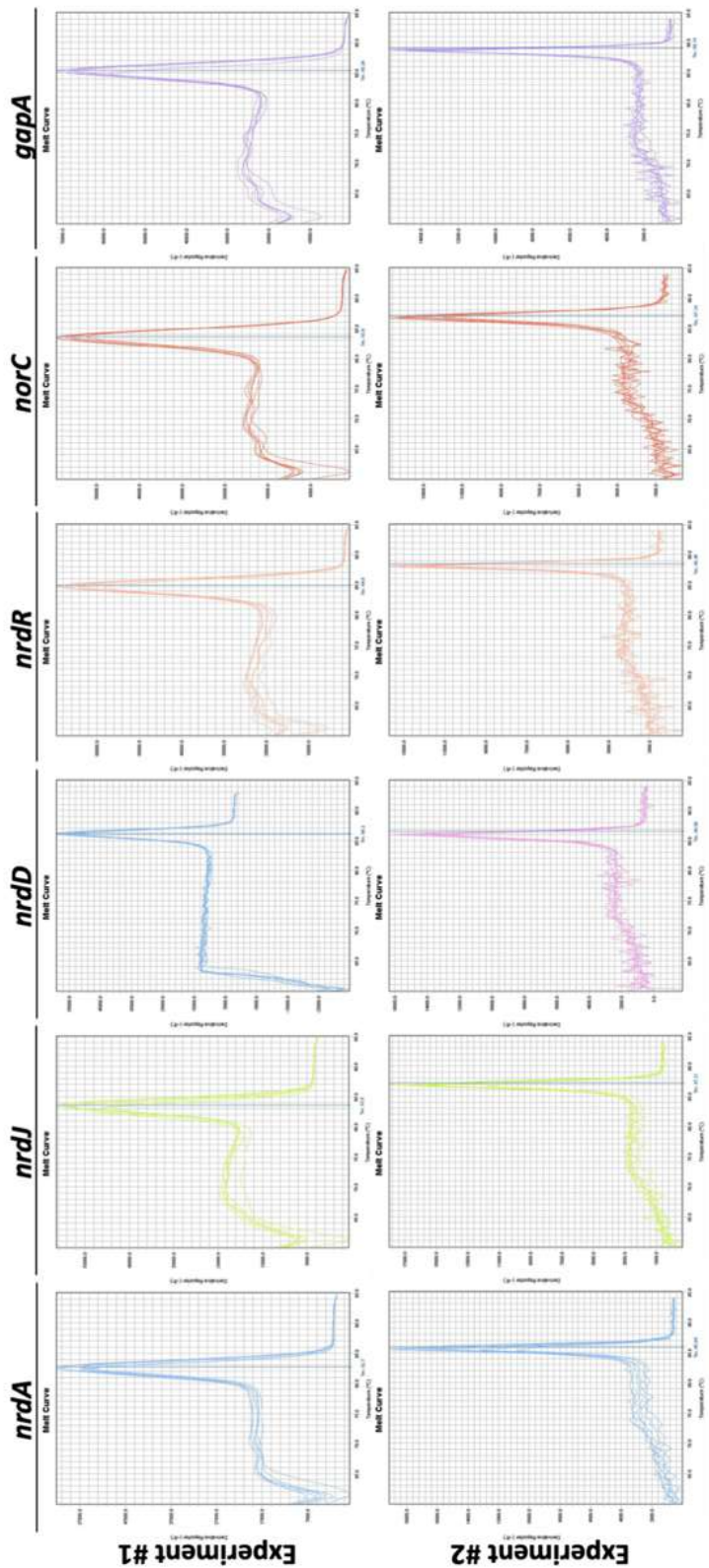
Table S2. Primers used in this study.

Name	Sequence (5' → 3')	Application
Lux_SmaI_fw	CCCCGGCATTAAATGGATGGCAAATAT	Cloning
pBAM-Gm up	ACGAACCGAACAGGCTTATG	Cloning
pJET 1.2 fw	CGACTCACTATAGGGAGAGCGGC	Check cloning/Sequencing
pJET 1.2 rv	AAGAACATCGAITTTCCATGGCAG	Check cloning/Sequencing
pBBR1 up	CATCGCAGTCGGCCTATTGG	Check cloning/Sequencing
LuxC_rv	ACCAAGTTCATTTCTACAACATCA	Check cloning/Sequencing
PnrDA SmaI GFP low	ACCCGGGTCTCCGGTGTGGTGTCG	PnrDA promoter cloning
PnrDA BamHI EcoRI GFP up	AGGATCCGAATCTTGCTCCACACAGCCTC	PnrDA promoter cloning
PJ_SacI up	GAGCTCGGTCGGCCTGCATCTTC	PnrDJ promoter cloning
PnrDJ_SmaI_Rv	CCCCGGGACTGCGTGGTCTGTC	PnrDJ promoter cloning
PD SacI up	GAGCTCCCGCTCGCCAGG	PnrDD promoter cloning
PD EcoRI low	GAATTCTTCAACTTCTCCACAACATGAT	PnrDD promoter cloning
PR SacI up	GAGCTCCAGGAGAAGGACGGCCAG	PnrDR promoter cloning
PR EcoRI low	GAATTCACCGCAGAAGGGACAAT	PnrDR promoter cloning
Anr SacI up_2	GAGCTCTGTTCCGCCAGGGTGA	Anr cloning
Anr EcoRI lw	GAATTCTCTTCTCGACAGCAGCAG	Anr cloning
greenQRT_PAO-nrdA_fw	ACCTGGAGAAACTGGCAAG	qRT-PCR; <i>P. aeruginosa</i> RNR genes
greenQRT_PAO-nrdA_rv	TGTGGATGAAGTAGCGGTGCG	qRT-PCR; <i>P. aeruginosa</i> RNR genes
greenQRT_PAO-nrdJa_fw	CGAATTCATCCGCCCAAG	qRT-PCR; <i>P. aeruginosa</i> RNR genes
greenQRT_PAO-nrdJa_rv	TCCACCGCCTGCATGAAC	qRT-PCR; <i>P. aeruginosa</i> RNR genes
greenQRT_PAO-nrdD_fw2	TTGCTGAACGAAGGCCTGAA	qRT-PCR; <i>P. aeruginosa</i> RNR genes
greenQRT_PAO-nrdD_rv2	TGCCGAGGAAGTTGACCATC	qRT-PCR; <i>P. aeruginosa</i> RNR genes
greenQRT_PAO-nrdR_fw	AACGCTTCACCACCTTCGAG	qRT-PCR; <i>P. aeruginosa</i> RNR genes
greenQRT_PAO-nrdR_rv	GCAGCTTGCTCGTCGGAAC	qRT-PCR; <i>P. aeruginosa</i> RNR genes
greenQRT_PAO-norC_fw	AGGGCTTCAACACCTTCTC	qRT-PCR; <i>P. aeruginosa</i> control genes
greenQRT_PAO-norC_rv	CCTCGCTGAGATGGAACCTGC	qRT-PCR; <i>P. aeruginosa</i> control genes
greenQRT_PAO-gapA_fw	CCTCCATCGGATCGTCTC	qRT-PCR; <i>P. aeruginosa</i> control genes
greenQRT_PAO-gapA_rv	GGTCATCAGGCCGTGCTC	qRT-PCR; <i>P. aeruginosa</i> control genes

Table S3. RNA quality. RNA quality parameters obtained from Nanodrop™ analysis for PAO1 in *G. mellonella* infection and in planktonic LB culture for two independent experiments.

Sample	A260	A280	A260/A280	Concentration (ng/μl)
PAO1 in <i>G. mellonella</i> Experiment #1	0.258	0.130	1.98	206.72
	0.252	0.128	1.97	201.68
PAO1 in LB Experiment #1	0.272	0.145	1.98	230.08
	0.326	0.172	1.99	248.24
PAO1 in <i>G. mellonella</i> Experiment #2	0.078	0.038	2.03	62.56
	0.081	0.041	2.00	65.12
PAO1 in LB Experiment #2	0.123	0.061	2.00	98.16
	0.125	0.062	2.01	99.84

Figure S1. qRT-PCR melting curves. Melting curve analysis for each of the genes analyzed in two independent experiments. Each figure reflects the combined curves of both PAO1 in *G. mellonella* infection and in planktonic culture.



ARTICLE 2

Novel Oleanolic and Maslinic Acid Derivatives as a Promising Treatment against Bacterial Biofilm in Nosocomial Infections: An in Vitro and in Vivo Study

Published in *ACS Infectious Diseases* (Q1,D1, IF₂₀₁₉: 4.614)

DOI: 10.1021/acsinfecdis.9b00125

July 2019

Núria Blanco-Cabra¹, Karina Vega-Granados², **Laura Moya-Andérico**¹, Marija Vukomanovic¹, Andrés Parra², Luis Álvarez de Cienfuegos^{2,3,*}, and Eduard Torrents^{1,*}

¹Bacterial Infections and Antimicrobial Therapies group, Institute for Bioengineering of Catalonia (IBEC), The Barcelona Institute of Science and Technology (BIST), Baldori Reixac 15-21, 08028 Barcelona, Spain

²Department of Organic Chemistry, Faculty of Science, University of Granada, Campus Universitario Fuentenueva s/n, 18071 Granada, Spain

³Instituto de Investigación Biosanitaria ibs. GRANADA, Universidad de Granada, 18012, Granada, Spain

*Corresponding authors: Luis Álvarez de Cienfuegos (lac@ugr.es) and Eduard Torrents (etorrents@ibecbarcelona.eu)

Novel Oleanolic and Maslinic Acid Derivatives as a Promising Treatment against Bacterial Biofilm in Nosocomial Infections: An in Vitro and in Vivo Study

Núria Blanco-Cabra,[†] Karina Vega-Granados,[‡] Laura Moya-Andérico,[†] Marija Vukomanovic,[†] Andrés Parra,^{‡,§} Luis Álvarez de Cienfuegos,^{*,‡,§} and Eduard Torrents^{*,†,§}

[†]Bacterial Infections and Antimicrobial Therapies Group, Institute for Bioengineering of Catalonia (IBEC), The Barcelona Institute of Science and Technology (BIST), Baldiri Reixac 15-21, 08028 Barcelona, Spain

[‡]Department of Organic Chemistry, Faculty of Science, University of Granada, Campus Universitario Fuentenueva s/n, 18071 Granada, Spain

[§]Instituto de Investigación Biosanitaria ibs.GRANADA, Universidad de Granada, 18012 Granada, Spain

Supporting Information

ABSTRACT: Oleanolic acid (OA) and maslinic acid (MA) are pentacyclic triterpenic compounds that abound in industrial olive oil waste. These compounds have renowned antimicrobial properties and lack cytotoxicity in eukaryotic cells as well as resistance mechanisms in bacteria. Despite these advantages, their antimicrobial activity has only been tested in vitro, and derivatives improving this activity have not been reported. In this work, a set of 14 OA and MA C-28 amide derivatives have been synthesized. Two of these derivatives, MA-HDA and OA-HDA, increase the in vitro antimicrobial activity of the parent compounds while reducing their toxicity in most of the Gram-positive bacteria tested, including a methicillin-resistant *Staphylococcus aureus*-MRSA. MA-HDA also shows an enhanced in vivo efficacy in a *Galleria mellonella* invertebrate animal model of infection. A preliminary attempt to elucidate their mechanism of action revealed that these compounds are able to penetrate and damage the bacterial cell membrane. More significantly, their capacity to reduce antibiofilm formation in catheters has also been demonstrated in two sets of conditions: a static and a more challenged continuous-flow *S. aureus* biofilm.

KEYWORDS: maslinic and oleanolic acids, natural products, in vitro and in vivo antimicrobials, *Galleria mellonella*, antibiofilm, *Staphylococcus aureus*



Staphylococcus aureus is a major global healthcare problem because it is a leading cause of infections in hospitals and the major cause of biofilm formation in catheters and other medical devices like prostheses.¹ Because the bacteria embedded in biofilms can be 100 or even 1000 times more resistant to antibiotics than planktonic-growing bacteria,² these *S. aureus* biofilms can generate dangerous infections such as endocarditis, prosthetic joint infection, and even sepsis. The only effective treatment against these biofilms is the removal of the medical device and long-term antibiotic therapy,³ which can develop antibiotic-resistant bacteria such as methicillin-resistant *S. aureus* (MRSA) and a high increase in the overall treatment cost.^{4–6} MRSA infections are more related to bacteremia cases and have poorer clinical outcomes.⁴ As a result of the improper use of antibiotics, multiresistant bacteria are a worldwide worrying health problem and cause significant morbidity and mortality. Therefore, there is a critical need to find alternatives to common antibiotics with a smaller risk of resistance development.

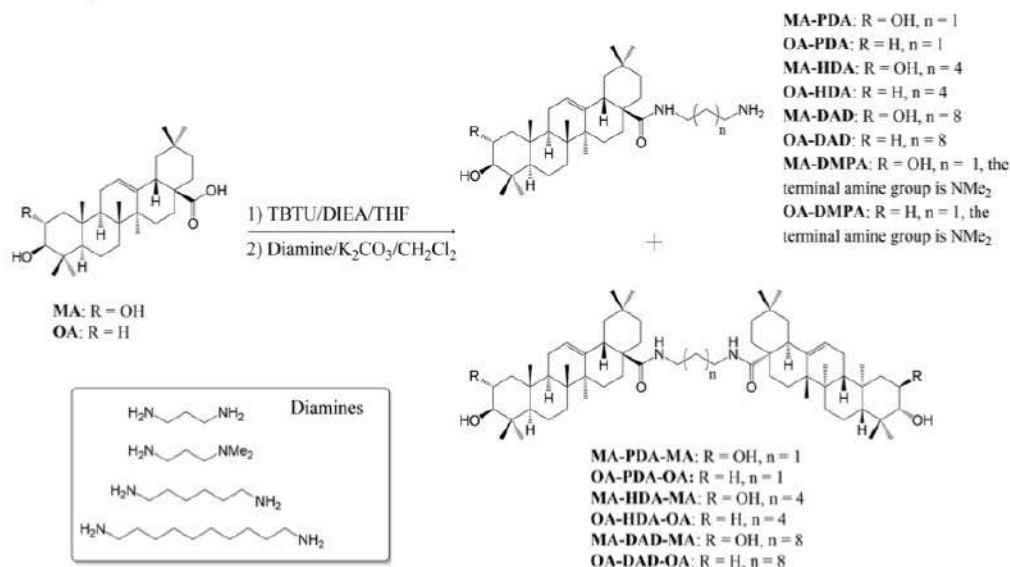
Oleanolic acid (OA) and maslinic acid (MA) are pentacyclic triterpenic compounds that can be widely isolated from plants. The function of these triterpenes seems to be protection against dehydration and microbes, as has been noticed with an increase in plant infections when the synthesis of these compounds diminishes.^{7,8} They are vastly present in the fruits of *Olea europaea* and consequently abound in industrial olive oil waste.^{8,9}

OA and MA have been extensively used in ancestral medicine and have, among others, long-recognized anti-inflammatory, anti-hyperlipidemic, antitumor, and hepatoprotective properties in addition to their known antimicrobial activity.^{7,8,10–17} Moreover, these triterpenes have no cytotoxicity on eukaryotic cells, and no resistance mechanisms in bacteria have been found yet.¹² Despite the fact that the exact antimicrobial mechanism of these compounds is still unknown,

Received: April 3, 2019

Published: July 3, 2019

Scheme 1. Synthesis of MA and OA Amine Derivatives



there are some works indicating the peptidoglycan synthesis as the principal target,^{10,18} which can explain why these antimicrobial activities have been mostly seen in Gram-positive species, whereas the compounds were devoid of antimicrobial activity against the Gram-negative bacteria tested.^{7,10–12,16,17} Despite the antimicrobial activity against Gram-positive bacteria and the lack of toxicity and resistance mechanisms, the activity of OA and MA has only been tested in vitro, and as far as we know, OA and MA derivatives with improved antimicrobial activity are not known.

In this respect, in this work, a set of 14 OA and MA C-28 amide derivatives (Scheme 1 and Table 1) have been synthesized and analyzed for their in vitro and in vivo antimicrobial efficacy and toxicity properties. Moreover, the antibiofilm activity in catheters and flow biofilms of the more active compounds has also been evaluated. The choice of these derivatives was proposed with the aim of simultaneously satisfying two essential criteria. The first one was to obtain two groups of molecules with very different polarities and molecular weights to study which factor could influence the antibacterial activity more. The second one was to obtain these derivatives by means of a simple and direct synthetic strategy which would allow us to obtain, on one hand, derivatives with minimal chemical modifications in order to maintain the low toxicity of the natural OA and MA and, on the other hand, their easy synthesis in large quantities. Furthermore, it has been recently shown that some OA and MA C-28 amide derivatives have enhanced anticancer activity with respect to the natural triterpenes.¹³

For the first time, two of these new derivatives (OA-HDA and MA-HDA) increase the in vitro antimicrobial activity and reduce the toxicity of the parent compounds by reducing the minimum inhibitory concentration (MIC) in most of the Gram-positive bacteria tested, highlighting the efficacy against *S. aureus* and MRSA. Remarkably, MA-HDA also shows enhanced activity in vivo in the *Galleria mellonella* animal

model of infection. A preliminary attempt to investigate their mechanism of action shows that these compounds are able to damage the bacterial cell membrane. Their antimicrobial properties have also been evaluated by their antibiofilm capacity. Again, these two derivatives are more effective than their parent compounds in reducing *S. aureus* biofilms in a static and continuous-flow manner. These two derivatives can serve as a guide for the development of useful antimicrobial and antibiofilm agents based on easily accessible natural compounds that can be used alone or in combination with other antimicrobials to promote synergy.¹⁷

RESULTS AND DISCUSSION

Antibacterial Activity and In Vitro Toxicity. The amide derivatives of oleoic acid (OA) and maslinic acid (MA) were tested for their antibacterial activity in planktonic bacterial growth. The antibacterial activity that can be seen in Table 1 is represented regarding minimal inhibitory concentration 50% (MIC_{50}) and defined as the compound concentration that inhibits bacterial growth by 50%.

As previously described,^{7,10–12,16,17,19} OA and MA inhibited the Gram-positive bacterial growth, whereas no effect was detected against Gram-negative pathogens. Similarly, the amide derivatives tested in this work did not show antibacterial activity against any Gram-negative pathogen tested (Table 1). Cholesterol (C) was used as a negative control. No antimicrobial activity was detected when OA-PDA, OA-DMPA, MA-PDA-MA, OA-PDA-OA, and OA-DAD-OA were used. Furthermore, the diamine chemical precursors HDA and DAD alone did not exhibit any antimicrobial activity at the highest concentration tested (120 $\mu g/mL$, data not shown).

Among the 14 derivatives tested in this work, MA-HDA and OA-HDA showed the highest efficacy by maintaining or enhancing the antimicrobial activity of MA and OA in most of the strains tested with particular relevance against *S. aureus* and

Table 1. MIC₅₀, Cytotoxicity, and Selectivity Index (SI) of Compounds^a

Compound	Formula	MIC ₅₀ (μg/ml)							CC ₅₀ (μg/ml)	LD ₅₀ (mg/kg)
		Gram-Positive				Gram-Negative				
		<i>S. aureus</i>	<i>S. aureus-MRSA</i>	<i>S. epidermidis</i>	<i>S. mutans</i>	<i>E. faecalis</i>	<i>E. coli</i>	<i>P. aeruginosa</i>		
C		NA	NA	NA	NA	NA	NA	NA	NT	>400
MA		15 (20.9/504)	75	25 (12.5/302)	15 (20.9/504)	15 (20.9/504)	NA	NA	314 ± 6	302.44 ± 67
OA		30 (10.5/302)	75	200	30 (10.5/302)	30 (10.5/302)	NA	NA	314 ± 9.8	361.8 ± 70
MA-PDA		200	200	NA	NA	NA	NA	200	310 ± 5.4	
OA-PDA		NA	NA	NA	NA	NA	NA	NA	312 ± 8.6	
MA-HDA		15 (17.9/661)	25 (10.7/397)	20 (13.4/496)	50 (5.4/198)	75	NA	NA	268 ± 5.3	396.56 ± 81.2
OA-HDA		4 (62.2/1313)	10 (24.9/525)	5 (49.8/1050)	5 (49.8/1050)	15 (16.6/350)	NA	NA	249 ± 10.1	210.08 ± 69.9
MA-DAD		20 (10.5)	25 (8.4)	10 (21)	25 (8.4)	25 (8.4)	NA	NA	250 ± 10.9	
OA-DAD		30 (10.4)	30 (10.4)	7.5 (41.7)	25 (12.5)	25 (12.52)	NA	NA	313 ± 5.3	
MA-DMPA		75	85	75	85	75	NA	NA	NT	
OA-DMPA		NA	NA	NA	NA	NA	NA	NA	NT	
MA-PDA-MA		NA	NA	NA	NA	NA	NA	NA	120 ± 19.5	
OA-PDA-OA		NA	NA	NA	NA	NA	NA	200	NT	
MA-HDA-MA		NA	NA	100	100	NA	NA	NA	312 ± 9.4	
OA-HDA-OA		NA	NA	75	100	100	NA	NA	314 ± 12.8	
MA-DAD-MA		NA	NA	50	NA	NA	NA	NA	317.5 ± 2.9	
OA-DAD-OA		NA	NA	NA	NA	NA	NA	NA	912 ± 3.3	

^aMIC₅₀ was evaluated on: *S. aureus*, *Staphylococcus aureus*; *S. aureus-MRSA*, *Staphylococcus aureus* methicillin-resistant; *S. epidermidis*, *Staphylococcus epidermidis*; *S. mutans*, *Streptococcus mutans*; *E. faecalis*, *Enterococcus faecalis*; *E. coli*, *Escherichia coli*; *P. aeruginosa*, *Pseudomonas aeruginosa*; C, cholesterol. NA, no-activity or MIC₅₀ > 250 μg/mL. Cytotoxicity (CC₅₀) was evaluated on human alveolar epithelial A459 cells. NT, non-cytotoxic or CC₅₀ > 1000 μg/mL. Lethal doses (LD₅₀) were evaluated in *Galleria mellonella* larvae. Selectivity index (SI), calculated as CC₅₀/MIC₅₀ and LD₅₀/MIC₅₀ are indicated in parentheses next to the MIC value.

Methicillin-Resistant *S. aureus* (MRSA). It is noteworthy that the HDA derivative compounds (MA-HDA and OA-HDA) increased their antimicrobial activity and reduced the MIC₅₀ against MRSA by 66% and 87%, respectively (MIC₅₀ of 25 and 10 μg/mL) compared to their original compounds (OA and MA, MIC₅₀ 75 μg/mL). The same behavior was seen with the DAD derivative compounds (MA-DAD and OA-DAD), which reduced MRSA MIC₅₀ by 66% and 60%, respectively. Since antibiotic-resistant bacteria like MRSA are nowadays a public health concern, it is crucial to find new antimicrobials that do not produce resistance mechanisms in these bacteria. Thus, the

improved activity of HDA and DAD compounds and the fact that resistance mechanisms have not yet been found in the parent compounds MA and OA^{12,16} identify these molecules as a possible good alternative for MRSA treatment.

Additional studies were performed to determine their in vitro toxicity using the A549 human epithelial pulmonary cell line. The in vitro toxicity in cells, expressed in Table 1 as the concentration that kills 50% of the cells (CC₅₀), demonstrates that the HDA and the DAD derivatives from MA and OA were not more toxic than their precursors, although they showed better antimicrobial activity in some bacterial strains.

In Vivo Toxicity and Efficacy in *Galleria mellonella*. *Galleria mellonella* was used to evaluate the toxicity (lethal dose) of the new antimicrobial compounds tested.²⁰ We evaluated the compound dose per kilogram of greater wax moth larvae that kills 50% of the animal population (lethal dose 50, LD₅₀). Using the MIC₅₀ and the toxicity indexes CC₅₀ and LD₅₀, the selectivity indexes (SI) were calculated. The selectivity indexes (in cells or *Galleria mellonella*) emphasize the improvement of the HDA derivatives' activity (OA-HDA, SI = 62.2 or 1313; MA-HDA, SI = 17.9 or 661) against *S. aureus* growth related to their toxicity, as seen with the 5-fold increase in the SI of OA-HDA compared to OA.

The use of *Galleria mellonella* as an invertebrate animal model to test in vivo toxicity and to calculate the SI is crucial because the selectivity index (SI) is increased considerably when calculated with the LD₅₀ rather than with the CC₅₀ (Table 1). In some cases, the toxicity in vivo can be significantly different; for example, the toxicity of the MA-HDA compound increased in vitro while the in vivo toxicity decreased in comparison to the predecessor MA. Our results highlight the use of an animal model for toxicity evaluation to better select a compound for further investigative steps or drug development. The use of *G. mellonella* is a cheap screening alternative for in vivo toxicity and efficacy prior to analysis in rodents or even more expensive options.

Additionally, *Galleria mellonella* larvae were used as a *S. aureus* model of infection to evaluate in vivo antibacterial efficacy of the best active amide derivatives (MA-HDA and OA-HDA). *G. mellonella* were infected with *S. aureus* at 1.5 × 10⁹ cfu/mL into the hemocoel and treated twice with the compounds at 240 mg/kg (1 and 6 h post-infection). As illustrated in Figure 1, treatment with MA-HDA and MA

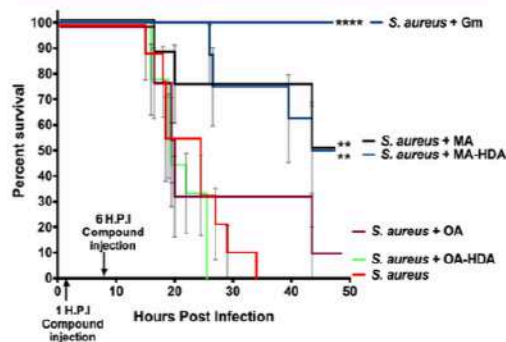


Figure 1. Kaplan–Meier survival curve of *Galleria mellonella* larvae infected with *S. aureus* and treated with the different compounds 1 and 6 h post-infection at a final concentration of 240 mg per kg of body weight. Gentamicin (Gm) at 20 mg/kg was used as a control. Asterisks: statistically significant difference versus *S. aureus* without treatment in a log-rank test, GraphPad 6.0 (**: p -value <0.005; ***: p -value <0.0001).

compounds resulted in 50% of the larvae surviving, whereas only 20% of *Galleria* survived the *S. aureus* infection after the treatment with OA. Nevertheless, no differences were seen between the untreated insects and the ones treated with OA-HDA, showing a lack of in vivo activity of this compound. As the in vivo toxicity diminished in the MA-HDA derivative, these results enhanced the antibacterial efficacy of MA-HDA

by increasing the survival of *Galleria mellonella* infected with *S. aureus* by 50%.

Since these two new compounds (MA-HDA and OA-HDA) have high activity and selectivity index, they could be considered good antibacterial agents in a modern therapy context, especially useful in the treatment of multidrug resistant bacteria. As the antibiotics used in chemotherapy no longer appear to be as effective as they were when created, there is an urgent need for the discovery of new antibacterial drugs with different action mechanisms to tackle the growing drug resistance.

Effect on Bacterial Cell Membrane and Possible

Mechanisms of Action. To identify a preliminary mechanism of action of the different compounds used in this work, Live/Dead and membrane damage staining analyses were first carried out. The Live/Dead analysis (Figure 2A) was performed by staining *S. aureus* cells after 4 h of treatment with the diverse compounds. This differential staining allowed discrimination of viable bacteria (stained with SYTO9 dye, green) from dead bacteria (stained with PI dye, red), as well as seeing the growth impairment that the treatment could cause. After 4 h of treatment, a notable decrease of viable cells could be detected when the OA, MA, OA-HDA, MA-HDA, OA-DAD, and MA-DAD compounds were used, as shown in Figure 2A with the average count in Table S1, while a persistence of these cells was seen when compounds without activity were used (MA-HDA-MA and MA-DMPA). Moreover, a specific membrane staining with FM 4-64 dye was performed. After staining for 10 min (Figure 2B), membrane impairment in the active compounds could be observed. Some dye accumulations could be appreciated in the membrane (red dots indicated by an arrow) when treated with the active antimicrobial compounds (OA, MA, OA-HDA, MA-HDA, OA-DAD, and MA-DAD). These accumulations reaffirmed the Live/Dead results and suggested a bacteriolytic mode of action.

Finally, scanning electron microscope (SEM) characterization of the treated *S. aureus* cells was carried out to validate our previous staining experiments. Figure 2C shows SEM images of *S. aureus* cells after exposure to the compounds. The images show that the bacteria's surface became rough and bubbly in many *S. aureus* treated cells while the nontreated cells' membrane remained smooth, thus suggesting membrane damage and further corroborating the results seen in the fluorescent microscope analysis.

Previous results show that MA and OA induced cell membrane destabilization and destruction.^{12,21} Proteases, protein kinases, and transcription factors have been proposed as a target for these compounds,^{10,22–25} but the exact molecular mechanism remains unknown. The mechanism of action of MA has not been reported in bacteria but only against protozoa, nematodes, viruses, and cancerogenic cells as a glycogen phosphorylase inhibitor,²⁶ regulator of transcription factors and protein kinases,²⁴ and inhibitor of proteases.^{27,28} However, a nonstandard binding mechanism of MA to these proteins²⁹ has also been suggested.

Regarding the mechanism of action of OA against bacteria, it is well-known that it inhibits peptidoglycan metabolism and prevents cell division in *Listeria monocytogenes*.¹⁸ Other studies demonstrate a similar effect of OA in the Gram-positive *Streptococcus mutans* by proving the effect in both the peptidoglycan metabolism at a transcriptional level¹⁰ and the adherence to the tooth surface to form the cariogenic

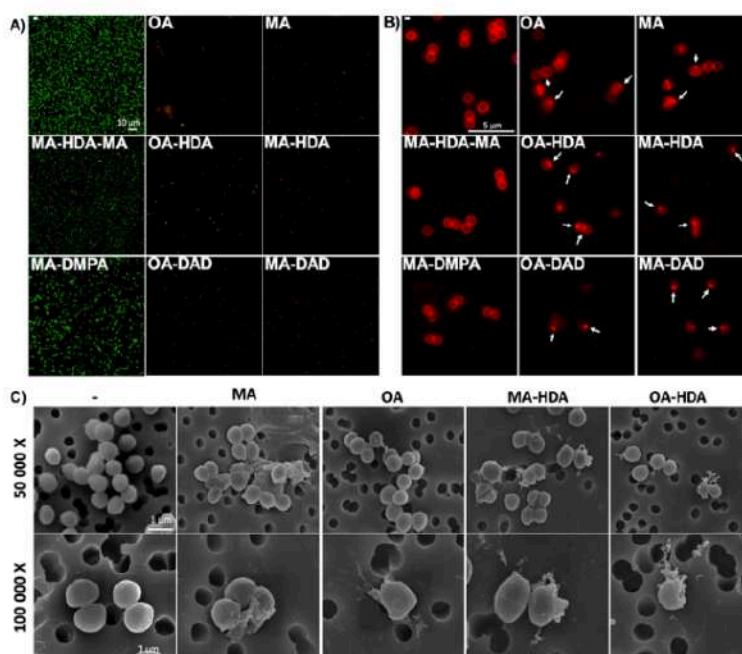


Figure 2. (A) Live/Dead analysis in *S. aureus*. Green fluorescence indicates live cells and red fluorescence indicates metabolically inactive (dead) cells. (B) Membrane damage analysis by FM 4-64 staining of *S. aureus*. The arrows show nonuniform stain accumulations in the membrane indicating cell damage. (C) SEM images of *S. aureus* cells after the compounds' treatment.

biofilm.³⁰ Despite not having antimicrobial activity in *Escherichia coli*, it has been demonstrated that OA affects the efflux of pumps in this bacteria²³ and acts as a stress inducer agent²² that reduces the expression of the cysteine regulon and induces heat shock response with the DnaK synthesis.

Nevertheless, the different activity among the OA and MA derivatives and concerning the parent OA and MA compounds suggests that the mechanism of action of these derivatives might be different from the natural triterpenic acids. The only structural difference between all the derivatives is the length of the diamine residue. It seems that these compounds require a certain chain length to be active, and for this reason, only the longer chain (HDA and DAD) derivatives are active. This might have some justification if the mechanism of action is due to bacterial cell membrane interaction and posterior destabilization, as suggested by the Live/Dead and membrane damage staining analyses and the SEM characterization. Both Gram-positive and Gram-negative bacteria have a negatively charged envelope due to the negative charge of teichoic acids and lipopolysaccharides, respectively, but regarding the plasma membrane, Gram-positive bacteria contain a larger portion of negatively charged phospholipids than Gram-negative bacteria.³¹ At a physiological pH, the terminal amine group is positively charged and can promote the interaction of the derivatives with the plasma membrane by electrostatic interactions which are going to be enhanced in the Gram-positive membrane. Once the derivatives are in contact with the membrane, they need to be inserted efficiently to produce membrane destabilization. This second step is where the length of the alkyl chain may have relevant importance. If the alkyl chain is short, the interaction is mainly superficial, and the

derivatives do not have the possibility of being inserted into the cell membrane. On the other hand, if the length of the chain is long enough, the derivatives can be inserted into the cell membrane, thus provoking disruption. It is known that the alkyl chain length in small organic compounds which tackle bacterial cell membranes has a major impact on the activity of the compounds.^{32–34} In our case, HDA-derivatives, having a diamine alkyl chain of 6 carbons, present the most effective combination.

Antibiofilm Activity against *Staphylococcus aureus* Static and Continuous Biofilms. Since bacteria within biofilms can be more resistant to antimicrobials than in planktonic state, the removal capacity of preformed *S. aureus* biofilms grown in static and continuous flow was tested.

First, we grew a *S. aureus* biofilm on catheter tubes for 72 h. Then, we treated them with different compounds at a concentration of 50 μg/mL for an additional 24 h. As we can see in Figure 3, the more active compounds (MA, MA-HDA, and OA-HDA) were able to remove more than 99% of the preformed biofilm when compared to the untreated biofilm. However, at the concentration tested, OA and MA-HDA-MA had subinhibitory concentration activity (Figure 3) without any ability to remove the biofilm, but they do enhance the formation of the biofilm³⁵ which could explain the increase in the biofilm growth produced. Note that the antibacterial activity was higher for the MA-HDA and OA-HDA compounds in contrast to the well-known antibiotic ciprofloxacin.

Second, we performed a continuous *S. aureus* flow biofilm to resemble the conditions in which this bacteria establishes a chronic infection. The *S. aureus* continuous biofilm was formed

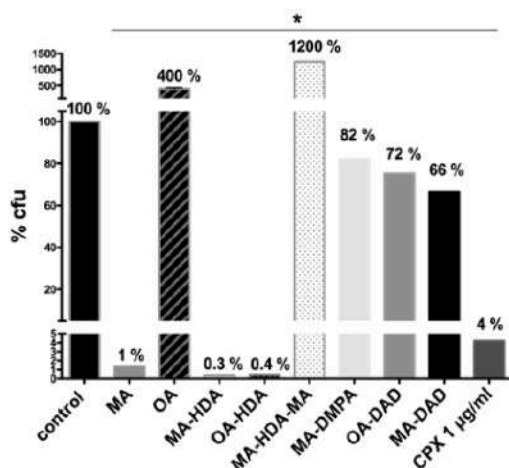


Figure 3. Antibacterial efficacy of compounds on *S. aureus* ATCC 12600 catheter biofilms. Bars indicate percentage (%) of viable biofilm cells (cfu) remaining on the catheter after 24 h treatment with the compounds. Cpx, ciprofloxacin. Asterisk (*): statistically significant difference versus control without treatment (p -value <0.05 in an unpaired t -test, GraphPad 6.0).

during 4 consecutive days and afterward treated with different compounds at a concentration of $50 \mu\text{g/mL}$ for an additional 24 h. The images of Figure 4A are confocal Z-projections with the corresponding orthogonal views of the biofilm after treatment and the plot in Figure 4B shows the average biofilm biomass. Clearly, the best antibiofilm activity was detected with the MA-HDA and OA-HDA compounds (30% and 45% reduction in biofilm biomass, respectively) with a corresponding decrease in thickness (around $10 \mu\text{m}$) as seen in the orthogonal views (Figure 4A and B). It is important to point out that these compounds have better antimicrobial efficacy compared to the MA and OA original compounds.

CONCLUSIONS

For the first time, novel OA and MA derivatives outperform the known antimicrobial activity of their parent compounds. Of the 14 OA and MA C-28 amide derivatives studied, two

derivatives, MA-HDA and OA-HDA, have shown better in vitro antimicrobial activity in all of the Gram-positive bacterial strains tested by significantly reducing the MIC_{50} against MRSA in 66% and 87%, respectively, when compared to the MA and OA compounds. In vitro toxicity studies also showed that these new derivatives did not increase the toxicity with respect to their parent compounds. Preliminary studies conducted to shed light on their mechanism of action revealed that these compounds were able to penetrate and damage the bacterial cellular membrane. These excellent in vitro results have also been validated in vivo in a *Galleria mellonella* animal model. In particular, MA-HDA showed the best results in terms of efficacy and toxicity, increasing the survival of *G. mellonella* infected with *S. aureus* by 50%.

Taken together, these results point out the relevance that natural feedstock has in providing bioactive compounds for therapeutic purposes. In this case, OA and MA are natural products obtained in large quantities from olive oil waste, and therefore, they are easily accessible and inexpensive. Through very few steps of very simple chemical transformations, we have obtained novel derivatives that are highly active in vitro and in vivo against dangerous Gram-positive bacterial strains including MRSA. Their mechanism of action suggests that these compounds could be used in combination with other antibiotics to promote synergy.

EXPERIMENTAL SECTION

Chemistry. Oleanolic (3β -hydroxyolean-12-en-28-oic acid, OA) and maslinic ($2\alpha,3\beta$ -dihydroxyolean-12-en-28-oic acid) acids were isolated from solid waste resulting from olive oil production, which were extracted in a Soxhlet with hexane and EtOAc successively.³⁶ Both acids were purified from these mixtures by flash chromatography over silica gel, eluting with CH_2Cl_2 /acetone of increasing polarity.³⁷ The C-28 amide derivatives were prepared following a protocol previously described (see Scheme 1).¹³ Very briefly, the carboxyl group of the OA and MA was first activated with *O*-(Benzotriazol-1-yl)-*N,N,N',N'*-tetramethyluronium tetrafluoroborate (TBTU). The OA and MA-TBTU derivatives were obtained by the addition of TBTU in the presence of diisopropylethylamine (DIEA) in dry THF and at room temperature. Second, the OA and MA-TBTU derivatives were dissolved in CH_2Cl_2 and reacted with the corresponding diamine reagents [propane-1,3-

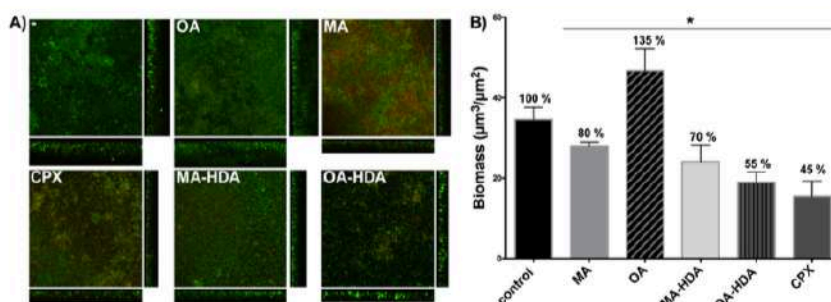


Figure 4. Antibiofilm efficacy of 24 h treatment of compounds against *S. aureus* biofilms grown on a continuous flow system for 96 h. (A) Confocal laser scanning microscope (CLSM) pictures (sum of stack images and orthogonal views) stained with LIVE/DEAD BacLight Bacterial Viability Kit. (B) Biomass ($\mu\text{m}^3/\mu\text{m}^2$) of the biofilms analyzed with COMSTAT2. Cpx, ciprofloxacin. Asterisk (*): statistically significant difference versus control without treatment (p -value <0.05 in an unpaired t -test, GraphPad 6.0).

diamine (PDA), hexane-1,6-diamine (HDA), and decane-1,10-diamine (DAD)] in the presence of K_2CO_3 to originate two products in all cases: monomers exceeding 60% yield (MA-PAD 63%, MA-HDA 64%, MA-DAD 62%, OA-PAD 65%, OA-HDA 62%, and OA-DAD 63%) and dimers close to 30% yield (MA-PAD-MA 27%, MA-HDA-MA 28%, MA-DAD-MA 30%, OA-PAD-OA 28%, OA-HDA-OA 29%, and OA-DAD-OA 29%).¹³ The reaction of OA and MA-TBTU derivatives with *N,N*-dimethyl-1,3-propanediamine afforded only one compound (MA-DMPA and OA-DMPA) with a 90% yield in both cases. In all instances, the compounds were purified by column chromatography. The purity of the compounds was determined by a Waters Acquity UPLC system (ultra-performance liquid chromatography) coupled with a Waters Synapt G2 HRMS spectrometer (high resolution mass spectra), with ESI (electrospray ionization) being $\geq 95\%$. Isolated compounds were characterized by 1H NMR and HRMS, matching what has already been reported. MA-DMPA and OA-DMPA were characterized by 1H and ^{13}C NMR and HRMS. Copies of NMR spectra and HRMS values are included in the Supporting Information.

Bacterial Strains and Growth Conditions. Wild-type *Staphylococcus aureus* CECT 86 (ATCC 12600), *Staphylococcus epidermidis* CECT 231 (ATCC 1798), *Streptococcus mutans* CECT 479 (ATCC 25175), *Enterococcus faecalis* CECT 481 (ATCC 19433), *Escherichia coli* K12 MG1655 CECT 433 (ATCC 700926), and *Pseudomonas aeruginosa* PAO1 CECT 4122 (ATCC 15692) were obtained from the Spanish Type Culture Collection (CECT). *Staphylococcus aureus* MRSA was from our laboratory stock.³⁸ *S. aureus* antimicrobial activity profiles are listed in Table S2. All strains were routinely cultivated in Tryptic Soy Broth (TSB) or Luria–Bertani (LB) medium (Scharlab) at 37 °C.

Antibacterial Susceptibility Testing (In Vitro Activity). The different compounds were tested against different bacterial strains as previously described.³⁸ Briefly, bacteria were grown in TSB or LB medium to an O.D.₅₅₀ ≈ 0.1 ($\approx 4.3 \times 10^7 \pm 1.4 \times 10^6$) cfu/mL and plated in a 96-well microtiter plate (Corning 3596 Polystyrene Flat Bottom 96 Well, Corning NY) containing several concentrations of the compounds according to the Clinical Laboratory Standards Institute (CLSI) guidelines.³⁹ The plate was incubated at 37 °C with shaking at 120 rpm for 8 h and the absorbance at 550 nm was read every 15 min in a SPARK Multimode microplate reader (Tecan).

The minimal inhibitory concentration 50% (MIC₅₀) was defined as the compound concentration that inhibited the bacterial growth by 50%.

Mammalian Cytotoxicity Determination (In Vitro Toxicity). Human alveolar epithelial A549 cells (ATCC CCL-185) were set and allowed to sediment in a microtiter plate (Corning 3596 Polystyrene Flat Bottom 96 Well, Corning NY) at 2×10^4 cells/well and compounds were added at several concentrations. After 24 h, a 10% of MTT solution [3-(4,5-dimethylthiazol-2-yl)-2,5-diphenyltetrazolium bromide, Sigma-Aldrich] was added and the formazan that precipitated 3 h later was dissolved with acidic isopropanol. Absorbance was read at 550 nm in a SPARK multimode microplate reader (Tecan) to determine cell viability. CC₅₀ was calculated with Prism 6.00 (GraphPad Software) as the concentration of the compound that diminished the cell population by 50%. Values \pm standard deviation for 3 independent experiments are shown.

Animal Toxicity Determination (In Vivo Toxicity). *Galleria mellonella* larvae were reared on an artificial diet (15% corn flour, 15% wheat flour, 15% baby cereal, 11% powdered milk, 6% brewer's yeast, 25% honey, and 13% glycerol) at 34 °C in darkness prior to use. *G. mellonella* larvae were injected with 10 μ L of each compound at 300 and 400 mg/kg with a microsyringe (Hamilton) into the hemocoel through the top left proleg. Five larvae (200–250 mg each) were injected per compound and concentration and larvae mortality was recorded daily. Control groups were injected with 10 μ L of 1 \times PBS (Phosphate Saline Buffer) or the vehicle (DMSO) at the highest concentration used.

LD₅₀ (median lethal dose) was calculated with Prism 6.00 (GraphPad Software) as the concentration of the compound that killed 50% of the larvae within 24 h. Values \pm standard deviation for 3 independent experiments are shown.

Survival Assay in *Galleria mellonella* Animal Model (In Vivo Efficacy). An infective dose of *S. aureus* (1.5×10^9 cfu/mL) was injected in *Galleria mellonella* larvae into the hemocoel through the upper left proleg. One hour and six hours post-infection, 10 μ L of the compound at 240 mg/kg were injected through a different proleg. Each compound was injected in a group of five larvae (200–250 mg each). Control groups were injected with 10 μ L of 1 \times PBS (Phosphate Saline Buffer), the vehicle (DMSO), or gentamicin at 20 mg/kg. *G. mellonella* larvae were incubated at 37 °C and mortality was recorded daily. Survival curves were plotted using Kaplan–Meier analysis and differences in survival rates were analyzed by the log-rank test (GraphPad Prism 6.00). Differences with *P* values of <0.005 were considered statistically significant.

Fluorescent Microscopy Viability and Membrane Analysis. *S. aureus* was grown in TSB medium to an O.D.₅₅₀ ≈ 0.3 ($\approx 1.3 \times 10^8 \pm 3 \times 10^7$) cfu/mL and the compounds were added at a concentration of 50 μ g/mL for 4 h in the live–dead test and for 10 min in the membrane analysis.

The bacterial cells were harvested and stained with the LIVE/DEAD BactLight Bacterial Viability kit (Thermo Fisher Scientific) for the viability test and with 10 μ g/mL of *N*-(3-triethylammoniumpropyl)-4-(6-(4-(diethylamino)phenyl)hexatrienyl)pyridinium dibromide (FM 4–64, Thermo Fisher Scientific) for the membrane analysis, according to the manufacturer's specifications. Bacteria were then visualized with a Nikon inverted fluorescent microscope ECLIPSE Ti–S/L100 (Nikon) coupled with a DS-Qi2 Nikon camera (Nikon).

Scanning Electronic Microscopy (SEM) Bacterial Analysis. Morphological analysis of *S. aureus* after exposure to antimicrobial compounds was performed using field emission scanning electron microscopy (Nova NanoSEM FEISEM). *S. aureus* was grown in TSB medium to an O.D.₅₅₀ ≈ 0.6 ($\approx 2 \times 10^8 \pm 4 \times 10^7$) cfu/mL and exposed to compounds at a concentration of 25 μ g/mL for 30 min. Nonexposed bacteria were used as a reference. Immediately after exposure, bacteria were fixed in glutaraldehyde. For that purpose, 100 μ L of treated culture were centrifuged for 5 min at 6000 rpm and TSB was replaced with 50 μ L of glutaraldehyde solution (3 wt.%). After 3 h at room temperature, the fixative was replaced with the same volume of fresh fixative and left at 4 °C overnight. Fixed bacteria were deposited on the top of the porous membranes by filtration in soft vacuum. To remove the fixative, deposited bacteria were washed three times with 1 \times PBS (during 15 min for each replacement) and dehydrated in serially diluted ethanol (30,

50, 70, 90, and 100 wt %) (30 min in each concentration). The cells in ethanol were finally dried using critical point technique (CPD Baltec 030). Before examination in SEM, bacteria deposited on membranes were sputtered with a thin layer of gold for better conductivity.

Antibacterial Effect of Compounds on Biofilms Growing on Catheters. Sterile silicone catheter pieces (2 mm diameter and 1 cm width) (SILT-002, SUDELAB) were placed in a 10 mL tube and covered with a *S. aureus* culture of O.D.₅₅₀ \approx 0.1 ($\approx(4.3 \times 10^7) \pm (1.43 \times 10^6)$ cfu/mL) in TSB medium +0.2% glucose. The tubes were incubated at 37 °C without shaking. After 72 h, the catheter pieces were washed three times with 1X phosphate buffer saline (PBS) (Fisher BioReagents) to discard the planktonic growth (nonbiofilm forming bacteria) and were treated with the different compounds at a concentration of 50 μ g/mL. After 24 h, the catheters were washed again and a solution of 1X PBS + TWEEN 0.05% was added. Then, the tubes were placed in an ultrasonic bath (USC100T, VWR) for 5 min and vortexed for 30 s to remove the bacteria growing in a biofilm. Serial dilutions were plated on TSB agar plates to determine the viable cells in the biofilm (cfu, colony forming units). The viable counts in the control experiment without treatment were $(4.4 \times 10^5) \pm (1.7 \times 10^5)$ cfu/mL.

Antibacterial Effect of Compounds on Continuous-Flow Biofilms. *S. aureus* continuous-flow biofilms were formed as previously described^{40,41} with some modifications and with an initial bacteria inoculum of O.D.₅₅₀ \approx 0.1 ($\approx(4.3 \times 10^7) \pm (1.43 \times 10^6)$ cfu/mL). The biofilms were grown in 2% (v/v) TSB + 0.2% glucose pumped through the flow cells chambers using a peristaltic pump ISM (Ismatec) at 42 μ L/min. These flow cells (DTU) were previously coated with 20% bovine plasma (Biowest) overnight prior to the inoculation of the bacteria. After 4 days of growth, the flow was stopped and different compounds diluted in media, including ciprofloxacin as a control, were injected into the formed biofilms. After 24 h treatment, biofilms were stained with the Live/Dead BacLight Bacterial Viability Kit (Thermo Fisher Scientific) and visualized under a Zeiss LSM 800 confocal laser scanning microscope (CLSM) with the 20X/0.8 air objective. Analysis of the images obtained was performed to quantify the biomass and thickness of the biofilms using ImageJ FIJI and COMSTAT2 software.⁴²

■ ASSOCIATED CONTENT

📄 Supporting Information

The Supporting Information is available free of charge on the ACS Publications website at DOI: 10.1021/acsinfecdis.9b00125.

General information and copies of NMR spectra and HRMS values (PDF)

■ AUTHOR INFORMATION

Corresponding Authors

*E-mail: lac@ugr.es.

*E-mail: etorrents@ibecbarcelona.eu.

ORCID

Andrés Parra: 0000-0001-7485-8753

Luis Álvarez de Cienfuegos: 0000-0001-8910-4241

Eduard Torrents: 0000-0002-3010-1609

Author Contributions

The manuscript was written through contributions of all authors. All authors have given approval to the final version of the manuscript. Karina Vega Granados and Andrés Parra designed and synthesized the library of oleanolic and maslinic acid derivatives and wrote the manuscript. Nùria Blanco-Cabra, Laura Moya-Andérico, and Marija Vukomanovic performed biological assays and wrote the manuscript. Eduard Torrents and Luis Álvarez de Cienfuegos directed the research, revised the experimental data, and wrote the manuscript. All authors have given approval to the final version of the manuscript.

Notes

The authors declare no competing financial interest.

■ ACKNOWLEDGMENTS

This study was partially supported by grants from the Ministerio de Economía, Industria y Competitividad, MINECO, and Agencia Estatal de Investigación, AEI, Spain, cofunded by Fondo Europeo de Desarrollo Regional, FEDER, European Union (BIO2015–63557-R, FIS2017–85954-R and RTI2018–098573-B-I00), the CERCA program and AGAUR-Generalitat de Catalunya (2017SGR-1079), the European Regional Development Fund (FEDER), Catalan and Spanish cystic fibrosis federation, the EIT Health and Obra Social “La Caixa”. K.V.G. thanks CONACYT (Consejo Nacional de Ciencia y Tecnología) Gobierno del estado de Baja California 2015 for her fellowship. The authors wish to thank Johanna Binding and Zoe Downer for technical assistance. L.A.C. wants to thank “Unidad de Excelencia Química aplicada a Biomedicina y Medioambiente” for support. Finally we would like to thank the Editor and reviewers whose suggestions greatly improved the manuscript.

■ REFERENCES

- (1) Otto, M. (2018) Staphylococcal Biofilms. *Microbiol. Spectrum* 6 (4), 1 DOI: 10.1128/microbiolspec.GPP3-0023-2018.
- (2) Stewart, P. S., and Costerton, J. W. (2001) Antibiotic resistance of bacteria in biofilms. *Lancet* 358 (9276), 135–8.
- (3) Costerton, J. W., Stewart, P. S., and Greenberg, E. P. (1999) Bacterial biofilms: a common cause of persistent infections. *Science* 284 (5418), 1318–22.
- (4) Hassoun, A., Linden, P. K., and Friedman, B. (2017) Incidence, prevalence, and management of MRSA bacteremia across patient populations—a review of recent developments in MRSA management and treatment. *Crit Care* 21 (1), 211.
- (5) Tong, S. Y., Davis, J. S., Eichenberger, E., Holland, T. L., and Fowler, V. G., Jr. (2015) *Staphylococcus aureus* infections: epidemiology, pathophysiology, clinical manifestations, and management. *Clin. Microbiol. Rev.* 28 (3), 603–61.
- (6) Suresh, M. K., Biswas, R., and Biswas, L. (2019) An update on recent developments in the prevention and treatment of *Staphylococcus aureus* biofilms. *Int. J. Med. Microbiol.* 309, 1.
- (7) Jesus, J. A., Lago, J. H., Laurenti, M. D., Yamamoto, E. S., and Passero, L. F. (2015) Antimicrobial activity of oleanolic and ursolic acids: an update. *Evid Based Complement Alternat Med.* 2015, 620472.
- (8) Rufino-Palomares, E. (2015) Anti-cancer and Anti-angiogenic Properties of Various Natural Pentacyclic Tri-terpenoids and Some of their Chemical Derivatives. *Curr. Org. Chem.* 19 (10), 1.
- (9) Fernández-Hernández, A., Martínez, A., Rivas, F., García-Mesa, J. A., and Parra, A. (2015) Effect of the Solvent and the Sample Preparation on the Determination of Triterpene Compounds in Two-Phase Olive-Mill-Waste Samples. *J. Agric. Food Chem.* 63 (17), 4269–4275.

- (10) Park, S. N., Ahn, S. J., and Kook, J. K. (2015) Oleonic acid and ursolic acid inhibit peptidoglycan biosynthesis in *Streptococcus mutans* UA159. *Braz. J. Microbiol.* 46 (2), 613–7.
- (11) Fontanay, S., Grare, M., Mayer, J., Finance, C., and Duval, R. E. (2008) Ursolic, oleonic and betulonic acids: antibacterial spectra and selectivity indexes. *J. Ethnopharmacol.* 120 (2), 272–6.
- (12) Kim, S., Lee, H., Lee, S., Yoon, Y., and Choi, K. H. (2015) Antimicrobial action of oleonic acid on *Listeria monocytogenes*, *Enterococcus faecium*, and *Enterococcus faecalis*. *PLoS One* 10 (3), No. e0118800.
- (13) Medina-O'Donnell, M., Rivas, F., Reyes-Zurita, F. J., Martinez, A., Lupianez, J. A., and Parra, A. (2018) Diamine and PEGylated-diamine conjugates of triterpenic acids as potential anticancer agents. *Eur. J. Med. Chem.* 148, 325–336.
- (14) Liu, J. (1995) Pharmacology of oleonic acid and ursolic acid. *J. Ethnopharmacol.* 49 (2), 57–68.
- (15) Lozano-Mena, G., Sanchez-Gonzalez, M., Juan, M. E., and Planas, J. M. (2014) Maslinic acid, a natural phytoalexin-type triterpene from olives—a promising nutraceutical? *Molecules* 19 (8), 11538–59.
- (16) Garcia-Salinas, S., Elizondo-Castillo, H., Arruebo, M., Mendoza, G., and Irusta, S. (2018) Evaluation of the Antimicrobial Activity and Cytotoxicity of Different Components of Natural Origin Present in Essential Oils. *Molecules* 23 (6), 1399.
- (17) Abreu, A. C., Paulet, D., Coqueiro, A., Malheiro, J., Borges, A., Saavedra, M. J., Choi, Y. H., and Simões, M. (2016) Antibiotic adjuvants from *Buxus sempervirens* to promote effective treatment of drug-resistant *Staphylococcus aureus* biofilms. *RSC Adv.* 6 (97), 95000–95009.
- (18) Kurek, A., Grudniak, A. M., Szwed, M., Klicka, A., Samluk, L., Wolska, K. I., Janiszowska, W., and Popowska, M. (2010) Oleonic acid and ursolic acid affect peptidoglycan metabolism in *Listeria monocytogenes*. *Antonie van Leeuwenhoek* 97 (1), 61–8.
- (19) Pavel, I. Z., Danciu, C., Oprean, C., Dehelean, C. A., Muntean, D., Csuk, R., and Muntean, D. M. (2016) In Vitro Evaluation of the Antimicrobial Ability and Cytotoxicity on Two Melanoma Cell Lines of a Benzylamide Derivative of Maslinic Acid. *Anal. Cell. Pathol.* 2016, 2787623.
- (20) Ignasiak, K., and Maxwell, A. (2017) *Galleria mellonella* (greater wax moth) larvae as a model for antibiotic susceptibility testing and acute toxicity trials. *BMC Res. Notes* 10 (1), 428.
- (21) Martin-Navarro, C. M., Lopez-Arencibia, A., Sifaoui, I., Reyes-Batlle, M., Fouque, E., Osuna, A., Valladares, B., Pintero, J. E., Hechard, Y., Maciver, S. K., and Lorenzo-Morales, J. (2017) Amoebicidal Activity of Caffeine and Maslinic Acid by the Induction of Programmed Cell Death in *Acanthamoeba*. *Antimicrob. Agents Chemother.* 61 (6), 1 DOI: 10.1128/AAC.02660-16.
- (22) Grudniak, A. M., Kurek, A., Szarlak, J., and Wolska, K. I. (2011) Oleonic and ursolic acids influence affect the expression of the cysteine regulon and the stress response in *Escherichia coli*. *Curr. Microbiol.* 62 (4), 1331–6.
- (23) Martins, A., Vasas, A., Viveiros, M., Molnar, J., Hohmann, J., and Amaral, L. (2011) Antibacterial properties of compounds isolated from *Carpobrotus edulis*. *Int. J. Antimicrob. Agents* 37 (5), 438–44.
- (24) Sharma, H., Kumar, P., Deshmukh, R. R., Bishayee, A., and Kumar, S. (2018) Pentacyclic triterpenes: New tools to fight metabolic syndrome. *Phytochemistry* 50, 166–177.
- (25) Liang, Z., Zhang, L., Li, L., Liu, J., Li, H., Zhang, L., Chen, L., Cheng, K., Zheng, M., Wen, X., Zhang, P., Hao, J., Gong, Y., Zhang, X., Zhu, X., Chen, J., Liu, H., Jiang, H., Luo, C., and Sun, H. (2011) Identification of pentacyclic triterpenes derivatives as potent inhibitors against glycogen phosphorylase based on 3D-QSAR studies. *Eur. J. Med. Chem.* 46 (6), 2011–21.
- (26) Mukaratirwa, S., Gcanga, L., and Kamau, J. (2016) Efficacy of maslinic acid and fenbendazole on muscle larvae of *Trichinella zimbabwensis* in laboratory rats. *J. Helminthol.* 90 (1), 86–90.
- (27) Moneriz, C., Marin-Garcia, P., Garcia-Granados, A., Bautista, J. M., Diez, A., and Puyet, A. (2011) Parasitostatic effect of maslinic acid. I. Growth arrest of *Plasmodium falciparum* intraerythrocytic stages. *Malar. J.* 10, 82.
- (28) De Pablos, L. M., dos Santos, M. F., Montero, E., Garcia-Granados, A., Parra, A., and Osuna, A. (2010) Anticoccidial activity of maslinic acid against infection with *Eimeria tenella* in chickens. *Parasitol. Res.* 107 (3), 601–4.
- (29) Moneriz, C., Mestres, J., Bautista, J. M., Diez, A., and Puyet, A. (2011) Multi-targeted activity of maslinic acid as an antimalarial natural compound. *FEBS J.* 278 (16), 2951–61.
- (30) Kozai, K., Miyake, Y., Kohda, H., Kametaka, S., Yamasaki, K., Suginaka, H., and Nagasaka, N. (1987) Inhibition of glucosyltransferase from *Streptococcus mutans* by oleonic acid and ursolic acid. *Caries Res.* 21 (2), 104–8.
- (31) Malanovic, N., and Lohner, K. (2016) Gram-positive bacterial cell envelopes: The impact on the activity of antimicrobial peptides. *Biochim. Biophys. Acta, Biomembr.* 1858 (5), 936–46.
- (32) Ghosh, C., Manjunath, G. B., Akkapeddi, P., Yarlagaadda, V., Hoque, J., Uppu, D. S., Konai, M. M., and Haldar, J. (2014) Small molecular antibacterial peptidomimics: the simpler the better! *J. Med. Chem.* 57 (4), 1428–36.
- (33) Hoque, J., Konai, M. M., Sequeira, S. S., Samaddar, S., and Haldar, J. (2016) Antibacterial and Antibiofilm Activity of Cationic Small Molecules with Spatial Positioning of Hydrophobicity: An In Vitro and In Vivo Evaluation. *J. Med. Chem.* 59 (23), 10750–10762.
- (34) Konai, M. M., and Haldar, J. (2017) Fatty Acid Comprising Lysine Conjugates: Anti-MRSA Agents That Display In Vivo Efficacy by Disrupting Biofilms with No Resistance Development. *Bioconjugate Chem.* 28 (4), 1194–1204.
- (35) Kaplan, J. B. (2011) Antibiotic-induced biofilm formation. *Int. J. Artif. Organs* 34 (9), 737–51.
- (36) Garcia-Granados, A. Process for the industrial recovery of oleonic and maslinic acids contained in the olive milling byproducts. *PCT Int. Appl. WO 9804331*, 1998.
- (37) Martinez, A., Perojil, A., Rivas, F., Parra, A., Garcia-Granados, A., and Fernandez-Vivas, A. (2015) Biotransformation of oleonic and maslinic methyl esters by *Rhizomucor miehei* CECT 2749. *Phytochemistry* 117, 500–508.
- (38) Barniol-Xicota, M., Escandell, A., Valverde, E., Julian, E., Torrents, E., and Vazquez, S. (2015) Antibacterial activity of novel benzopolycyclic amines. *Bioorg. Med. Chem.* 23 (2), 290–6.
- (39) Clinical and laboratory standards institute (2006) *Methods for dilution antimicrobial susceptibility test for bacteria that grow aerobically: approved standard*, CLSI document M7-A7, 7th ed., Clinical and Laboratory Standards Institute, Wayne, PA.
- (40) Baelo, A., Levato, R., Julian, E., Crespo, A., Astola, J., Gavaldà, J., Engel, E., Mateos-Timoneda, M. A., and Torrents, E. (2015) Disassembling bacterial extracellular matrix with DNase-coated nanoparticles to enhance antibiotic delivery in biofilm infections. *J. Controlled Release* 209, 150–8.
- (41) Crespo, A., Blanco-Cabra, N., and Torrents, E. (2018) Aerobic Vitamin B12 Biosynthesis Is Essential for *Pseudomonas aeruginosa* Class II Ribonucleotide Reductase Activity During Planktonic and Biofilm Growth. *Front. Microbiol.* 9, 986.
- (42) Givskov, M., Hentzer, M., Ersbøll, B. K., Heydorn, A., Sternberg, C., Nielsen, A. T., and Molin, S. (2000) Quantification of biofilm structures by the novel computer program COMSTAT. *Microbiology* 146, 2395–407.

Supplementary Material

Table S1: Average \pm standard deviation and ratio of green and red cells in the Live/Dead analysis.

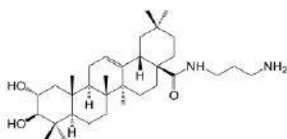
	CONTROL	OA	MA	MA-HDA-MA	OA-HDA	MA-HDA	MA-DMPA	OA-DAD	MA-DAD
GREEN CELLS (alive)	4450 \pm 296.6	15.17 \pm 7.3	4 \pm 2.8	1570.7 \pm 20.8	0.8 \pm 1.09	5 \pm 2.55	1241 \pm 153.9	6.67 \pm 4	2.67 \pm 3.05
RED CELLS (dead)	76 \pm 8.485	68.8 \pm 32.16	44.5 \pm 14.1	144.33 \pm 24.5	34.2 \pm 7.12	68.7 \pm 18.7	96.25 \pm 19.2	31.67 \pm 22.85	98 \pm 13
RATIO (green/ red)	58.55	0.22	0.09	10.88	0.02	0.07	12.89	0.21	0.03

Table S2: *Staphylococcus aureus* antimicrobial activity profile.

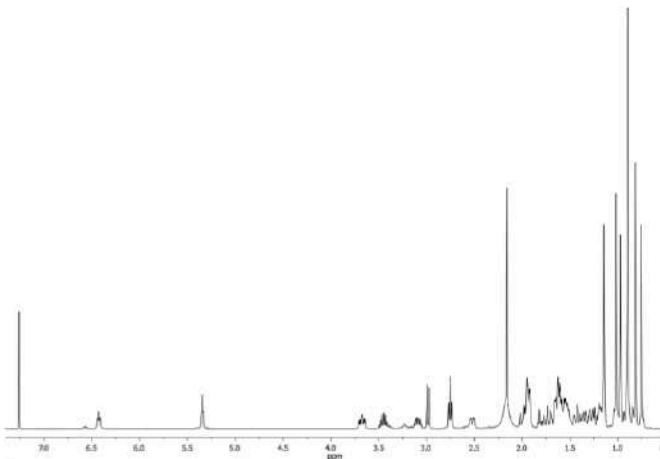
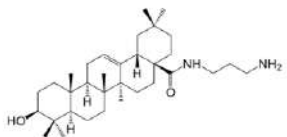
Antimicrobial activity profile (MIC ₅₀ μ g/ml)		
Antibiotic	<i>S. aureus</i> CECT 86 (ATCC 12600)	<i>S. aureus</i> MRSA
Linezolid	2	4
Oxacillin	1	>250
Vancomycin	1	1
Daptomycin	0.25	0.5
Ciprofloxacin	0.25	

General Information

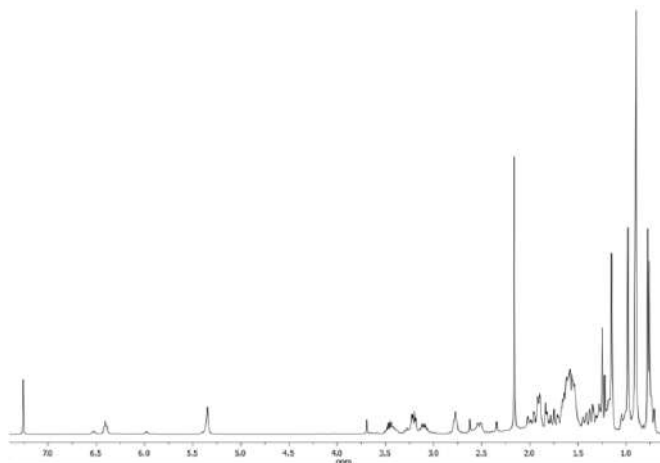
To obtain the extract of the raw material, n-Hexane (Merck, ref. 1.04374) and EtOAc (Fisher Scientific, ref. E/0900/17) solvents were used with previous distillation. The isolation of the amino compounds, maslinic and oleanolic acids was carried out by flash chromatography, using silica gel 60 (Merck, ref. 1.09385) as the stationary phase, and CH₂Cl₂ (Fisher Scientific, ref. D/1852/17), with increasing amounts of Me₂CO (Fisher Scientific, ref. A/0600/17) as the mobile phase. For the control of flash chromatography and reactions, silica gel 60 aluminum sheets (Merk. ref. 1.16835) were used, the compounds were made visible by spraying a mixture of H₂SO₄ and AcOH, followed by heating at 120 °C, and finally observed with UV light at 254 nm. For the amidation reactions were used DIEA (Sigma-Aldrich, ≥99%, ref. D125806), TBTU (Apollo Scientific, ref. PC0921), 3-(Dimethylamino)-1-propylamine (Sigma-Aldrich, ≥98.0%, ref. 39380), 1,3-Diaminopropane (Sigma-Aldrich, ≥98.0%, ref. 239984), 1,6-Diaminohexane (Sigma-Aldrich, 98%, ref. H11696), 1,10-Diaminodecane (ACROS Organics 97%, ref. 112130250), Na₂SO₄ Anhydrous (Fisher Chemical, 99+%, ref. S/6600/65), K₂CO₃ (PanReac AppliChem, ref. 141490), the solvents THF (Sigma-Aldrich, HPLC ≥99%, ref. 270385) with previous distillation, and CH₂Cl₂ (Fisher Scientific, ref. D/1852/17). The reagents were used without further purification. Measurements of NMR spectra were made in VARIAN direct drive (400 and 500 MHz ¹H NMR) spectrometers. The ¹³C chemical shifts were assigned with the aid of distortion less enhancement by polarization transfer (DEPT) using a flip angle of 135.

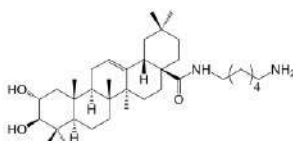
MA-PDA

$^1\text{H NMR}$ (CDCl_3 , 400 MHz): δ 6.43 (dd, 1H, $J_1 = J_2 = 5.4$ Hz), 5.35 (dd, 1H, $J_1 = J_2 = 3.2$ Hz), 3.70 (ddd, 1H, $J_1 = 4.8$, $J_2 = 9.6$, $J_3 = 14.0$ Hz), 3.50–3.41 (m, 1H), 3.13–3.10 (m, 1H), 2.98 (d, 1H, $J = 9.6$ Hz), 2.75 (t, 1H, $J = 6.4$ Hz), 2.52 (dd, 1H, $J_1 = 3.6$, $J_2 = 12.8$ Hz), 1.15, 1.02, 0.97, 0.90, 0.90, 0.81, 0.75 (s, 3H); ESI-HRMS m/z calculated for $\text{C}_{33}\text{H}_{57}\text{N}_2\text{O}_3$ $[\text{M}+1]^+$ 529.4369, found 529.4336.

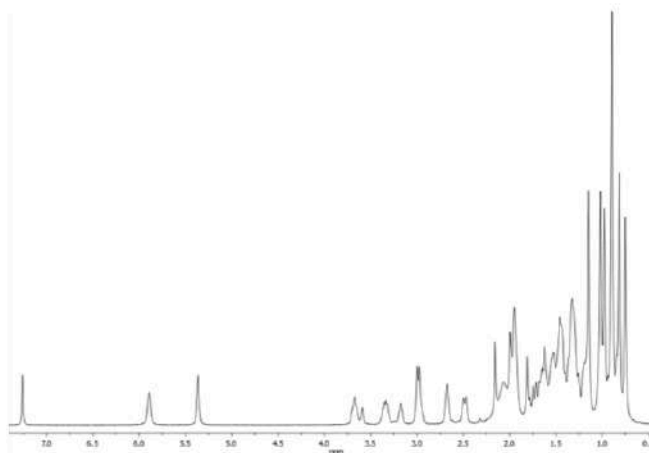
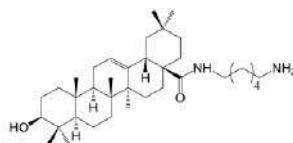
**OA-PDA**

$^1\text{H NMR}$ (CDCl_3 , 400 MHz): δ 6.41 (dd, 1H, $J_1 = J_2 = 5.0$ Hz), 5.35 (dd, 1H, $J_1 = J_2 = 3.2$ Hz), 3.49–3.44 (m, 1H), 3.21 (dd, 1H, $J_1 = 4.6$, $J_2 = 8.8$ Hz), 3.13–3.10 (m, 1H), 2.77 (t, 2H, $J = 6.0$ Hz), 2.52 (dd, 1H, $J_1 = 3.4$, $J_2 = 13.0$ Hz), 1.25, 1.15, 0.98, 0.90, 0.90, 0.78, 0.76 (s, 3H); ESI-HRMS m/z calculated for $\text{C}_{33}\text{H}_{57}\text{N}_2\text{O}_2$ $[\text{M}+1]^+$ 513.4420, found 513.4426.

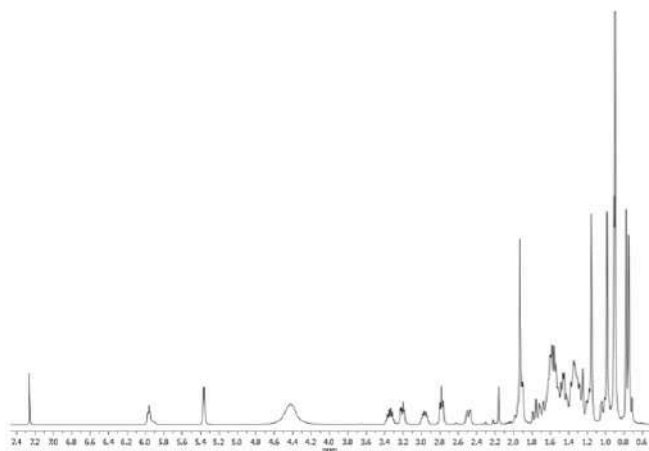


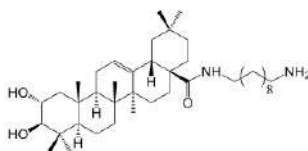
MA-HDA

$^1\text{H NMR}$ (CDCl_3 , 400 MHz): δ 5.90 (dd, 1H, $J_1 = J_2 = 5.4$ Hz), 5.36 (dd, 1H, $J_1 = J_2 = 3.2$ Hz), 3.68 (ddd, 1H, $J_1 = 4.8$, $J_2 = 9.2$, $J_3 = 14.0$ Hz), 3.35–3.32 (m, 1H), 3.19–3.15 (m, 1H), 2.98 (d, 1H, $J = 9.2$ Hz), 2.69 (t, 2H, $J = 6.4$ Hz), 2.49 (dd, 1H, $J_1 = 3.6$, $J_2 = 12.8$ Hz), 1.15, 1.02, 0.98, 0.90, 0.90, 0.82, 0.75 (s, 3H); ESI-HRMS m/z calculated for $\text{C}_{36}\text{H}_{63}\text{N}_2\text{O}_3$ $[\text{M}+1]^+$ 571.4839, found 571.4842.

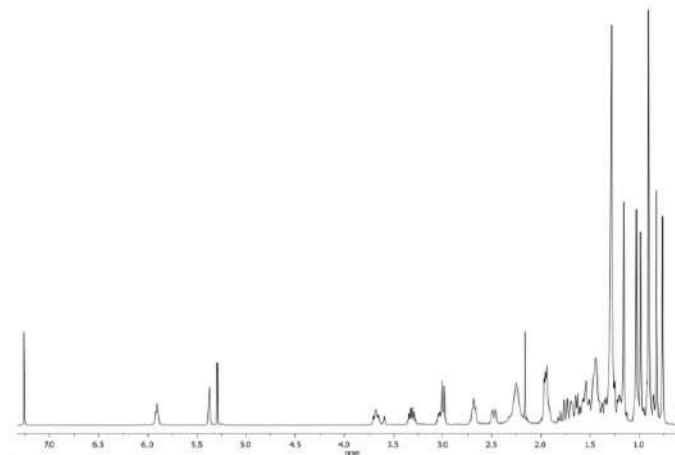
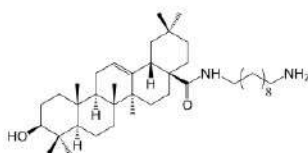
**OA-HDA**

$^1\text{H NMR}$ (CDCl_3 , 400 MHz): δ 5.96 (dd, 1H, $J_1 = J_2 = 6.0$ Hz), 5.37 (dd, 1H, $J_1 = J_2 = 2.8$ Hz), 3.37–3.32 (m, 1H), 3.21 (dd, 1H, $J_1 = 4.4$, $J_2 = 10.8$ Hz), 2.98–2.94 (m, 1H), 2.78 (t, 2H, $J = 6.0$ Hz), 2.50 (dd, 1H, $J_1 = 2.8$, $J_2 = 13.2$ Hz), 1.15, 0.98, 0.91, 0.90, 0.90, 0.78, 0.75 (s, 3H); ESI-HRMS m/z calculated for $\text{C}_{38}\text{H}_{63}\text{N}_2\text{O}_2$ $[\text{M}+1]^+$ 555.4890, found 555.4874.

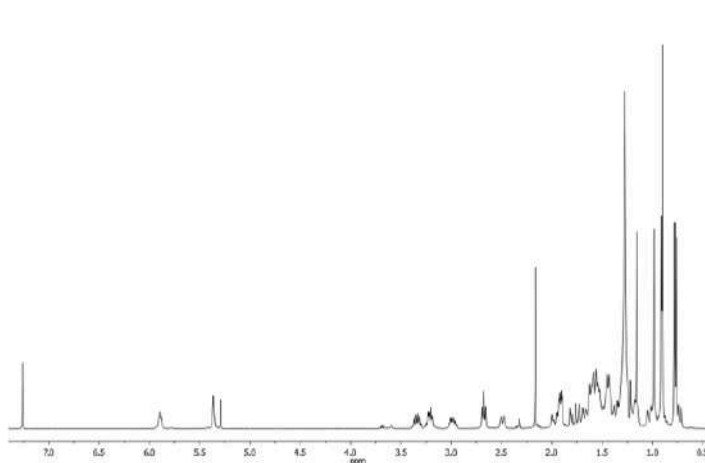


MA-DAD

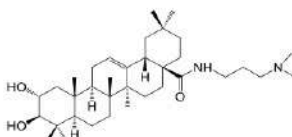
$^1\text{H NMR}$ (CDCl_3 , 400 MHz): δ 5.91 (dd, 1H, $J_1 = J_2 = 4.8$ Hz), 5.36 (dd, 1H, $J_1 = J_2 = 2.8$ Hz), 3.68 (ddd, 1H, $J_1 = 4.0$, $J_2 = 9.6$, $J_3 = 14.0$ Hz), 3.36–3.28 (m, 1H), 3.06–2.99 (m, 1H), 3.00 (d, 1H, $J = 9.6$ Hz), 2.68 (t, 2H, $J = 6.4$ Hz), 2.50 (dd, 1H, $J_1 = 2.4$, $J_2 = 12.4$ Hz), 1.28, 1.16, 1.03, 0.99, 0.90, 0.82, 0.76 (s, 3H); ESI-HRMS m/z calculated for $\text{C}_{40}\text{H}_{71}\text{N}_2\text{O}_3$ $[\text{M}+1]^+$ 627.5386, found 627.5478.

**OA-DAD**

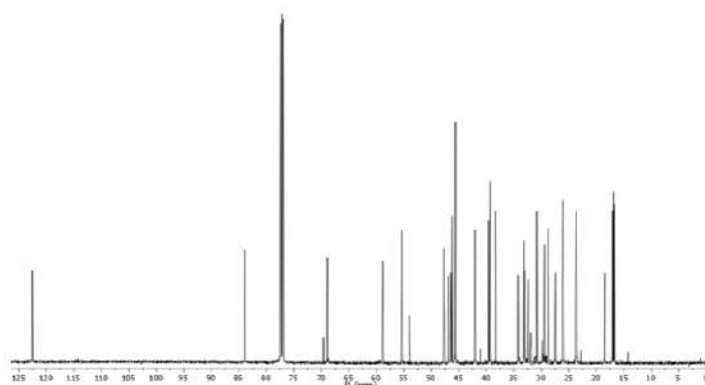
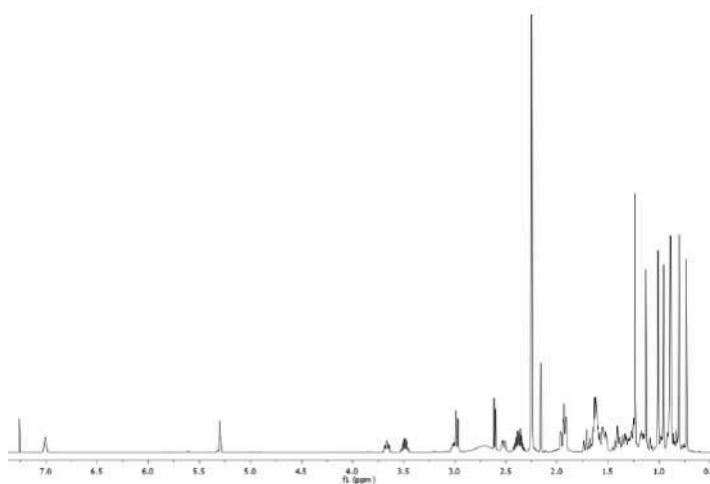
$^1\text{H NMR}$ (CDCl_3 , 400 MHz): δ 6.41 (dd, 1H, $J_1 = J_2 = 5.2$ Hz), 5.35 (dd, 1H, $J_1 = J_2 = 3.2$ Hz), 3.49–3.39 (m, 1H), 3.21 (dd, 1H, $J_1 = 4.6$, $J_2 = 11.1$ Hz), 3.14–3.07 (m, 1H), 2.77 (t, 2H, $J = 6.0$ Hz), 2.52 (dd, 1H, $J_1 = 3.6$, $J_2 = 13.2$ Hz), 1.25, 1.15, 0.98, 0.91, 0.90, 0.78, 0.76 (s, 3H); ESI-HRMS m/z calculated for $\text{C}_{40}\text{H}_{71}\text{N}_2\text{O}_2$ $[\text{M}+1]^+$ 611.5516, found 611.5534.

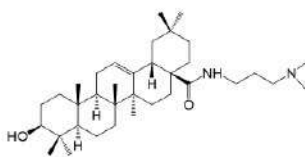


MA-DMPA

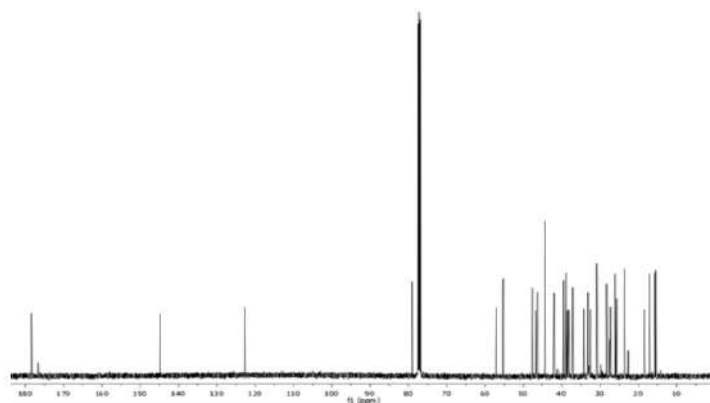
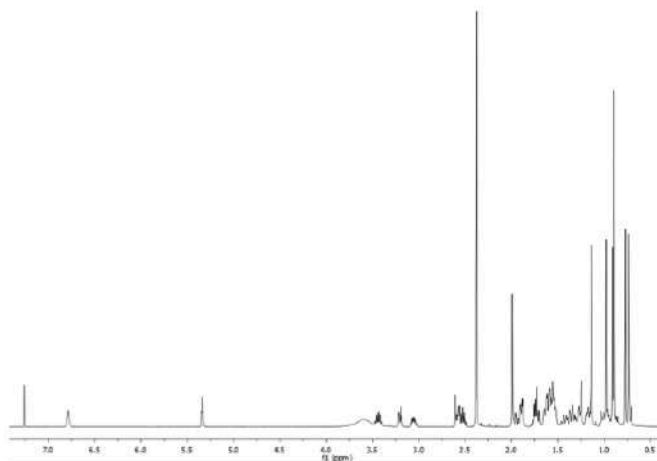


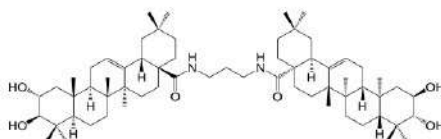
$^1\text{H NMR}$ (CDCl_3 , 500 MHz): δ 7.01 (dd, 1H, $J_1 = J_2 = 5.4$ Hz), 5.30 (dd, 1H, $J_1 = J_2 = 3.6$ Hz), 3.66 (ddd, 1H, $J_1 = 4.8$, $J_2 = 9.6$, $J_3 = 14.0$ Hz), 3.53–3.45 (m, 1H), 3.00–2.98 (m, 1H), 2.97 (d, 1H, $J = 9.5$ Hz), 2.51 (dd, 1H, $J_1 = 3.6$, $J_2 = 12.8$ Hz), 2.25, 2.25, 1.12, 1.01, 0.95, 0.89, 0.88, 0.80 0.73 (s, 3H). $^{13}\text{C NMR}$ (CDCl_3 , 126 MHz): δ 178.10 (C), 144.80 (C), 122.53 (CH), 83.92 (CH), 68.90 (CH), 58.81 (CH₂), 55.34 (CH), 53.95 (CH₂), 47.68 (CH), 46.88 (CH₂), 46.44 (CH₂), 46.22 (C), 45.62 (CH), 42.04 (C), 41.99 (CH₃), 39.54 (C), 39.30 (CH₂), 38.32 (C), 34.24 (CH₂), 33.16 (CH₃), 32.99 (CH₂), 32.39 (CH₂), 31.86 (C), 30.84 (C), 29.39 (CH₃), 28.75 (CH₃), 27.44 (CH₂), 26.07 (CH₃), 26.05 (CH₂), 23.67 (CH₃), 23.63 (CH₂), 18.44 (CH₂), 17.04 (CH₃), 16.90 (CH₃), 16.73 (CH₃). ESI-HRMS m/z calculated for $\text{C}_{35}\text{H}_{61}\text{N}_2\text{O}_3$ $[\text{M}+1]^+$ 557.4604, found 557.4682.



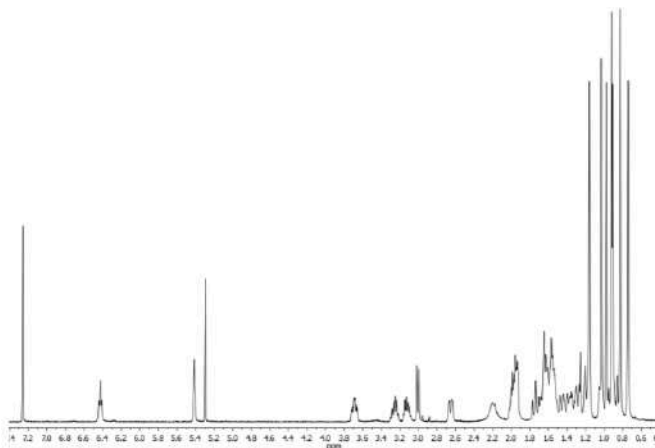
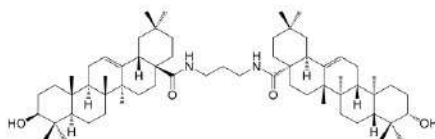
OA-DMPA

$^1\text{H NMR}$ (CDCl_3 , 500 MHz): δ 6.78 (dd, 1H, $J_1 = J_2 = 5.3$ Hz), 5.34 (dd, 1H, $J_1 = J_2 = 3.7$ Hz), 3.47–3.40 (m, 1H), 3.18 (dd, 1H, $J_1 = 4.6$, $J_2 = 11$ Hz), 3.09–3.02 (m, 1H), 2.58 (dd, 1H, $J_1 = 3.4$, $J_2 = 13.0$ Hz), 2.37, 2.37, 1.13, 0.97, 0.90, 0.89, 0.89, 0.77, 0.73 (s, 3H). $^{13}\text{C NMR}$ (CDCl_3 , 126 MHz): δ 178.44 (C), 144.80 (C), 122.75 (CH), 79.09 (CH), 57.17 (CH_2), 55.28 (CH), 47.71 (CH), 46.85 (CH_2), 46.34 (C), 44.43 (CH), 42.04 (C), 41.95 (CH_3), 39.51 (C), 38.89 (C), 38.57 (CH_2), 38.17 (CH_2), 37.13 (C), 34.28 (CH_2), 33.18 (CH_3), 33.03 (CH_2), 32.54 (CH_2), 30.86 (C), 28.23 (CH_3), 27.50 (CH_2), 27.29 (CH_2), 26.03 (CH_3), 25.69 (CH_2), 23.73 (CH_3), 23.64 (CH_2), 23.60 (CH_2), 22.68 (CH_3), 18.44 (CH_2), 17.07 (CH_3), 15.71 (CH_3), 15.46 (CH_3). ESI-HRMS m/z calculated for $\text{C}_{35}\text{H}_{61}\text{N}_2\text{O}_2$ $[\text{M}+1]^+$ 541.4655, found 541.4733.

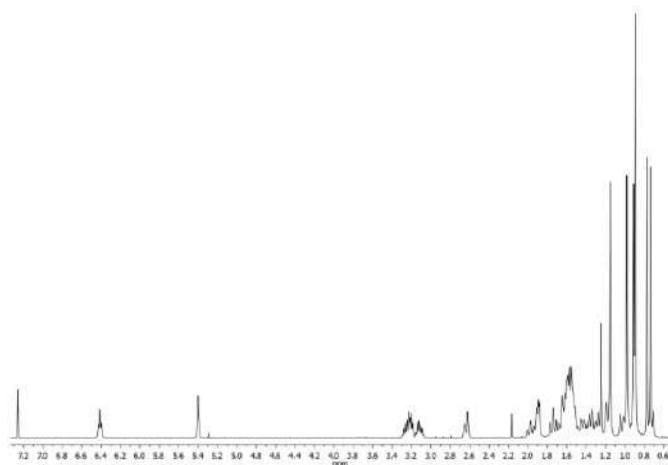


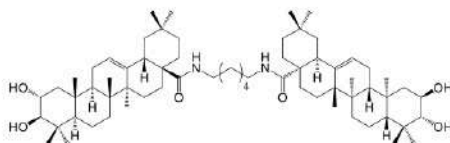
MA-PDA-MA

$^1\text{H NMR}$ (CDCl_3 , 400 MHz): δ 6.43 (dd, 1H, $J_1 = J_2 = 6.0$ Hz), 5.35 (dd, 1H, $J_1 = J_2 = 3.2$ Hz), 3.70 (ddd, 1H, $J_1 = 4.0$, $J_2 = 9.2$, $J_3 = 14.0$ Hz), 3.28–3.23 (m, 1H), 3.15–3.10 (m, 1H), 3.01 (d, 1H, $J = 9.2$ Hz), 2.65 (dd, 1H, $J_1 = 3.6$, $J_2 = 13.2$ Hz), 1.16, 1.03, 0.98, 0.92, 0.91, 0.83, 0.74 (s, 3H); ESI-HRMS m/z calculated for $\text{C}_{63}\text{H}_{103}\text{N}_2\text{O}_6$ $[\text{M}+1]^+$ 983.7816, found 983.7781.

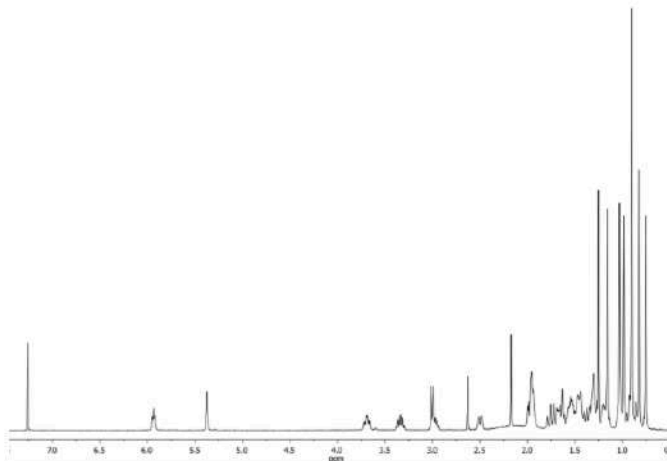
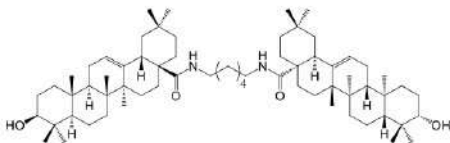
**OA-PDA-OA**

$^1\text{H NMR}$ (CDCl_3 , 400 MHz): δ 6.41 (dd, 1H, $J_1 = J_2 = 6.0$ Hz), 5.40 (dd, 1H, $J_1 = J_2 = 3.2$ Hz), 3.28–3.24 (m, 1H), 3.21 (dd, 1H, $J_1 = 4.8$, $J_2 = 11.21$ Hz), 3.14–3.10 (m, 1H), 2.64 (dd, 1H, $J_1 = 3.2$, $J_2 = 14.4$ Hz), 1.25, 1.15, 0.98, 0.91, 0.90, 0.77, 0.74 (s, 3H); ESI-HRMS m/z calculated for $\text{C}_{63}\text{H}_{101}\text{N}_2\text{O}_4$ $[\text{M}+1]^+$ 949.7761, found 949.7772.

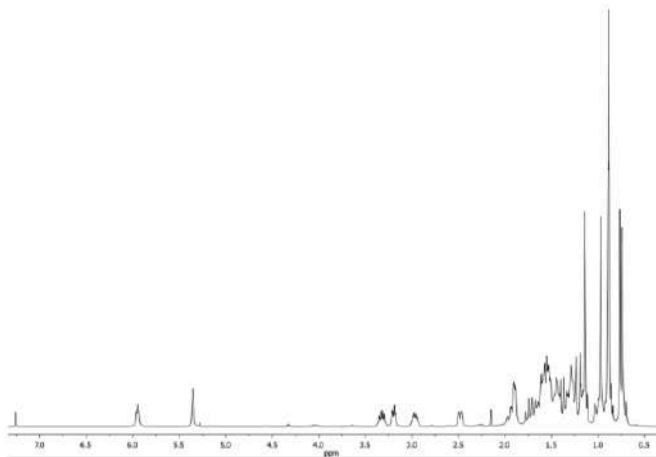


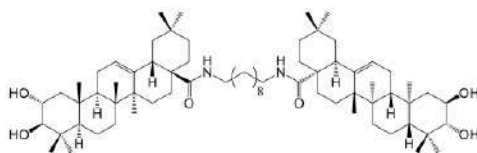
MA-HDA-MA

¹HNMR(CDCl₃, 400 MHz): δ 5.94 (dd, 1H, *J*₁ = *J*₂ = 5.4 Hz), 5.38 (dd, 1H, *J*₁ = *J*₂ = 3.2 Hz), 3.70 (ddd, 1H, *J*₁ = 4.4, *J*₂ = 9.2, *J*₃ = 13.6 Hz), 3.38–3.30 (m, 1H), 3.01–2.94 (m, 1H), 3.00 (d, 1H, *J* = 9.2 Hz), 2.50 (dd, 1H, *J*₁ = 3.2, *J*₂ = 12.8 Hz), 1.25, 1.16, 1.03, 0.99, 0.90, 0.83, 0.76 (s, 3H); ESI-HRMS *m/z* calculated for C₆₆H₁₀₆N₂O₆ [M+1]⁺ 1025.8286, found 1025.8268.

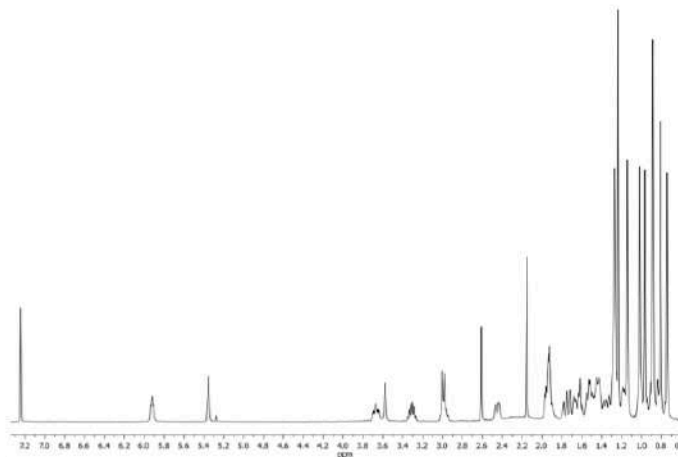
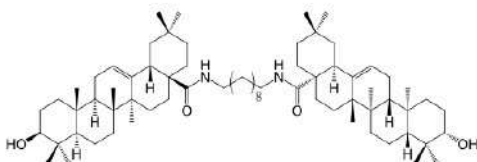
**OA-HDA-OA**

¹HNMR(CDCl₃, 400 MHz): δ 5.95 (dd, 1H, *J*₁ = *J*₂ = 5.2 Hz), 5.36 (dd, 1H, *J*₁ = *J*₂ = 3.0 Hz), 3.35–3.30 (m, 1H), 3.20 (dd, 1H, *J*₁ = 4.2, *J*₂ = 11.0 Hz), 3.00–2.93 (m, 1H), 2.48 (dd, 1H, *J*₁ = 3.2, *J*₂ = 13.2 Hz), 1.14, 0.97, 0.89, 0.89, 0.88, 0.77, 0.74 (s, 3H); ESI-HRMS *m/z* calculated for C₆₈H₁₀₇N₂O₄ [M+1]⁺ 991.8231, found 991.8235.

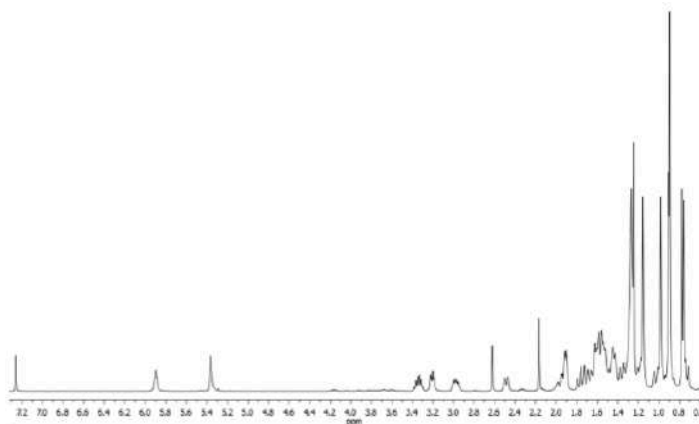


MA-DAD-MA

$^1\text{H NMR}$ (CDCl_3 , 400 MHz): δ 5.94 (dd, 1H, $J_1 = J_2 = 5.2$ Hz), 5.37 (dd, 1H, $J_1 = J_2 = 3.2$ Hz), 3.69 (ddd, 1H, $J_1 = 4.4$, $J_2 = 9.6$, $J_3 = 14$ Hz), 3.35–3.29 (m, 1H), 3.02–2.96 (m, 1H), 3.51 (d, 1H, $J = 9.6$ Hz), 2.47 (dd, 1H, $J_1 = 3.2$, $J_2 = 12.4$ Hz), 1.25, 1.16, 1.03, 0.98, 0.90, 0.83, 0.76 (s, 3H); ESI-HRMS m/z calculated for $\text{C}_{70}\text{H}_{117}\text{N}_2\text{O}_6$ $[\text{M}+1]^+$ 1081.8912, found 1081.8900.

**OA-DAD-OA**

$^1\text{H NMR}$ (CDCl_3 , 400 MHz): δ 5.90 (dd, 1H, $J_1 = J_2 = 4.8$ Hz), 5.36 (dd, 1H, $J_1 = J_2 = 2.8$ Hz), 3.37–3.32 (m, 1H), 3.21 (dd, 1H, $J_1 = 4.4$, $J_2 = 10.8$ Hz), 3.00–2.93 (m, 1H), 2.49 (dd, 1H, $J_1 = 2.6$, $J_2 = 12.6$ Hz), 1.25, 1.15, 0.98, 0.91, 0.90, 0.78, 0.76 (s, 3H); ESI-HRMS m/z calculated for $\text{C}_{70}\text{H}_{117}\text{N}_2\text{O}_4$ $[\text{M}+1]^+$ 1049.9013, found 1049.8990.



ARTICLE 3

Utility of *Galleria mellonella* larvae for evaluating nanoparticle toxicology

Published in *Chemosphere* (Q1, IF₂₀₁₉: 5.778)

DOI: 10.1016/j.chemosphere.2020.129235

December 2020

Laura Moya-Andérico¹, Marija Vukomanovic², Maria del Mar Cendra¹,
Miriam Segura-Feliu^{3,4,5,6}, Vanessa Gil^{3,4,5,6}, José A. del Río^{3,4,5,6} and
Eduard Torrents^{1,7,*}

¹Bacterial Infections and Antimicrobial Therapies group, Institute for Bioengineering of Catalonia (IBEC), The Barcelona Institute of Science and Technology (BIST), Barcelona, Spain

²Advanced Materials Department, Jozef Stefan Institute, Ljubljana, Slovenia

³Molecular and Cellular Neurobiotechnology, Institute for Bioengineering of Catalonia (IBEC), The Barcelona Institute of Science and Technology (BIST), Barcelona, Spain

⁴Centro de Investigación Biomédica en Red sobre Enfermedades Neurodegenerativas (CIBERNED), Madrid, Spain

⁵Department of Cell Biology, Physiology and Immunology, Universitat de Barcelona, Barcelona, Spain

⁶Institute of Neurosciences, Universitat de Barcelona, Barcelona, Spain

⁷Microbiology Section, Department of Genetics, Microbiology and Statistics, Faculty of Biology, University of Barcelona, Barcelona, Spain

*Corresponding author: Eduard Torrents (etorrents@ibecbarcelona.eu)



Contents lists available at ScienceDirect

Chemosphere

journal homepage: www.elsevier.com/locate/chemosphere

Utility of *Galleria mellonella* larvae for evaluating nanoparticle toxicology



Laura Moya-Andérico^a, Marija Vukomanovic^b, Maria del Mar Cendra^a,
Miriam Segura-Feliu^{c,d,e,f}, Vanessa Gil^{c,d,e,f}, José A. del Río^{c,d,e,f}, Eduard Torrents^{a,g,*}

^a Bacterial Infections: Antimicrobial Therapies group, Institute for Bioengineering of Catalonia (IBEC), The Barcelona Institute of Science and Technology (BIST), Barcelona, Spain

^b Advanced Materials Department, Jozef Stefan Institute, Ljubljana, Slovenia

^c Molecular and Cellular Neurobiotechnology, Institute for Bioengineering of Catalonia (IBEC), The Barcelona Institute of Science and Technology (BIST), Barcelona, Spain

^d Centro de Investigación Biomédica en Red sobre Enfermedades Neurodegenerativas (CIBERNED), Madrid, Spain

^e Department of Cell Biology, Physiology and Immunology, Universitat de Barcelona, Barcelona, Spain

^f Institute of Neurosciences, Universitat de Barcelona, Barcelona, Spain

^g Microbiology Section, Department of Genetics, Microbiology, and Statistics, Biology Faculty, Universitat de Barcelona, Barcelona, Spain

HIGHLIGHTS

- The LD₅₀ values in *G. mellonella* were better correlated with values from murine studies than with *in vitro* experiments.
- The NPs activated the *G. mellonella* immune system as seen by hemocyte proliferation and internalization of NPs by hemocytes.
- The NPs triggered acute toxicity effects in *G. mellonella* as seen by motility reduction and histological damage.
- *G. mellonella* larvae is an efficient pre-screening animal model to reduce the number of toxicity tests done in murine models.

ARTICLE INFO

Article history:

Received 10 November 2020

Received in revised form

3 December 2020

Accepted 4 December 2020

Available online 7 December 2020

Handling Editor: Willie Peijnenburg

Keywords:

Galleria mellonella

Nanoparticles

Nanotoxicity

Non-rodent *in vivo* model

Toxicity screening

Hemocytes

ABSTRACT

The use of nanoparticles in consumer products is currently on the rise, so it is important to have reliable methods to predict any associated toxicity effects. Traditional *in vitro* assays fail to mimic true physiological responses of living organisms against nanoparticles whereas murine *in vivo* models are costly and ethically controversial. For these reasons, this study aimed to evaluate the efficacy of *Galleria mellonella* as an alternative, non-rodent *in vivo* model for examining nanoparticle toxicity. Silver, selenium, and functionalized gold nanoparticles were synthesized, and their toxicity was assessed in *G. mellonella* larvae. The degree of acute toxicity effects caused by each type of NP was efficiently detected by an array of indicators within the larvae: LD₅₀ calculation, hemocyte proliferation, NP distribution, behavioral changes, and histological alterations. *G. mellonella* larvae are proposed as a nanotoxicological model that can be used as a bridge between *in vitro* and *in vivo* murine assays in order to obtain better predictions of NP toxicity.

© 2020 Elsevier Ltd. All rights reserved.

1. Introduction

In recent years, nanoparticles (NPs) have become the target of

numerous studies as they have shown promising potential in a wide range of human applications. Their unique physicochemical properties such as nanosize, solubility, surface area, and surface chemistry, among others, deem nanoparticles as an attractive technology in many industrial and biomedical fields (Bouwmeester et al., 2014). Popular elements like silver, gold, and selenium have been used as nanomaterials due to their known beneficial properties. Silver nanoparticles (AgNPs) are commonly used in a variety of

* Corresponding author. Bacterial Infections: Antimicrobial Therapies group, Institute for Bioengineering of Catalonia (IBEC), The Barcelona Institute of Science and Technology (BIST), Barcelona, Spain.

E-mail address: etorrents@ibecbarcelona.eu (E. Torrents).

consumer products such as cosmetics, textiles, home appliances, and medical devices and treatments (Ahamed et al., 2010; Schluesener and Schluesener, 2013; Vance et al., 2015) due to the renowned antimicrobial properties of silver (Mijnendonckx et al., 2013; Schluesener and Schluesener, 2013). Gold nanoparticles (AuNPs) have been used as a treatment for rheumatoid arthritis as well as in cancer therapy, drug delivery, and biosensors, among other uses (Finkelstein et al., 1976; Alkilany and Murphy, 2010; Zhang et al., 2010). Selenium nanoparticles (SeNPs) have also been used extensively in cancer therapy studies due to the potential anti-carcinogenic activity of selenium compounds. Selenium also provides several health benefits as it has been shown to improve immune, cognitive, and reproductive functions (Rayman, 2012; Fernandes and Gandin, 2015; Evans et al., 2017). Despite their plethora of applications, the use of nanoparticles has exhibited certain toxic effects, so it is critical to obtain a better understanding of their potential adverse effects on humans and the environment.

AgNPs have been reported to produce several toxic effects. Previous *in vitro* studies have shown that these nanoparticles can commonly induce oxidative stress due to the generation of reactive oxygen species (ROS) within the cells which can lead to DNA damage and apoptotic cell death (Hsin et al., 2008; Kim et al., 2009b; Chairuangkitti et al., 2013; Rinna et al., 2015). Furthermore, *in vivo* studies also showed increased ROS levels and revealed that AgNPs may also cause toxic effects in main organs such as brain, lung, liver, kidney, spleen, and intestine as well as in the nervous and immune systems. Besides the route of administration, the cytotoxic and genotoxic effects of AgNPs are also dependent on the size, dose, and coating of the nanoparticles (Tang et al., 2009; Kim et al., 2010; Xue et al., 2012; De Jong et al., 2013; Recordati et al., 2016; Shrivastava et al., 2016; Souza et al., 2016). AuNPs have also displayed the capability to induce oxidative stress generated by the production of nitric oxide which oxidizes DNA, proteins, and lipids followed by potential cell necrosis or apoptosis. The toxic effects are size-dependent with smaller nanoparticles having the most distribution throughout body organs and mainly target the liver and spleen (De Jong et al., 2008; Chen et al., 2009; Jia et al., 2009; Shrivastava et al., 2016). The effects also depend on whether the nanoparticles are functionalized or not. Metallic gold is considered biologically safe while functionalized AuNPs have reported higher cytotoxic effects (Goodman et al., 2004; Zhang et al., 2010). On the other hand, functionalization enhances the stability of the nanoparticles and can facilitate targeted drug delivery (Khoshnevisan et al., 2018). The toxicity of selenium compounds is greatly dependent on the concentration of selenium administered as high levels have been reported to be toxic as well as mutagenic and carcinogenic. The chemical form of selenium also plays a role in toxicity with inorganic forms like sodium selenite being more genotoxic when compared to organic forms like methyl-selenocysteine. Other toxic effects include selenosis, production of oxidative stress, induction of DNA damage, and interference in endocrine function and hormone synthesis (Yan and Spallholz, 1993; Bronzetti et al., 2001; Letavayova et al., 2008; Valdiglesias et al., 2010). The majority of these toxic effects were found *in vitro* while few toxicity studies have been done *in vivo*. One study tested selenium concentrations commonly used in the poultry industry in broiler chickens, and it found that selenium concentrated mainly in the spleen with no histopathological damage seen in any of the tissues tested (Gangadool et al., 2020). Other *in vivo* studies mainly focus on selenium effects on cellular and neurological functions combined with organism mortality (Rohn et al., 2018).

The majority of NP toxicity data is usually obtained with *in vitro* assays. Instead, it should be generated with *in vivo* models that replicate the true physiological responses of living organisms to

nanomaterials. (Valdiglesias et al., 2010; Barile, 2013). The use of mammals for toxicological testing is expensive, time-consuming, and ethically controversial so alternative models need to be used. For this reason, non-mammalian animal models such as *Danio rerio*, *Drosophila melanogaster*, and *Caenorhabditis elegans* are commonly used in the laboratory for toxicological screenings (Leung et al., 2008; Ahamed et al., 2010; Rand et al., 2014). Another invertebrate that has been gaining popularity as an *in vivo* model is *Galleria mellonella* (greater wax moth). When compared to other *in vivo* models, the larval stage of *G. mellonella* has many attractive advantages: convenient size for manipulation, inexpensive to purchase and breed, does not require much space or special infrastructure, low biohazard risk, and are more ethically accepted. Larvae used for testing are about 2 cm in length and weigh about 200 mg which facilitates the administration of the precise dose of nanomaterials by injection. Unlike other alternative models, the larvae can survive at 37 °C which allows for the study of nanomaterials at the same temperature of the human body (Desbois and Coote, 2012; Junqueira, 2012; Champion et al., 2016). Furthermore, the immune system of the larvae closely resembles the innate immune response of mammals (Browne et al., 2013; Wojda, 2017). *G. mellonella* has been used to evaluate the behavior, efficacy, and toxicity of antimicrobial compounds, and the results obtained have been proven useful for predicting human response to antibiotics (Thomas et al., 2013; Ignasiak and Maxwell, 2017). The model has also been used to test the toxicity of ionic liquids and food preservatives as well as many other compounds (Megaw et al., 2015; Dolan et al., 2016; Maguire et al., 2016; Allegra et al., 2018).

The aim of this study was to test the potential of *G. mellonella* as an *in vivo* model for the study of specific nanoparticles in order to provide a simple, economical, and robust toxicity model for the nanomedicine field.

2. Materials and methods

2.1. Nanoparticle (NP) synthesis and characterization

Silver nanoparticles (AgNPs) were synthesized using silver nitrate precursor (AgNO₃, 0.8 mg/ml, 50 ml) which was pre-heated to 100 °C. Instant addition of sodium borohydride (0.2 mg/ml, 10 ml) into the boiling precursor resulted in a color change from transparent to yellow or brown indicating finalization of the reaction.

Selenium nanoparticles (SeNPs) were synthesized using sodium selenite precursor (Na₂SeO₃, 0.8 mg/ml, 50 ml). The NPs formation took place slowly and in the following 2 h, a color change from transparent to intense orange indicated the end of the reaction. Mixing was continued overnight at room temperature to ensure NPs stabilization and agglomeration prevention.

Gold nanoparticles (AuNPs) were synthesized in the presence of amino acids which functionalized their surface to grant antimicrobial properties (Vukomanović et al., 2014). This way, increased toxicity by functionalization will be assayed. Since apatite is not toxic and can be used to stabilize AuNPs, it was used as a template and was synthesized using homogeneous sonochemical precipitation (jevtić et al., 2008). The template was dispersed by 10-min sonication in water containing 1 ml of isopropanol (amplitude 80%, on:off cycles 0.2:0.1s; VCX 750, Sonics®, Newtown, CT, USA). Chloroauric acid (HAuCl₄, 0.8 mg/ml, 50 ml), used as a gold precursor, was added to pre-sonicated apatite template (1.5 mg/ml, 50 ml). Upon addition of amino acid solutions containing histidine, arginine, and lysine amino acids (HAL) (0.15 mg/ml for each amino acid), the sonication was continued for an additional 30 min. The reaction was finished when the yellow-colored precursor turned violet indicating NPs formation.

All the NPs were centrifuged at 2500×g for 20 min to separate the supernatant, re-dispersed in 20 ml of water, and frozen on dry ice. After 24 h at −80 °C, they were freeze-dried.

For morphological and structural characteristics, NPs were sonochemically dispersed in water, deposited on copper grids, and observed using a transmission electron microscope (TEM, Tecnai™ Spirit 120 kV, FEI™, Hillsboro, OR, USA). The zeta potential measurements were performed using a Nanosizer (Malvern Panalytical, Malvern, UK).

2.2. Cell culture and nanoparticle in vitro toxicity

The toxicity of the different nanoparticles was assessed in the adenocarcinomic lung epithelial cell line A549 (ATCC® CCL-185). Cells were cultured in a 96-well polystyrene plate and grown in Dulbecco's Modified Eagle Medium (complete DMEM): Nutrient mixture F12 (DMEM/F12; Thermo Fisher Scientific, Madrid, Spain) supplemented with 10% (v/v) decomplexed fetal bovine serum (dFBS), 100 Units/ml penicillin, and 100 Units/ml streptomycin (Thermo Fisher Scientific, Madrid, Spain). Cells were maintained in a humidified incubator at 37 °C and 5% (v/v) CO₂ (IComed, Memmert, Schwabach, Germany). On the other hand, Au(HAL)NPs, AgNPs, and SeNPs were dispersed in complete DMEM by ultrasonication (amplitude: 18%, W = 250W, on:off = 2:1s for 30s; Digital Sonifier® 250, Branson Ultrasonics, Danbury, CT, USA). Dispersed NPs were subsequently adjusted in 200 μl of complete DMEM to be tested, in triplicates, at the concentrations of 0, 0.001, 0.005, 0.01, 0.05, 0.1, 0.15, 0.2, 0.5, 1.0 and 2.0 mg/ml in the A549 cells. Cell incubation with 1:10 dilution of dimethyl sulfoxide (DMSO) was used as a positive control for toxicity. After 24-h incubation, cellular toxicity was determined using the PrestoBlue™ Cell Viability Reagent (Invitrogen, Carlsbad, CA, USA) following the manufacturers' instructions. Briefly, 20 μl of PrestoBlue™ was added to each well and the plate was subsequently incubated for 1 h at 37 °C. After incubation, absorbance was read at λ = 570 using a microplate reader (Infinite® M200 Microplate reader, Tecan, Männedorf, Switzerland), and the given values were corrected by the respective absorbance at λ = 600, as recommended by the manufacturer. Greater metabolic activity of the cells (live cells) correlates to higher absorbance values.

Cell toxicity was determined using the absorbance values of the untreated cells (Abs₅₇₀/Abs₆₀₀ ~ 44532) as 100% cell viability. The concentration of each NP that caused 50% of cell toxicity (cytotoxicity 50%; CC₅₀) was calculated using Prism 8.0 (GraphPad Software, San Diego, CA, USA).

2.3. *G. mellonella* growth and maintenance

G. mellonella larvae were reared at 34 °C and fed an artificial diet consisting of corn flour, wheat flour, skim milk powder, cereals, dried brewer's yeast, honey, and glycerol as previously described (Moya-Andérico et al., 2020). Prior to inoculation, last instar larvae were incubated without food at 15 °C for a maximum period of 24 h (Ramarao et al., 2012).

2.4. *G. mellonella* in vivo nanoparticle toxicity

Groups of 5 larvae (200–250 mg each) were injected with a 22-gauge syringe (Hamilton, Reno, NV, USA) through the top right proleg using a 10 μl inoculum of various nanoparticle concentrations. The control group was inoculated with 10 μl of 1x PBS (Fisher Scientific, Madrid, Spain) in the same manner. After inoculation, the larvae were kept at 37 °C for 37–72 h with larval mortality observations done at 3, 16, 24, 37, 48, and 72 h post-injection. Survival

curves were plotted using Kaplan-Meier analysis and statistically significant differences were determined by the log-rank test (Prism 8.0, GraphPad Software, San Diego, CA, USA). The median lethal dose (LD₅₀) was determined as the nanoparticle concentration required to kill 50% of the larvae in 48 h (Prism 8.0, GraphPad Software, San Diego, CA, USA).

2.5. *G. mellonella* hemocyte proliferation

To measure hemocyte proliferation, the hemolymph was extracted from the larvae by cutting the tail off with a sterile surgical blade (size 23, Paramount Surgimed, New Delhi, India) and allowing the hemolymph to drain out into an Eppendorf tube for 10 min on ice. The hemolymph was centrifuged at 4 °C for 5 min at 1000×g to isolate hemocytes. The supernatant was removed and the hemocytes were washed once with PBS 1x. The washed cells were resuspended in PBS 1x, diluted 1:2 with trypan blue (Sigma-Aldrich, Lyon, France), and loaded onto a Neubauer counting chamber (Blaubrand®, Brand®, Wertheim, Germany) to determine hemocyte count.

2.6. Nanoparticle distribution and microscopy studies

G. mellonella larvae were injected with 250 mg/kg body weight of AgNPs and 1250 mg/kg body weight of Au(HAL)NPs and 20 h later, hemocytes were extracted and stained with FM™ 4–64 dye (Thermo Fisher Scientific, Madrid, Spain) according to the manufacturer's specifications. The hemocytes were then imaged using a confocal laser scanning microscope (LSM 800, Zeiss, Jena, Germany) and nanoparticles were visualized by light reflection using the 640 nm laser and the 40x/1.3 oil objective. All microscopy images were analyzed with ImageJ FIJI (National Institutes of Health, Bethesda, MD, USA).

For NP distribution, larvae were injected with different concentrations of NPs and after 37 h (for SeNPs) and 72 h (for Au(HAL) and Ag nanoparticles), the larvae were imaged to monitor nanoparticle accumulations within the body using an inverted fluorescent microscope (ECLIPSE Ti-S/L100, Nikon, Tokyo, Japan) connected to a DS-Qi2 camera (Nikon, Tokyo, Japan).

2.7. Behavioral tracking studies

10 μl of nanoparticles were injected into three larvae per group at a final concentration of 2841 mg/kg body weight of Au(HAL)NPs, 2841 mg/kg body weight of AgNPs, and 114 mg/kg body weight of SeNPs. As a control, two larvae were injected with 10 μl of PBS. About 1 h after inoculation, two or three larvae were deposited in the center of a 150 mm diameter plastic petri dish which was then placed on a homemade transilluminator. Larval movement was monitored for about 73 s using a USB twain supported camera (C270, Logitech, Lausanne, Switzerland) and the OPTIKA Vision Pro video time-lapse software (100 ms/frame at 640 × 360 dpi; OPTIKA, Ponteranica, Italy). Images were then compiled as single image stacks and exported as uncompressed AVI video files. The resulting paths were analyzed using the MTrack2 plug-in of the ImageJ software (National Institutes of Health, Bethesda, MD, USA) and the data was analyzed by determining statistically significant differences with an unpaired *t*-test (Prism 8.0, GraphPad Software, San Diego, CA, USA).

2.8. Histological analysis

The same larvae used in the tracking studies were subsequently used for the histological analysis. In order to avoid excessive body bending during processing, larvae were fixed and dehydrated

inside 1 cm diameter glass tubes. Thus, larvae were fixed in 1% phosphate-buffered paraformaldehyde (pH 7.3) overnight at 4 °C. After rinsing in PBS 1x, samples were dehydrated with increasing concentrations of ethanol (70, 90, and 96%), cleared in butanol, and embedded in low melting paraffin (56–58 °C, Lab-o-wax, Histo-line Laboratories, Pantigliate, Italy). Paraffin blocks were sectioned at 10 µm on a standard rotary microtome (Leica, Wetzlar, Germany). These sections were collected on gelatinized slides and then stained by hematoxylin eosin (HE) following standard protocols. The stained sections were mounted in Eukitt® and examined microscopically in an optical microscope (BX61, Olympus®, Tokyo, Japan) equipped with a DP12 digital camera (Olympus®, Tokyo, Japan). Low magnification images were obtained using an MPIan Apo 1.24/0.04 objective (Olympus®, Tokyo, Japan).

3. Results

3.1. NP characterization

The nanoparticles to be used as nano-toxicity models, AgNPs, Au(HAL)NPs, and SeNPs, were characterized by a negative net surface charge with very similar surface charge magnitudes (−17 mV, −14 mV, and −16 mV, respectively) (Fig. 1). Morphologically, all of them have a spherical shape with a very narrow size distribution. AgNPs are small spheres with 12 nm diameter which were detected as small and large clusters with an average size of 60 nm and 306 nm, respectively. The Au(HAL)NPs are 15 nm-sized particles coated by an organic layer and deposited to the surface of apatite plates. The average size of these structures is 76 nm and 194 nm. In the case of SeNPs, they are small particles with a size of

9 nm and very stable. They were detected as individual NPs as well as in clusters with 36 nm in size.

3.2. *In vitro* nanoparticle toxicity

The toxicity of all NPs was first studied *in vitro* using A549 cells. Cells incubated without any treatment resulted in 100% survival while the DMSO-exposed cells remained blue after the addition of PrestoBlue™ which indicated cell death. As the concentrations of NPs tested increased, cell survival decreased. The Au(HAL)NPs were the least cytotoxic with a CC₅₀ of 1.018 mg/ml. SeNPs and AgNPs were more cytotoxic with a CC₅₀ of 0.163 mg/ml and 0.190 mg/ml, respectively. The CC₅₀ of similar NPs tested in macrophages were gathered from the literature (see Table 1) and compared against the CC₅₀ values in A549 cells. The AgNPs and SeNPs were more toxic to macrophages than to A549 cells while the toxicity of Au(HAL)NPs was in a similar range for both types of cells.

3.3. *In vivo* nanoparticle toxicity and hemocyte proliferation

Different concentrations of Au(HAL), Ag, and Se nanoparticles were injected into *G. mellonella* larvae to study their toxicity *in vivo*. The LD₅₀ was calculated and it was found that the NPs exhibit different levels of toxicity (Fig. 2). Au(HAL)NPs were the least toxic with an LD₅₀ of 2023 mg/kg while AgNPs and SeNPs yielded much lower LD₅₀ values (939 mg/kg and 89 mg/kg, respectively) thus demonstrating their high toxicity to the larvae, especially the SeNPs. All LD₅₀ values obtained were compared to LD₅₀ values acquired with murine models which were compiled from the literature (Table 1). The LD₅₀ values obtained with Au(HAL)NPs, AgNPs,

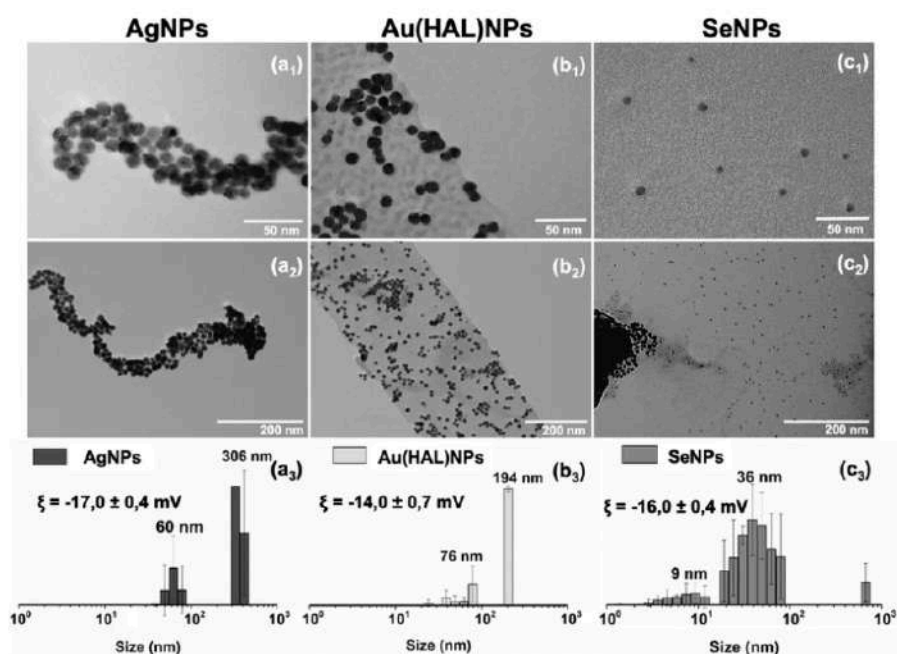


Fig. 1. Morphology, size distribution, and zeta potential of (a) Ag, (b) Au(HAL), and (c) Se nanoparticles used for the toxicological study. Synthesized nanoparticles were characterized using TEM and Nanosizer techniques.

Table 1

Comparison of toxicity values obtained in both *in vitro* and *in vivo* studies. CC₅₀ and LD₅₀ values in gray columns (macrophages and murine models) were obtained from the literature while CC₅₀ and LD₅₀ values in white columns (A549 and *G. mellonella*) were gathered from this study. Asterisk (*) refers to values obtained with non-functionalized AuNPs. ((Arai et al., 2015; Hashimoto et al., 2015; Kim et al., 2009a; Makama et al., 2018; Mannerström et al., 2016; Pinzaru et al., 2018; Pratsinis et al., 2013; Ren et al., 2019; Shahabi et al., 2019; Sonavane et al., 2008; Yazhinprabha and Vaseeharan, 2019; Zhang et al., 2011, 2013).

	<i>In vitro</i> - CC ₅₀ (mg/ml)		<i>In vivo</i> - LD ₅₀ (mg/kg)	
	A549	Macrophages	<i>G. mellonella</i>	Murine models
Au(HAL)NPs	1.018	> 0,1* (Zhang et al., 2011; Hashimoto et al., 2015)	2023	> 1000* (Sonavane et al., 2008; Kim et al., 2009a)
AgNPs	0.190	0.008-0.0384 (Pratsinis et al., 2013; Arai et al., 2015; Mannerström et al., 2016; Makama et al., 2018)	939	> 60 (Xue et al., 2012; Zhang et al., 2013; Pinzaru et al., 2018)
SeNPs	0.163	< 0.01 (Yazhinprabha and Vaseeharan, 2019)	89	> 2,5 (Ren et al., 2019; Shahabi et al., 2019)

and SeNPs in *G. mellonella* were higher than those acquired with murine models.

Nanoparticles are often recognized as foreign materials that can trigger various innate immune responses (Jones and Grainger, 2009). The activation of the innate immune system in *G. mellonella* can cause changes in the number of circulating hemocytes (Browne et al., 2013). For this reason, hemocyte levels were monitored in all larval test groups. All NP concentrations produced an increase in the number of hemocytes present in the larvae when compared to the PBS control group (Fig. 3). However, hemocyte proliferation did not rise with the ascending nanoparticle concentrations as it was expected. For Au(HAL)NPs, hemocyte proliferation was highest (3.6×10^6 cells/ml) with the lowest concentration (50 mg/kg) and the values descended as the NP concentrations increased (Fig. 3a). For AgNPs, the two highest hemocyte proliferation values (2.6×10^6 and 3.1×10^6 cells/ml) were obtained with the two lowest concentrations (50 and 250 mg/kg, respectively) (Fig. 3b). On the other hand, the hemocyte values did not change much among the different concentrations of SeNPs (Fig. 3c).

3.4. *In vivo* nanoparticle distribution

To determine whether the nanoparticles triggered hemocyte-driven internalization, hemocytes were isolated from larvae that were injected with 1250 mg/kg body weight of Au(HAL)NPs and 250 mg/kg body weight of AgNPs and then imaged under a confocal microscope. These concentrations were chosen as they were the concentrations prior to the corresponding LD₅₀. Using light reflection, aggregates of nanoparticles (depicted in cyan) could be observed inside the hemocytes as pointed by the white arrows in Fig. 4. As it can be distinctly observed in the orthogonal views, a single hemocyte was able to internalize more than one nanoparticle simultaneously.

The NPs were not only found within hemocytes, but they were also present in the body of the larvae with the majority being

accumulated in the caudal area (tails) (Fig. 5). Other NP accumulations throughout the rest of the larval body were not clearly seen (Fig. 5a). This event was still seen when the movement of the larvae was partially or fully restricted. To check whether NP accumulation in the tails was due to the peristaltic movement, larvae were injected with 250 mg/kg body weight and 1250 mg/kg body weight of AgNPs and Au(HAL)NPs, respectively. Then, the larvae were kept in three different conditions: without movement (cooled at 15 °C), with limited movement (inside Eppendorf tubes), and without restricted movement (free inside petri dishes). In all three conditions, the NPs accumulated towards the caudal part of the larvae with the majority concentrating in the tails (Fig. 5b).

3.5. Histological analysis

An interesting aspect also worth studying was the histological analysis of larvae injected with NPs. Stained sections of the injected larvae showed that most of the nanoparticles (easily distinguished due to the darkness in bright field optics over the HE staining) were mainly intermingled with lymphatic cells while digestive or Malpighian tubules appeared free of nanoparticles (Fig. 6). In contrast, PBS injected larvae showed no changes in the gross anatomical organ distribution as reported in other studies (Kristensen, 2003) (Fig. 6a). SeNPs showed the largest degree of accumulation leading to the biggest stellate-like aggregates that were particularly abundant in the most caudal portions of the larvae (Fig. 6 b and c). These aggregates largely differ from those observed after Ag- or Au(HAL) NPs injections that showed smaller and dispersed aggregates along the rostrocaudal axis of the larvae (Fig. 6 d and e). Additionally, SeNPs aggregates were often surrounded by large extracellular spaces and numerous lymphoid cells were observed intermingled in these aggregates. However, in some cases, NPs were close to striate muscle fascicles or Malpighi tubes. A similar situation, although less relevant, was observed after AgNPs injection (Fig. 6d) and was not determined after Au(HAL)NPs treatment (Fig. 6e).

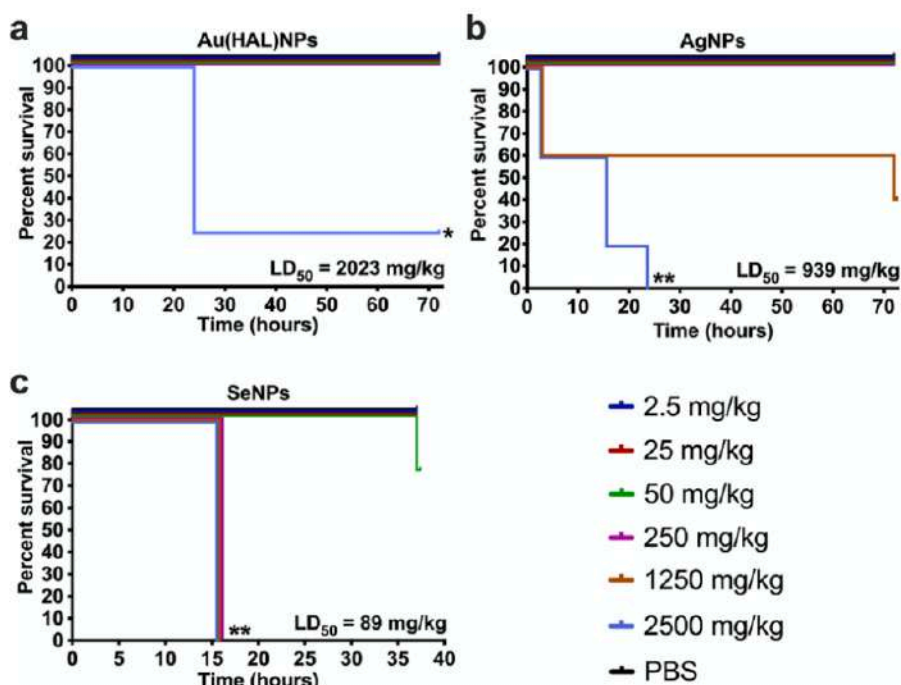


Fig. 2. Kaplan-Meier survival curve of *G. mellonella* larvae injected with various concentrations of (a) Au(HAL), (b) Ag, and (c) Se nanoparticles. As a control, larvae were injected with only PBS. Larval mortality was monitored for 37–72 h post-injection with observations done at 3, 16, 24, 37, 48, and 72 h post-injection. Asterisks: statistically significant difference versus PBS control in a log-rank test (*: p -value <0.05; **: p -value <0.01). The results presented in this figure are representative of the same experiment that was repeated several times, and it yielded identical results every time.

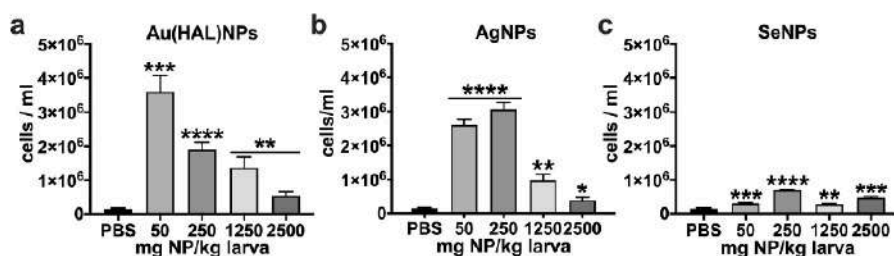


Fig. 3. Effect of (a) Au(HAL), (b) Ag, and (c) Se nanoparticles on hemocyte density in *G. mellonella*. Hemocytes were counted at 72 h post-injection for Au(HAL)NPs and AgNPs and at 37 h post-injection for SeNPs. As a control, hemocytes from larvae injected with only PBS were also counted. Asterisks: statistically significant difference versus PBS control in an unpaired t -test (*: p -value <0.05; **: p -value <0.01; ***: p -value <0.001; ****: p -value <0.0001).

3.6. Behavioral tracking studies

For behavioral studies, toxic concentrations of Au(HAL), Ag, and Se nanoparticles were injected into *G. mellonella* larvae. One hour post-injection, the behavior of the larvae was monitored for 73 s (Fig. 7). The larvae with Au(HAL)NPs had behavioral patterns not significantly different when compared to the control group. On the other hand, the larvae with AgNPs and SeNPs yielded impaired movement with the latter ceasing movement entirely (Fig. 7a). This

was further determined by also measuring the distance traveled by the larvae at the same time point. The larvae with Au(HAL)NPs traveled 10.9 cm which is similar to the 12.4 cm traveled by the control larvae. On the other hand, the larvae with AgNPs and SeNPs had significantly reduced motility (Fig. 7b). The larvae with AgNPs traveled 3.9 cm while the larvae with SeNPs only moved 0.1 cm during the duration of the measurement.

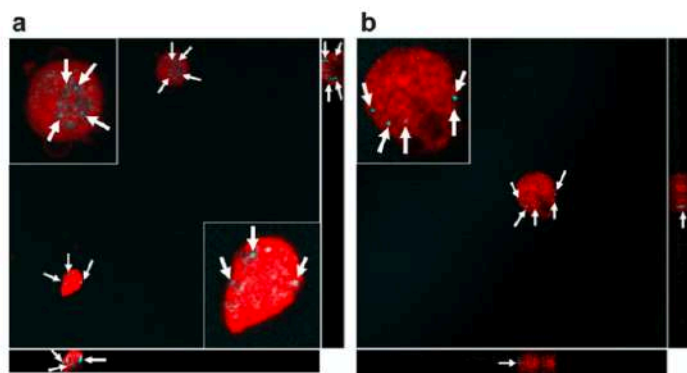


Fig. 4. Confocal laser scanning microscope images of *G. mellonella* hemocytes stained with FM™ 4–64 dye. Larvae were injected with (a) 1250 mg/kg body weight of Au(HAL)NPs and with (b) 250 mg/kg body weight of AgNPs followed by hemocyte extraction 20 h later. Center images are the sum of all stack images and the orthogonal views are seen to the side and underneath. The membrane of the hemocytes stained red while aggregates of NPs were visualized using light reflection and shown in cyan while pointed at by white arrows. (For interpretation of the references to color in this figure legend, the reader is referred to the Web version of this article.)

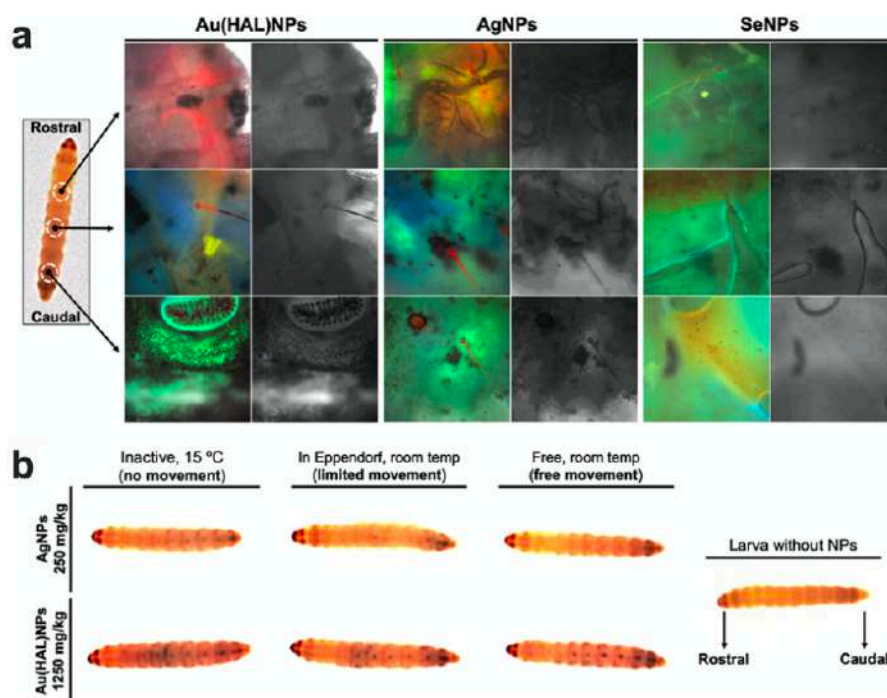


Fig. 5. Distribution of Au(HAL), Ag, and Se nanoparticles throughout the body of *G. mellonella* larvae. (a) To determine NP accumulations, larvae were imaged with a fluorescent microscope at 72 h post-injection for Au(HAL) and Ag nanoparticles and at 37 h post-injection for SeNPs. (b) 250 mg/kg body weight of AgNPs and 1250 mg/kg body weight of Au(HAL)NPs were injected into larvae that were then kept in three different conditions. As a control, a larva without any nanoparticles injected was also imaged. All larvae images are in the same orientation as the control larvae with the head (rostral) facing left and the tail (caudal) on the right.

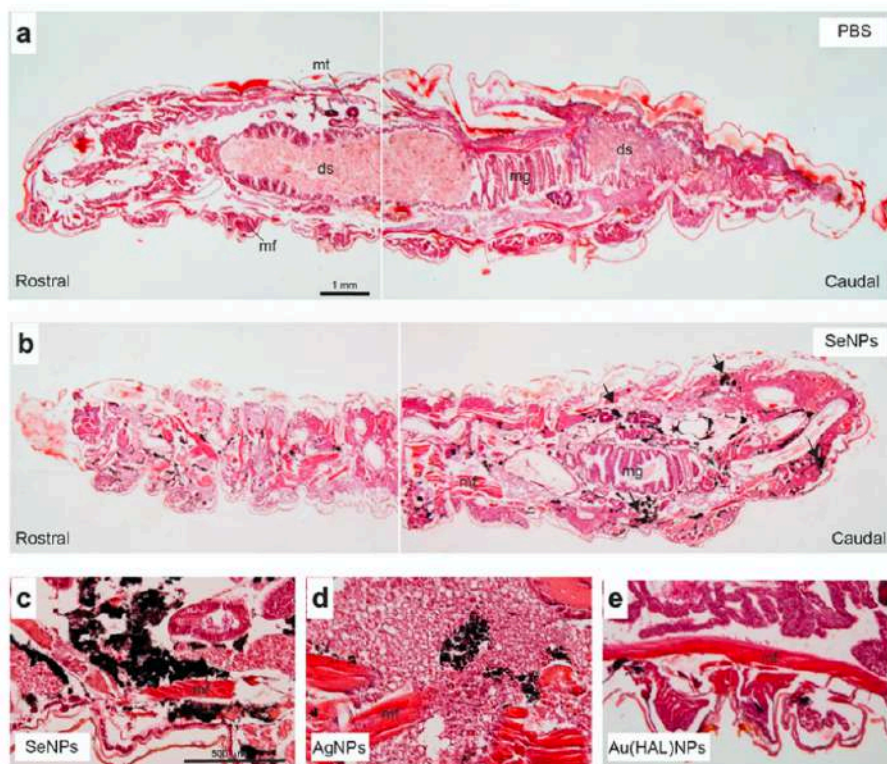


Fig. 6. Histological characterization of the distribution of Se, Ag, and Au(HAL) nanoparticles injected in *G. mellonella* larvae. (a–b) Examples of low power photomicrographs of *G. mellonella* larvae injected with (a) PBS and (b) SeNPs. The rostral and caudal portions of the larvae are indicated. Sections were processed for HE (see Materials and methods section for details). After staining, the digestive system (ds) with the transitional midgut/hindgut transition (mg), groups of muscle fascicles (mf) as well as the Malpighian tubules (mt) can be seen. Also, the intense dark labeling of the injected nanoparticles (i.e., SeNPs) can be seen (arrows in B). (c–e) High power photomicrographs illustrating examples of (c) Se, (d) Ag, and (e) Au(HAL) nanoparticle aggregates after injection. Notice the relevant size of the SeNPs aggregates compared to Ag or Au(HAL) NPs and the large extracellular spaces that surround the aggregates. Most aggregates are located in the lymphoid tissue and can be seen close to other larval structures like the mf or ds in some cases. Scale bars: A = 1 mm pertains to B; C = 500 nm pertains to D–E.

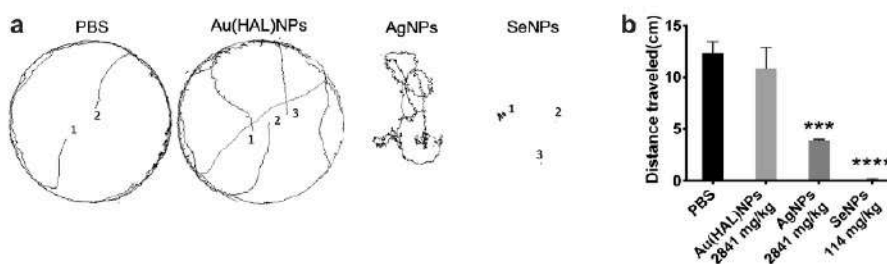


Fig. 7. Tracking of *G. mellonella* larvae movement after NPs injection. (a) Behavioral patterns of larvae injected with different concentrations of NPs and (b) distance traveled by larvae after NPs injection. Larvae were injected with PBS as a control. Asterisks: statistically significant difference versus PBS control in an unpaired t-test (***: p-value < 0.001; ****: p-value < 0.0001).

4. Discussion

As the use of nanoparticles is rapidly expanding, there is a critical need for efficient assays to first determine the potential toxicity of NPs before their use in human applications. Unlike toxicity studies *in vitro*, *in vivo* models tend to simulate the real conditions of the human body more closely. Due to the ethical controversies surrounding murine models, it is currently not possible to justify passing directly from nanomaterial synthesis to toxicity testing in rodents. Therefore, toxicity screenings in non-rodent *in vivo* models are necessary as an intermediate step. In this study, various types of nanoparticles were synthesized to evaluate the efficacy of *G. mellonella* as an *in vivo* toxicological model.

The synthesis of Au(HAL)NPs, AgNPs, and SeNPs resulted in small yet stable spherical particles which were found individually and for some of them, in aggregates. Small-sized nanomaterials have a higher surface area that leads to a higher reactivity compared to their bulk materials and this can be associated with possible toxic effects (Raboli et al., 2011). Besides size, the toxicity of NPs is also dependent on their shape, stability, agglomeration degree, surface coating, functionalization, and purity (Luque-Garcia et al., 2013). Due to the increasing applications of nanoparticles, numerous studies have been carried out to better understand their toxicity. Here, the toxicity of different nanoparticles was tested both *in vitro* and *in vivo*. Various concentrations of NPs were tested in A549 cells and in *G. mellonella* larvae to determine their toxicity by defining the CC₅₀ and LD₅₀ of each type of nanoparticle. To see how our *in vivo* model compared to already published data, LD₅₀ values were gathered from literature in which similar NPs were studied (Table 1). The A549 results were compared to data obtained in macrophages to determine whether toxicity varies between cancerous epithelial lung cells and macrophage cells. All types of nanoparticles tested were more toxic to macrophages than to A549 cells. This could be due to the macrophages' ability to intake nanoparticles more efficiently when compared to A549 cells (Kuhn et al., 2014). Cytotoxic effects of NPs in culture media not only depend on the number of nanoparticles internalized by cells but also on other factors such as incubation times, concentrations tested, and, clearly, the type of cell lines used (Mukherjee et al., 2012; Luque-Garcia et al., 2013). Furthermore, the same NPs can have inconsistent toxicity results when tested in different cell lines. In one study, the same dose of AuNPs was toxic to A549 cells but not to BHK21 and HepG2 cells (Patra et al., 2007). In another study, SeNPs inhibited the proliferation of A375, CNE2, HepG2, and MCF-7 cancer cells but were much less cytotoxic to normal Hs68 human fibroblasts (Chen et al., 2008). For these reasons, *in vitro* cytotoxicity assays are not the most optimal method to predict the toxicity of NPs as they are extremely dependent on the cell line used. Based on the literature, toxicity assays in murine models are oftentimes carried out by administering very few doses of nanoparticles to establish tissue accumulation and the levels of various hematological and biochemical markers. These assays are not done to determine LD₅₀ values, most probably due to ethical and monetary motives. For this reason, it would be greatly advantageous to first define the LD₅₀ doses in a model that screens a high number of samples and concentrations to reduce the number of NPs and mammals needed for testing. All of these conditions can be accomplished with the *G. mellonella in vivo* model. The LD₅₀ values obtained with *G. mellonella* larvae are more similar to the values obtained with murine models when compared to *in vitro* models (Table 1). Therefore, *G. mellonella* shows to be a reliable and efficient non-rodent model for initial toxicity screenings of various nanoparticles over traditional cell assays.

To better understand the interactions between NPs and cells and

other living organisms, it is important to determine whether NPs are taken up by cells and how they localize within cells and tissues. One study showed that NPs can quickly enter cells and disperse through the cytoplasm and nucleus which led to cytotoxicity that was more pronounced in the cells that had NPs within the nucleus (Lovrić et al., 2005). Another study revealed that NPs were found inside macrophages' lysosomes and mitochondria which was also related to higher cytotoxicity over time (Clift et al., 2011). These findings suggest that the intracellular fate of NPs could be directly linked to their toxicity. One of the proposed uptake mechanisms of NPs into cells is endocytosis (Dobrovolskaia and McNeil, 2007; Kettler et al., 2014). This process is defined as the uptake of extracellular material into eukaryotic cells by engulfing it with their cell membrane. Several types of endocytosis exist, and the type employed by the cell depends on the particle being internalized (Kuhn et al., 2014). Macrophages are known for their ability to rapidly ingest and efficiently remove foreign particles (Juliano, 1988; Gustafson et al., 2015). *In vitro* studies have shown that NPs are taken up by macrophages via phagocytosis and other endocytosis pathways (Shukla et al., 2005; Krpetić et al., 2010; Kuhn et al., 2014). For this reason, macrophages are a suitable cellular model to study the toxicity effects of NPs. Due to the limitations of *in vitro* studies, the *G. mellonella* model offers a more valuable alternative. *G. mellonella* larvae have an innate immune system, which consists of cellular and humoral responses, that closely resembles the innate immune system in mammals. Cellular immune responses are mediated by hemocytes and include phagocytosis, nodulation, and encapsulation while humoral immune responses include melanization and synthesis of antimicrobial peptides. Hemocytes present in the hemolymph of *G. mellonella* larvae are similar to macrophages found in mammals. These cells can recognize foreign intruders by identifying humoral immune effectors or through direct interaction of pathogen recognition proteins with pathogen-associated molecular patterns (Cutuli et al., 2019).

The similarities between the cellular immune system of both *G. mellonella* and mammals suggest that hemocyte density could be a good indicator of toxicity. Aneja et al. demonstrated that triazole analogs were not toxic to *G. mellonella* larvae as seen by the lack of hemocyte proliferation (Aneja et al., 2018). Maguire et al. administered potassium nitrate to *G. mellonella* larvae and acute effects were evidenced by a significant increase in the number of circulating hemocytes (Maguire et al., 2017). In this study, hemocyte density was quantified in all groups of larvae injected with the different nanoparticles tested. As seen in Fig. 3, significant hemocyte proliferation was seen in all of the concentrations and with all of the nanoparticles tested. For both Au(HAL)NPs and AgNPs, the proliferation was highest with the lowest concentrations tested while the proliferation decreased as the concentrations increased (Fig. 3 a and b). This could be due to hormesis which is characterized by stimulatory effects produced by low doses of potentially toxic compounds (Stebbing, 1982). Jiao et al. found that non-cytotoxic concentrations of AgNPs led to an accelerated proliferation of HepG2 cells due to hormesis effects (Jiao et al., 2014). This acceleration was also seen with the lowest concentration of Au(HAL)NPs tested in the present cytotoxicity studies. Therefore, hemocyte proliferation could also be boosted by exposure of the larvae to low doses of AgNPs and Au(HAL)NPs. In the case of functionalized AuNPs, the immunomodulatory effects seen could be further explained by the surface functionalization. AuNPs functionalized with amino acids are cationic, so they can be easily deposited by corona proteins and then recognized by phagocytic or other clearing systems (Moyano et al., 2016). Another pattern seen with the results was that as the concentrations of the Au(HAL) and Ag nanoparticles increased, the hemocyte density decreased. This is

most likely due to potential damage of hemopoietic organs in the larvae due to NP toxicity (Eskin et al., 2019). For SeNPs, the hemocyte density remained more or less constant throughout all of the concentrations tested (Fig. 3c). SeNPs were the most toxic to the larvae so the absence of hemocyte proliferation could be due to increased cell death as a result of the high toxicity.

To further demonstrate the similarities in the immune responses between *G. mellonella* and mammals, NP internalization within cells was determined using confocal microscopy (Fig. 4). The obtained images clearly show that hemocytes were able to internalize Au(HAL) and Ag nanoparticles. Although the exact mechanism of internalization cannot be determined by confocal microscopy alone, it demonstrates that hemocytes are able to identify NPs as foreign and thus trigger the larval immune response as it would occur in mammals. While hemocyte proliferation is a clear indicator of an activated immune system, it is not a strong indicator of the degree of toxicity being experienced by the larvae. This would be better determined by combining hemocyte density measurements along with evaluating changes in hemocyte morphology, proteomics, enzymatic activity, and histology, among others.

Nanoparticle distribution was also examined in the whole larvae. Microscopy images revealed that the NPs were located in the caudal part of the larvae with the majority of the NPs accumulating at the tails (Figs. 5 and 6). This event was still seen when the movement of the larvae was partially or fully restricted (Fig. 5b) thus suggesting that the NP accumulation is not due to the peristaltic motility movement of the worm. Although the movement was limited, NPs could still possibly move through the hemolymph due to contractions of the larval abdominal spiracles during respiration (Wasserthal, 1996). Another unknown mechanism could be further responsible for the accumulation of large quantities of NPs in the caudal part of the larvae, but more studies are needed to better understand this phenomenon. Histological findings confirmed that the NPs were found in aggregates in the most caudal part of the larvae (Fig. 6). In terms of aggregates and the appearance of extracellular spaces, it seems that the presence (in the case of SeNPs) of i) an enlarged accumulation of lymphoid/hemocytes cells after SeNPs injection compared to AgNPs and Au(HAL)NPs or ii) increased cell death is due to toxic activity. AgNPs were observed in the same locations as the SeNPs; however, the size of the aggregates is smaller and the size of the extracellular space around these aggregates is also smaller. Thus, cell or larval death could be observed at higher survival times as it occurred with the LD₅₀ experiments. This could also be the case for the AgNPs that were only present in the hemolymph. As the larvae were killed 1-h post-injection, more time might be needed to see tissue damage like the one seen with SeNPs. Regardless, 1 h was enough for the larvae to undergo a faster color change after injection with SeNPs compared to the other NPs. A drawback of HE is that dying cells cannot be fully characterized and only gross anatomical changes can be clearly ascertained. For this reason, histological findings should be combined with other studies. In this case, the histological results corroborate the results obtained with the hemocyte density experiments as well as the microscopy studies.

Finally, another way to study the toxicity of NPs in *G. mellonella* is to examine the behavior of the larvae after NP inoculation. Changes in movement and behavior were seen in *Drosophila melanogaster* and *Danio rerio*, respectively, after exposure to AgNPs (Armstrong et al., 2013; Krishnaraj et al., 2016). The NPs in both studies were administered through feeding which does not truly mimic the typical administration route for drug delivery. In contrast, the injection of NPs into *G. mellonella* larvae can be easily

accomplished. In this study, the behavior of larvae injected with toxic concentrations of NPs was assessed (Fig. 7). The larvae injected with Au(HAL)NPs maintained a normal behavior similar to the larvae injected with PBS. This result was expected as this NP concentration was lethal to the larvae after several hours post-injection. On the other hand, the toxicity of AgNPs and SeNPs was soon witnessed by the color changes of the larvae from cream to dark accompanied with significantly reduced motility. SeNPs were the most toxic to the larvae as evidenced by the complete lack of movement soon after injection. These results further validate the toxicity effects observed with all of the experiments mentioned above.

The consistency in all of the results obtained with the different experiments performed to study NP toxicity using *G. mellonella* demonstrates the significant utility of this animal model. With this alternative model, toxicity screenings of various NPs can be performed economically and conveniently, and the results obtained will be more reliable than traditional *in vitro* models without any ethical limitations. *G. mellonella* can be used as a bridge between cytotoxicity and *in vivo* murine assays, thus allowing for more accurate predictions of the toxicity effects brought upon by nanoparticles.

Credit author statement

Laura Moya-Andérico: Conceptualization, Methodology, Validation, Investigation, Writing – original draft, Writing – review & editing. Marija Vukomanovic: Conceptualization, Methodology, Validation, Investigation, Writing – original draft, Writing – review & editing. Maria del Mar Cendra: Methodology, Investigation, Writing – review & editing. Miriam Segura-Feliu: Methodology, Investigation, Writing – review & editing. – Vanessa Gil: Methodology, Investigation, Writing – review & editing. José A. del Río: Conceptualization, Investigation, Resources, Writing – original draft, Writing – review & editing, Supervision, Funding acquisition. Eduard Torrents: Conceptualization, Investigation, Resources, Writing – original draft, Writing – review & editing, Supervision, Funding acquisition.

Declaration of competing interest

The authors declare that they have no known competing financial interests or personal relationships that could have appeared to influence the work reported in this paper.

Acknowledgments

This work was supported in part by grants from the La Caixa Foundation, Ministerio de Ciencia, Innovación y Universidades (MCIU), Agencia Estatal de Investigación (AEI) and Fondo Europeo de Desarrollo Regional (FEDER) (RTI2018-098573-B-I00) to ET and RTI2018-099773-B-I00 to JADR, the Catalan Cystic Fibrosis association, the CERCA program/Generalitat de Catalunya (2017 SGR01079 to ET and 2017 SGR648 to JADR). LMA is thankful to the Generalitat de Catalunya for its financial support through the FI program (2019FI-B2-00197). MV was supported by the grant from European Commission under Horizon 2020's Marie Skłodowska-Curie Actions COFUND scheme (Grant Agreement no. 712754), Severo Ochoa program of the Spanish Ministry of Science and Competitiveness (Grant SEV-2014-0425 (2015–2019)) and the Slovenian Research Agency (ARRS) (Grants J2-8169and N2-0150). VG was supported by from "la Caixa" Foundation (ID 100010434) under the agreement LCF/PR/HR19/52160007.

References

- Ahamed, M., Alsahli, M.S., Siddiqui, M.K., 2010. Silver nanoparticle applications and human health. *Clin. Chim. Acta* 411, 1841–1848.
- Akilany, A.M., Murphy, C.J., 2010. Toxicity and cellular uptake of gold nanoparticles: what we have learned so far? *J. Nano Res.* 12, 2313–2333.
- Allegre, E., Tibbitt, R.W., Carter, J., Champion, O.L., 2018. *Galleria mellonella* larvae allow the discrimination of toxic and non-toxic chemicals. *Chemosphere* 198, 469–472.
- Aneja, B., Azam, M., Alam, S., Perwez, A., Maguire, R., Yadava, U., Kavanagh, K., Daniluc, C.G., Rizvi, M.M.A., Haq, Q.M.R., Abid, M., 2018. Natural product-based 1,2,3-triazole/sulfonate analogues as potential chemotherapeutic agents for bacterial infections. *ACS Omega* 3, 6912–6930.
- Arai, Y., Miyayama, T., Hirano, S., 2015. Difference in the toxicity mechanism between ion and nanoparticle forms of silver in the mouse lung and in macrophages. *Toxicology* 328, 84–92.
- Armstrong, N., Ramanorothy, M., Lyon, D., Jones, K., Duttaroy, A., 2013. Mechanism of silver nanoparticles action on insect pigmentation reveals intervention of copper homeostasis. *PLoS One* 8, e53186.
- Bartle, E.A., 2013. Principles of Toxicology Testing, 2 ed. CRC Press, Boca Raton.
- Bouwmeester, H., Brandhoff, P., Marvin, H.J.P., Weigel, S., Peters, R.J.B., 2014. State of the safety assessment and current use of nanomaterials in food and food production. *Trends Food Sci. Technol.* 40, 200–210.
- Bronzetti, G., Cini, M., Andreoli, E., Galtavuturo, L., Fanunzio, M., Croce, C.D., 2001. Protective effects of vitamins and selenium compounds in yeast. *Mutat. Res.* 496, 105–115.
- Browne, N., Heelan, M., Kavanagh, K., 2013. An analysis of the structural and functional similarities of insect hemocytes and mammalian phagocytes. *Virulence* 4, 597–603.
- Chaiyuanakittit, P., Lawanprasert, S., Roytrakul, S., Aueviriyavit, S., Phummiratch, D., Kuitthong, K., Chanvorachote, P., Maniratanachote, R., 2013. Silver nanoparticles induce toxicity in A549 cells via ROS-dependent and ROS-independent pathways. *Toxicol. Vitro* 27, 330–338.
- Champion, O.L., Wagley, S., Tibbitt, R.W., 2015. *Galleria mellonella* as a model host for microbiological and toxin research. *Virulence* 7, 840–845.
- Chen, T., Wong, Y.S., Zheng, W., Bai, Y., Huang, L., 2008. Selenium nanoparticles fabricated in *Undaria pinnatifida* polysaccharide solutions induce mitochondria-mediated apoptosis in A375 human melanoma cells. *Colloids Surf. B Biointerfaces* 67, 26–31.
- Chen, Y.S., Hung, Y.C., Liu, L., Huang, G.S., 2009. Assessment of the in vivo toxicity of gold nanoparticles. *Nanoscale Res Lett* 4, 858–864.
- Cliff, M.J., Brandenberger, C., Rothen-Rutishauser, B., Brown, D.M., Stone, V., 2011. The uptake and intracellular fate of a series of different surface coated quantum dots in vitro. *Toxicology* 285, 58–68.
- Cutuli, M.A., Petronio Petronio, G., Vergalito, F., Magnifico, L., Pietrangelo, L., Venditti, N., Di Marco, R., 2019. *Galleria mellonella* as a consolidated in vivo model hosts: new developments in antibacterial strategies and novel drug testing. *Virulence* 10, 527–541.
- De Jong, W.H., Hagens, W.J., Krystek, P., Burger, M.C., Sips, A.J., Geertsma, R.E., 2008. Particle size-dependent organ distribution of gold nanoparticles after intravenous administration. *Biomaterials* 29, 1912–1919.
- De Jong, W.H., Van Der Ven, L.T., Sleijffers, A., Park, M.V., Jansen, E.H., Van Loveren, H., Vandebriel, R.J., 2013. Systemic and immunotoxicity of silver nanoparticles in an intravenous 28 days repeated dose toxicity study in rats. *Biomaterials* 34, 8333–8343.
- Desbois, A.P., Coote, P.J., 2012. Utility of greater wax moth larva (*Galleria mellonella*) for evaluating the toxicity and efficacy of new antimicrobial agents. *Adv. Appl. Microbiol.* 78, 25–53.
- Dobrovol'skaia, M.A., McNeil, S.E., 2007. Immunological properties of engineered nanomaterials. *Nat. Nanotechnol.* 2, 469–478.
- Dolan, N., Gavin, D.P., Eshwika, A., Kavanagh, K., McGinley, J., Stephens, J.C., 2016. Synthesis, antibacterial and anti-MRSA activity, in vivo toxicity and a structure-activity relationship study of a quinoline thiourea. *Bioorg. Med. Chem. Lett* 26, 630–635.
- Eskin, A., Ozturk, S., K or kc u, M., 2019. Determination of the acute toxic effects of zinc oxide nanoparticles (ZnO NPs) in total hemocytes counts of *Galleria mellonella* (Lepidoptera: Pyralidae) with two different methods. *Ecotoxicology* 28, 801–808.
- Evans, S.O., Khairuddin, P.F., Jameson, M.B., 2017. Optimising selenium for modulation of cancer treatments. *Anticancer Res.* 37, 6497–6509.
- Fernandes, A.P., Gandin, V., 2015. Selenium compounds as therapeutic agents in cancer. *Biochim. Biophys. Acta* 1850, 1642–1660.
- Finkelstein, A.E., Walz, D.T., Batista, V., Mizraji, M., Roisman, F., Misher, A., 1976. Auranofin. New oral gold compound for treatment of rheumatoid arthritis. *Ann. Rheum. Dis.* 35, 251–257.
- Gangadot, S., Dinev, I., Willson, N.L., Moore, R.J., Chapman, J., Stanley, D., 2020. Nanoparticles of selenium as high bioavailable and non-toxic supplement alternatives for broiler chickens. *Environ. Sci. Pollut. Res.* 27, 16159–16166.
- Goodman, C.M., McCusker, C.D., Yilmaz, T., Rotello, V.M., 2004. Toxicity of gold nanoparticles functionalized with cationic and anionic side chains. *Bioconjugate Chem.* 15, 897–900.
- Gustafson, H.H., Holt-Casper, D., Grainger, D.W., Ghandehari, H., 2015. Nanoparticle uptake: the phagocyte problem. *Nano Today* 10, 487–510.
- Hashimoto, M., Sasaki, J.I., Yamaguchi, S., Kawai, K., Kawakami, H., Iwasaki, Y., Imazato, S., 2015. Gold nanoparticles inhibit matrix metalloproteinases without cytotoxicity. *J. Dent. Res.* 94, 1085–1091.
- Hsin, Y.H., Chen, C.F., Huang, S., Shih, T.S., Lai, P.S., Chueh, P.J., 2008. The apoptotic effect of nanosilver is mediated by a ROS- and JNK-dependent mechanism involving the mitochondrial pathway in NIH3T3 cells. *Toxicol. Lett.* 179, 130–139.
- Ignasiak, K., Maxwell, A., 2017. *Galleria mellonella* (greater wax moth) larvae as a model for antibiotic susceptibility testing and acute toxicity trials. *BMC Res. Notes* 10, 428.
- Jevtic, M., Mitric, M., Skapin, S., Jancar, B., Ignjatovic, N., Uskokovic, D., 2008. Crystal structure of hydroxyapatite nanorods synthesized by sonochemical homogeneous precipitation. *Cryst. Growth Des.* 8, 2217–2222.
- Jia, H.Y., Liu, Y., Zhang, X.J., Han, L., Du, L.B., Tian, Q., Xu, Y.C., 2009. Potential oxidative stress of gold nanoparticles by induced-NO releasing in serum. *J. Am. Chem. Soc.* 131, 40–41.
- Jiao, Z.H., Li, M., Feng, Y.X., Shi, J.C., Zhang, J., Shao, B., 2014. Hormesis effects of silver nanoparticles at non-cytotoxic doses to human hepatoma cells. *PLoS One* 9, e102564.
- Jones, C.F., Grainger, D.W., 2009. In vitro assessments of nanomaterial toxicity. *Adv. Drug Deliv. Rev.* 61, 438–456.
- Juliano, R.L., 1988. Factors affecting the clearance kinetics and tissue distribution of liposomes, microspheres and emulsions. *Adv. Drug Deliv. Rev.* 2, 31–54.
- Junqueira, J.C., 2012. *Galleria mellonella* as a model host for human pathogens: recent studies and new perspectives. *Virulence* 3, 474–476.
- Kettler, K., Veltman, K., van de Meent, D., van Wezel, A., Hendriks, A.J., 2014. Cellular uptake of nanoparticles as determined by particle properties, experimental conditions, and cell type. *Environ. Toxicol. Chem.* 33, 481–492.
- Khoshtehnevis, K., Daneshpour, M., Barkhi, M., Gholami, M., Samadian, H., Maleki, H., 2018. The promising potentials of capped gold nanoparticles for drug delivery systems. *J. Drug Target.* 26, 525–532.
- Kim, J.H., Kim, K.W., Kim, M.H., Yu, Y.S., 2009a. Intravenously administered gold nanoparticles pass through the blood-retinal barrier depending on the particle size, and induce no retinal toxicity. *Nanotechnology* 20, 505101.
- Kim, S., Choi, J.E., Choi, J., Chung, K.H., Park, K., Yi, J., Ryu, D.Y., 2009b. Oxidative stress-dependent toxicity of silver nanoparticles in human hepatoma cells. *Toxicol. Vitro* 23, 1076–1084.
- Kim, Y.S., Song, M.Y., Park, J.D., Song, K.S., Ryu, H.R., Chung, Y.H., Chang, H.K., Lee, J.H., Oh, K.H., Kelman, B.J., Hwang, I.K., Yu, I.J., 2010. Subchronic oral toxicity of silver nanoparticles. *Part. Fibre Toxicol.* 7, 20.
- Krishnaraj, C., Harper, S.L., Yun, S.I., 2016. In vivo toxicological assessment of biologically synthesized silver nanoparticles in adult Zebrafish (*Danio rerio*). *J. Hazard Mater.* 301, 480–491.
- Kristensen, N., 2003. *Arthropoda: insecta*. In: Kristensen, N. (Ed.), *Lepidoptera: Moths and Butterflies*. *Handbuch der Zoologie*, vol. 4. De Gruyter.
- Kretzic, Z., Porta, F., Caneva, E., Dal Santo, V., Scarf, G., 2010. Phagocytosis of biocompatible gold nanoparticles. *Langmuir* 26, 14799–14805.
- Kuhn, D.A., Vanhecke, D., Michen, B., Blank, F., Gehr, P., Petri-Fink, A., Rothen-Rutishauser, B., 2014. Different endocytic uptake mechanisms for nanoparticles in epithelial cells and macrophages. *Biochim. Biophys. Acta* 1843, 1625–1636.
- Letavayova, L., Vlasakova, D., Spallholz, J.E., Brozmanova, J., Chovanec, M., 2008. Toxicity and mutagenicity of selenium compounds in *Saccharomyces cerevisiae*. *Mutat. Res.* 638, 1–10.
- Leung, M.C., Williams, P.L., Benedetto, A., Au, C., Heimcke, K.J., Aschner, M., Meyer, J.N., 2008. *Cuenorhabditis elegans*: an emerging model in biomedical and environmental toxicology. *Toxicol. Sci.* 106, 5–28.
- Lovric, J., Bazzi, H.S., Cui, Y., Fortin, G.R., Winnik, F.M., Maysinger, D., 2005. Differences in subcellular distribution and toxicity of green and red emitting CdTe quantum dots. *J. Mol. Med. (Berl.)* 83, 377–385.
- Luque-Garc a, J.L., Sanchez-D az, R., Lopez-Heras, I., Martin, P., Camara, C., 2013. Bioanalytical strategies for in-vitro and in-vivo evaluation of the toxicity induced by metallic nanoparticles. *Trends Anal. Chem.* 43, 254–268.
- Maguire, R., Duggan, O., Kavanagh, K., 2016. Evaluation of *Galleria mellonella* larvae as an in vivo model for assessing the relative toxicity of food preservative agents. *Cell Biol. Toxicol.* 32, 209–216.
- Maguire, R., Kunc, M., Hyrsl, P., Kavanagh, K., 2017. Analysis of the acute response of *Galleria mellonella* larvae to potassium nitrate. *Comp. Biochem. Physiol. C Toxicol. Pharmacol.* 195, 44–51.
- Makama, S., Klot, S.K., Piella, J., van den Berg, H., de Ruijter, N.C.A., Puentes, V.F., Rietjens, I.M.C.M., van den Brink, N.W., 2018. Effects of systematic variation in size and surface coating of silver nanoparticles on their in vitro toxicity to macrophage RAW 264.7 cells. *Toxicol. Sci.* 162, 79–88.
- Mannerstr om, M., Zou, J., Toimela, T., Pyykk o, I., Heinonen, T., 2016. The applicability of conventional cytotoxicity assays to predict safety/toxicity of mesoporous silica nanoparticles, silver and gold nanoparticles and multi-walled carbon nanotubes. *Toxicol. Vitro* 37, 113–120.
- Megaw, J., Thompson, T.P., Lafferty, R.A., Gilmore, B.F., 2015. *Galleria mellonella* as a novel in vivo model for assessment of the toxicity of 1-alkyl-3-methylimidazolium chloride ionic liquids. *Chemosphere* 139, 197–201.
- Mijnendonckx, K., Leys, N., Mahillon, J., Silver, S., Van Hout, R., 2013. Antimicrobial silver: uses, toxicity and potential for resistance. *Biomaterials* 26, 609–621.
- Moya-Andr ico, L., Admella, J., Torrents, E., 2020. A clearing protocol for *Galleria mellonella* larvae: visualization of internalized fluorescent nanoparticles. *N. Biotechnol.* 60, 20–26.
- Moyano, D.F., Liu, Y., Ayaz, F., Hou, S., Puangploy, P., Duncan, B., Osborne, B.A.,

- Rotello, V.M., 2016. Immunomodulatory effects of coated gold nanoparticles in LPS-stimulated. *Inside Chem.* 1, 320–327.
- Mukherjee, S.G., O'Clonadh, N., Casey, A., Chambers, G., 2012. Comparative in vitro cytotoxicity study of silver nanoparticle on two mammalian cell lines. *Toxicol. Vitro* 26, 238–251.
- Patra, H.K., Banerjee, S., Chaudhuri, U., Lahiri, P., Dasgupta, A.K., 2007. Cell selective response to gold nanoparticles. *Nanomedicine* 3, 111–119.
- Pinzaru, I., Coricovac, D., Dehelean, C., Moacă, E.A., Mloc, M., Baderca, F., Sizemore, I., Brittle, S., Marti, D., Galina, C.D., Tsatsakis, A.M., Soica, C., 2018. Stable PEG-coated silver nanoparticles – a comprehensive toxicological profile. *Food Chem. Toxicol.* 111, 546–556.
- Pratsinis, A., Hervella, P., Leroux, J.C., Pratsinis, S.E., Sotiropoulos, G.A., 2013. Toxicity of silver nanoparticles in macrophages. *Small* 9, 2576–2584.
- Rabouli, V., Thomassen, L.C., Uwambayinema, F., Martens, J.A., Lison, D., 2011. The cytotoxic activity of amorphous silica nanoparticles is mainly influenced by surface area and not by aggregation. *Toxicol. Lett.* 206, 197–203.
- Ramarao, N., Nielsen-Leroux, C., Lereclus, D., 2012. The insect *Galleria mellonella* as a powerful infection model to investigate bacterial pathogenesis. *JoVE*, e4392.
- Rand, M.D., Montgomery, S.L., Prince, L., Vorobjikina, D., 2014. Developmental toxicity assays using the *Drosophila* model. *Curr Protoc Toxicol* 59, 12 11–20.
- Rayman, M.P., 2012. Selenium and human health. *Lancet* 379, 1256–1268.
- Recordati, C., De Maglie, M., Bianchessi, S., Agentiere, S., Cella, C., Mattiello, S., Cubadda, F., Aureli, F., D'Amato, M., Raggi, A., Lenardi, C., Milani, P., Scanziani, E., 2016. Tissue distribution and acute toxicity of silver after single intravenous administration in mice: nano-specific and size-dependent effects. *Part. Fibre Toxicol.* 13, 12.
- Ren, S.X., Zhan, B., Lin, Y., Ma, D.S., Yan, H., 2019. Selenium nanoparticles dispersed in phytochemical exert anti-inflammatory activity by modulating catalase, GPx1, and COX-2 gene expression in a rheumatoid arthritis rat model. *Med. Sci. Mon. Int. Med. J. Exp. Clin. Res.* 25, 991–1000.
- Rinna, A., Magdolenova, Z., Hudecova, A., Kruszewski, M., Refsnes, M., Dusinska, M., 2015. Effect of silver nanoparticles on mitogen-activated protein kinases activation: role of reactive oxygen species and implication in DNA damage. *Mutagenesis* 30, 59–66.
- Rohn, L., Marschall, T.A., Kneppf, N., Jensen, K.B., Aschner, M., Tuck, S., Kuehnelt, D., Schwerdtle, T., Bornhorst, J., 2018. Selenium species-dependent toxicity, bioavailability and metabolic transformations in *Caenorhabditis elegans*. *Metalloids* 10, 818–827.
- Schluesener, J.K., Schluesener, H.J., 2013. Nanosilver: application and novel aspects of toxicology. *Arch. Toxicol.* 87, 569–576.
- Shahabi, R., Anissian, A., Javadmoosavi, S.A., Nasirinezhad, F., 2019. Protective and anti-inflammatory effect of selenium nano-particles against bleomycin-induced pulmonary injury in male rats. *Drug Chem. Toxicol.* 1–9.
- Shrivastava, R., Kushwaha, P., Bhuila, Y.C., Flora, S., 2016. Oxidative stress following exposure to silver and gold nanoparticles in mice. *Toxicol. Ind. Health* 32, 1391–1404.
- Shukla, R., Bansal, V., Chaudhary, M., Basu, A., Bhonde, R.R., Sastry, M., 2005. Biocompatibility of gold nanoparticles and their endocytotic fate inside the cellular compartment: a microscopic overview. *Langmuir* 21, 10644–10654.
- Sonavane, G., Tomoda, K., Makino, K., 2008. Biodistribution of colloidal gold nanoparticles after intravenous administration: effect of particle size. *Colloids Surf. B Biointerfaces* 66, 274–280.
- Souza, T.A., Franchi, L.P., Rosa, L.R., da Veiga, M.A., Takahashi, C.S., 2015. Cytotoxicity and genotoxicity of silver nanoparticles of different sizes in CHO-K1 and CHO-XRS5 cell lines. *Mutat. Res. Genet. Toxicol. Environ. Mutagen* 795, 70–83.
- Stebbing, A.R., 1982. Hormesis—the stimulation of growth by low levels of inhibitors. *Sci. Total Environ.* 22, 213–234.
- Tang, J., Xiong, L., Wang, S., Wang, J., Liu, L., Li, J., Yuan, F., Xi, T., 2009. Distribution, translocation and accumulation of silver nanoparticles in rats. *J. Nanosci. Nanotechnol.* 9, 4924–4932.
- Thomas, R.J., Hamblin, K.A., Armstrong, S.J., Muller, C.M., Bokori-Brown, M., Goldman, S., Atkins, H.S., Titball, K.W., 2013. *Galleria mellonella* as a model system to test the pharmacokinetics and efficacy of antibiotics against *Burkholderia pseudomallei*. *Int. J. Antimicrob. Agents* 41, 330–336.
- Valdiglesias, V., Pasaro, E., Mendez, J., Laffon, B., 2010. In vitro evaluation of selenium genotoxic, cytotoxic, and protective effects: a review. *Arch. Toxicol.* 84, 337–351.
- Vance, M.E., Kuiken, T., Vejerano, E.P., McGinnis, S.P., Hochella Jr., M.F., Rejeski, D., Hull, M.S., 2015. Nanotechnology in the real world: redeveloping the nanomaterial consumer products inventory. *Beilstein J. Nanotechnol.* 6, 1769–1780.
- Vukomanović, M., Logar, M., Skapin, S.D., Suvorov, D., 2014. Hydroxyapatite/gold/arginine: designing the structure to create antibacterial activity. *J. Mater. Chem. B* 2, 1557–1564.
- Wasserthal, L.T., 1996. Interaction of circulation and tracheal ventilation in holometabolous insects. In: Evans, P.D. (Ed.), *Advances in Insect Physiology*. Academic Press, pp. 297–351.
- Wojda, L., 2017. Immunity of the greater wax moth *Galleria mellonella*. *Insect Sci.* 24, 342–357.
- Xue, Y., Zhang, S., Huang, Y., Zhang, T., Liu, X., Hu, Y., Zhang, Z., Tang, M., 2012. Acute toxic effects and gender-related biokinetics of silver nanoparticles following an intravenous injection in mice. *J. Appl. Toxicol.* 32, 890–899.
- Yan, L., Spallholz, J.E., 1993. Generation of reactive oxygen species from the reaction of selenium compounds with thiols and mammary tumor cells. *Biochem. Pharmacol.* 45, 429–437.
- Yazhiniprabha, M., Vaseeharan, B., 2019. In vitro and in vivo toxicity assessment of selenium nanoparticles with significant larvicidal and bacteriostatic properties. *Mater Sci Eng C Mater Biol Appl* 103, 109763.
- Zhang, Q., Hitchins, V.M., Schrand, A.M., Hussain, S.M., Goering, P.L., 2011. Uptake of gold nanoparticles in murine macrophage cells without cytotoxicity or production of pro-inflammatory mediators. *Nanotoxicology* 5, 284–295.
- Zhang, X.D., Wu, H.Y., Wu, D., Wang, Y.Y., Chang, J.H., Zhai, Z.B., Meng, A.M., Liu, P.X., Zhang, L.A., Fan, F.Y., 2010. Toxicologic effects of gold nanoparticles in vivo by different administration routes. *Int. J. Nanomed.* 5, 771–781.
- Zhang, Y., Ferguson, S.A., Watanabe, F., Jones, Y., Xu, Y., Biris, A.S., Hussain, S., Ali, S.F., 2013. Silver nanoparticles decrease body weight and locomotor activity in adult male rats. *Small* 9, 1715–1720.

ARTICLE 4

A clearing protocol for *Galleria mellonella* larvae: Visualization of internalized fluorescent nanoparticles

Published in *New Biotechnology* (Q1, IF₂₀₁₉: 4.674)

DOI: 10.1016/j.nbt.2020.08.002

August 2020

Laura Moya-Andérico^{a,1}, Joana Admella^{a,1}, and Eduard Torrents^{a,b,*}

^aBacterial Infections and Antimicrobial Therapies group, Institute for Bioengineering of Catalonia (IBEC), The Barcelona Institute of Science and Technology (BIST), Barcelona, Spain

^bMicrobiology Section, Department of Genetics, Microbiology and Statistics, Faculty of Biology, University of Barcelona, Barcelona, Spain

*Corresponding author: Eduard Torrents (etorrents@ibecbarcelona.eu)

¹These authors contributed equally to this work



Contents lists available at ScienceDirect

New BIOTECHNOLOGY

journal homepage: www.elsevier.com/locate/nbt

A clearing protocol for *Galleria mellonella* larvae: Visualization of internalized fluorescent nanoparticles

Laura Moya-Andérico^{a,1}, Joana Admella^{a,1}, Eduard Torrents^{a,b,*}

^a Bacterial Infections and Antimicrobial Therapies Group, Institute for Bioengineering of Catalonia (IBEC), The Barcelona Institute of Science and Technology (BIST), Baldiri Reixac 15-21, 08028, Barcelona, Spain

^b Microbiology Section, Department of Genetics, Microbiology and Statistics, Faculty of Biology, University of Barcelona, 643 Diagonal Ave., 08028, Barcelona, Spain

ARTICLE INFO

Keywords:

Galleria mellonella
Nanotoxicology
Tissue clearance

ABSTRACT

Light scattering is a challenge for imaging three-dimensional organisms. A number of new tissue clearing methodologies have been described in recent years, increasing the utilities of clearing techniques to obtain transparent samples. Here, we describe the optimization of a suitable and novel protocol for clearing *Galleria mellonella* larvae, an alternative infection animal model with a promising potential for the toxicological evaluation of different molecules and materials. This has allowed the visualization of internalized fluorescent nanoparticles using confocal microscopy, opening the door to a wide range of different applications.

Introduction

Imaging a three-dimensional specimen may be quite challenging due to obscuring effects. This opacity is mainly caused by light scattering [1]. Biological samples can comprise several cellular and extracellular structures, each with its own refractive index (RI). RI mismatches in the interfaces of different substances cause the scattering. Most tissues are formed of 70–80 % of water (with low RI) with the rest proteins and lipids, which are the primary source of light scattering due to their high RI. Therefore, delipidation is a relevant point to permeabilize cell membranes [1–3]. Optical clearing aims to minimize lateral scattering, so that all light wavelengths can pass through the sample, making it transparent. Tissue clearing usually involves sample fixation, permeabilization, and/or decolorization, ending with RI matching with a high-RI solvent [3]. Clearing methodologies can be critical for the observation of large samples. Classical histological techniques based on slice preparations are tedious and time-consuming. Indeed, clearing has a wide range of applications in many fields, improving the three-dimensional visualization of tissues and organs to study their physiological and biological functions [4].

As microscopy has evolved over recent years, several new optical clearing methods and techniques have been described. Choosing the best

procedure may depend on cost, speed, sample conservation, and fluorescence preservation, etc. [1,4]. Clearing protocols are chemically divided into organic solvent-based and hydrophilic reagent-based methods. The former consists of fixation, dehydration with either alcohols or ethers, delipidation, and RI matching (benzyl alcohol, benzyl benzoate, dibenzyl ether, 2,2'-thiodiethanol). The second group is based on fixation, delipidation (Triton X-100, Tween-20, Triethanolamine), and/or decolorization ending with RI matching (sucrose, fructose, glycerol, 2,2'-thiodiethanol, formamide, sorbitol, and others) [3]. The hydrophilic reagent-based methods are usually more limited to small samples and may require longer clearing times, while organic solvent-based procedures have advantages such as clearing speed and quality, but imply the use of very toxic and corrosive chemicals [4]. BABB (Benzyl Alcohol+ Benzyl Benzoate) - based optical clearing involves several dehydration steps that can lead to sample shrinkage and also alter protein fluorescence. Samples are then incubated in a BABB solution (1 part benzyl alcohol and 2 parts benzyl benzoate), achieving a final RI ≈ 1.55 that matches the RI of the remaining dehydrated proteins [4,5].

Several successful BABB clearing experiments described in the literature have been mainly performed in mouse organs, mouse embryos and fruit flies [6–8]. *Galleria mellonella* clearing is an attractive approach

Abbreviations: BABB, benzyl alcohol and benzyl benzoate; CLSM, confocal laser scanning microscope; NPs, nanoparticles; PFA, paraformaldehyde; PLGA, poly (lactic co-glycolic acid); RI, refraction index; RFUs, relative fluorescence units.

* Corresponding author at: Bacterial Infections and Antimicrobial Therapies Group, Institute for Bioengineering of Catalonia (IBEC), The Barcelona Institute of Science and Technology (BIST), Baldiri Reixac 15-21, 08028, Barcelona, Spain.

E-mail address: etorrents@ibecbarcelona.eu (E. Torrents).

¹ These authors contributed equally to this work.

<https://doi.org/10.1016/j.nbt.2020.08.002>

Received 23 June 2020; Received in revised form 1 August 2020; Accepted 6 August 2020

Available online 29 August 2020

1871-6784/© 2020 Elsevier B.V. All rights reserved.

with no precedents, able to provide new insights on larvae visualization, otherwise inaccessible. *G. mellonella* larvae clearing is appealing for studying the course of bacterial infections, toxicity of different compounds, and also to study nanoparticle interactions with living systems, among others. In the nanomedicine field, it is essential to provide an easy and cheap animal model to study the behavior and, more specifically, the interaction of different nanoparticles and nanomaterials with cells, tissues, and within organisms in general. Considering that *G. mellonella* is an alternative animal model for different purposes [9–12], this clearing protocol will be significantly useful for further applications in the microbiology or nanomedicine fields. Here, we report the optimization of a clearing protocol in *G. mellonella* larvae injected with fluorescent rhodamine nanoparticles as proof of concept.

Material and methods

Galleria mellonella maintenance and injection

G. mellonella larvae were fed an artificial diet (15 % corn flour, 15 % wheat flour, 15 % infant cereal, 11 % powdered milk, 6 % brewer's yeast, 25 % honey, and 13 % glycerol) and reared at 34 °C in the dark. *G. mellonella* larvae, 180–200 mg each, were injected with 10 μ L of red fluorescent rhodamine nanoparticles (1 mg/mL) [13] through the top right proleg using a microsyringe (Hamilton, Reno, USA). Control groups were injected with 10 μ L of 1x PBS (phosphate buffered saline) pH = 7.5 (Fisher Scientific, Madrid, Spain).

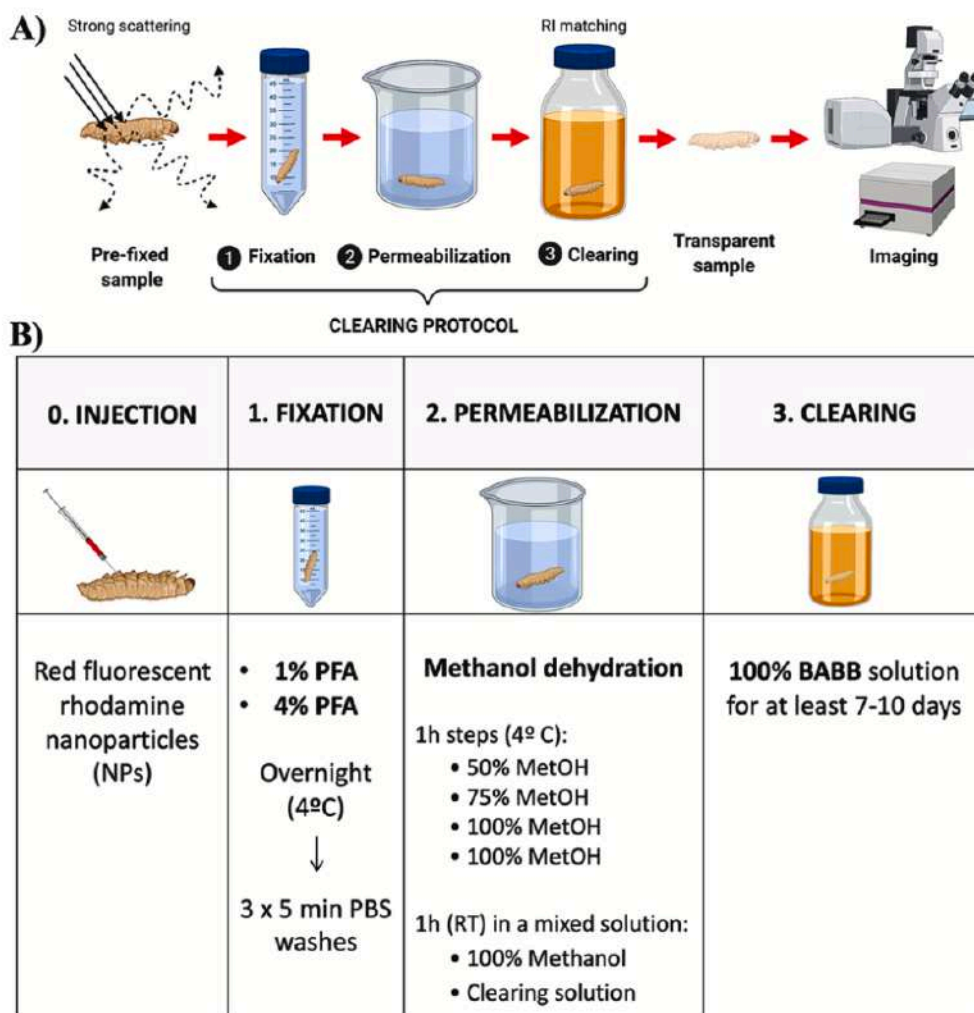


Fig. 1. Clearing protocol used for *G. mellonella* larvae. (A) RI matching can reduce light scattering in biological samples. Incubation in a dehydration solvent removes lipids and dehydrates the larvae. Clearing can be achieved by RI matching and further lipid solvation in a high-RI clearing solvent (e.g. BABB). *G. mellonella* clearing involves three steps: fixation, permeabilization, and clearing. (B) Schematic representation of the main steps of the optimized *G. mellonella* larvae clearing protocol used in this work. Created with BioRender.com.

Clearing

The procedure for *G. mellonella* clearance involved three steps: fixation, permeabilization and clearing (Fig. 1A). A schematic summary of the clearing protocol used can be seen in Fig. 1B. In the standardized clearance protocol, larvae were fixed right after injection in a 50 mL solution of 1 %–4 % paraformaldehyde (PFA) (Fisher Scientific, Madrid, Spain) and left overnight at 4 °C. Three washes of 5 min with 1x PBS pH 7.5 were performed the following day in a rotatory tube mixer (LabNet, Madrid, Spain) at room temperature (RT). In the dehydration step, several methanol (Fisher Scientific, Madrid, Spain) gradual series (50 %, 75 %, 2 × 100 %) were carried out, each in 50 mL and incubated at 4 °C for 1 h. Larvae were then placed in a 1:1 solution of 100 % methanol - BABB for a further hour to improve the transition between dehydrating and clearing. BABB is the clearing solvent, composed of 1 part benzyl alcohol (Sigma-Aldrich, Lyon, France) and 2 parts of benzyl benzoate (Sigma-Aldrich). Finally, larvae were left for at least 7–10 d in a 100 % BABB solution, at RT and protected from light. Every step involving BABB was performed using glass material as it is a very corrosive solvent.

Confocal microscopy

Unstained cleared *G. mellonella* larvae were visualized directly under a Zeiss LSM 800 confocal laser scanning microscope (CLSM) (Zeiss, Jena, Germany) with the 20x/0.8 air objective. Depth visualization was determined as the Z-axis point where the image disappeared since the laser could no longer penetrate. Analysis of all images was performed with ImageJ FIJI and Zen software (Zeiss, Jena, Germany).

Fluorescence measurements

Relative fluorescence of cleared and non-cleared *G. mellonella* larvae was measured from the top of a 6-well microtiter plate (Caphugs Evergreen, Buffalo, New York) in a Spark multimode microplate reader (TECAN, M annedorf, Switzerland). The gain was adjusted to the optimal 139. Rhodamine B was selected as the fluorophore (the excitation wavelength was fixed at 545 nm and the emission wavelength at 625 nm). Z- position was established as 27,000  m, and the integration time was set at 40  s. Multiple readings per well were defined as 14 × 14 circles (filled) with a 500  m border. The results obtained were analyzed using GraphPad Prism 8.0 software.

Results and discussion

Clearing optimization in *Galleria mellonella*

As a proof of concept for a protocol for *G. mellonella* larvae clearance, fluorescent nanoparticles were injected into the larvae and confocal microscopy used for visualization. 250 nm PLGA nanoparticles loaded with rhodamine 0.18 % w/w were used as previously described [13]. *G. mellonella* larvae were injected with 10  L of the nanoparticles (1 mg NP/mL) with 10  L of 1x PBS as a negative control. All different approaches used for *G. mellonella* larvae clearance used in the investigations are schematically represented in Fig. 2. After injection, larvae must first be fixed (Step 1) so as to preserve the molecules of interest. Several clearance protocols, including for *Drosophila melanogaster* [14,15], have been previously described using 4% PFA for fixation. However, it was initially decided to test different PFA concentrations ranging from 1 %–4 % and concluded that all

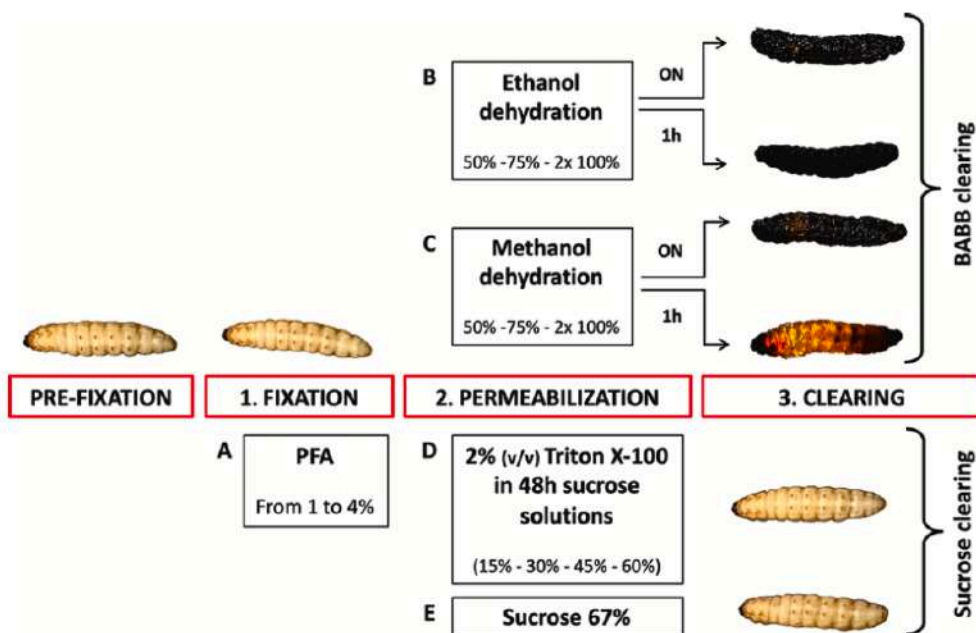


Fig. 2. Optimization of the clearing protocol for *Galleria mellonella* larvae. (A) Dehydration with alcohols was first employed with several ethanol solutions, both overnight and hourly, followed by BABB clearing without success. (B) Dehydration with methanol was also tested both overnight and hourly before larvae were eventually cleared in BABB. (C) Permeabilization performed with Triton X-100 and gradually increasing sucrose solutions failed to accomplish optical clearing. (D) Larvae were immersed in a concentrated solution of sucrose with unsuccessful clearance.

concentrations worked the same for the purpose (Fig. 2A). Also, it was noted that better fixation results were accomplished when performed soon after larvae injection (Fig. 1B). This may have been due to the injection wound remaining open and this, combined with the small molecular size of PFA, might aid the fixation solution to penetrate the worms more efficiently [3].

The permeabilization step (Step 2) removes lipids by substituting water with a high-RI medium. Various protocols have been described for permeabilization of other tissue types, some involving alcohols [6,16] and others including detergents [17–19]. In the former group, permeabilization occurs through dehydration with ethanol or methanol. Different gradual alcohol concentration series were chosen for both hourly and overnight dehydration steps. The procedure carried out with ethanol never reached full delipidation [3], and the larvae turned completely dark once left clearing in the BABB solution (Fig. 2B). Ethanol was then replaced by methanol and several concentrations and

incubation times were also screened for larval dehydration. Methanol dehydration seemed to prevent melanization more efficiently than ethanol. The final methodology used in the protocol (Fig. 1B) involved 1 h steps of dehydrating methanol solutions (50 %, 75 %, 2 × 100 %). It was also noticed that by leaving the larvae in a mixture of pure methanol and BABB in a volume ratio of 1:1 for 1 h after the dehydration step, better clearance results were obtained as seen in Fig. 2C. The 1:1 solution was drained and replaced by a 100 % BABB solution (Step 3). Larvae were incubated at RT, protected from light, and for more than a week to achieve optical clearing (Fig. 1B). However, limited reproducibility between worms was occasionally observed in the same sample type. Melanization is an innate immune response based on melanin deposition to encapsulate pathogens or foreign agents [9]. This has been the main issue hindering the clearing of *G. mellonella* larvae due to the blackish color that the larvae develop, making their microscope visualization impossible.

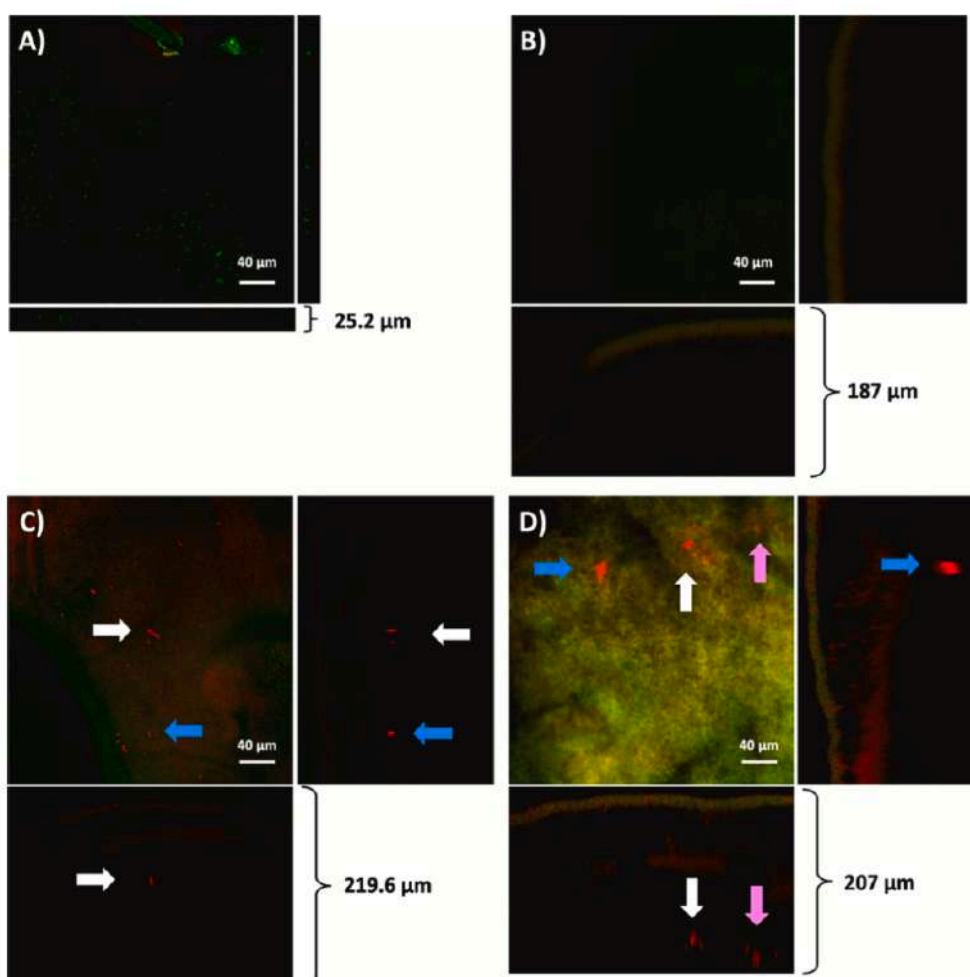


Fig. 3. Confocal images of *G. mellonella* larvae. The size of the orthogonal views was measured for each image, showing differences in the larval depth reached with the microscope. (A) Not cleared larvae injected with fluorescent rhodamine NPs. (B) Cleared larvae injected with PBS instead as a negative control. (C) Cleared larvae containing fluorescent rhodamine NPs (arrows) fixed in 1% PFA. (D) Cleared larvae containing fluorescent rhodamine NPs (arrows) fixed in 4% PFA.

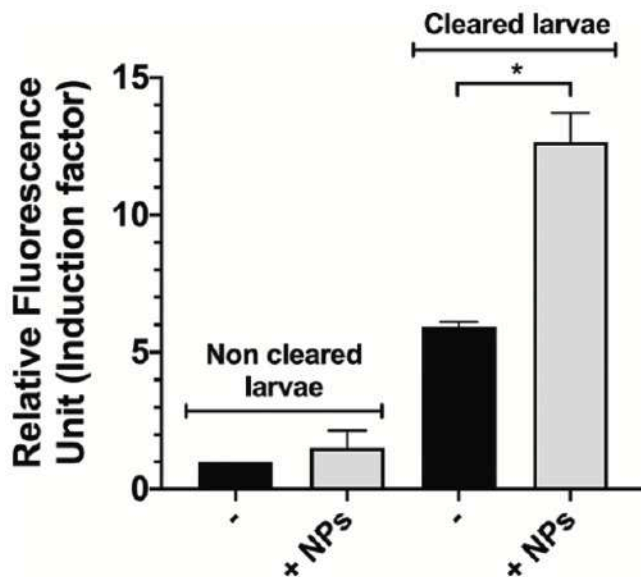


Fig. 4. Difference in Relative Fluorescence Units (represented by induction factor) between non-cleared and cleared *G. mellonella* larvae, both injected with rhodamine fluorescent nanoparticles (+ NP) and PBS (-) as a negative control and fixed with 1% PFA. The Relative Fluorescence Units (RFUs) in the non-cleared negative control are represented by an induction factor of 1, which corresponds to 42082 ± 10730 RFUs. Statistical significance between cleared larvae with NPs and without NPs is indicated with an * ($p < 0.05$) using the unpaired *t*-test in GraphPad Prism 8.0.

Permeabilization with detergents also appeared to be an easy alternative methodology. Such procedures can be followed by sample immersion in high RI solutions such as certain sugars. As seen in Fig. 2D, 2% (v/v) Triton X-100 along with 48 h gradual sucrose solutions (15%, 30%, 45%, and 60%) were tested [20]. In another experiment, the fixed larvae were introduced directly into a 67% sucrose solution which saturated the sample (Fig. 2E) [21]. Sucrose increases osmotic pressure, hence facilitating cell permeability and making this a very rapid and efficient method for clarifying, as seen, for example, in the case of brain tissue slices [3,21]. However, neither of the sucrose protocols were able to achieve optical clearing for *G. mellonella* larvae despite preserving the worms with an excellent appearance for several weeks. Simple immersion clearing is particularly well suited for smaller samples, although it can sometimes be inconvenient due to the dense viscosity of highly concentrated sugars [1].

After attempting several protocols unsuccessfully, *G. mellonella* clearing was eventually optimized as hourly methanol dehydration with subsequent BABB clearing as a protocol schematically described in Fig. 1B.

Microscope imaging of cleared larvae

Due to the light impermeability [22], it is unfeasible to observe inside a *G. mellonella* larva under any type of microscope. As a proof of concept of the clearance protocol, the aim was to observe the presence of internal NPs injected into larvae. With the available conditions, entire larvae were visualized under a confocal microscope using green (488 nm) and red (561 nm) lasers as shown in Fig. 3. As seen in Fig. 3A, it was only possible to observe the larval cuticle with a shallow depth of 25 μm . Clearly, fluorescence was not able to go deeper into the larvae, and the NPs injected as control could not be visualized. Only after optical clearing were visual observations through the cuticle achieved to a depth of 187 μm (Fig. 3B), as the obscuring effects were quite reduced. Nevertheless, confocal microscopy has some disadvantages on image depth as the limit is 100–200 μm in non-cleared samples [1]. Although a significant increase in laser penetration was achieved with cleared larvae, ultramicroscopy [6] or multiphoton microscopy [7] techniques

would be more suitable as they could obtain image depths up to several mm inside the larvae. This combined with labeling protocols could allow the visualization of internal structures to reconstruct the larval anatomy, as already accomplished with cleared *Drosophila* flies [16] and cleared mouse brains [23].

G. mellonella autofluorescence in the green channel [24] may be noticed (Fig. 3A,B) and had also been detected preliminary studies. When using NPs as a proof of concept to access within cleared larvae, the presence of internal fluorescent NPs was observed at a depth of 219.5 μm (Fig. 3C) and 207 μm (Fig. 3D) due to the reduced light scattering achieved by optical clearing. Note that in the orthogonal views of these two images, it is possible to visualize internal layers that could correspond to the hemocoel, hemolymph, and even potential adipose bodies, but specialized histopathology analysis is needed to confirm this. The observation of NPs was only possible in cleared larvae. This paves the way for further studies using super-resolution microscopy for a more thorough analysis of the behavior of nanomaterials within living organisms.

With regard to imaging, *Drosophila melanogaster* is another experimental insect which presents similar limitations by showing strong light scattering mainly due to the cuticle's pigments and dense structure. With a novel tissue clearing approach that also preserves fluorescence, it has been possible to visualize their neuronal networks using both confocal and ultramicroscopy by differentiated fluorescent staining [25]. BABB clearing has also allowed ultramicroscopy to obtain a 3D reconstruction of the fly's anatomy [26]. Dehydrated toadfish embryos and larvae have been cleared in BABB for subsequent imaging in optical tomography and confocal microscopy. This has provided new insights into the embryonic development of Batrachoidids, a fish family unknown in developmental biology but widely studied in other fields [27]. Moreover, in mammals, transparent mouse brains and embryos have been accomplished by Scale clearing, providing a 3D reconstruction and imaging of the brain structures and the neuronal network. Unlike BABB, this methodology guarantees the preservation of fluorescence over time [23]. In this way, conventional fluorophores like GFP would be better conserved, and this would improve the study of fluorescent NP interactions with different *G. mellonella* living material (cells, tissues, etc.).

For our purposes, BABB did not affect the fluorescence emission as seen by the bright rhodamine signal in our confocal images.

Relative fluorescence quantification

To further investigate the behavior of NPs inside the cleared *G. mellonella* larvae, it was possible to quantify the relative fluorescence of cleared larvae injected with rhodamine nanoparticles and compare it against a control group of cleared larvae injected with PBS alone (Fig. 4). The larvae were fixed with 1% PFA, and while the same analysis was performed with larvae fixed with 2, 3 and 4% PFA concentrations, the same results were obtained (data not shown). It was also possible to measure the fluorescence in both a non-cleared group of larvae injected with the same NPs and a non-cleared control group, both of which only revealed a small amount of larval background fluorescence. Emission from fluorescent cleared larvae (injected with rhodamine NPs) showed an increase in relative fluorescence by an induction factor (i.e. the factor by which RFU expression increases) of nearly 13. As can be seen in Fig. 4, the fluorescence of cleared larvae with NPs is statistically significant when compared to the cleared negative control. Moreover, it is clear that the difference in fluorescence emission is also enormous when compared to the non-cleared larvae group containing NPs. The increase in relative fluorescence observed in the cleared negative control compared to the non-cleared negative control can be explained as the larvae are now transparent and their autofluorescence is, therefore, more detectable.

By clearing the larvae, the quantification of the NP fluorescence was improved, and thus the technique could prove valuable in experiments using fluorophore-tagged bacteria or other types of NP to measure infection or hemocyte proliferation *in vivo*. Solvent-based clearing methodologies such as BABB might present an important disadvantage for fluorescent or chemiluminescent labeling. Since the dehydration step may not preserve the fluorescent or chemiluminescent emission signal, other clearing methodologies or labeling techniques can address this limitation. Immunofluorescent labeling using antibodies against the target fluorescent protein and conjugated to organic dyes resistant to dehydration could be a good alternative. Another potential strategy could involve the use of optimized fluorescent proteins that can survive dehydration procedures [1].

Conclusions

This study describes an optimized protocol for clearing *Galleria mellonella* larvae. Rhodamine fluorescent NPs have been used as a proof of concept to visualize their internalization in cleared larvae using confocal microscopy. Our research can contribute to the study of the interactions of nanoparticles and nanomaterials within living organisms as well as further applications in both the microbiology and nanomedicine fields.

Author contribution

The manuscript was written through the contributions of all authors. Laura Moya-Andr  ico and Joana Admella performed biological assays and wrote the manuscript. Eduard Torrents directed the research, revised the experimental data, and wrote the manuscript. All authors have approved the final version of the manuscript.

Declaration of Competing Interest

The authors declare no financial or commercial conflict of interest.

Acknowledgments

The authors wish to thank Dr. Ana Morton (Department de Biologia Animal, Biologia Vegetal I Ecologia (BABVE) at the UAB for providing

G. mellonella eggs.

This study was partially supported by grants from the Ministerio de Econom  a, Industria y Competitividad, MINECO, and Agencia Estatal de Investigaci  n (AEI), Spain, co-funded by Fondo Europeo de Desarrollo Regional, FEDER, European Union (BIO2015-63557-R and RTI2018-098573-B-I00), the CERCA programme and AGAUR-Generalitat de Catalunya (2017SGR-1079), Spain, co-funded by the European Regional Development Fund - FEDER, Catalan Cystic Fibrosis association, Spain and Obra Social ‘‘La Caixa’’, Spain.

References

- Richardson DS, Lichtman JW. Clarifying tissue clearing. *Cell* 2015;162(2):246–57. <https://doi.org/10.1016/j.cell.2015.06.067>.
- Seo J, Choe M, Kim SY. Clearing and labeling techniques for large-scale biological tissues. *Mol Cells* 2016;39(6):439–46. <https://doi.org/10.14348/molcells.2016.0088>.
- Tainaka K, Kuno A, Kubota SI, Murakami T, Ueda HR. Chemical principles in tissue clearing and staining protocols for whole-body cell profiling. *Annu Rev Cell Dev Biol* 2016;32:713–41. <https://doi.org/10.1146/annurev-cellbio-111315-125001>.
- Ariel P. A beginner’s guide to tissue clearing. *Int J Biochem Cell Biol* 2017;84:35–9. <https://doi.org/10.1016/j.biocel.2016.12.005>.
- Costa EC, Silva DN, Moreira AF, Correia LJ. Optical clearing methods: an overview of the techniques used for the imaging of 3D spheroids. *Bioelectron Bioeng* 2019;116(10):2742–63. <https://doi.org/10.1002/bt.27105>.
- Doth HU, Leischner U, Schierloh A, Jahrling N, Mauch CP, Deininger K, et al. Ultramicroscopy: three-dimensional visualization of neuronal networks in the whole mouse brain. *Nat Methods* 2007;4(4):331–6. <https://doi.org/10.1038/nmeth1036>.
- Parra SG, Chia TH, Zinter JP, Levene MJ. Multiphoton microscopy of cleared mouse organs. *J Biomed Opt* 2010;15(3):036017. <https://doi.org/10.1117/1.3454391>.
- Megurk L, Morrison H, Keegan LP, Sharpe J, O’Connell MA. Three-dimensional imaging of *Drosophila melanogaster*. *PLoS One* 2007;2(9):e834. <https://doi.org/10.1371/journal.pone.0000834>.
- Tsai CJ, Loh JM, Proft T. *Galleria mellonella* infection models for the study of bacterial diseases and for antimicrobial drug testing. *Virulence* 2016;7(3):214–29. <https://doi.org/10.1080/21505594.2015.1135299>.
- Ignasiak K, Maxwell A. *Galleria mellonella* (greater wax moth) larvae as a model for antibiotic susceptibility testing and acute toxicity trials. *BMC Res Notes* 2017;10(1):428. <https://doi.org/10.1186/s13104-017-2757-8>.
- Champion OI, Wagley S, Tibball RW. *Galleria mellonella* as a model host for microbiological and toxin research. *Virulence* 2016;7(7):840–5. <https://doi.org/10.1080/21505594.2016.1203486>.
- Andrea A, Krogfelt KA, Jensen H. Methods and challenges of using the greater wax moth (*Galleria mellonella*) as a model organism in antimicrobial compound discovery. *Microorganisms* 2019;7(3). <https://doi.org/10.3390/microorganisms7030085>.
- Baelo A, Levato R, Julian E, Crespo A, Astola J, Gavalda J, et al. Disassembling bacterial extracellular matrix with DNase-coated nanoparticles to enhance antibiotic delivery in biofilm infections. *J Control Release* 2015;209:150–8. <https://doi.org/10.1016/j.jconrel.2015.04.028>.
- Becker K, Jahrling N, Saghaei S, Doth HU. Dehydration and clearing of whole mouse brains and dissected hippocampi for ultramicroscopy. *Cold Spring Harb Protoc* 2013;2013(7):683–4. <https://doi.org/10.1101/pdb.prot075820>.
- Becker K, Jahrling N, Saghaei S, Doth HU. Dehydration and clearing of adult *Drosophila* for ultramicroscopy. *Cold Spring Harb Protoc* 2013;2013(7):681–2. <https://doi.org/10.1101/pdb.prot075812>.
- Jahrling N, Becker K, Saghaei S, Doth HU. Light-sheet fluorescence microscopy: chemical clearing and labeling protocols for ultramicroscopy. *Methods Mol Biol* 2017;1563:33–49. https://doi.org/10.1007/978-1-4939-6810-7_3.
- Costantini I, Ghobril JP, Di Giovanni AP, Allegra Mascaro AL, Silvestri L, Mullenbroich MC, et al. A versatile clearing agent for multi-modal brain imaging. *Sci Rep* 2015;5:9808. <https://doi.org/10.1038/srep09808>.
- Chung K, Wallace J, Kim SY, Kalyanasundaram S, Andalman AS, Davidson TJ, et al. Structural and molecular interrogation of intact biological systems. *Nature* 2013;497(7449):332–7. <https://doi.org/10.1038/nature12107>.
- Susaki EA, Tainaka K, Perrin D, Kishino F, Tawara T, Watanabe TM, et al. Whole-brain imaging with single-cell resolution using chemical cocktails and computational analysis. *Cell* 2014;157(3):726–39. <https://doi.org/10.1016/j.cell.2014.03.042>.
- Tsai PS, Kauthoff JP, Blinder P, Friedman B, Drew PJ, Karten HJ, et al. Correlations of neuronal and microvascular densities in murine cortex revealed by direct counting and colocalization of nuclei and vessels. *J Neurosci* 2009;29(46):14553–70. <https://doi.org/10.1523/JNEUROSCI.3287-09.2009>.
- Yu T, Qi Y, Wang J, Feng W, Xu J, Zhu J, et al. Rapid and pridium iodide-compatible optical clearing method for brain tissue based on sugar/sugar-alcohol. *J Biomed Opt* 2016;21(8):081203. <https://doi.org/10.1117/1.JBO.21.8.081203>.
- Smolla M, Ruchty M, Nagel M, Kleinsaidam CJ. Clearing pigmented insect cuticle to investigate small insects’ organs in situ using confocal laser-scanning microscopy (CLSM). *Arthropod Struct Dev* 2014;43(2):175–81. <https://doi.org/10.1016/j.asd.2013.12.006>.

L. Moya-Anderico et al.

New BIOTECHNOLOGY 60 (2021) 20–26

- [23] Hama H, Kurokawa H, Kawano H, Ando R, Shimogori T, Noda H, et al. Scale: a chemical approach for fluorescence imaging and reconstruction of transparent mouse brain. *Nat Neurosci* 2011;14(11):1461–9. <https://doi.org/10.1038/nn.2928>.
- [24] Parthuisot N, Rouquette J, Ferdy JB. A high-throughput technique to quantify bacterial pathogens' virulence on the insect model *Galleria mellonella*. *J Microbiol Methods* 2018;152:69–72. <https://doi.org/10.1016/j.jmimet.2018.07.013>.
- [25] Pende M, Becker K, Wanis M, Saghaei S, Kaur R, Hahn C, et al. High-resolution ultramicroscopy of the developing and adult nervous system in optically cleared *Drosophila melanogaster*. *Nat Commun* 2018;9(1):4731. <https://doi.org/10.1038/s41467-018-07192-z>.
- [26] Jährling N, Becker K, Schonbauer C, Schnorrer F, Dodt HU. Three-dimensional reconstruction and segmentation of intact *Drosophila* by ultramicroscopy. *Front Syst Neurosci* 2010;4:1. <https://doi.org/10.3389/fnro.06.001.2010>.
- [27] Felix PM, Goncalves A, Vicente JR, Fonseca PJ, Amorim MC, Costa JL, et al. Optical micro-tomography "OPenT" allows the study of large toadfish *Halobatrachus didactylus* embryos and larvae. *Mech Dev* 2016;140:19–24. <https://doi.org/10.1016/j.mod.2016.03.001>.

SUMMARY OF THE RESULTS PRESENTED

Galleria mellonella has been gaining popularity as an alternative *in vivo* model for many applications. The larval stage of this insect has been used to study the virulence of different microorganisms, the antimicrobial efficacy of various drugs, and the toxicity of several compounds, among other uses (see Introduction, sections 3 and 4). For this reason, we sought to implement the *G. mellonella* animal model for this work. In **Objective 1**, we aimed to optimize the necessary experimental conditions for using *G. mellonella* as an infection model. This objective is addressed in all the articles presented in this thesis, as all the experiments involving *G. mellonella* testing were carried out using the optimized experimental conditions. The first *G. mellonella* eggs were kindly donated by Dr. Ana Morton from the Departament de Biologia Animal, Biologia Vegetal i Ecologia (BABVE) at the Universitat Autònoma de Barcelona. The first generation of *G. mellonella* was used to optimize the growing conditions. First, an initial temperature of 25°C was tried, but it was deemed too low since the cycle took a long time (>8 weeks). Therefore, the temperature was raised to 34°C. At this temperature, the cycle took about 5 weeks and the larvae thrived. For subsequent life cycles, *G. mellonella* was reared at 34°C and protected from light at 34°C as they are sensitive to light [1]. As recommended by Dr. Morton, the larvae were fed a diet consisting of corn flour, wheat flour, powdered milk, cereals, brewer's yeast, honey, and glycerol, but we adjusted the concentration of each component to the one that worked best for us.

Next, the injection procedure for the larvae was optimized, and it was defined as 10 µl of bacteria (Article 1 and 2), nanoparticle (Article 3 and 4), or antimicrobial suspensions (Article 2) injected through the upper prolegs using a Hamilton microsyringe. The optimal infection dose was calculated for the different bacterial strains used in the articles of this thesis. For *P. aeruginosa* PAO1, different dilutions were injected into the larvae and the optimal dose was determined to be 20-40 CFU per larva, thus it was subsequently used in all virulence studies involving PAO1 (**Article 1**). To see whether the same infection dose applied for different *P. aeruginosa* strains, 20-40 CFU/larva of the PA14 and PAET1 strains were injected into the larvae. PA14 is a laboratory strain that was isolated from a burn patient while PAET1 is a clinical strain that was isolated from a cystic fibrosis patient [103,241]. The PA14 strain was more virulent to the larvae as they all died within 18 hours post-infection (Appendix Figure 1A). On the other hand, the larvae were able to survive a similar dose of PAET1, and the larvae only died when the infection dose was increased to 1×10^5 CFU/larva. Similar differences in virulence were also seen with testing other *P. aeruginosa* clinical

strains in *G. mellonella* (Appendix Figure 1B). Larvae were injected with the optimized infection dose of two acute and multi-resistant clinical isolates (PA54 and PA166) and two chronic isolates (PAET2 and PAET3). PA54 killed all the larvae within 21 hours post-infection while only 13% of the larvae survived the infection with PA166. In contrast, 38% of the larvae infected with PAET2 and 100% of the larvae infected with PAET3 survived, respectively.

Other infection studies were done in *G. mellonella* that involved *S. aureus* (**Article 2**) and *M. brumae* [242]. For these, the optimal infection dose had to first be optimized for each strain. For *S. aureus*, a range of concentrations were injected into the larvae to find that the optimal infection dose was 1×10^7 CFU/larva (Appendix Figure 2A) which was then used in all the larval experiments performed in **Article 2**. For *M. brumae*, the initial dosing tests were done with concentrations ranging from 1×10^5 to 1×10^7 CFU/larva (Appendix Figure 2B). Since *M. brumae* takes about 5 days to grow [144], the infected larvae had to be incubated for at least that long. Since the larvae were first incubated without food, the deaths seen prior to 120 hours post-infection were probably due to cannibalism or food deprivation. The infection dose studies were repeated using 1×10^4 , 1×10^5 , and 1×10^6 CFU/larva, and the larvae were incubated with food for 6 days [242]. As seen in Appendix Figure 2C, all the larvae survived with all three concentrations. On the other hand, significantly different survival rates were seen with 1×10^5 and 1×10^6 CFU/larva of *M. bovis* BCG. During all the infection dose optimizations, we standardized a protocol so we could obtain the desired CFU/larva for every experiment. For this, we washed the bacterial cells three times to remove any virulence factors that were secreted by the bacteria during overnight growth. Then, the OD₅₉₀ of the culture was measured and it was equalized to a final OD₅₉₀ of 1 which was equivalent to 1×10^7 CFU/larva. Serial dilutions from the equalized culture were done until the desired concentration of bacteria was reached. After infection, the larvae were monitored at different time points and were considered dead when they were fully melanized and did not move in response to touch. No deaths were seen in any of the control groups in all of the experiments. This indicates that the inoculation procedure was always successful and did not cause any injury to the larvae.

Bacterial growth curves inside *G. mellonella* larvae were also optimized to determine bacterial load at various time points by plating the hemolymph on media plates to count CFUs (Figure 5B, **Article 1**). We also tried to assess bacterial load using fluorescently-tagged bacteria in whole larvae, but we found that the natural autofluorescence and thick cuticle of the worms diffculted the detection of the fluorescence from inside the larvae (see **Article 1**). Consequently, bacterial load was determined using bioluminescent bacteria in whole larvae. Additionally, we found that gene expression levels were best measured using bioluminescence in whole larvae, so the pETS220-

BIATlux vector was constructed (see **Article 1**). Immune response measurements were also optimized in *G. mellonella*. The activation of the larval immune system was determined by optimizing hemocyte density measurements. This was done by extracting the hemolymph from immune-challenged larvae at different time points and isolating the hemocytes for quantification. For microscopy studies, the hemocytes were stained with different dyes to determine the best one for confocal microscopy imaging to detect whether NPs were internalized by the hemocytes (see **Article 3**).

G. mellonella has been frequently used to study the virulence of different bacteria. Typically, microorganisms (wild-type or mutants) are injected in the larvae and then virulence is assessed by measuring survival rates and humoral response levels (see Introduction, section 3). *P. aeruginosa* is a major opportunistic pathogen that causes fulminant infections in immunocompromised hosts and chronic lung infections in cystic fibrosis patients. Since *G. mellonella* has been proven to be a suitable model to study *P. aeruginosa* infections (see Introduction, section 3.1.2), we intended to study the infection process of *P. aeruginosa* using *G. mellonella* larvae by measuring gene expression levels during an *in vivo* infection. This refers to **Objective 2**, and it is addressed in **Article 1**. In this article, we discovered that fluorescent promoter probe vectors could not be used due to the autofluorescence of the hemocytes. Therefore, we developed a promoter probe vector with bioluminescence expression (pETS220-BIATlux). As a proof of concept, we used RNR genes (*nrd*) as these are involved in an active infection. The promoters of the different RNR genes (*PnrdA*, *PnrdJ*, *PnrdD*, and *PnrdR*) were successfully cloned into the pETS220-BIATlux vector. These *nrd* promoter-lux fusion vectors were incorporated into *P. aeruginosa* PAO1 and then injected into *G. mellonella* larvae. First, the bioluminescence in whole larvae was determined qualitatively at various time points, and the results showed that the larvae emitted more or less bioluminescence. This luminescence was then quantified by measuring relative luminescence in the same larvae. The results show that differences in RLU values could be observed for the different strains depending on their respective *nrd* expression during the course of infection. *PnrdR*-lux and *PnrdJ*-lux were the first to begin rising during the infection while *PnrdA*-lux and *PnrdD*-lux peaked towards the end of the infection. Furthermore, the *nrdR* gene was highly induced throughout the whole infection. The *Anr*-lux negative control (pETS220-BIATlux containing a fragment of the *anr* gene) had low background signals as seen by the low RLU values obtained at all time points.

Galleria mellonella has also been used to test the efficacy of different antimicrobial agents (see Introduction, section 3.4). Since this model can be used to do preliminary screenings of potential antimicrobials, it facilitates the rapid detection of novel lead compounds and therapeutic strategies

that are effective against *in vivo* infections. Moreover, precise concentrations of the compounds can be injected directly into the hemocoel of the larvae, and the larvae can be used to pre-screen numerous drugs so to reduce the number of compounds and animals needed for additional efficacy studies in mammalian models [174]. In **Objective 3**, we aimed to optimize our *G. mellonella* model to include *in vivo* antimicrobial testing. This objective is addressed in **Article 2** where we evaluated the antimicrobial efficacy of oleanolic acid (OA) and maslinic acid (MA) amide derivatives in *G. mellonella*. First, the infection dose of *S. aureus* was optimized to 1×10^7 CFU/larva. Then, the active amide derivatives that had the highest antimicrobial efficacy *in vitro* (MA-HDA and OA-HDA) were tested in *G. mellonella*. The compounds were injected 1 hour and 6 hours after infection with the optimized *S. aureus* dose, and the results showed that MA-HDA and its parent compound (MA) reduced the larval mortality by 50%.

Generally, antimicrobial agents that are tested in *G. mellonella* for efficacy are simultaneously tested for toxicity. This animal model has also been used to study the toxicity of other compounds as well as nanomaterials (see Introduction, section 4). In **Objective 4**, we aimed to test the effectiveness of the *G. mellonella* model in determining the toxicity of different agents. This objective is addressed in **Articles 2 and 3**. In **Article 2**, the toxicity of the different compounds used for antimicrobial testing was evaluated. *G. mellonella* larvae were injected with different concentrations of the MA-HDA and OA-HDA compounds, and larval mortality was recorded to calculate the LD₅₀ (compound concentration that kills 50% of the larvae within 24 hours). The SI of the compounds was improved when using the *in vivo* LD₅₀ instead of the *in vitro* CC₅₀ (compound concentration that kills 50% of the cells). As a potential therapy for non-muscle-invasive bladder cancer, the toxicity of *M. brumae* was also assessed using *G. mellonella* [242]. Larvae were infected with 1×10^4 , 1×10^5 , and 1×10^6 CFU/larva of *M. brumae*. The larvae were also injected with the same concentrations of *M. bovis* BCG which is the current immunotherapy option. Even at the highest concentration tested, all larvae survived until the end of the experiment (6 days) (Appendix Figure 2C). On the other hand, only about 43% of the larvae infected with *M. bovis* BCG survived. *M. brumae* was not found in the hemolymph of the infected larvae at 144 hours (6 days) post-infection, but *M. bovis* BCG was found in concentrations ranging from 10^3 to 10^5 CFU/ml (Appendix Figure 3).

In **Article 3**, we determined the toxicity effects of different types of nanoparticles in *G. mellonella*. Various concentrations of functionalized gold (Au(HAL)), silver (Ag), and selenium (Se) nanoparticles were injected into the larvae to calculate the LD₅₀. The results revealed that the most toxic NPs were the SeNPs followed by AgNPs and Au(HAL)NPs. The NPs were internalized by the hemocytes, and they also triggered hemocyte proliferation. The lowest concentrations of

Au(HAL)NPs and AgNPs yielded the highest hemocyte proliferation values, but these values decreased as the NP concentrations increased. In contrast, the hemocyte density did not vary much among the different concentrations of SeNPs. Additionally, the toxicity of the NPs resulted in NP accumulations, histological damage, and motility reduction in the larvae. NP accumulations were seen in the caudal (tail) area of the larvae, even when the movement of the worms was partially or fully restricted. Histological analysis of the larvae injected with SeNPs revealed large stellate-like aggregates of NPs intermingled with hemocytes and surrounded by large extracellular spaces. For the larvae injected with AgNPs and Au(HAL)NPs, the aggregates seen were smaller and more dispersed. The larvae injected with Au(HAL)NPs had motility patterns similar to the control larvae that were injected with PBS. On the other hand, the movement of the larvae injected with AgNPs and SeNPs was significantly reduced.

G. mellonella testing has applied a wide array of methodologies (see Introduction, section 5). In **Objective 5**, we strived to validate new methodology approaches in *G. mellonella* larvae. This objective is addressed in **Articles 1 and 4**. In **Article 1**, we optimized an RNA extraction protocol for bacteria derived from a *G. mellonella* infection. Larvae were injected with an infective dose of *P. aeruginosa* PAO1 and incubated for 16 hours. Then, the hemolymph was extracted from the larvae, the bacteria were isolated from the hemolymph, and the RNA was extracted from the bacteria. The RNA was used for cDNA preparation for subsequent qRT-PCR analysis. Finally, RNR gene expression levels were quantified to see how they varied in infection compared to a planktonic culture. The highest inductions were seen with *nrdR* and *nrdJ* followed by *nrdA* and *nrdD*. The *norC* gene (anaerobiosis marker) was also analyzed, which was found to be highly induced during the infection. In this same article, we also used a technique that we previously optimized to measure gene expression using fluorescent bacteria. Larvae were infected with *P. aeruginosa* PAO1 wild-type strain, two *P. aeruginosa* PAO1 strains expressing GFP (*PnrdA*-GFP and *PnrdJ*-GFP), two *P. aeruginosa* PAO1 strains expressing E2Crimson (*PnrdA*-E2Crimson and *PnrdJ*-E2Crimson), and PBS. After infection, the larvae were incubated for 16 and 20 hours. Afterward, the hemolymph was extracted from the larvae and relative fluorescence was measured using a microplate reader. The hemolymph of larvae injected with PBS and the PAO1 wild-type strain had RFU/ml values comparable to ones seen with the hemolymph of larvae injected with the PAO1 strains with GFP and E2Crimson expression. Still, some differences in fluorescence could be seen between the *PnrdA* and *PnrdJ* strains. The same hemolymphs used for the RFU measurements were visualized under a fluorescence microscope. The bacteria fluoresced green or red according to their respective fluorophore, but the hemocytes also showed green and red fluorescence. With both of these

techniques, we were able to discover that hemocytes have natural autofluorescence that interfered with the measurements of the fluorescence emitted by the bacteria present in the hemolymph.

In **Article 4**, we optimized a clearing protocol for *G. mellonella* larvae. As proof of concept, we used fluorescent rhodamine NPs which were injected into *G. mellonella* larvae. Several attempts were done using different approaches, which included fixation of the larvae in different concentrations of paraformaldehyde (PFA) and the dehydration of the larvae with ethanol or methanol (at different concentrations with different incubation times) followed by immersion in a clearing solvent. Another approach involved the immersion of larvae in increasing concentrations of sucrose mixed with a detergent solution or directly in a highly concentrated sucrose solution. The final protocol involved the following steps: i) overnight fixation of the larvae in 1-4% PFA, ii) three PBS washes to remove remaining PFA, iii) dehydration of the larvae using increasing concentrations of methanol (1-hour incubation at 4°C with each concentration), iv) one-hour incubation with 1:1 solution of 100% methanol and 100% BABB as the clearing solution (1 part of Benzyl Alcohol + 2 parts of Benzyl Benzoate), and v) incubation for 7-10 days in 100% BABB. The fluorescent NPs were able to be seen deep within cleared larvae using confocal microscopy, but they could not be seen in the non-cleared larvae. Furthermore, the fluorescence emitted by the NPs was quantified using a microplate reader. The cleared larvae with NPs yielded high RFU values while the non-cleared larvae with NPs did not. The cleared larvae injected with PBS as a control revealed an increase in RFU values when compared to the non-cleared larvae injected with PBS.

Report on the impact factor of the articles presented

I, Dr. Eduard Torrents, hereby declare that the impact factor of the articles presented in this thesis at the date of submission is as follows:

- **Article 1, titled “Monitoring Gene Expression during a *Galleria mellonella* Bacterial Infection.”** Published in *Microorganisms* in November 2020 (Second Quartile). As the impact factor of this journal in 2020 is not available, the impact factor in 2019 was 4.152.
- **Article 2, titled “Novel Oleanolic and Maslinic Acid Derivatives as a Promising Treatment against Bacterial Biofilm in Nosocomial Infections: An in Vitro and in Vivo Study.”** Published in *ACS Infectious Diseases* in July 2019 (First Quartile and First Decile). The impact factor in 2019 was 4.614.
- **Article 3, titled “Utility of *Galleria mellonella* larvae for evaluating nanoparticle toxicity.”** Published in *Chemosphere* in December 2020 (First Quartile). As the impact factor of this journal in 2020 is not available, the impact factor in 2019 was 5.778.
- **Article 4, titled “A clearing protocol for *Galleria mellonella* larvae: Visualization of internalized fluorescent nanoparticles.”** Published in *New Biotechnology* in August 2020 (First Quartile). As the impact factor of this journal in 2020 is not available, the impact factor in 2019 was 4.674.

Thesis Director and Tutor
Dr. Eduard Torrents Serra

Report on the participation in the articles presented

I, Dr. Eduard Torrents, hereby declare that the participation of Laura Moya-Andérico in the articles presented in this thesis is as follows:

- **Article 1, titled “Monitoring Gene Expression during a *Galleria mellonella* Bacterial Infection.”** Laura is the first author of this article and shares with me the role of corresponding author. Laura was involved in the design and supervision of all the experiments. She actively contributed to all the experimental work and data analysis illustrated in all of the figures, and she also wrote the manuscript.
- **Article 2, titled “Novel Oleanolic and Maslinic Acid Derivatives as a Promising Treatment against Bacterial Biofilm in Nosocomial Infections: An in Vitro and in Vivo Study.”** Laura was involved in the experimental work illustrated in Figure 1, including the rearing of the *G. mellonella* larvae and the optimization of the *S. aureus* infective dose used in the article. The published article is also included as part of the doctoral thesis of Núria Blanco-Cabra. However, since Laura’s contribution relates to Objectives 1 and 3 of her thesis, I consider it adequate to include the article as part of her thesis as well.
- **Article 3, titled “Utility of *Galleria mellonella* larvae for evaluating nanoparticle toxicity.”** Laura is the first author of this article. She was involved in the experimental work and data analysis illustrated in Figures 2, 3, 4, 5, and 7, and she also wrote the manuscript.
- **Article 4, titled “A clearing protocol for *Galleria mellonella* larvae: Visualization of internalized fluorescent nanoparticles.”** As stated in the published article, the first two authors (Laura Moya-Andérico and Joana Admella) contributed equally to this work. Laura was involved in the design and supervision of all the experiments. She also carried out the experimental work illustrated in Figures 3 and 4, and she was involved in the writing of the manuscript.

Thesis Director and Tutor
Dr. Eduard Torrents Serra

DISCUSSION

The articles presented in this thesis address the different aspects involved in the implementation of *Galleria mellonella* as an animal model to study bacterial infections as well as the efficacy and toxicity of different compounds. In this section, the main results of all the articles will be discussed according to the objectives involved. For a more detailed discussion, refer to the corresponding Discussion section of each article. Figures that were not included in the articles but are used to support this discussion can be found in the Appendix section (see page 134).

Galleria mellonella as an animal model of infection

Before starting to use the *G. mellonella* animal model, many experimental conditions had to first be optimized. The growing conditions that worked best for us were found and therefore, all the *G. mellonella* larvae used in this work were reared at 34°C in the dark and fed a diet consisting of corn flour, wheat flour, powdered milk, cereals, brewer's yeast, honey, and glycerol. The dietary components of this diet and similar components have been reported as optimal for *G. mellonella* rearing [8,67]. The first larvae were utilized to optimize the infection dose of different bacteria, including *P. aeruginosa*, *S. aureus*, and *M. brumae* (Appendix Figure 1 and 2). For *P. aeruginosa*, both laboratory and clinical strains were analyzed. We found that the larvae had higher survival rates when infected with small doses of the chronic strains, yet they succumbed to low doses of the acute laboratory strains. Only when the larvae were infected with a high dose of the PAET1 chronic strain, the larvae died in the same time frame as with the acute strains. These results demonstrate the difference in virulence between acute and chronic *P. aeruginosa* strains and how these distinctions can be easily determined using the *G. mellonella* model. In contrast to acute *P. aeruginosa* strains, *S. aureus* is more virulent to the larvae at much higher concentrations. Similar concentrations of *M. brumae* and *M. bovis* BCG also had variable results. *M. brumae* was not virulent to the larvae while *M. bovis* BCG yielded low survival rates. This further validates the diverse virulence levels of different bacterial strains which can be efficiently determined using *G. mellonella*.

Besides assessing the survival rate of infected larvae, bacterial virulence was also evaluated by determining the degree of larval melanization and bacterial proliferation within the larvae. The criteria to determine larval death during experiments was established as full melanization and lack of movement in response to touch; both conditions had to occur to classify a larva as dead. Bacterial burden inside the larvae was optimized by doing growth curves, which allowed us to estimate how

many bacteria were present inside the larvae at a given time. This data was useful for further experiments such as the RNA extraction done with bacteria isolated from *G. mellonella* larvae seen in **Article 1**. By previously doing a *P. aeruginosa* PAO1 growth curve in larvae, we were able to know that at 16 hours post-infection, sufficient bacterial load was present for RNA extraction (Figure 5B, **Article 1**). Bacterial burden was also studied using bioluminescence. Whole larvae infected with bacteria expressing bioluminescence could be monitored at different time points to see how the bacteria grew inside the larvae. In Figure 1C from **Article 1**, larvae were imaged at death, and bioluminescence could be seen throughout the entire larval body. Fluorescently-tagged bacteria could not be used in *G. mellonella* because we found that the larval hemocytes have intrinsic autofluorescence that interferes with the fluorescence measurements of the bacteria (Figure 2, **Article 1**).

To determine whether the immune system of *G. mellonella* larvae was activated in response to foreign invaders, we optimized a way to measure hemocyte proliferation within the larvae. The hemolymph of larvae injected with bacteria, NPs, or PBS was extracted at different time points and hemocytes were isolated through low-speed centrifugation. Hemocytes were then counted with a Neubauer counting chamber. During the optimization for this protocol, we learned the importance of keeping the hemolymph and hemocytes on ice (or 4°C during centrifugation) to prevent melanization. In Figure 3 from **Article 4**, hemocyte proliferation was seen with all concentrations of NPs tested. Hemocyte proliferation was also seen in response to sub-lethal doses of bacterial antigens (results not shown). Additionally, we optimized a microscope staining technique to determine whether hemocytes were capable of internalizing NPs (Figure 4, **Article 4**). Different dyes were individually tested, such as Syto™ 60 (red, stains nucleic acids), Concanavalin A, Alexa Fluor™ 350 (blue, stains polysaccharides), Concanavalin A, Alexa Fluor™ 647 (red, stains polysaccharides), FM™ 4-64 (red, stains lipids in cell membrane), and DAPI (blue, stains DNA). The one that worked best for our purposes was FM™4-64 as it stained the membrane of the hemocytes red while allowing the visualization of the internalized NPs (Figure 4, **Article 3**). By optimizing this methodology, we were able to easily determine whether hemocytes were proliferating in response to the invaders and whether they were capable of internalizing NPs as part of the immune response.

Bacterial infection studies in *Galleria mellonella*

Fluorescent proteins have been previously used to detect bacterial infection sites *in vivo*, and fluorescent promoter probe vectors have been utilized to analyze gene expression during bacterial

infections [103,243,244]. Therefore, these vectors would be ideal to study gene expression in *G. mellonella*, and this is the focus of **Article 1**. Initial gene expression studies were done by infecting larvae with *P. aeruginosa* PAO1 strains expressing GFP and E2Crimson (Figure 2, **Article 1**). As a control, larvae were also infected with PAO1 (without any fluorescence marker) and PBS. The hemolymph of the infected larvae was extracted, and the fluorescence from the bacteria was measured using a microplate reader. The relative fluorescence measurements revealed that the hemolymph and hemocytes of *G. mellonella* larvae have intrinsic autofluorescence. Therefore, we have demonstrated that fluorescent vectors cannot be used for this type of study as changes in fluorescence due to genetic expression cannot be easily distinguished from the autofluorescence of the larvae. Our experiments with bioluminescent *P. aeruginosa* PAO1 revealed that the larvae that were not infected with the bioluminescent bacteria had almost imperceptible background bioluminescence (Figure 1, **Article 1**). For this reason, vectors expressing bioluminescence seem like the most optimal alternative for gene expression studies.

To study gene expression using bioluminescence in *G. mellonella* larvae, we constructed a promoter probe vector expressing bioluminescence that was named pETS220-BIATlux. This plasmid contains a *luxCDABE* operon and is a broad-host-range vector, has a multi-cloning site that contains unique restriction sites for easy insertion of the promoter fragment of interest, and carries gentamicin resistance for simple clone selection (Figure 3, **Article 1**). As a proof of concept for our new vector, we evaluated the expression of the ribonucleotide reductase (*nrd*) genes during an *in vivo* infection. The promoters of the different *P. aeruginosa* ribonucleotide reductase genes (*PnrdA*, *PnrdJ*, *PnrdD*, and *PnrdR*) were cloned into the pETS220-BIATlux vector. All promoters were included to efficiently detect differences in gene expression during the infection. As a negative control, a fragment of the *anr* gene similar in size to the promoters used was also cloned into the vector. This was done to detect the intrinsic bioluminescence of the vector. After all the promoter fusions were successfully constructed, they were easily transformed into *P. aeruginosa* PAO1 cells by electroporation. *G. mellonella* larvae were injected with the PAO1 strains containing the different constructions, and bioluminescence was measured with two instruments at different time points during the infection. With the ImageQuant™ LAS 4000 mini imager, bioluminescence could only be seen qualitatively (Figure 4B, **Article 1**). In contrast, bioluminescence could be measured quantitatively using the Spark® multimode microplate reader (Figure 4A, **Article 1**). Nevertheless, the results obtained with both instruments coincided at the corresponding time points. The bioluminescence quantitative measurements showed that the infection could be monitored as the RLU values within the larvae increased over time for the different strains according to the level of

expression of the different *nrd* genes, as regulated by the promoters controlling the *luxCDABE* operon (Figure 4A, **Article 1**). The expression of both *PnrdR*-lux and *PnrdJ*-lux began to rise at 14 hours post-infection and continued to increase throughout the remainder of the infection. In contrast, *PnrdD*-lux and *PnrdA*-lux had lower expression levels during most of the infection which did not peak until 17-20 hours post-infection. At 20 hours post-infection (death), *PnrdR*-lux had the highest RLU values, thus demonstrating that *nrdR* is highly expressed not only at death but throughout the whole infection. The negative control, *Anr*-lux, had low levels of bioluminescence that were consistent with background signals caused by leaking reporter expression. Despite the leaking, the values of all the other strains were much higher than *Anr*-lux at all time points. The highest RLU value obtained with *Anr*-lux was only 2600 at 20 hours post-infection, which is about 46 times less than the lowest corresponding value (*PnrdD*-lux, 1.2×10^5 RLU). The results were also represented by induction factors. As previously mentioned, the negative control had a luminescent background signal, so it was first subtracted from each of the corresponding strains and time points. The induction values seen in Figure 4C from **Article 1** are the induction factors of each strain at the different time points when compared to itself at the initial time point (8 hours post-infection). A high induction in *nrdR* expression was clearly seen during all time points (119, 18217, and 106174-fold induction at 14, 17, and 20 hours, respectively). At the same time points, the second and third highest expressions were seen with *nrdJ* (73, 3988, and 6706-fold induction) and *nrdD* (12, 543, and 3557-fold induction), respectively. A small induction (4–46-fold) was seen with *nrdA* expression in the first hours until it suddenly increased at the last time point (up to 6838 times).

By using the different *nrd* promoter-lux fusion constructions, we were able to observe and monitor a shift of *nrd* expression during an *in vivo P. aeruginosa* infection. This shift is reported for the first time in *G. mellonella*, and it corresponds with previous results obtained in our lab with other *in vivo* models. In the *Drosophila melanogaster* and *Danio rerio* infection models, the expression of *nrdJ* and *nrdD* was also highly induced throughout the course of a *P. aeruginosa* infection [102,103]. Our results corroborate the importance of anaerobic environments for the *in vivo* expression of RNR class II and III [102,104,245]. Furthermore, while *nrdR* expression has been reported to increase *in vitro* [245], our experiments with *G. mellonella* are the first ones to report *nrdR* induction during an *in vivo* bacterial infection. Our promoter probe vector with bioluminescence expression offers a simple and effective method for monitoring gene expression *in vivo* using whole *G. mellonella* larvae.

Antimicrobial efficacy studies in *G. mellonella*

As the emergence and global spread of drug-resistant pathogens is rapidly rising, there is an urgent need for new antimicrobials. One of the main causes of antimicrobial resistance is the misuse and overuse of antimicrobials. Unless people change these bad habits, new antimicrobials will eventually become ineffective as well [191]. The development of antimicrobial alternatives with a reduced risk of resistance would be ideal. Generally, new antimicrobials are first tested *in vitro* to assess their effectiveness, and the most promising candidates will be tested *in vivo* using murine models prior to human testing. *G. mellonella* offers a simple and inexpensive alternative for quick *in vivo* evaluations of antimicrobial effectiveness. Furthermore, it can decrease the probabilities of obtaining unsuccessful results in murine models with drugs that showed promise *in vitro* [41].

In **Article 2**, the antimicrobial efficacy of novel oleanolic and maslinic acid derivatives was tested in *G. mellonella* larvae. OA and MA are pentacyclic triterpenic compounds that are found in the fruits and leaves of *Olea europaea* and therefore, copious amounts are found in industrial olive oil waste [246]. OA and MA have known antimicrobial properties and more importantly, no bacterial resistance mechanisms have been reported yet. In this article, 14 OA and MA amide derivatives were synthesized and their antimicrobial efficiency was tested *in vitro* and *in vivo*. The *in vitro* efficacy was tested using an array of Gram-positive and Gram-negative bacteria to determine the concentration of each compound that inhibits bacterial growth by 50% (MIC₅₀). The amide derivatives had no antimicrobial effects against any of the Gram-negative bacteria tested (Table 1, **Article 2**). In contrast, better efficacy was seen against Gram-positive strains. The MA-HDA and OA-HDA derivatives had the highest efficacy against *S. aureus* and Methicillin-Resistant *S. aureus* (MRSA) since they either matched or increased the antimicrobial activity of their parent compounds as seen by the same or reduced MIC₅₀. Since MA-HDA and OA-HDA were deemed the best amide derivatives, they were used (along with their parent compounds) to test their *in vivo* efficacy against *S. aureus* using *G. mellonella* larvae. The larvae were injected with *S. aureus* at a concentration of 1.5x10⁷ CFU/larvae. Then, a dose of each compound was given at 1 hour and 6 hours post-infection (240 mg/kg total concentration). The MA and MA-HDA treatments saved 50% of the larvae from succumbing to the *S. aureus* infection. On the other hand, only 10% of the larvae survived after OA treatment, and OA-HDA treatment failed to save the larvae. By using *G. mellonella* larvae, we were able to determine that OA and OA-HDA lacked *in vivo* activity against *S. aureus* without involving murine models. We also confirmed that both MA and MA-HDA have antimicrobial efficiency against *S. aureus*, so these could now be tested in rodents with sufficient justification. Additionally, the

treatment conditions can be further optimized with this model (e.g., more treatment doses) to reduce the number of rodents even further. For this, one experiment that would be helpful is to measure the bacterial load within the larvae at different time points after treatment, and the results would determine whether the compounds are actively killing the bacteria. All of these reasons demonstrate the practicality of the *G. mellonella* model for antimicrobial efficacy studies.

Toxicity studies in *G. mellonella*

The *G. mellonella* animal model has been widely used to assess efficacy and toxicity of many therapeutic compounds. As the efficacy of the MA, OA, MA-HDA, and OA-HDA compounds was being studied in **Article 2**, the toxicity of these compounds was also determined in *G. mellonella*. The larvae were injected with different concentrations of the compounds to calculate the LD₅₀ which was then used to calculate the SI (Table I, **Article 2**). For half of the compounds tested, the toxicity obtained *in vivo* was higher than the toxicity obtained *in vitro*, but it can be different in other instances. For example, the toxicity of the MA-HDA compound increased *in vivo*, but the toxicity of its parent compound (MA) decreased *in vivo*. These results highlight the importance of using an animal model to evaluate toxicity as it allows for a better selection of a compound for further investigative steps. Another way to analyze the efficacy was to calculate the SI, which is a largely accepted parameter that can be used to predict whether a drug is effective and safe during *in vivo* treatment [247]. The SI of the compounds improved considerably when using the *in vivo* LD₅₀ instead of the *in vitro* CC₅₀. For instance, the SI for MA-HDA was 17.9 when calculated using the CC₅₀ and it increased to 661 when using the LD₅₀. Therefore, this compound would be described as active against *S. aureus* and safe to use if using the 661 SI value, but it would be more likely to be discarded as unsafe and ineffective if it depended only on the 17.9 SI value. These results demonstrate the importance of using an *in vivo* model to calculate the SI of a potential antimicrobial agent to better predict its performance in humans. The *G. mellonella* model can be used to achieve this as it offers a cheap screening alternative for *in vivo* toxicity and efficacy prior to analysis in rodents or other more expensive mammalian models.

G. mellonella can also be used to test the toxicity of other therapeutical strategies. The current gold standard treatment for non-muscle-invasive bladder cancer patients is intravesical immunotherapy with *M. bovis* BCG [248]. Since half of these patients develop adverse effects, the safety of *M. brumae* as a potential alternative therapy was assessed [242]. At all concentrations tested, *M. brumae* was not lethal to *G. mellonella* larvae (Appendix Figure 2C). Furthermore, the

larvae were able to eliminate the bacteria since no bacteria was recovered from the hemolymph of the infected larvae at the end of the experiments (6 days post-infection) (Appendix Figure 3). In contrast, less survivability was seen in larvae infected with *M. bovis* BCG (Appendix Figure 2C), and these larvae were not able to eliminate the bacteria since high concentrations of *M. bovis* BCG were recovered from the hemolymph of the infected larvae (Appendix Figure 3). Additionally, *M. brumae* did not cause any toxicity effects in mice and was deemed safe to use as treatment for non-muscle-invasive bladder cancer. The toxicity results obtained with *G. mellonella* correlated with the results obtained with mice, which further proves the efficacy of the model.

The toxicity of nanoparticles can also be assessed using *G. mellonella* larvae. We performed several experiments to exploit the potential of this animal model as a nanotoxicological *in vivo* model. First, the larvae were used to calculate the LD₅₀ for every type of NP tested. For this, various NP concentrations were injected into the larvae and mortality was assessed at different time points. The results revealed that the SeNPs were the most toxic to the larvae followed by AgNPs and Au(HAL)NPs (Figure 2, **Article 3**). Although the cytotoxicity results with A549 cells had the same pattern, the CC₅₀ values were much lower than the LD₅₀ values. *In vitro* cytotoxicity assays are not the most optimal method to predict NPs toxicity as the results are affected by a variety of factors such as the cell line used, incubation times, and NP concentrations tested [249,250]. On the other hand, LD₅₀ doses can be defined in a more efficient way using *G. mellonella* larvae since large groups of larvae can be used to screen numerous types and concentrations of NPs. The LD₅₀ values acquired in our studies are more comparable to the LD₅₀ values obtained with murine models (Table 1, **Article 3**) which demonstrates that *G. mellonella* is a more reliable model for initial toxicity screenings.

The cellular immune response found in *G. mellonella* is mediated by hemocytes and these cells have been found to be involved in phagocytosis, encapsulation, and nodulation of foreign intruders [15]. Our toxicity studies demonstrated that circulating hemocytes were able to internalize more than one nanoparticle simultaneously (Figure 4, **Article 3**). The histological analysis of larvae injected with NPs revealed an accumulation of hemocytes surrounding the NPs (Figure 6, **Article 3**). These results further indicate that hemocytes are actively involved in an immune response against the foreign NPs, although further studies are needed to determine the exact uptake mechanism. Another way to determine whether the innate immune system of the larvae is activated is to measure changes in the number of circulating hemocytes [15]. Some studies have demonstrated that increases in hemocyte density in *G. mellonella* is linked to toxicity of compounds [17,204]. For this reason, hemocyte density was quantified in all larval groups injected with the different NPs (Figure 3, **Article 3**). All NP concentrations resulted in significant hemocyte proliferation when

compared to the control group (larvae injected with PBS only). An interesting result was obtained with the lowest concentrations of Au(HAL)NPs and AgNPs, as these concentrations yielded the highest hemocyte proliferation (Figure 3A and 3B, **Article 3**). This finding suggests that exposure of the larvae to low doses of these NPs boosted hemocyte proliferation due to hormesis, which is described as the production of stimulatory effects by low doses of potentially toxic compounds [251]. The surface functionalization of the AuNPs with amino acids could also play a role since these NPs are cationic and can be easily recognized by phagocytic or other removal systems [252]. In contrast, the hemocyte density decreased as the concentrations of Au(HAL)NPs and AgNPs increased. The most probable explanation for this is that the larvae were experiencing potential damage of hemopoietic organs due to the toxicity of the NPs [215]. The hemocyte density values obtained with SeNPs were more or less constant with all the concentrations tested (Figure 3C, **Article 3**). Since the LD₅₀ experiments showed that these NPs were the most toxic, the lack of hemocyte proliferation is probably due to increased cell death from the high toxicity of the NPs. This argument was reinforced with the histology results. Stained sections of the larvae injected with SeNPs showed that large clusters of these NPs were surrounded by large extracellular spaces (Figure 6C, **Article 3**) which is indicative of increased cell death due to the toxic activity of the NPs. The larvae injected with AgNPs and Au(HAL)NPs also had the extracellular spaces surrounding the clusters of NPs (Figure 6D and 6E, **Article 3**), but these were significantly smaller than the ones seen with SeNPs. Since the larvae were killed 1 hour after injection, more time might be needed to visualize tissue damage like the one seen with the larvae injected with SeNPs. The histology results seem to correlate with the reduced toxicity of the Ag and Au(HAL) nanoparticles seen with our previous experiments.

The different NPs injected into *G. mellonella* larvae were found to accumulate primarily in the caudal area (tails) of the larvae (Figure 5A, **Article 3**). This phenomenon continued to occur even after the larval movement was partially or fully restricted (Figure 5B, **Article 3**). This suggests that the accumulation is not due to the peristaltic movement of the worms. However, the NPs could still potentially move through the hemolymph of the larvae due to the contractions of the abdominal spiracles during respiration [253] or another unknown mechanism, so further studies are needed to decipher this event. The histological analysis confirmed the presence of NP aggregates in the caudal parts of the larvae. The largest degree of accumulation was seen with SeNPs which resulted in big stellate-like aggregates that were predominant in the most caudal part of the larvae (Figure 6B and 6C, **Article 3**). The aggregates seen with AgNPs and Au(HAL)NPs were smaller and more dispersed along the rostrocaudal axis of the larvae (Figure 6D and 6E, **Article 3**). The control larvae that were

injected with PBS showed no alterations in the gross anatomical distribution as reported by other studies [254] (Figure 6A, **Article 3**).

The final way that we used to study NP toxicity in *G. mellonella* larvae was to assess the behavior of the larvae after injection with a toxic concentration of the NPs (Figure 7, **Article 3**). The larvae injected with Au(HAL)NPs behaved similarly to the larvae injected with PBS as a control, but this was expected as the concentration of Au(HAL)NPs tested was not lethal to the larvae until several hours post-injection. On the other hand, the larvae injected with AgNPs experienced significantly reduced motility while the larvae injected with SeNPs completely lacked mobility (Figure 7B, **Article 3**). Furthermore, the larvae blackened in color in response to the toxicity of AgNPs and SeNPs with the latter causing the fastest darkening. These behavioral results further validate the toxicity effects seen with the rest of the experiments performed in this study.

The results obtained with all of the experiments performed in **Article 3** were all consistent according to the level of toxicity of each type of NP. This demonstrates the significant utility of this animal model as the results obtained are more reliable than with traditional *in vitro* models and toxicity screenings can be performed in an inexpensive, convenient, and more ethical manner. This study revealed that *G. mellonella* offers an array of indicators to assess NP toxicity *in vivo*, and it is proposed as a nanotoxicological model that can be used as a bridge between *in vitro* and *in vivo* murine assays to better predict NP toxicity.

Methodology advances in *G. mellonella*

Due to the wide applicability of the *G. mellonella* model, new methodologies are warranted to exploit its full potential. For this work, a few different methodologies were optimized using *G. mellonella* larvae. The first one was a protocol to extract RNA from bacterial cells derived from a *G. mellonella* infection (Figure 5A, **Article 1**). As a proof of concept, we used the extracted RNA to measure RNR gene expression during a *P. aeruginosa* infection in *G. mellonella*. The larvae were injected with *P. aeruginosa* PAO1 wild-type cells and then incubated at 37°C for 16 hours. Based on previous growth curves done with PAO1 in *G. mellonella*, we knew that about 10⁸ CFU/ml were present inside the larvae at 16 hours post-infection (Figure 5B, **Article 1**). This bacterial concentration was deemed sufficient for RNA extraction as it is close to the ~10⁹ CFU/ml concentration recommended by the manufacturer of the RNA purification kit. The PAO1 growth curves also verified an active and ongoing DNA synthesis due to the involvement of RNR during the infection process. After the 16-hour incubation, the larvae were anesthetized on ice for 10 minutes

and then the hemolymph was removed. The hemolymph was centrifuged at low speed for 5 minutes at 4°C to remove the hemocytes. The cell-free hemolymph containing the PAO1 cells was used for RNA purification that resulted in high and pure RNA concentrations (Supplementary Table 3, **Article 1**).

The purified RNA was used for cDNA preparation and qRT-PCR analysis to measure RNR gene expression. As a reference, the gene expression of *P. aeruginosa* PAO1 wild-type cells grown in LB medium to mid-exponential growth phase was also measured. This control was chosen based on the growth curve in Figure 5B from Article 1 that shows that the PAO1 cells within the larvae are in mid-exponential growth phase during sample collection. The qRT-PCR results were analyzed using the comparative Ct (cycle threshold) method ($\Delta\Delta Ct$) by comparing the Cts of the different genes in a PAO1 infection against the Cts of the same genes in a PAO1 exponential culture. The transcript levels of each gene were normalized using the *gapA* as an internal control since the expression of *gapA* is vital during *P. aeruginosa* growth. The results clearly showed variations in the expression of the different *nrd* genes (Figure 5C, **Article 1**). The highest inductions were seen with *nrdR* and *nrdJ* as they were both about 7 times more induced during infection than in planktonic culture. On the other hand, *nrdA* was induced 3.1 times more while *nrdD* was less induced (1.7 times more) when compared to the reference planktonic culture. We also measured the expression of the *norC* gene (an anaerobiosis marker), and it revealed a 5.3-fold increase that indicated a shift in the anaerobic metabolism of PAO1 during infection. The results obtained with this methodology are very similar to the ones obtained with the different pETS220-BIATlux constructions (Figure 4, **Article 1**). The only difference was seen with *nrdD* and *nrdA* since higher expression was seen with *PnrdD*-lux than with *PnrdA*-lux. This could be due to the RNA extraction occurring at 16 hours post-infection while the pETSlux measurements were done at 17 hours post-infection, and gene expression levels depend on the metabolic state of the bacteria during RNA extraction. By using this optimized RNA extraction protocol, *P. aeruginosa* PAO1 cells derived from an *in vivo* *G. mellonella* infection were able to be isolated for efficient RNA purification that was successfully used in downstream applications.

The RNR gene expression studies in *G. mellonella* were first attempted using fluorescent promoter probe vectors that were previously constructed [100,102]. *G. mellonella* larvae were injected with four *P. aeruginosa* PAO1 strains that contain plasmids which encode transcriptional fusions of the *nrdA* and *nrdJ* promoters with GFP and E2Crimson. As a control, groups of larvae were injected with *P. aeruginosa* PAO1 wild-type and PBS. The hemolymph from the infected larvae was extracted at different time points and it was used for relative fluorescence quantification as well as fluorescence microscopy imaging. The hemolymph containing PAO1 wild-type cells revealed high

levels of green and red fluorescence that were similar to the values obtained with the PAO1 strains expressing GFP and E2Crimson (Figures 2A and 2B, **Article 1**). The hemolymph of the larvae injected with PBS also had high fluorescence values, and the values were also comparable to the ones obtained with the expression vectors. Since the hemolymph alone had such high RFU/ml values, we concluded that the hemolymph has natural autofluorescence. Furthermore, the hemocytes also appear to have intrinsic autofluorescence. This is indicated by the high RFU/ml values seen with the hemolymph of the larvae infected with the PAO1 wild-type strain even though it does not have any fluorophores. This hemolymph does have a high concentration of hemocytes as larval hemocytes proliferate in response to an infection [255], so this indicates that the hemocytes are the ones responsible for the high fluorescence values. The same hemolymphs were used for fluorescence microscopy analysis. The hemolymph containing PAO1 wild-type strain showed the hemocytes glowing green and red with the GFP and Texas red channels, respectively, thus confirming their natural autofluorescence (Figure 2C, **Article 1**). The fluorescence of the PAO1 strains expressing GFP and E2Crimson was difficult to differentiate from the autofluorescence of the hemocytes (Figures 2D and 2E, **Article 1**). The same was true with the RFU measurements as differences in gene expression were difficult to assess. The *PnrdA* strains had higher RFU values than the *PnrdJ* strains, but the true extent of the induction could not be determined. Regardless, *nrdA* was previously shown to be more induced than *nrdJ* during infection [102]. The results obtained with this technique show that the autofluorescence of hemocytes present an important limitation with the use of fluorescent vectors in *G. mellonella* as variations in fluorescence expression cannot be easily identified. By using this technique, we were able to discover the autofluorescence problems which led us to create a promoter probe vector with bioluminescence expression (pETS220-BIATlux) as an alternative vector for gene expression studies in *G. mellonella* (Figure 3, **Article 1**).

The last methodology optimized for this work was a clearing protocol for *G. mellonella* larvae. Imaging three-dimensional samples can be challenging due to obscuring effects caused by light scattering [224]. Optical clearing reduces lateral scattering thus allowing all light wavelengths to pass through the sample and making it transparent. The steps typically involved are sample fixation, permeabilization, and/or decolorization followed by refractive index (RI) matching [223]. *G. mellonella* clearing is an attractive approach as it would provide new insights on larval visualization and it would enable the study of bacterial infection processes, toxicity of various compounds, and NP interactions *in vivo*. Since clearing protocols in *G. mellonella* have not been previously reported, we had to optimize one from the start. The optimization was carried out using *G. mellonella* larvae injected with fluorescent rhodamine NPs as a proof of concept. A schematic representation of all

the different approaches used for the clearance can be seen in Figure 2 from **Article 4**. The first step optimized was the fixation. A few clearance protocols found in the literature fixed samples with paraformaldehyde (PFA) to preserve the molecules of interest [256,257]. Therefore, we tested different concentrations of PFA ranging from 1% to 4%, and they were all found to work the same for our purpose. We found that the fixation worked best when it was performed right after the larvae were injected, which is probably due to a better penetration of PFA through the open wound site. Nevertheless, successful clearance was achieved even when larval fixation was performed up to 16 hours post-infection.

The permeabilization and clearing steps were optimized next. These steps aim to remove lipids by replacing water with a high-RI medium. Two different strategies were attempted, one with alcohols and the other one with detergents. Permeabilization through dehydration alcohols involved testing different gradual concentrations of ethanol or methanol during both hourly and overnight incubation steps. Dehydration with ethanol never reached full delipidation as seen by the complete darkening of the larvae (Figure 2B, **Article 4**) caused by melanization. On the other hand, methanol dehydration seemed to work better at preventing melanization although it still affected the reproducibility sometimes. After dehydration with both types of alcohols, the larvae were incubated in 100% BABB (1 part Benzyl Alcohol + 2 parts Benzyl Benzoate) clearing solution. This high-RI medium was selected as the clearing solution as several experiments have reported successful clearing with BABB [226,233,237]. Cleared larvae were only obtained after dehydration with hourly incubation steps of increasing concentrations of methanol (Figure 2C, **Article 4**). We also noticed that better clearing results were obtained after incubating the larvae for 1 hour in a 1:1 mixture of pure methanol and BABB prior to the clearing step with 100% BABB. Permeabilization involving delipidation with detergents followed by RI matching with certain sugars was also attempted. For this, we tested 2% Triton X-100 combined with gradually increasing concentrations of sucrose (Figure 2D, **Article 4**). We also tried immersing fixed larvae directly in a 67% sucrose solution (Figure 2E, **Article 4**). Sucrose was selected since it has been reported to be an efficient tissue clarifying method due to its ability to facilitate cell permeability [223,258]. Neither of the sucrose protocols were able to achieve optical clearing in the larvae. The final optimized clearing protocol for *G. mellonella* larvae involved overnight incubation with 1% or 4% PFA, hourly incubations with increasing concentrations of methanol, 1-hour incubation in a 1:1 solution of pure methanol and BABB, and final incubation in 100% BABB for 7-10 days. A schematic representation of the protocol is seen in Figure 1B from **Article 4**.

To determine whether the clearing protocol was successful, the cleared larvae were visualized under a confocal microscope to see if the internal NPs could be detected. As a control, non-cleared larvae injected with NPs were also visualized. For these larvae, the fluorescence from the NPs could not be detected as the laser could not penetrate the cuticle, so visualizations deeper than 25 μm could not be obtained (Figure 3A, **Article 4**). On the other hand, NPs could be observed inside cleared larvae fixed with 1% PFA at a depth of 219.6 μm (Figure 3C, **Article 4**). Similar results were obtained with cleared larvae fixed with 4% PFA (Figure 3D, **Article 4**). These depth visualizations were only possible due to the reduced light scattering achieved by optical clearing. The extent of the clearing efficiency could not be determined using confocal microscopy since it has image depth limitations [224]. In contrast, image depths up to several millimeters inside cleared larvae could be obtained with ultramicroscopy or multiphoton microscopy techniques [226,233].

Another way to test the efficiency of our clearing protocol was attempted by measuring the relative fluorescence of the cleared larvae injected with the rhodamine fluorescent NPs. Cleared and non-cleared larvae injected with PBS as well as non-cleared larvae with NPs were included as controls. Low RFU values were obtained from the non-cleared larvae injected with PBS and NPs which is most likely due to the background fluorescence of the larvae (Figure 4, **Article 4**). In contrast, the cleared larvae injected with NPs revealed a considerable increase in RFU values as indicated by an induction factor of almost 13 that is statistically significant when compared to the cleared larvae without NPs. Furthermore, the difference in fluorescence emission between cleared and non-cleared larvae with NPs is clearly vast. The cleared larvae injected with PBS yielded a 6-fold increase in RFU values, but this is due to the larval autofluorescence being more detectable now that the larvae are cleared. Autofluorescence was also seen with the green channel during confocal microscopy analysis (Figure 3A and 3B, **Article 4**), so the autofluorescence of the larvae can also be a limitation when analyzing fluorescence in whole larvae. Regardless, we were able to visualize and quantify the fluorescence emitted by the NPs without any interference from the autofluorescence. Although the dehydration and BABB steps have been reported to weaken protein fluorescence [222], it did not affect the fluorescence of the NPs as seen by the intense rhodamine signal in our confocal images and in our fluorescence measurements. In fact, the clearing greatly improved the quantification of the NP fluorescence. Still, this limitation can be overcome by using other labeling techniques that are more resistant to dehydration, such as immunofluorescent labeling using antibodies conjugated with organic dyes or optimized fluorescent proteins [224]. Our optimized clearing protocol paves the way for further applications in the microbiology and nanomedicine fields.

CONCLUSIONS

The information and data presented in this thesis as well as in the articles have answered the proposed objectives by demonstrating the advances accomplished for the utilization of *G. mellonella* as an animal model for infection and toxicity studies. Therefore, the conclusions for this thesis are as follows:

1. The hemolymph and hemocytes of *G. mellonella* larvae exhibit intrinsic autofluorescence that limits the use of fluorescent promoter probe vectors in this animal model of infection
2. A promoter probe vector with bioluminescence expression (pETS220-BIATlux) was constructed which offers a simple and effective method for measuring gene expression *in vivo* using the *G. mellonella* animal model of infection.
3. An RNA extraction protocol for bacterial cells derived from a *G. mellonella* infection was optimized to enable the study of transcriptional levels of genes during an *in vivo* infection.
4. Antimicrobial efficacy results obtained *in vitro* can be easily and inexpensively validated *in vivo* using *G. mellonella* larvae prior to testing in murine models.
5. MA-HDA showed the most efficient antimicrobial efficacy by increasing the survival of *G. mellonella* larvae infected with *S. aureus* by 50%, and it also exhibited reduced toxicity by improving its SI after *G. mellonella* testing.
6. The toxicity results achieved with *M. brumae* in *G. mellonella* larvae correlate well with the toxicity results obtained with *M. brumae* in mice.
7. *G. mellonella* larvae can be used to do toxicity screenings of various NPs in an economical, convenient, and ethical manner.
8. The extent of NP toxicity can be efficiently determined using *G. mellonella* larvae by evaluating mortality, hemocyte density, larval behavior, and histological changes.
9. *G. mellonella* can be used as a bridge between *in vitro* models and *in vivo* murine assays to reduce the number of toxicity testing done in mammals.

10. A clearing protocol was optimized for *G. mellonella* larvae that involved three steps: fixation with PFA, permeabilization with methanol dehydration, and optical clearing with BABB.
11. Cleared *G. mellonella* larvae enabled the visualization of internalized fluorescent NPs using confocal microscopy, and it also facilitated the quantification of the fluorescence emitted by the same NPs.

REFERENCES

1. Ellis, J.D.; Graham, J.R.; Mortensen, A. Standard methods for wax moth research. *Journal of Apicultural Research* **2013**, *52*, 1-17, doi:10.3896/IBRA.1.52.1.10.
2. Williams, J.L. Insects: Lepidoptera (moths). In *Honey bee pests, predators, and diseases.*, Morse, R., Flottum, K., Eds. Al Root Company: Medina, OH, USA, 1997; pp. 121-141.
3. Nielsen, R.A.; Brister, C.D. Greater Wax Moth: Behavior of Larvae. *Annals of the Entomological Society of America* **1979**, *72*, 811–815, doi:10.1093/aesa/72.6.811.
4. Krams, I.; Kecko, S.; Kangassalo, K.; Moore, F.R.; Jankevics, E.; Inashkina, I.; Krama, T.; Lietuviētis, V.; Meija, L.; Rantala, M.J. Effects of food quality on trade-offs among growth, immunity and survival in the greater wax moth *Galleria mellonella*. *Insect Sci* **2015**, *22*, 431-439, doi:10.1111/1744-7917.12132.
5. Awmack, C.S.; Leather, S.R. Host plant quality and fecundity in herbivorous insects. *Annu Rev Entomol* **2002**, *47*, 817-844, doi:10.1146/annurev.ento.47.091201.145300.
6. Warren, L.; Huddleston, P. Life history of the greater wax moth, *Galleria mellonella* L., in Arkansas. *Journal of the Kansas Entomological Society* **1962**, *35*, 212-216.
7. Charrière, J.-D.; Imdorf, A. Protection of honey combs from moth damage. *American Bee Journal* **1999**, *139*, 627-630.
8. Jorjão, A.L.; Oliveira, L.D.; Scorzoni, L.; Figueiredo-Godoi, L.M.A.; Cristina A Prata, M.; Jorge, A.O.C.; Junqueira, J.C. From moths to caterpillars: Ideal conditions for *Galleria mellonella* rearing for in vivo microbiological studies. *Virulence* **2018**, *9*, 383-389, doi:10.1080/21505594.2017.1397871.
9. Shimanuki, H. *Controlling the Greater Wax Moth: A Pest of Honeycombs*; Administration, S.a.E., Ed. United States Department of Agriculture: Washington, DC, USA, 1981; Vol. 2217.
10. Kwadha, C.A.; Ong'amo, G.O.; Ndegwa, P.N.; Raina, S.K.; Fombong, A.T. The Biology and Control of the Greater Wax Moth, *Galleria mellonella*. *Insects* **2017**, *8*, doi:10.3390/insects8020061.
11. Wojda, I. Immunity of the greater wax moth *Galleria mellonella*. *Insect Sci* **2017**, *24*, 342-357, doi:10.1111/1744-7917.12325.
12. Pereira, T.C.; de Barros, P.P.; Fugisaki, L.R.O.; Rossoni, R.D.; Ribeiro, F.C.; de Menezes, R.T.; Junqueira, J.C.; Scorzoni, L. Recent Advances in the Use of *Galleria mellonella* Model to Study Immune Responses against Human Pathogens. *J Fungi (Basel)* **2018**, *4*, doi:10.3390/jof4040128.
13. Moussian, B. Recent advances in understanding mechanisms of insect cuticle differentiation. *Insect Biochem Mol Biol* **2010**, *40*, 363-375, doi:10.1016/j.ibmb.2010.03.003.
14. Ratcliffe, N.A. Invertebrate immunity-a primer for the non-specialist. *Immunology Letters* **1985**, *10*, 253-270, doi:10.1016/0165-2478(85)90100-2.
15. Browne, N.; Heelan, M.; Kavanagh, K. An analysis of the structural and functional similarities of insect hemocytes and mammalian phagocytes. *Virulence* **2013**, *4*, 597-603, doi:10.4161/viru.25906.
16. Matha, V.; Mráček, Z. Changes in haemocyte counts in *Galleria mellonella* (L.) (Lepidoptera: Galleriidae) larvae infected with *Steinernema* Sp. (Nematoda: Steinernematidae). *Nematologica* **1984**, *30*, 86-89, doi:10.1163/187529284X00482.
17. Maguire, R.; Kunc, M.; Hyrsl, P.; Kavanagh, K. Analysis of the acute response of *Galleria mellonella* larvae to potassium nitrate. *Comp Biochem Physiol C Toxicol Pharmacol* **2017**, *195*, 44-51, doi:10.1016/j.cbpc.2017.02.007.
18. Ratcliffe, N.A.; Gagen, S.J. Studies on the *in vivo* cellular reactions of insects: an ultrastructural analysis of nodule formation in *Galleria mellonella*. *Tissue Cell* **1977**, *9*, 73-85, doi:10.1016/0040-8166(77)90050-7.

19. Lavine, M.D.; Strand, M.R. Insect hemocytes and their role in immunity. *Insect Biochem Mol Biol* **2002**, *32*, 1295-1309, doi:10.1016/s0965-1748(02)00092-9.
20. Arteaga Blanco, L.A.; Crispim, J.S.; Fernandes, K.M.; de Oliveira, L.L.; Pereira, M.F.; Bazzoli, D.M.S.; Martins, G.F. Differential cellular immune response of *Galleria mellonella* to *Actinobacillus pleuropneumoniae*. *Cell Tissue Res* **2017**, *370*, 153-168, doi:10.1007/s00441-017-2653-5.
21. Strand, M.R. Insect Hemocytes and Their Role in Immunity. In *Insect Immunology*, Beckage, N.E., Ed. Academic Press/Elsevier: San Diego, CA, 2008; Vol. 15, pp. 25-47.
22. Tojo, S.; Naganuma, F.; Arakawa, K.; Yokoo, S. Involvement of both granular cells and plasmatocytes in phagocytic reactions in the greater wax moth, *Galleria mellonella*. *J Insect Physiol* **2000**, *46*, 1129-1135, doi:10.1016/s0022-1910(99)00223-1.
23. Baggiolini, M.; Wymann, M.P. Turning on the respiratory burst. *Trends Biochem Sci* **1990**, *15*, 69-72, doi:10.1016/0968-0004(90)90179-f.
24. Strand, M.R.; Pech, L.L. Immunological basis for compatibility in parasitoid-host relationships. *Annu Rev Entomol* **1995**, *40*, 31-56, doi:10.1146/annurev.en.40.010195.000335.
25. Pech, L.L.; Strand, M.R. Granular cells are required for encapsulation of foreign targets by insect haemocytes. *J Cell Sci* **1996**, *109* (Pt 8), 2053-2060.
26. Grizanova, E.V.; Semenova, A.D.; Komarov, D.A.; Chertkova, E.A.; Slepneva, I.A.; Dubovskiy, I.M. Maintenance of redox balance by antioxidants in hemolymph of the greater wax moth *Galleria mellonella* larvae during encapsulation response. *Arch Insect Biochem Physiol* **2018**, *98*, e21460, doi:10.1002/arch.21460.
27. Kavanagh, K.; Reeves, E.P. Exploiting the potential of insects for *in vivo* pathogenicity testing of microbial pathogens. *FEMS Microbiol Rev* **2004**, *28*, 101-112, doi:10.1016/j.femsre.2003.09.002.
28. Kopáček, P.; Weise, C.; Götz, P. The prophenoloxidase from the wax moth *Galleria mellonella*: purification and characterization of the proenzyme. *Insect Biochem Mol Biol* **1995**, *25*, 1081-1091, doi:10.1016/0965-1748(95)00040-2.
29. Demir, D.; Gençer, N.; Er, A. Purification and characterization of prophenoloxidase from *Galleria mellonella* L. *Artif Cells Blood Substit Immobil Biotechnol* **2012**, *40*, 391-395, doi:10.3109/10731199.2012.696060.
30. Schmit, A.R.; Rowley, A.F.; Ratcliffe, N.A. The role of *Galleria mellonella* hemocytes in melanin formation. *Journal of Invertebrate Pathology* **1977**, *29*, 232-234.
31. Bidla, G.; Hauling, T.; Dushay, M.S.; Theopold, U. Activation of insect phenoloxidase after injury: endogenous versus foreign elicitors. *J Innate Immun* **2009**, *1*, 301-308, doi:10.1159/000168009.
32. Hoffmann, J.A.; Reichhart, J.M.; Hetru, C. Innate immunity in higher insects. *Curr Opin Immunol* **1996**, *8*, 8-13, doi:10.1016/s0952-7915(96)80098-7.
33. Li, D.; Scherfer, C.; Korayem, A.M.; Zhao, Z.; Schmidt, O.; Theopold, U. Insect hemolymph clotting: evidence for interaction between the coagulation system and the prophenoloxidase activating cascade. *Insect Biochem Mol Biol* **2002**, *32*, 919-928, doi:10.1016/s0965-1748(02)00030-9.
34. Gillespie, J.P.; Kanost, M.R.; Trenczek, T. Biological mediators of insect immunity. *Annu Rev Entomol* **1997**, *42*, 611-643, doi:10.1146/annurev.ento.42.1.611.
35. Rowley, A.F.; Ratcliffe, N.A. The granular cells of *Galleria mellonella* during clotting and phagocytic reactions in vitro. *Tissue Cell* **1976**, *8*, 437-446, doi:10.1016/0040-8166(76)90004-5.
36. Dushay, M.S. Insect hemolymph clotting. *Cell Mol Life Sci* **2009**, *66*, 2643-2650, doi:10.1007/s00018-009-0036-0.

37. Altincicek, B.; Stötzel, S.; Wygrecka, M.; Preissner, K.T.; Vilcinskas, A. Host-derived extracellular nucleic acids enhance innate immune responses, induce coagulation, and prolong survival upon infection in insects. *J Immunol* **2008**, *181*, 2705-2712, doi:10.4049/jimmunol.181.4.2705.
38. Nagai, T.; Kawabata, S. A link between blood coagulation and prophenol oxidase activation in arthropod host defense. *J Biol Chem* **2000**, *275*, 29264-29267, doi:10.1074/jbc.M002556200.
39. Yi, H.Y.; Chowdhury, M.; Huang, Y.D.; Yu, X.Q. Insect antimicrobial peptides and their applications. *Appl Microbiol Biotechnol* **2014**, *98*, 5807-5822, doi:10.1007/s00253-014-5792-6.
40. Rahnamaeian, M. Antimicrobial peptides: modes of mechanism, modulation of defense responses. *Plant Signal Behav* **2011**, *6*, 1325-1332, doi:10.4161/psb.6.9.16319.
41. Tsai, C.J.; Loh, J.M.; Proft, T. *Galleria mellonella* infection models for the study of bacterial diseases and for antimicrobial drug testing. *Virulence* **2016**, *7*, 214-229, doi:10.1080/21505594.2015.1135289.
42. Schuhmann, B.; Seitz, V.; Vilcinskas, A.; Podsiadlowski, L. Cloning and expression of gallerimycin, an antifungal peptide expressed in immune response of greater wax moth larvae, *Galleria mellonella*. *Arch Insect Biochem Physiol* **2003**, *53*, 125-133, doi:10.1002/arch.10091.
43. Cytryńska, M.; Mak, P.; Zdybicka-Barabas, A.; Suder, P.; Jakubowicz, T. Purification and characterization of eight peptides from *Galleria mellonella* immune hemolymph. *Peptides* **2007**, *28*, 533-546, doi:10.1016/j.peptides.2006.11.010.
44. Lee, Y.S.; Yun, E.K.; Jang, W.S.; Kim, I.; Lee, J.H.; Park, S.Y.; Ryu, K.S.; Seo, S.J.; Kim, C.H.; Lee, I.H. Purification, cDNA cloning and expression of an insect defensin from the great wax moth, *Galleria mellonella*. *Insect Mol Biol* **2004**, *13*, 65-72, doi:10.1111/j.1365-2583.2004.00462.x.
45. Brown, S.E.; Howard, A.; Kasprzak, A.B.; Gordon, K.H.; East, P.D. A peptidomics study reveals the impressive antimicrobial peptide arsenal of the wax moth *Galleria mellonella*. *Insect Biochem Mol Biol* **2009**, *39*, 792-800, doi:10.1016/j.ibmb.2009.09.004.
46. Brown, S.E.; Howard, A.; Kasprzak, A.B.; Gordon, K.H.; East, P.D. The discovery and analysis of a diverged family of novel antifungal moricin-like peptides in the wax moth *Galleria mellonella*. *Insect Biochem Mol Biol* **2008**, *38*, 201-212, doi:10.1016/j.ibmb.2007.10.009.
47. Kelley, L.A.; Mezulis, S.; Yates, C.M.; Wass, M.N.; Sternberg, M.J. The PyMol web portal for protein modeling, prediction and analysis. *Nat Protoc* **2015**, *10*, 845-858, doi:10.1038/nprot.2015.053.
48. Reynolds, C.R.; Islam, S.A.; Sternberg, M.J.E. EzMol: A Web Server Wizard for the Rapid Visualization and Image Production of Protein and Nucleic Acid Structures. *J Mol Biol* **2018**, *430*, 2244-2248, doi:10.1016/j.jmb.2018.01.013.
49. Zdybicka-Barabas, A.; Mak, P.; Klys, A.; Skrzypiec, K.; Mendyk, E.; Fiołka, M.J.; Cytryńska, M. Synergistic action of *Galleria mellonella* anionic peptide 2 and lysozyme against Gram-negative bacteria. *Biochim Biophys Acta* **2012**, *1818*, 2623-2635, doi:10.1016/j.bbame.2012.06.008.
50. Park, S.Y.; Kim, C.H.; Jeong, W.H.; Lee, J.H.; Seo, S.J.; Han, Y.S.; Lee, I.H. Effects of two hemolymph proteins on humoral defense reactions in the wax moth, *Galleria mellonella*. *Dev Comp Immunol* **2005**, *29*, 43-51, doi:10.1016/j.dci.2004.06.001.
51. Reeves, E.; Lu, H.; Jacobs, H.; al, e. Killing activity of neutrophils is mediated through activation of proteases by K + flux. *Nature* **2002**, *416*, 291-297, doi:10.1038/416291a.
52. Bogdan, C.; Rölinghoff, M.; Diefenbach, A. Reactive oxygen and reactive nitrogen intermediates in innate and specific immunity. *Curr Opin Immunol* **2000**, *12*, 64-76, doi:10.1016/s0952-7915(99)00052-7.
53. Whitten, M.M.; Mello, C.B.; Gomes, S.A.; Nigam, Y.; Azambuja, P.; Garcia, E.S.; Ratcliffe, N.A. Role of superoxide and reactive nitrogen intermediates in *Rhodnius prolixus* (Reduviidae)/*Trypanosoma rangeli* interactions. *Exp Parasitol* **2001**, *98*, 44-57, doi:10.1006/expr.2001.4615.

54. Lanz-Mendoza, H.; Hernández-Martínez, S.; Ku-López, M.; Rodríguez, M.e.C.; Herrera-Ortiz, A.; Rodríguez, M.H. Superoxide anion in *Anopheles albimanus* hemolymph and midgut is toxic to *Plasmodium berghei* ookinetes. *J Parasitol* **2002**, *88*, 702-706, doi:10.1645/0022-3395(2002)088[0702:SAIAAH]2.0.CO;2.
55. Krishnan, N.; Hyrsl, P.; Simek, V. Nitric oxide production by hemocytes of larva and pharate prepupa of *Galleria mellonella* in response to bacterial lipopolysaccharide: Cytoprotective or cytotoxic? *Comp Biochem Physiol C Toxicol Pharmacol* **2006**, *142*, 103-110, doi:10.1016/j.cbpc.2005.10.016.
56. Komarov, D.A.; Slepneva, I.A.; Glupov, V.V.; Khramtsov, V.V. Superoxide and hydrogen peroxide formation during enzymatic oxidation of DOPA by phenoloxidase. *Free Radic Res* **2005**, *39*, 853-858, doi:10.1080/10715760500166693.
57. Slepneva, I.A.; Glupov, V.V.; Sergeeva, S.V.; Khramtsov, V.V. EPR detection of reactive oxygen species in hemolymph of *Galleria mellonella* and *Dendrolimus superans sibiricus* (Lepidoptera) larvae. *Biochem Biophys Res Commun* **1999**, *264*, 212-215, doi:10.1006/bbrc.1999.1504.
58. Scandalios, J.G. Oxidative stress: molecular perception and transduction of signals triggering antioxidant gene defenses. *Braz J Med Biol Res* **2005**, *38*, 995-1014, doi:10.1590/s0100-879x2005000700003.
59. Champion, O.L.; Cooper, I.A.M.; James, S.L.; Ford, D.; Karlyshev, A.; Wren, B.W.; Duffield, M.; Oyston, P.C.F.; Titball, R.W. *Galleria mellonella* as an alternative infection model for *Yersinia pseudotuberculosis*. *Microbiology* **2009**, *155*, 1516-1522, doi:10.1099/mic.0.026823-0.
60. Felton, G.W.; Summers, C.B. Antioxidant systems in insects. *Arch Insect Biochem Physiol* **1995**, *29*, 187-197, doi:10.1002/arch.940290208.
61. Dubovskii, I.M.; Grizanova, E.V.; Chertkova, E.A.; Slepneva, I.A.; Komarov, D.A.; Vorontsova, I.L.; Glupov, V.V. Generation of reactive oxygen species and activity of antioxidants in larva hemolymph of *Galleria mellonella* (L.) (Lepidoptera: Piralidae) at development of process of encapsulation. *Zh Evol Biokhim Fiziol* **2010**, *46*, 30-36.
62. Fearon, D.T. Seeking wisdom in innate immunity. *Nature* **1997**, *388*, 323-324, doi:10.1038/40967.
63. Little, T.J.; Kraaijeveld, A.R. Ecological and evolutionary implications of immunological priming in invertebrates. *Trends Ecol Evol* **2004**, *19*, 58-60, doi:10.1016/j.tree.2003.11.011.
64. Bergin, D.; Murphy, L.; Keenan, J.; Clynes, M.; Kavanagh, K. Pre-exposure to yeast protects larvae of *Galleria mellonella* from a subsequent lethal infection by *Candida albicans* and is mediated by the increased expression of antimicrobial peptides. *Microbes Infect* **2006**, *8*, 2105-2112, doi:10.1016/j.micinf.2006.03.005.
65. Mowlds, P.; Coates, C.; Renwick, J.; Kavanagh, K. Dose-dependent cellular and humoral responses in *Galleria mellonella* larvae following beta-glucan inoculation. *Microbes Infect* **2010**, *12*, 146-153, doi:10.1016/j.micinf.2009.11.004.
66. Wu, G.; Zhao, Z.; Liu, C.; Qiu, L. Priming *Galleria mellonella* (Lepidoptera: Pyralidae) larvae with heat-killed bacterial cells induced an enhanced immune protection against *Photobacterium luminescens* TT01 and the role of innate immunity in the process. *J Econ Entomol* **2014**, *107*, 559-569, doi:10.1603/ec13455.
67. Ramarao, N.; Nielsen-Leroux, C.; Lereclus, D. The insect *Galleria mellonella* as a powerful infection model to investigate bacterial pathogenesis. *J Vis Exp* **2012**, e4392, doi:10.3791/4392.
68. Salamitou, S.; Ramišse, F.; Brehélin, M.; Bourguet, D.; Gilois, N.; Gominet, M.; Hernandez, E.; Lereclus, D. The *plcR* regulon is involved in the opportunistic properties of *Bacillus thuringiensis* and *Bacillus cereus* in mice and insects. *Microbiology (Reading)* **2000**, *146* (Pt 11), 2825-2832, doi:10.1099/00221287-146-11-2825.

69. Peleg, A.Y.; Monga, D.; Pillai, S.; Mylonakis, E.; Moellering, R.C.; Eliopoulos, G.M. Reduced susceptibility to vancomycin influences pathogenicity in *Staphylococcus aureus* infection. *J Infect Dis* **2009**, *199*, 532-536, doi:10.1086/596511.
70. Desbois, A.P.; Coote, P.J. Wax moth larva (*Galleria mellonella*): an *in vivo* model for assessing the efficacy of antistaphylococcal agents. *J Antimicrob Chemother* **2011**, *66*, 1785-1790, doi:10.1093/jac/dkr198.
71. Konkel, M.E.; Tilly, K. Temperature-regulated expression of bacterial virulence genes. *Microbes Infect* **2000**, *2*, 157-166, doi:10.1016/s1286-4579(00)00272-0.
72. Loh, J.M.; Adenwalla, N.; Wiles, S.; Proft, T. *Galleria mellonella* larvae as an infection model for group A streptococcus. *Virulence* **2013**, *4*, 419-428, doi:10.4161/viru.24930.
73. La Rosa, S.L.; Diep, D.B.; Nes, I.F.; Brede, D.A. Construction and application of a *luxABCDE* reporter system for real-time monitoring of *Enterococcus faecalis* gene expression and growth. *Appl Environ Microbiol* **2012**, *78*, 7003-7011, doi:10.1128/AEM.02018-12.
74. Wand, M.E.; Bock, L.J.; Turton, J.F.; Nugent, P.G.; Sutton, J.M. *Acinetobacter baumannii* virulence is enhanced in *Galleria mellonella* following biofilm adaptation. *J Med Microbiol* **2012**, *61*, 470-477, doi:10.1099/jmm.0.037523-0.
75. Richter, A.M.; Fazli, M.; Schmid, N.; Shilling, R.; Suppiger, A.; Givskov, M.; Eberl, L.; Tolker-Nielsen, T. Key Players and Individualists of Cyclic-di-GMP Signaling in *Burkholderia cenocepacia*. *Front Microbiol* **2018**, *9*, 3286, doi:10.3389/fmicb.2018.03286.
76. Seed, K.D.; Dennis, J.J. Development of *Galleria mellonella* as an alternative infection model for the *Burkholderia cepacia* complex. *Infect Immun* **2008**, *76*, 1267-1275, doi:10.1128/IAI.01249-07.
77. Senior, N.J.; Bagnall, M.C.; Champion, O.L.; Reynolds, S.E.; La Ragione, R.M.; Woodward, M.J.; Salguero, F.J.; Titball, R.W. *Galleria mellonella* as an infection model for *Campylobacter jejuni* virulence. *J Med Microbiol* **2011**, *60*, 661-669, doi:10.1099/jmm.0.026658-0.
78. Dunphy, G.B.; Oberholzer, U.; Whiteway, M.; Zakarian, R.J.; Boomer, I. Virulence of *Candida albicans* mutants toward larval *Galleria mellonella* (Insecta, Lepidoptera, Galleridae). *Can J Microbiol* **2003**, *49*, 514-524, doi:10.1139/w03-064.
79. Heitmueller, M.; Billion, A.; Dobrindt, U.; Vilcinskis, A.; Mukherjee, K. Epigenetic Mechanisms Regulate Innate Immunity against Uropathogenic and Commensal-Like *Escherichia coli* in the Surrogate Insect Model *Galleria mellonella*. *Infect Immun* **2017**, *85*, doi:10.1128/IAI.00336-17.
80. Meir, M.; Grosfeld, T.; Barkan, D. Establishment and Validation of *Galleria mellonella* as a Novel Model Organism To Study *Mycobacterium abscessus* Infection, Pathogenesis, and Treatment. *Antimicrob Agents Chemother* **2018**, *62*, doi:10.1128/AAC.02539-17.
81. Li, Y.; Spiropoulos, J.; Cooley, W.; Khara, J.S.; Gladstone, C.A.; Asai, M.; Bossé, J.T.; Robertson, B.D.; Newton, S.M.; Langford, P.R. *Galleria mellonella* - a novel infection model for the *Mycobacterium tuberculosis* complex. *Virulence* **2018**, *9*, 1126-1137, doi:10.1080/21505594.2018.1491255.
82. Jander, G.; Rahme, L.G.; Ausubel, F.M. Positive correlation between virulence of *Pseudomonas aeruginosa* mutants in mice and insects. *J Bacteriol* **2000**, *182*, 3843-3845, doi:10.1128/jb.182.13.3843-3845.2000.
83. Sheehan, G.; Dixon, A.; Kavanagh, K. Utilization of *Galleria mellonella* larvae to characterize the development of *Staphylococcus aureus* infection. *Microbiology (Reading)* **2019**, *165*, 863-875, doi:10.1099/mic.0.000813.
84. McMillan, S.; Verner-Jeffreys, D.; Weeks, J.; Austin, B.; Desbois, A.P. Larva of the greater wax moth, *Galleria mellonella*, is a suitable alternative host for studying virulence of fish pathogenic *Vibrio anguillarum*. *BMC Microbiol* **2015**, *15*, 127, doi:10.1186/s12866-015-0466-9.

85. Strong, P.C.; Hinchliffe, S.J.; Patrick, H.; Atkinson, S.; Champion, O.L.; Wren, B.W. Identification and characterisation of a novel adhesin Ifp in *Yersinia pseudotuberculosis*. *BMC Microbiol* **2011**, *11*, 85, doi:10.1186/1471-2180-11-85.
86. Azam, M.W.; Khan, A.U. Updates on the pathogenicity status of *Pseudomonas aeruginosa*. *Drug Discov Today* **2019**, *24*, 350-359, doi:10.1016/j.drudis.2018.07.003.
87. Gellatly, S.L.; Hancock, R.E. *Pseudomonas aeruginosa*: new insights into pathogenesis and host defenses. *Pathog Dis* **2013**, *67*, 159-173, doi:10.1111/2049-632X.12033.
88. Moradali, M.F.; Ghods, S.; Rehm, B.H. *Pseudomonas aeruginosa* Lifestyle: A Paradigm for Adaptation, Survival, and Persistence. *Front Cell Infect Microbiol* **2017**, *7*, 39, doi:10.3389/fcimb.2017.00039.
89. Hancock, R.E.; Speert, D.P. Antibiotic resistance in *Pseudomonas aeruginosa*: mechanisms and impact on treatment. *Drug Resist Updat* **2000**, *3*, 247-255, doi:10.1054/drup.2000.0152.
90. Stover, C.K.; Pham, X.Q.; Erwin, A.L.; Mizoguchi, S.D.; Warrener, P.; Hickey, M.J.; Brinkman, F.S.; Hufnagle, W.O.; Kowalik, D.J.; Lagrou, M., et al. Complete genome sequence of *Pseudomonas aeruginosa* PAO1, an opportunistic pathogen. *Nature* **2000**, *406*, 959-964, doi:10.1038/35023079.
91. Galán-Vásquez, E.; Luna, B.; Martínez-Antonio, A. The Regulatory Network of *Pseudomonas aeruginosa*. *Microb Inform Exp* **2011**, *1*, 3, doi:10.1186/2042-5783-1-3.
92. Drenkard, E.; Ausubel, F.M. *Pseudomonas* biofilm formation and antibiotic resistance are linked to phenotypic variation. *Nature* **2002**, *416*, 740-743, doi:10.1038/416740a.
93. King, J.D.; Kocincová, D.; Westman, E.L.; Lam, J.S. Review: Lipopolysaccharide biosynthesis in *Pseudomonas aeruginosa*. *Innate Immun* **2009**, *15*, 261-312, doi:10.1177/1753425909106436.
94. Hogardt, M.; Heesemann, J. Adaptation of *Pseudomonas aeruginosa* during persistence in the cystic fibrosis lung. *Int J Med Microbiol* **2010**, *300*, 557-562, doi:10.1016/j.ijmm.2010.08.008.
95. Martin, D.W.; Schurr, M.J.; Mudd, M.H.; Govan, J.R.; Holloway, B.W.; Deretic, V. Mechanism of conversion to mucoidy in *Pseudomonas aeruginosa* infecting cystic fibrosis patients. *Proc Natl Acad Sci U S A* **1993**, *90*, 8377-8381, doi:10.1073/pnas.90.18.8377.
96. Costerton, J.W.; Stewart, P.S.; Greenberg, E.P. Bacterial biofilms: a common cause of persistent infections. *Science* **1999**, *284*, 1318-1322, doi:10.1126/science.284.5418.1318.
97. Maurice, N.M.; Bedi, B.; Sadikot, R.T. *Pseudomonas aeruginosa* Biofilms: Host Response and Clinical Implications in Lung Infections. *Am J Respir Cell Mol Biol* **2018**, *58*, 428-439, doi:10.1165/rcmb.2017-0321TR.
98. Vilaplana, L.; Marco, M.P. Phenazines as potential biomarkers of *Pseudomonas aeruginosa* infections: synthesis regulation, pathogenesis and analytical methods for their detection. *Anal Bioanal Chem* **2020**, *412*, 5897-5912, doi:10.1007/s00216-020-02696-4.
99. Torrents, E. Ribonucleotide reductases: essential enzymes for bacterial life. *Front Cell Infect Microbiol* **2014**, *4*, 52, doi:10.3389/fcimb.2014.00052.
100. Crespo, A.; Pedraz, L.; Torrents, E. Function of the *Pseudomonas aeruginosa* NrdR Transcription Factor: Global Transcriptomic Analysis and Its Role on Ribonucleotide Reductase Gene Expression. *PLoS One* **2015**, *10*, e0123571, doi:10.1371/journal.pone.0123571.
101. Grinberg, I.; Shteinberg, T.; Gorovitz, B.; Aharonowitz, Y.; Cohen, G.; Borovok, I. The *Streptomyces* NrdR transcriptional regulator is a Zn ribbon/ATP cone protein that binds to the promoter regions of class Ia and class II ribonucleotide reductase operons. *J Bacteriol* **2006**, *188*, 7635-7644, doi:10.1128/JB.00903-06.
102. Sjöberg, B.M.; Torrents, E. Shift in ribonucleotide reductase gene expression in *Pseudomonas aeruginosa* during infection. *Infect Immun* **2011**, *79*, 2663-2669, doi:10.1128/IAI.01212-10.
103. Crespo, A.; Gavalda, J.; Julian, E.; Torrents, E. A single point mutation in class III ribonucleotide reductase promoter renders *Pseudomonas aeruginosa* PAO1 inefficient for anaerobic growth and infection. *Sci Rep* **2017**, *7*, 13350, doi:10.1038/s41598-017-14051-2.

104. Crespo, A.; Pedraz, L.; Astola, J.; Torrents, E. *Pseudomonas aeruginosa* Exhibits Deficient Biofilm Formation in the Absence of Class II and III Ribonucleotide Reductases Due to Hindered Anaerobic Growth. *Front Microbiol* **2016**, *7*, 688, doi:10.3389/fmicb.2016.00688.
105. Doberenz, S.; Eckweiler, D.; Reichert, O.; Jensen, V.; Bunk, B.; Spröer, C.; Kordes, A.; Frangipani, E.; Luong, K.; Korfach, J., et al. Identification of a *Pseudomonas aeruginosa* PAO1 DNA Methyltransferase, Its Targets, and Physiological Roles. *mBio* **2017**, *8*, doi:10.1128/mBio.02312-16.
106. Raneri, M.; Pinatel, E.; Peano, C.; Rampioni, G.; Leoni, L.; Bianconi, I.; Jousson, O.; Dalmasio, C.; Ferrante, P.; Briani, F. *Pseudomonas aeruginosa* mutants defective in glucose uptake have pleiotropic phenotype and altered virulence in non-mammal infection models. *Sci Rep* **2018**, *8*, 16912, doi:10.1038/s41598-018-35087-y.
107. Andrejko, M.; Mizerska-Dudka, M. Elastase B of *Pseudomonas aeruginosa* stimulates the humoral immune response in the greater wax moth, *Galleria mellonella*. *J Invertebr Pathol* **2011**, *107*, 16-26, doi:10.1016/j.jip.2010.12.015.
108. Andrejko, M.; Mizerska-Dudka, M.; Jakubowicz, T. Changes in *Galleria mellonella* apolipoprotein III level during *Pseudomonas aeruginosa* infection. *J Invertebr Pathol* **2008**, *97*, 14-19, doi:10.1016/j.jip.2007.06.003.
109. Andrejko, M.; Mizerska-Dudka, M. Effect of *Pseudomonas aeruginosa* elastase B on level and activity of immune proteins/peptides of *Galleria mellonella* hemolymph. *J Insect Sci* **2012**, *12*, 88, doi:10.1673/031.012.8801.
110. Andrejko, M.; Zdybicka-Barabas, A.; Cytryńska, M. Diverse effects of *Galleria mellonella* infection with entomopathogenic and clinical strains of *Pseudomonas aeruginosa*. *J Invertebr Pathol* **2014**, *115*, 14-25, doi:10.1016/j.jip.2013.10.006.
111. Mizerska-Dudka, M.; Andrejko, M. *Galleria mellonella* hemocytes destruction after infection with *Pseudomonas aeruginosa*. *J Basic Microbiol* **2014**, *54*, 232-246, doi:10.1002/jobm.201200273.
112. Wertheim, H.F.; Melles, D.C.; Vos, M.C.; van Leeuwen, W.; van Belkum, A.; Verbrugh, H.A.; Nouwen, J.L. The role of nasal carriage in *Staphylococcus aureus* infections. *Lancet Infect Dis* **2005**, *5*, 751-762, doi:10.1016/S1473-3099(05)70295-4.
113. Tong, S.Y.; Davis, J.S.; Eichenberger, E.; Holland, T.L.; Fowler, V.G. *Staphylococcus aureus* infections: epidemiology, pathophysiology, clinical manifestations, and management. *Clin Microbiol Rev* **2015**, *28*, 603-661, doi:10.1128/CMR.00134-14.
114. Kourtis, A.P.; Hatfield, K.; Baggs, J.; Mu, Y.; See, I.; Epton, E.; Nadle, J.; Kainer, M.A.; Dumyati, G.; Petit, S., et al. Vital Signs: Epidemiology and Recent Trends in Methicillin-Resistant and in Methicillin-Susceptible *Staphylococcus aureus* Bloodstream Infections - United States. *MMWR Morb Mortal Wkly Rep* **2019**, *68*, 214-219, doi:10.15585/mmwr.mm6809e1.
115. Hassoun, A.; Linden, P.K.; Friedman, B. Incidence, prevalence, and management of MRSA bacteremia across patient populations-a review of recent developments in MRSA management and treatment. *Crit Care* **2017**, *21*, 211, doi:10.1186/s13054-017-1801-3.
116. Dantes, R.; Mu, Y.; Belflower, R.; Aragon, D.; Dumyati, G.; Harrison, L.H.; Lessa, F.C.; Lynfield, R.; Nadle, J.; Petit, S., et al. National burden of invasive methicillin-resistant *Staphylococcus aureus* infections, United States, 2011. *JAMA Intern Med* **2013**, *173*, 1970-1978, doi:10.1001/jamainternmed.2013.10423.
117. Levine, D.P. Vancomycin: a history. *Clin Infect Dis* **2006**, *42 Suppl 1*, S5-12, doi:10.1086/491709.
118. Gardete, S.; Tomasz, A. Mechanisms of vancomycin resistance in *Staphylococcus aureus*. *J Clin Invest* **2014**, *124*, 2836-2840, doi:10.1172/JCI68834.
119. Rooijackers, S.H.; van Kessel, K.P.; van Strijp, J.A. Staphylococcal innate immune evasion. *Trends Microbiol* **2005**, *13*, 596-601, doi:10.1016/j.tim.2005.10.002.

120. Jin, T.; Bokarewa, M.; Foster, T.; Mitchell, J.; Higgins, J.; Tarkowski, A. *Staphylococcus aureus* resists human defensins by production of staphylokinase, a novel bacterial evasion mechanism. *J Immunol* **2004**, *172*, 1169-1176, doi:10.4049/jimmunol.172.2.1169.
121. Sieprawska-Lupa, M.; Mydel, P.; Krawczyk, K.; Wójcik, K.; Puklo, M.; Lupa, B.; Suder, P.; Silberring, J.; Reed, M.; Pohl, J., et al. Degradation of human antimicrobial peptide LL-37 by *Staphylococcus aureus*-derived proteinases. *Antimicrob Agents Chemother* **2004**, *48*, 4673-4679, doi:10.1128/AAC.48.12.4673-4679.2004.
122. Mandell, G.L. Catalase, superoxide dismutase, and virulence of *Staphylococcus aureus*. In vitro and in vivo studies with emphasis on staphylococcal-leukocyte interaction. *J Clin Invest* **1975**, *55*, 561-566, doi:10.1172/JCI107963.
123. Rooijackers, S.H.; Ruyken, M.; Roos, A.; Daha, M.R.; Presanis, J.S.; Sim, R.B.; van Wamel, W.J.; van Kessel, K.P.; van Strijp, J.A. Immune evasion by a staphylococcal complement inhibitor that acts on C3 convertases. *Nat Immunol* **2005**, *6*, 920-927, doi:10.1038/ni1235.
124. Kane, T.L.; Carothers, K.E.; Lee, S.W. Virulence Factor Targeting of the Bacterial Pathogen *Staphylococcus aureus* for Vaccine and Therapeutics. *Curr Drug Targets* **2018**, *19*, 111-127, doi:10.2174/1389450117666161128123536.
125. Thammavongsa, V.; Kim, H.K.; Missiakas, D.; Schneewind, O. Staphylococcal manipulation of host immune responses. *Nat Rev Microbiol* **2015**, *13*, 529-543, doi:10.1038/nrmicro3521.
126. Chavakis, T.; Preissner, K.T.; Herrmann, M. The anti-inflammatory activities of *Staphylococcus aureus*. *Trends Immunol* **2007**, *28*, 408-418, doi:10.1016/j.it.2007.07.002.
127. Hartleib, J.; Köhler, N.; Dickinson, R.B.; Chhatwal, G.S.; Sixma, J.J.; Hartford, O.M.; Foster, T.J.; Peters, G.; Kehrel, B.E.; Herrmann, M. Protein A is the von Willebrand factor binding protein on *Staphylococcus aureus*. *Blood* **2000**, *96*, 2149-2156.
128. Gómez, M.I.; O'Seaghda, M.; Magargee, M.; Foster, T.J.; Prince, A.S. *Staphylococcus aureus* protein A activates TNFR1 signaling through conserved IgG binding domains. *J Biol Chem* **2006**, *281*, 20190-20196, doi:10.1074/jbc.M601956200.
129. McA Dow, M.; Missiakas, D.M.; Schneewind, O. *Staphylococcus aureus* secretes coagulase and von Willebrand factor binding protein to modify the coagulation cascade and establish host infections. *J Innate Immun* **2012**, *4*, 141-148, doi:10.1159/000333447.
130. Fournier, B.; Philpott, D.J. Recognition of *Staphylococcus aureus* by the innate immune system. *Clin Microbiol Rev* **2005**, *18*, 521-540, doi:10.1128/CMR.18.3.521-540.2005.
131. Bohach, G.A.; Fast, D.J.; Nelson, R.D.; Schlievert, P.M. Staphylococcal and streptococcal pyrogenic toxins involved in toxic shock syndrome and related illnesses. *Crit Rev Microbiol* **1990**, *17*, 251-272, doi:10.3109/10408419009105728.
132. Liu, G.Y.; Essex, A.; Buchanan, J.T.; Datta, V.; Hoffman, H.M.; Bastian, J.F.; Fierer, J.; Nizet, V. *Staphylococcus aureus* golden pigment impairs neutrophil killing and promotes virulence through its antioxidant activity. *J Exp Med* **2005**, *202*, 209-215, doi:10.1084/jem.20050846.
133. Fedtke, I.; Götz, F.; Peschel, A. Bacterial evasion of innate host defenses--the *Staphylococcus aureus* lesson. *Int J Med Microbiol* **2004**, *294*, 189-194, doi:10.1016/j.ijmm.2004.06.016.
134. Clarke, S.R.; Foster, S.J. Surface adhesins of *Staphylococcus aureus*. *Adv Microb Physiol* **2006**, *51*, 187-224, doi:10.1016/S0065-2911(06)51004-5.
135. Choi, J.H.; Seo, H.S.; Lim, S.Y.; Park, K. Cutaneous Immune Defenses Against *Staphylococcus aureus* Infections. *J Lifestyle Med* **2014**, *4*, 39-46, doi:10.15280/jlm.2014.4.1.39.
136. Vuong, C.; Saenz, H.L.; Götz, F.; Otto, M. Impact of the *agr* quorum-sensing system on adherence to polystyrene in *Staphylococcus aureus*. *J Infect Dis* **2000**, *182*, 1688-1693, doi:10.1086/317606.
137. Weese, J.S.; van Duijkeren, E. Methicillin-resistant *Staphylococcus aureus* and *Staphylococcus pseudintermedius* in veterinary medicine. *Vet Microbiol* **2010**, *140*, 418-429, doi:10.1016/j.vetmic.2009.01.039.

138. Rich, M. Staphylococci in animals: prevalence, identification and antimicrobial susceptibility, with an emphasis on methicillin-resistant *Staphylococcus aureus*. *Br J Biomed Sci* **2005**, *62*, 98-105, doi:10.1080/09674845.2005.11732694.
139. Zecconi, A.; Piccinini, R.; Fox, L.K. Epidemiologic study of intramammary infections with *Staphylococcus aureus* during a control program in nine commercial dairy herds. *J Am Vet Med Assoc* **2003**, *223*, 684-688, doi:10.2460/javma.2003.223.684.
140. Zecconi, A.; Scali, F. *Staphylococcus aureus* virulence factors in evasion from innate immune defenses in human and animal diseases. *Immunol Lett* **2013**, *150*, 12-22, doi:10.1016/j.imlet.2013.01.004.
141. Quiblier, C.; Seidl, K.; Roschitzki, B.; Zinkernagel, A.S.; Berger-Bächli, B.; Senn, M.M. Secretome analysis defines the major role of SecDF in *Staphylococcus aureus* virulence. *PLoS One* **2013**, *8*, e63513, doi:10.1371/journal.pone.0063513.
142. Mannala, G.K.; Koettnitz, J.; Mohamed, W.; Sommer, U.; Lips, K.S.; Spröer, C.; Bunk, B.; Overmann, J.; Hain, T.; Heiss, C., et al. Whole-genome comparison of high and low virulent *Staphylococcus aureus* isolates inducing implant-associated bone infections. *Int J Med Microbiol* **2018**, *308*, 505-513, doi:10.1016/j.ijmm.2018.04.005.
143. Graf, A.C.; Leonard, A.; Schäuble, M.; Rieckmann, L.M.; Hoyer, J.; Maass, S.; Lalk, M.; Becher, D.; Pané-Farré, J.; Riedel, K. Virulence Factors Produced by *Staphylococcus aureus* Biofilms Have a Moonlighting Function Contributing to Biofilm Integrity. *Mol Cell Proteomics* **2019**, *18*, 1036-1053, doi:10.1074/mcp.RA118.001120.
144. Luquin, M.; Ausina, V.; Vincent-Lévy-Frébault, V.; Lanéelle, M.A.; Belda, F.; García-Barceló, M.; Prats, G.; Daffé, M. *Mycobacterium brumae* sp. nov., a Rapidly Growing, Nonphotochromogenic Mycobacterium. *International Journal of Systematic Bacteriology* **1993**, *43*, 405-413, doi:10.1099/00207713-43-3-405.
145. D'Auria, G.; Torrents, E.; Luquin, M.; Comas, I.; Julián, E. Draft Genome Sequence of *Mycobacterium brumae* ATCC 51384. *Genome Announc* **2016**, *4*, doi:10.1128/genomeA.00237-16.
146. Lee, S.A.; Raad, I.I.; Adachi, J.A.; Han, X.Y. Catheter-related bloodstream infection caused by *Mycobacterium brumae*. *J Clin Microbiol* **2004**, *42*, 5429-5431, doi:10.1128/JCM.42.11.5429-5431.2004.
147. Jiménez, M.S.; Julián, E.; Luquin, M. Misdiagnosis of *Mycobacterium brumae* infection. *J Clin Microbiol* **2011**, *49*, 1190-1191; author reply 1191-1192, doi:10.1128/JCM.01540-10.
148. Etienne, G.; Villeneuve, C.; Billman-Jacobe, H.; Astarie-Dequeker, C.; Dupont, M.A.; Daffé, M. The impact of the absence of glycopeptidolipids on the ultrastructure, cell surface and cell wall properties, and phagocytosis of *Mycobacterium smegmatis*. *Microbiology (Reading)* **2002**, *148*, 3089-3100, doi:10.1099/00221287-148-10-3089.
149. Linares, C.; Bernabéu, A.; Luquin, M.; Valero-Guillén, P.L. Cord factors from atypical mycobacteria (*Mycobacterium alvei*, *Mycobacterium brumae*) stimulate the secretion of some pro-inflammatory cytokines of relevance in tuberculosis. *Microbiology (Reading)* **2012**, *158*, 2878-2885, doi:10.1099/mic.0.060681-0.
150. Noguera-Ortega, E.; Secanella-Fandos, S.; Eraña, H.; Gasió, J.; Rabanal, R.M.; Luquin, M.; Torrents, E.; Julián, E. Nonpathogenic *Mycobacterium brumae* Inhibits Bladder Cancer Growth In Vitro, Ex Vivo, and In Vivo. *Eur Urol Focus* **2016**, *2*, 67-76, doi:10.1016/j.euf.2015.03.003.
151. Noguera-Ortega, E.; Rabanal, R.M.; Secanella-Fandos, S.; Torrents, E.; Luquin, M.; Julián, E. γ Irradiated Mycobacteria Enhance Survival in Bladder Tumor Bearing Mice Although Less Efficaciously than Live Mycobacteria. *J Urol* **2016**, *195*, 198-205, doi:10.1016/j.juro.2015.07.011.

152. Desbois, A.P.; Coote, P.J. Utility of Greater Wax Moth Larva (*Galleria mellonella*) for Evaluating the Toxicity and Efficacy of New Antimicrobial Agents. *Adv Appl Microbiol* **2012**, *78*, 25-53, doi:10.1016/b978-0-12-394805-2.00002-6.
153. Aperis, G.; Fuchs, B.B.; Anderson, C.A.; Warner, J.E.; Calderwood, S.B.; Mylonakis, E. *Galleria mellonella* as a model host to study infection by the *Francisella tularensis* live vaccine strain. *Microbes Infect* **2007**, *9*, 729-734, doi:10.1016/j.micinf.2007.02.016.
154. Hornsey, M.; Wareham, D.W. *In vivo* efficacy of glycopeptide-colistin combination therapies in a *Galleria mellonella* model of *Acinetobacter baumannii* infection. *Antimicrob Agents Chemother* **2011**, *55*, 3534-3537, doi:10.1128/AAC.00230-11.
155. Peleg, A.Y.; Jara, S.; Monga, D.; Eliopoulos, G.M.; Moellering, R.C.; Mylonakis, E. *Galleria mellonella* as a model system to study *Acinetobacter baumannii* pathogenesis and therapeutics. *Antimicrob Agents Chemother* **2009**, *53*, 2605-2609, doi:10.1128/AAC.01533-08.
156. Thomaz, L.; Gustavo de Almeida, L.; Silva, F.R.O.; Cortez, M.; Taborda, C.P.; Spira, B. *In vivo* Activity of Silver Nanoparticles Against *Pseudomonas aeruginosa* Infection in *Galleria mellonella*. *Front Microbiol* **2020**, *11*, 582107, doi:10.3389/fmicb.2020.582107.
157. Kavanagh, K.; Sheehan, G. The Use of *Galleria mellonella* Larvae to Identify Novel Antimicrobial Agents against Fungal Species of Medical Interest. *J Fungi (Basel)* **2018**, *4*, doi:10.3390/jof4030113.
158. Piatek, M.; Sheehan, G.; Kavanagh, K. Utilising *Galleria mellonella* larvae for studying *in vivo* activity of conventional and novel antimicrobial agents. *Pathog Dis* **2020**, *78*, doi:10.1093/femspd/ftaa059.
159. Khalil, M.A.F.; Moawad, S.S.; Hefzy, E.M. *In vivo* activity of co-trimoxazole combined with colistin against *Acinetobacter baumannii* producing OXA-23 in a *Galleria mellonella* model. *J Med Microbiol* **2019**, *68*, 52-59, doi:10.1099/jmm.0.000872.
160. Naguib, M.M.; Valvano, M.A. Vitamin E Increases Antimicrobial Sensitivity by Inhibiting Bacterial Lipocalin Antibiotic Binding. *mSphere* **2018**, *3*, doi:10.1128/mSphere.00564-18.
161. Nale, J.Y.; Chutia, M.; Carr, P.; Hickenbotham, P.T.; Clokie, M.R. Get in Early'; Biofilm and Wax Moth (*Galleria mellonella*) Models Reveal New Insights into the Therapeutic Potential of *Clostridium difficile* Bacteriophages. *Front Microbiol* **2016**, *7*, 1383, doi:10.3389/fmicb.2016.01383.
162. Yang, H.; Chen, G.; Hu, L.; Liu, Y.; Cheng, J.; Ye, Y.; Li, J. Enhanced efficacy of imipenem-colistin combination therapy against multiple-drug-resistant *Enterobacter cloacae*: *in vitro* activity and a *Galleria mellonella* model. *J Microbiol Immunol Infect* **2018**, *51*, 70-75, doi:10.1016/j.jmii.2016.01.003.
163. Skinner, K.; Sandoe, J.A.T.; Rajendran, R.; Ramage, G.; Lang, S. Efficacy of rifampicin combination therapy for the treatment of enterococcal infections assessed *in vivo* using a *Galleria mellonella* infection model. *Int J Antimicrob Agents* **2017**, *49*, 507-511, doi:10.1016/j.ijantimicag.2016.12.006.
164. Vergis, J.; Malik, S.S.; Pathak, R.; Kumar, M.; Ramanjaneya, S.; Kurkure, N.V.; Barbudde, S.B.; Rawool, D.B. Antimicrobial Efficacy of Indolicidin Against Multi-Drug Resistant Enterococcal *Escherichia coli* in a *Galleria mellonella* Model. *Front Microbiol* **2019**, *10*, 2723, doi:10.3389/fmicb.2019.02723.
165. Tharmalingam, N.; Port, J.; Castillo, D.; Mylonakis, E. Repurposing the anthelmintic drug niclosamide to combat *Helicobacter pylori*. *Sci Rep* **2018**, *8*, 3701, doi:10.1038/s41598-018-22037-x.
166. Manohar, P.; Nachimuthu, R.; Lopes, B.S. The therapeutic potential of bacteriophages targeting gram-negative bacteria using *Galleria mellonella* infection model. *BMC Microbiol* **2018**, *18*, 97, doi:10.1186/s12866-018-1234-4.

167. Marini, E.; Magi, G.; Ferretti, G.; Bacchetti, T.; Giuliani, A.; Pugnali, A.; Rippo, M.R.; Facinelli, B. Attenuation of *Listeria monocytogenes* Virulence by *Cannabis sativa* L. Essential Oil. *Front Cell Infect Microbiol* **2018**, *8*, 293, doi:10.3389/fcimb.2018.00293.
168. Meir, M.; Bifani, P.; Barkan, D. The addition of avibactam renders piperacillin an effective treatment for *Mycobacterium abscessus* infection in an in vivo model. *Antimicrob Resist Infect Control* **2018**, *7*, 151, doi:10.1186/s13756-018-0448-4.
169. Asai, M.; Li, Y.; Khara, J.S.; Robertson, B.D.; Langford, P.R.; Newton, S.M. *Galleria mellonella*: An Infection Model for Screening Compounds Against the *Mycobacterium tuberculosis* Complex. *Front Microbiol* **2019**, *10*, 2630, doi:10.3389/fmicb.2019.02630.
170. Aparecida Procópio Gomes, L.; Alves Figueiredo, L.M.; Luiza do Rosário Palma, A.; Corrêa Geraldo, B.M.; Isler Castro, K.C.; Ruano de Oliveira Fugisaki, L.; Jorge, A.O.C.; de Oliveira, L.D.; Junqueira, J.C. *Punica granatum* L. (Pomegranate) Extract: *In Vivo* Study of Antimicrobial Activity against *Porphyromonas gingivalis* in *Galleria mellonella* Model. *ScientificWorldJournal* **2016**, *2016*, 8626987, doi:10.1155/2016/8626987.
171. D'Angelo, F.; Baldelli, V.; Halliday, N.; Pantalone, P.; Polticelli, F.; Fiscarelli, E.; Williams, P.; Visca, P.; Leoni, L.; Rampioni, G. Identification of FDA-Approved Drugs as Antivirulence Agents Targeting the *pqs* Quorum-Sensing System of *Pseudomonas aeruginosa*. *Antimicrob Agents Chemother* **2018**, *62*, doi:10.1128/AAC.01296-18.
172. Mirza, Z.R.M.H.; Hasan, T.; Seidel, V.; Yu, J. Geraniol as a novel antivirulence agent against bacillary dysentery-causing *Shigella sonnei*. *Virulence* **2018**, *9*, 450-455, doi:10.1080/21505594.2017.1412031.
173. Dong, C.L.; Li, L.X.; Cui, Z.H.; Chen, S.W.; Xiong, Y.Q.; Lu, J.Q.; Liao, X.P.; Gao, Y.; Sun, J.; Liu, Y.H. Synergistic Effect of Pleuromutilins with Other Antimicrobial Agents against *Staphylococcus aureus* *In Vitro* and in an Experimental *Galleria mellonella* Model. *Front Pharmacol* **2017**, *8*, 553, doi:10.3389/fphar.2017.00553.
174. Pereira, M.F.; Rossi, C.C.; da Silva, G.C.; Rosa, J.N.; Bazzolli, D.M.S. *Galleria mellonella* as an infection model: an in-depth look at why it works and practical considerations for successful application. *Pathog Dis* **2020**, *78*, doi:10.1093/femspd/ftaa056.
175. Brackman, G.; Cos, P.; Maes, L.; Nelis, H.J.; Coenye, T. Quorum sensing inhibitors increase the susceptibility of bacterial biofilms to antibiotics *in vitro* and *in vivo*. *Antimicrob Agents Chemother* **2011**, *55*, 2655-2661, doi:10.1128/AAC.00045-11.
176. Silva, L.N.; Da Hora, G.C.A.; Soares, T.A.; Bojer, M.S.; Ingmer, H.; Macedo, A.J.; Trentin, D.S. Myricetin protects *Galleria mellonella* against *Staphylococcus aureus* infection and inhibits multiple virulence factors. *Sci Rep* **2017**, *7*, 2823, doi:10.1038/s41598-017-02712-1.
177. Ferro, T.A.; Araújo, J.M.; Dos Santos Pinto, B.L.; Dos Santos, J.S.; Souza, E.B.; da Silva, B.L.; Colares, V.L.; Novais, T.M.; Filho, C.M.; Struve, C., et al. Cinnamaldehyde Inhibits *Staphylococcus aureus* Virulence Factors and Protects against Infection in a *Galleria mellonella* Model. *Front Microbiol* **2016**, *7*, 2052, doi:10.3389/fmicb.2016.02052.
178. Mishra, B.; Wang, X.; Lushnikova, T.; Zhang, Y.; Golla, R.M.; Narayana, J.L.; Wang, C.; McGuire, T.R.; Wang, G. Antibacterial, antifungal, anticancer activities and structural bioinformatics analysis of six naturally occurring temporins. *Peptides* **2018**, *106*, 9-20, doi:10.1016/j.peptides.2018.05.011.
179. Johnston, T.; Hendricks, G.L.; Shen, S.; Chen, R.F.; Kwon, B.; Kelso, M.J.; Kim, W.; Burgwyn Fuchs, B.; Mylonakis, E. Raf-kinase inhibitor GW5074 shows antibacterial activity against methicillin-resistant *Staphylococcus aureus* and potentiates the activity of gentamicin. *Future Med Chem* **2016**, *8*, 1941-1952, doi:10.4155/fmc-2016-0104.
180. Tharmalingam, N.; Jayamani, E.; Rajamuthiah, R.; Castillo, D.; Fuchs, B.B.; Kelso, M.J.; Mylonakis, E. Activity of a novel protonophore against methicillin-resistant *Staphylococcus aureus*. *Future Med Chem* **2017**, *9*, 1401-1411, doi:10.4155/fmc-2017-0047.

181. Betts, J.W.; Hornsey, M.; Wareham, D.W.; La Ragione, R.M. In vitro and In vivo Activity of Theaflavin-Epicatechin Combinations versus Multidrug-Resistant *Acinetobacter baumannii*. *Infect Dis Ther* **2017**, *6*, 435-442, doi:10.1007/s40121-017-0161-2.
182. Lazarini, J.G.; Sardi, J.C.O.; Franchin, M.; Nani, B.D.; Freires, I.A.; Infante, J.; Paschoal, J.A.R.; de Alencar, S.M.; Rosalen, P.L. Bioprospection of *Eugenia brasiliensis*, a Brazilian native fruit, as a source of anti-inflammatory and antibiofilm compounds. *Biomed Pharmacother* **2018**, *102*, 132-139, doi:10.1016/j.biopha.2018.03.034.
183. Israili, Z.H. Antimicrobial properties of honey. *Am J Ther* **2014**, *21*, 304-323, doi:10.1097/MJT.0b013e318293b09b.
184. Lange, A.; Beier, S.; Huson, D.H.; Parusel, R.; Iglauer, F.; Frick, J.S. Genome Sequence of *Galleria mellonella* (Greater Wax Moth). *Genome Announc* **2018**, *6*, doi:10.1128/genomeA.01220-17.
185. Cutuli, M.A.; Petronio Petronio, G.; Vergalito, F.; Magnifico, I.; Pietrangelo, L.; Venditti, N.; Di Marco, R. *Galleria mellonella* as a consolidated in vivo model hosts: New developments in antibacterial strategies and novel drug testing. *Virulence* **2019**, *10*, 527-541, doi:10.1080/21505594.2019.1621649.
186. Champion, O.L.; Titball, R.W.; Bates, S. Standardization of *G. mellonella* Larvae to Provide Reliable and Reproducible Results in the Study of Fungal Pathogens. *J Fungi (Basel)* **2018**, *4*, doi:10.3390/jof4030108.
187. Mowlds, P.; Barron, A.; Kavanagh, K. Physical stress primes the immune response of *Galleria mellonella* larvae to infection by *Candida albicans*. *Microbes Infect* **2008**, *10*, 628-634, doi:10.1016/j.micinf.2008.02.011.
188. Banville, N.; Browne, N.; Kavanagh, K. Effect of nutrient deprivation on the susceptibility of *Galleria mellonella* larvae to infection. *Virulence* **2012**, *3*, 497-503, doi:10.4161/viru.21972.
189. Büyükgüzel, E.; Kalender, Y. Penicillin-induced oxidative stress: effects on antioxidative response of midgut tissues in instars of *Galleria mellonella*. *J Econ Entomol* **2007**, *100*, 1533-1541, doi:10.1603/0022-0493(2007)100[1533:poseoa]2.0.co;2.
190. Wagley, S.; Champion, O.L.; Titball, R.W. Case Study: Identification of Virulence Genes. Available online: <https://biosystemstechnology.com/applications> (accessed on 20 December 2020).
191. Antimicrobial resistance [Fact sheet]. World Health Organization: 2020.
192. Zak, O.; O'Reilly, T. Animal models in the evaluation of antimicrobial agents. *Antimicrob Agents Chemother* **1991**, *35*, 1527-1531, doi:10.1128/aac.35.8.1527.
193. Bryda, E.C. The Mighty Mouse: the impact of rodents on advances in biomedical research. *Mo Med* **2013**, *110*, 207-211.
194. Fako, V.E.; Furgeson, D.Y. Zebrafish as a correlative and predictive model for assessing biomaterial nanotoxicity. *Adv Drug Deliv Rev* **2009**, *61*, 478-486, doi:10.1016/j.addr.2009.03.008.
195. Rand, M.D.; Montgomery, S.L.; Prince, L.; Vorojeikina, D. Developmental toxicity assays using the *Drosophila* model. *Curr Protoc Toxicol* **2014**, *59*, 1 12 11-20, doi:10.1002/0471140856.tx0112s59.
196. Leung, M.C.; Williams, P.L.; Benedetto, A.; Au, C.; Helmcke, K.J.; Aschner, M.; Meyer, J.N. *Caenorhabditis elegans*: an emerging model in biomedical and environmental toxicology. *Toxicol Sci* **2008**, *106*, 5-28, doi:10.1093/toxsci/kfn121.
197. Maguire, R.; Duggan, O.; Kavanagh, K. Evaluation of *Galleria mellonella* larvae as an in vivo model for assessing the relative toxicity of food preservative agents. *Cell Biol Toxicol* **2016**, *32*, 209-216, doi:10.1007/s10565-016-9329-x.
198. Thomas, R.J.; Hamblin, K.A.; Armstrong, S.J.; Müller, C.M.; Bokori-Brown, M.; Goldman, S.; Atkins, H.S.; Titball, R.W. *Galleria mellonella* as a model system to test the pharmacokinetics and efficacy of antibiotics against *Burkholderia pseudomallei*. *Int J Antimicrob Agents* **2013**, *41*, 330-336, doi:10.1016/j.ijantimicag.2012.12.009.

199. Allegra, E.; Titball, R.W.; Carter, J.; Champion, O.L. *Galleria mellonella* larvae allow the discrimination of toxic and non-toxic chemicals. *Chemosphere* **2018**, *198*, 469-472, doi:10.1016/j.chemosphere.2018.01.175.
200. Ignasiak, K.; Maxwell, A. *Galleria mellonella* (greater wax moth) larvae as a model for antibiotic susceptibility testing and acute toxicity trials. *BMC Res Notes* **2017**, *10*, 428, doi:10.1186/s13104-017-2757-8.
201. Megaw, J.; Thompson, T.P.; Lafferty, R.A.; Gilmore, B.F. *Galleria mellonella* as a novel in vivo model for assessment of the toxicity of 1-alkyl-3-methylimidazolium chloride ionic liquids. *Chemosphere* **2015**, *139*, 197-201, doi:10.1016/j.chemosphere.2015.06.026.
202. Maguire, R.; Kunc, M.; Hyrsl, P.; Kavanagh, K. Caffeine administration alters the behaviour and development of *Galleria mellonella* larvae. *Neurotoxicol Teratol* **2017**, *64*, 37-44, doi:10.1016/j.ntt.2017.10.002.
203. Rochford, G.; Molphy, Z.; Browne, N.; Surlis, C.; Devereux, M.; McCann, M.; Kellett, A.; Howe, O.; Kavanagh, K. *In-vivo* evaluation of the response of *Galleria mellonella* larvae to novel copper(II) phenanthroline-phenazine complexes. *J Inorg Biochem* **2018**, *186*, 135-146, doi:10.1016/j.jinorgbio.2018.05.020.
204. Aneja, B.; Azam, M.; Alam, S.; Perwez, A.; Maguire, R.; Yadava, U.; Kavanagh, K.; Daniliuc, C.G.; Rizvi, M.M.A.; Haq, Q.M.R., et al. Natural Product-Based 1,2,3-Triazole/Sulfonate Analogues as Potential Chemotherapeutic Agents for Bacterial Infections. *ACS Omega* **2018**, *3*, 6912-6930, doi:10.1021/acsomega.8b00582.
205. Dolan, N.; Gavin, D.P.; Eshwika, A.; Kavanagh, K.; McGinley, J.; Stephens, J.C. Synthesis, antibacterial and anti-MRSA activity, in vivo toxicity and a structure-activity relationship study of a quinoline thiourea. *Bioorg Med Chem Lett* **2016**, *26*, 630-635, doi:10.1016/j.bmcl.2015.11.058.
206. Cruz, L.I.B.; Lopes, L.F.F.; de Camargo Ribeiro, F.; de Sá, N.P.; Lino, C.I.; Tharmalingam, N.; de Oliveira, R.B.; Rosa, C.A.; Mylonakis, E.; Fuchs, B.B., et al. Anti-*Candida albicans* Activity of Thiazolyldihydrazone Derivatives in Invertebrate and Murine Models. *J Fungi (Basel)* **2018**, *4*, doi:10.3390/jof4040134.
207. McCann, M.; Santos, A.L.S.; da Silva, B.A.; Romanos, M.T.V.; Pyrrho, A.S.; Devereux, M.; Kavanagh, K.; Fichtner, I.; Kellett, A. *In vitro* and *in vivo* studies into the biological activities of 1,10-phenanthroline, 1,10-phenanthroline-5,6-dione and its copper(ii) and silver(i) complexes. *Toxicology Research* **2012**, *1*, 47-54, doi:10.1039/c2tx00010e.
208. Cé, R.; Silva, R.C.; Trentin, D.S.; Marchi, J.G.B.; Paese, K.; Guterres, S.S.; Macedo, A.J.; Pohlmann, A.R. *Galleria mellonella* Larvae as an *In Vivo* Model to Evaluate the Toxicity of Polymeric Nanocapsules. *Journal of Nanoscience and Nanotechnology* **2020**, *20*, 1486-1494, doi:10.1166/jnn.2020.17170.
209. Deacon, J.; Abdelghany, S.M.; Quinn, D.J.; Schmid, D.; Megaw, J.; Donnelly, R.F.; Jones, D.S.; Kissenpennig, A.; Elborn, J.S.; Gilmore, B.F., et al. Antimicrobial efficacy of tobramycin polymeric nanoparticles for *Pseudomonas aeruginosa* infections in cystic fibrosis: formulation, characterisation and functionalisation with dornase alfa (DNase). *J Control Release* **2015**, *198*, 55-61, doi:10.1016/j.jconrel.2014.11.022.
210. Ottoni, C.A.; Maria, D.A.; Gonçalves, P.J.R.O.; de Araújo, W.L.; de Souza, A.O. Biogenic *Aspergillus tubingensis* silver nanoparticles' *in vitro* effects on human umbilical vein endothelial cells, normal human fibroblasts, HEPG2, and *Galleria mellonella*. *Toxicol Res (Camb)* **2019**, *8*, 789-801, doi:10.1039/c9tx00091g.
211. Spadari, C.C.; de Bastiani, F.W.M.D.; Lopes, L.B.; Ishida, K. Alginate nanoparticles as non-toxic delivery system for miltefosine in the treatment of candidiasis and cryptococcosis. *Int J Nanomedicine* **2019**, *14*, 5187-5199, doi:10.2147/IJN.S205350.

212. Passos, J.S.; Martino, L.C.; Dartora, V.F.C.; Araujo, G.L.B.; Ishida, K.; Lopes, L.B. Development, skin targeting and antifungal efficacy of topical lipid nanoparticles containing itraconazole. *Eur J Pharm Sci* **2020**, *149*, 105296, doi:10.1016/j.ejps.2020.105296.
213. Costabile, G.; Provenzano, R.; Azzalin, A.; Scoffone, V.C.; Chiarelli, L.R.; Rondelli, V.; Grillo, I.; Zinn, T.; Lepioshkin, A.; Savina, S., et al. PEGylated mucus-penetrating nanocrystals for lung delivery of a new FtsZ inhibitor against *Burkholderia cenocepacia* infection. *Nanomedicine: NBM* **2020**, *23*, 102113, doi:10.1016/j.nano.2019.102113.
214. Almeida Furquim de Camargo, B.; Soares Silva, D.E.; Noronha da Silva, A.; Campos, D.L.; Machado Ribeiro, T.R.; Mieli, M.J.; Borges Teixeira Zanatta, M.; Bento da Silva, P.; Pavan, F.R.; Gallina Moreira, C., et al. New Silver(I) Coordination Compound Loaded into Polymeric Nanoparticles as a Strategy to Improve *In Vitro* Anti-*Helicobacter pylori* Activity. *Mol Pharmaceutics* **2020**, *17*, 2287-2298, doi:10.1021/acs.molpharmaceut.9b01264.
215. Eskin, A.; Öztürk, Ş.; Körükçü, M. Determination of the acute toxic effects of zinc oxide nanoparticles (ZnO NPs) in total hemocytes counts of *Galleria mellonella* (Lepidoptera: Pyralidae) with two different methods. *Ecotoxicology* **2019**, *28*, 801-808, doi:10.1007/s10646-019-02078-2.
216. Sezer Tuncsoy, B.; Tuncsoy, M.; Gomes, T.; Sousa, V.; Teixeira, M.R.; Bebianno, M.J.; Ozalp, P. Effects of Copper Oxide Nanoparticles on Tissue Accumulation and Antioxidant Enzymes of *Galleria mellonella* L. *Bull Environ Contam Toxicol* **2019**, *102*, 341-346, doi:10.1007/s00128-018-2529-8.
217. Barnoy, S.; Gancz, H.; Zhu, Y.; Honnold, C.L.; Zurawski, D.V.; Venkatesan, M.M. The *Galleria mellonella* larvae as an *in vivo* model for evaluation of *Shigella* virulence. *Gut Microbes* **2017**, *8*, 335-350, doi:10.1080/19490976.2017.1293225.
218. Parthuisot, N.; Rouquette, J.; Ferdy, J.B. A high-throughput technique to quantify bacterial pathogens' virulence on the insect model *Galleria mellonella*. *J Microbiol Methods* **2018**, *152*, 69-72, doi:10.1016/j.mimet.2018.07.013.
219. Campos-Silva, R.; Brust, F.R.; Trentin, D.S.; Macedo, A.J. Alternative method in *Galleria mellonella* larvae to study biofilm infection and treatment. *Microb Pathog* **2019**, *137*, 103756, doi:10.1016/j.micpath.2019.103756.
220. Entwistle, F.M.; Coote, P.J. Evaluation of greater wax moth larvae, *Galleria mellonella*, as a novel *in vivo* model for non-tuberculosis *Mycobacteria* infections and antibiotic treatments. *J Med Microbiol* **2018**, *67*, 585-597, doi:10.1099/jmm.0.000696.
221. Senior, N.J.; Titball, R.W. Isolation and primary culture of *Galleria mellonella* hemocytes for infection studies [version 1; peer review: awaiting peer review]. *F1000Research* **2020**, *9*, doi:10.12688/f1000research.27504.1.
222. Ariel, P. A beginner's guide to tissue clearing. *Int J Biochem Cell Biol* **2017**, *84*, 35-39, doi:10.1016/j.biocel.2016.12.009.
223. Tainaka, K.; Kuno, A.; Kubota, S.I.; Murakami, T.; Ueda, H.R. Chemical Principles in Tissue Clearing and Staining Protocols for Whole-Body Cell Profiling. *Annu Rev Cell Dev Biol* **2016**, *32*, 713-741, doi:10.1146/annurev-cellbio-111315-125001.
224. Richardson, D.S.; Lichtman, J.W. Clarifying Tissue Clearing. *Cell* **2015**, *162*, 246-257, doi:10.1016/j.cell.2015.06.067.
225. Manicam, C.; Pitz, S.; Brochhausen, C.; Grus, F.H.; Pfeiffer, N.; Gericke, A. Effective melanin depigmentation of human and murine ocular tissues: an improved method for paraffin and frozen sections. *PLoS One* **2014**, *9*, e102512, doi:10.1371/journal.pone.0102512.
226. Dodt, H.U.; Leischner, U.; Schierloh, A.; Jährling, N.; Mauch, C.P.; Deininger, K.; Deussing, J.M.; Eder, M.; Ziegglängsberger, W.; Becker, K. Ultramicroscopy: three-dimensional visualization of neuronal networks in the whole mouse brain. *Nat Methods* **2007**, *4*, 331-336, doi:10.1038/nmeth1036.

227. Costa, E.C.; Silva, D.N.; Moreira, A.F.; Correia, I.J. Optical clearing methods: An overview of the techniques used for the imaging of 3D spheroids. *Biotechnol Bioeng* **2019**, *116*, 2742-2763, doi:10.1002/bit.27105.
228. Costantini, I.; Ghobril, J.P.; Di Giovanna, A.P.; Allegra Mascaro, A.L.; Silvestri, L.; Müllenbroich, M.C.; Onofri, L.; Conti, V.; Vanzi, F.; Sacconi, L., et al. A versatile clearing agent for multi-modal brain imaging. *Sci Rep* **2015**, *5*, 9808, doi:10.1038/srep09808.
229. Yang, B.; Treweek, J.B.; Kulkarni, R.P.; Deverman, B.E.; Chen, C.K.; Lubeck, E.; Shah, S.; Cai, L.; Gradinaru, V. Single-cell phenotyping within transparent intact tissue through whole-body clearing. *Cell* **2014**, *158*, 945-958, doi:10.1016/j.cell.2014.07.017.
230. Pan, C.; Cai, R.; Quacquarelli, F.P.; Ghasemigharagoz, A.; Loubopoulos, A.; Matryba, P.; Plesnila, N.; Dichgans, M.; Hellal, F.; Ertürk, A. Shrinkage-mediated imaging of entire organs and organisms using uDISCO. *Nat Methods* **2016**, *13*, 859-867, doi:10.1038/nmeth.3964.
231. Becker, K.; Jährling, N.; Saghafi, S.; Weiler, R.; Dodt, H.U. Chemical clearing and dehydration of GFP expressing mouse brains. *PLoS One* **2012**, *7*, e33916, doi:10.1371/journal.pone.0033916.
232. Susaki, E.A.; Tainaka, K.; Perrin, D.; Kishino, F.; Tawara, T.; Watanabe, T.M.; Yokoyama, C.; Onoe, H.; Eguchi, M.; Yamaguchi, S., et al. Whole-brain imaging with single-cell resolution using chemical cocktails and computational analysis. *Cell* **2014**, *157*, 726-739, doi:10.1016/j.cell.2014.03.042.
233. Parra, S.G.; Chia, T.H.; Zinter, J.P.; Levene, M.J. Multiphoton microscopy of cleared mouse organs. *J Biomed Opt* **2010**, *15*, 036017, doi:10.1117/1.3454391.
234. Ertürk, A.; Becker, K.; Jährling, N.; Mauch, C.P.; Hojer, C.D.; Egen, J.G.; Hellal, F.; Bradke, F.; Sheng, M.; Dodt, H.U. Three-dimensional imaging of solvent-cleared organs using 3DISCO. *Nat Protoc* **2012**, *7*, 1983-1995, doi:10.1038/nprot.2012.119.
235. Renier, N.; Wu, Z.; Simon, D.J.; Yang, J.; Ariel, P.; Tessier-Lavigne, M. iDISCO: A Simple, Rapid Method to Immunolabel Large Tissue Samples for Volume Imaging. *Cell* **2014**, *159*, 896-910, doi:10.1016/j.cell.2014.10.010.
236. Jährling, N.; Becker, K.; Saghafi, S.; Dodt, H.U. Light-Sheet Fluorescence Microscopy: Chemical Clearing and Labeling Protocols for Ultramicroscopy. *Methods Mol Biol* **2017**, *1563*, 33-49, doi:10.1007/978-1-4939-6810-7_3.
237. McGurk, L.; Morrison, H.; Keegan, L.P.; Sharpe, J.; O'Connell, M.A. Three-dimensional imaging of *Drosophila melanogaster*. *PLoS One* **2007**, *2*, e834, doi:10.1371/journal.pone.0000834.
238. Smolla, M.; Ruchty, M.; Nagel, M.; Kleinedam, C.J. Clearing pigmented insect cuticle to investigate small insects' organs *in situ* using confocal laser-scanning microscopy (CLSM). *Arthropod Struct Dev* **2014**, *43*, 175-181, doi:10.1016/j.asd.2013.12.006.
239. Felix, P.M.; Gonçalves, A.; Vicente, J.R.; Fonseca, P.J.; Amorim, M.C.; Costa, J.L.; Martins, G.G. Optical micro-tomography "OPenT" allows the study of large toadfish *Halobatrachus didactylus* embryos and larvae. *Mech Dev* **2016**, *140*, 19-24, doi:10.1016/j.mod.2016.03.001.
240. Lee, E.; Choi, J.; Jo, Y.; Kim, J.Y.; Jang, Y.J.; Lee, H.M.; Kim, S.Y.; Lee, H.J.; Cho, K.; Jung, N., et al. ACT-PRESTO: Rapid and consistent tissue clearing and labeling method for 3-dimensional (3D) imaging. *Sci Rep* **2016**, *6*, 18631, doi:10.1038/srep18631.
241. Schroth, M.N.; Cho, J.J.; Green, S.K.; Kominos, S.D.; Microbiology Society Publishing. Epidemiology of *Pseudomonas aeruginosa* in agricultural areas. *J Med Microbiol* **2018**, *67*, 1191-1201, doi:10.1099/jmm.0.000758.
242. Bach-Griera, M.; Campo-Pérez, V.; Barbosa, S.; Traserra, S.; Guallar-Garrido, S.; Moya-Andérico, L.; Herrero-Abadía, P.; Luquin, M.; Rabanal, R.M.; Torrents, E., et al. *Mycolicibacterium brumae* Is a Safe and Non-Toxic Immunomodulatory Agent for Cancer Treatment. *Vaccines (Basel)* **2020**, *8*, doi:10.3390/vaccines8020198.

243. O'Toole, R.; Von Hofsten, J.; Rosqvist, R.; Olsson, P.E.; Wolf-Watz, H. Visualisation of zebrafish infection by GFP-labelled *Vibrio anguillarum*. *Microb Pathog* **2004**, *37*, 41-46, doi:10.1016/j.micpath.2004.03.001.
244. García-Cayuela, T.; de Cadiñanos, L.P.; Mohedano, M.L.; de Palencia, P.F.; Boden, D.; Wells, J.; Peláez, C.; López, P.; Requena, T. Fluorescent protein vectors for promoter analysis in lactic acid bacteria and *Escherichia coli*. *Appl Microbiol Biotechnol* **2012**, *96*, 171-181, doi:10.1007/s00253-012-4087-z.
245. Dreux, N.; del Mar Cendra, M.; Massier, S.; Darfeuille-Michaud, A.; Barnich, N.; Torrents, E. Ribonucleotide reductase NrdR as a novel regulator for motility and chemotaxis during adherent-invasive *Escherichia coli* infection. *Infect Immun* **2015**, *83*, 1305-1317, doi:10.1128/IAI.02772-14.
246. Sánchez-Quesada, C.; López-Biedma, A.; Warleta, F.; Campos, M.; Beltrán, G.; Gaforio, J.J. Bioactive properties of the main triterpenes found in olives, virgin olive oil, and leaves of *Olea europaea*. *J Agric Food Chem* **2013**, *61*, 12173-12182, doi:10.1021/jf403154e.
247. Pritchett, J.C.; Naesens, L.; Montoya, J. Chapter 19 - Treating HHV-6 Infections: The Laboratory Efficacy and Clinical Use of Anti-HHV-6 Agents. In *Human Herpesviruses HHV-6A, HHV-6B & HHV-7*, Third ed.; Flamand, L., Lautenschlager, I., Krueger, G.R.F., Ablashi, D.V., Eds. Elsevier: 2014; pp. 311-331.
248. Sanli, O.; Dobruch, J.; Knowles, M.A.; Burger, M.; Alemozaffar, M.; Nielsen, M.E.; Lotan, Y. Bladder cancer. *Nat Rev Dis Primers* **2017**, *3*, 17022, doi:10.1038/nrdp.2017.22.
249. Mukherjee, S.G.; O'Clonadh, N.; Casey, A.; Chambers, G. Comparative in vitro cytotoxicity study of silver nanoparticle on two mammalian cell lines. *Toxicol In Vitro* **2012**, *26*, 238-251, doi:10.1016/j.tiv.2011.12.004.
250. Luque-García, J.L.; Sánchez-Díaz, R.; Lopez-Heras, I.; Martín, P.; Camara, C. Bioanalytical strategies for *in-vitro* and *in-vivo* evaluation of the toxicity induced by metallic nanoparticles. *Trends in Analytical Chemistry* **2013**, *43*, 254-268, doi:10.1016/j.trac.2012.11.004.
251. Stebbing, A.R. Hormesis—the stimulation of growth by low levels of inhibitors. *Sci Total Environ* **1982**, *22*, 213-234, doi:10.1016/0048-9697(82)90066-3.
252. Moyano, D.F.; Liu, Y.; Ayaz, F.; Hou, S.; Puangploy, P.; Duncan, B.; Osborne, B.A.; Rotello, V.M. Immunomodulatory effects of coated gold nanoparticles in LPS-stimulated. *Chem* **2016**, *1*, 320-327, doi:10.1016/j.chempr.2016.07.007.
253. Wasserthal, L.T. Interaction of Circulation and Tracheal Ventilation in Holometabolous Insects. In *Advances in Insect Physiology*, Evans, P.D., Ed. Academic Press: 1996; pp. 297-351.
254. Kristensen, N. Arthropoda: Insecta. In *Lepidoptera: Moths and Butterflies. Handbuch der Zoologie Volume 4*, Kristensen, N., Ed. De Gruyter: 2003.
255. Bergin, D.; Brennan, M.; Kavanagh, K. Fluctuations in haemocyte density and microbial load may be used as indicators of fungal pathogenicity in larvae of *Galleria mellonella*. *Microbes Infect* **2003**, *5*, 1389-1395, doi:10.1016/j.micinf.2003.09.019.
256. Becker, K.; Jährling, N.; Saghafi, S.; Dodt, H.U. Dehydration and clearing of adult *Drosophila* for ultramicroscopy. *Cold Spring Harb Protoc* **2013**, *2013*, 681-682, doi:10.1101/pdb.prot075812.
257. Becker, K.; Jährling, N.; Saghafi, S.; Dodt, H.U. Dehydration and clearing of whole mouse brains and dissected hippocampi for ultramicroscopy. *Cold Spring Harb Protoc* **2013**, *2013*, 683-684, doi:10.1101/pdb.prot075820.
258. Yu, T.; Qi, Y.; Wang, J.; Feng, W.; Xu, J.; Zhu, J.; Yao, Y.; Gong, H.; Luo, Q.; Zhu, D. Rapid and prodium iodide-compatible optical clearing method for brain tissue based on sugar/sugar-alcohol. *J Biomed Opt* **2016**, *21*, 081203, doi:10.1117/1.JBO.21.8.081203.

APPENDIX

In this Appendix section, three supplementary figures are provided. These figures were not published in the articles but are necessary to support certain findings described in the Discussion section of this thesis.

Figure 1. Differences in virulence of different *P. aeruginosa* strains..... 135

Figure 2. Optimization of *S. aureus*, *M. brumae*, and *M. bovis* BCG infection doses using *G. mellonella* larvae 135

Figure 3. Toxicity assessment of *M. brumae* and *M. bovis* BCG using hemocytes from *G. mellonella* larvae 136

Figure 1. Kaplan-Meier survival curve of *G. mellonella* larvae infected with different *P. aeruginosa* strains. **A)** Comparison of doses between acute laboratory strains (PAO1 and PA14) and a chronic clinical strain (PAET1). Statistically significant difference seen with PA14 and PAET1 strains compared to the PAO1 strain in a Log-rank test (*: p -value <0.05, **: p -value <0.01). **B)** Comparison between acute and chronic clinical isolates using the same infection dose (20-40 CFU per larva).

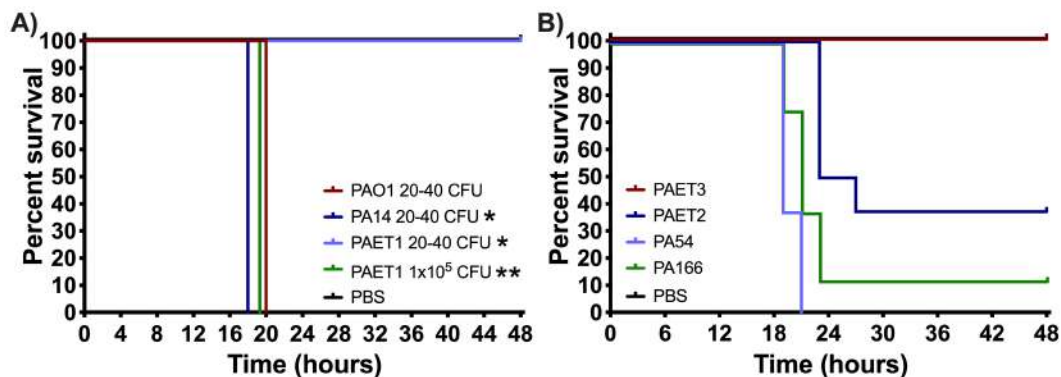


Figure 2. Kaplan-Meier survival curves of *G. mellonella* larvae infected with different concentrations of **A)** *S. aureus* and **B)** *M. brumae*. **C)** Final Kaplan-Meier survival curve using optimized dose of *M. brumae* and *M. bovis* BCG. *** p < 0.0005, **** p < 0.0001 (Mantel-Cox test). All concentrations tested are the number of CFU per larva.

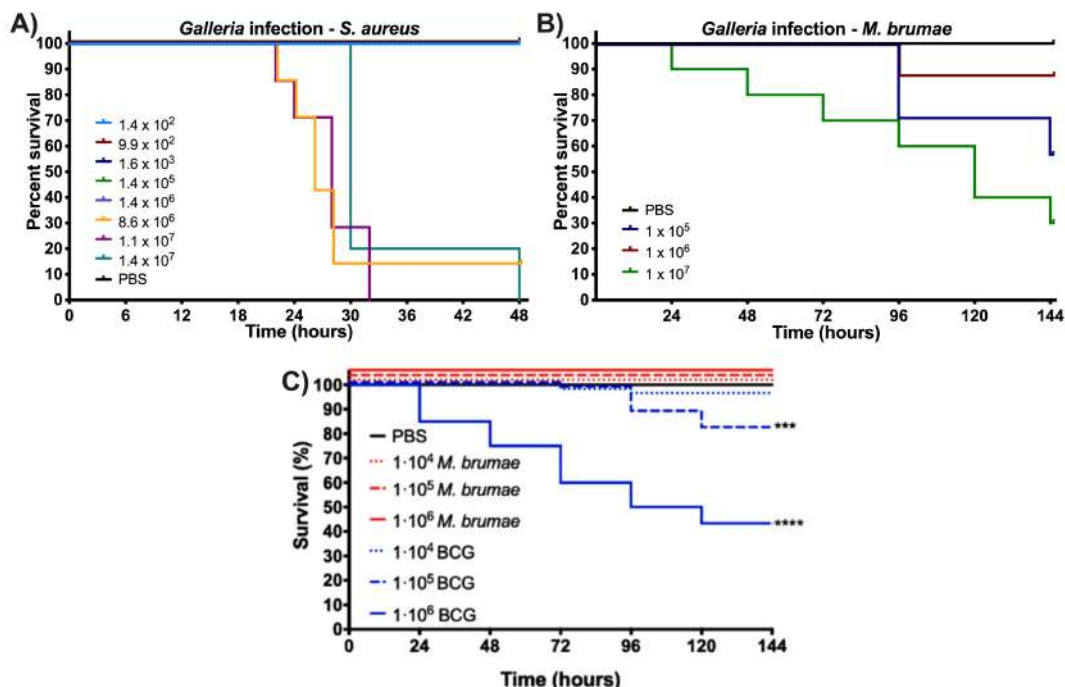


Figure 3. Bacterial burden recovered in hemolymph samples from *G. mellonella* larvae. Data are presented as the mean values \pm SD of the mycobacteria CFU counts. ** $p < 0.01$, **** $p < 0.0001$ (Kruskal-Wallis H test).

